

Fingerprinting Spin Liquids Using Spin Noise Spectroscopy

Hiroto Takahashi

Merton College
University of Oxford

*A thesis submitted for the degree of
Doctor of Philosophy*

Trinity 2024

Abstract

Spin liquids, not showing a spontaneous-symmetry-breaking order down to low temperature, serve as the platform for unconventional spin-correlated phenomena beyond the Landau paradigm. Numerous varieties of classical and quantum spin liquids (QSL) motivate the experimental identification of different spin liquid states. However, the lack of an unambiguous signature makes the identification attempts often unsuccessful. A new experimental approach is clearly needed, and an emerging concept is to use spin noise as the fingerprints of spin liquid states.

In this thesis, I perform spin noise spectroscopy on spin liquid compounds whose specific state has not been established. Chapter 1 presents an introduction to different classes of spin liquid states and the difficulty in their identification, motivating a new experimental approach. Chapter 2 explains the principle of spin noise spectroscopy, together with more conventional AC susceptometry. I also introduce a spin noise spectrometer that employs a Superconducting QUantum Interference Device (SQUID). In Chapter 3, I present the SQUID spin noise spectrometers that I designed and assembled during my DPhil. They have an extreme sensitivity approaching 10^{-14} T/ $\sqrt{\text{Hz}}$, broad bandwidth of DC to 100 kHz, and a temperature range of 10 mK to 6000 mK. I utilize them to study QSL candidate compounds with controversial spin liquid states. Chapter 4 presents the spin noise study of $\text{Ca}_{10}\text{Cr}_7\text{O}_{28}$, which has been hypothesized to be either a QSL or a spiral spin liquid (SSL). A powerful spin noise spanning a frequency range from 0.1 Hz to 50 kHz is discovered in $\text{Ca}_{10}\text{Cr}_7\text{O}_{28}$, and its overall correspondence with the prediction of SSL noise simulation evidences $\text{Ca}_{10}\text{Cr}_7\text{O}_{28}$ as a SSL. Lastly, Chapter 5 presents the spin noise study of $\text{ZnCu}_3(\text{OH})_6\text{Cl}_2$, an iconic QSL candidate with a spin-1/2 kagome lattice. Spins substituted in the interlayer are discovered to generate powerful spin noise spanning from 0.1 Hz to 100 Hz and to undergo a sharp transition at 260 mK. The experimental observations are consistent with spinon-mediated interactions between the interlayer spins, via the spectrum of spinons in a quantum spin liquid state within the kagome layer.

Fingerprinting Spin Liquids Using Spin Noise Spectroscopy



Hiroto Takahashi
Merton College
University of Oxford

A thesis submitted for the degree of
Doctor of Philosophy

Trinity 2024

Acknowledgements

First and foremost, I would like to thank my family, Toyomi, Shizuko, Masato, and Akito. Their love and support have been a source of motivation throughout my DPhil. This thesis is dedicated to them.

I spent most of my DPhil life in the Davis lab in Oxford. I had the great privilege of working with Chun-Chih Hsu, with whom I built the ^4He refrigerator and its integrated SQUID noise spectrometer (Andromeda). Fun discussions with him on physics and engineering were a continuous encouragement throughout my DPhil, for which I can be no more thankful. I am grateful to Fabian Jerzembeck for his continuous support and advice on the project. We had a good time dining when he visited us from Dresden. I enjoyed collaborating closely with Jack D. Enright and Jan Knapp. Their contributions to the installation of the ^3He refrigerator (Tertia) and the implementation of the custom low-temperature vibration isolator were essential for the successful development of the spin noise spectrometer. I would like to extend my gratitude to Wangping Ren, Weijiong Chen, and Shuqiu Wang, with whom I shared the COVID-19 era. Thanks to them, I had a productive research life and a lot of fun memories, even in the challenging times. I am also thankful to Ritika Dusad and Kent Shirer for their guidance, especially in the first year when I needed the most support. A special mention goes to Harris Pirie for teaching me valuable lessons on general scientific research and writing, as well as for our rivalry over favorite Formula 1 teams. Niall Kennedy, Yutong Dai, and Sam O'Sullivan were all cheerful colleagues whose company I really enjoyed. I thank Claudia Teixeira Azevedo and Elery Pellagatti for managing the finances. My sincere gratitude goes to Prof. Stephen J. Blundell for giving me theoretical guidance throughout the DPhil and supervising me for a Monte Carlo simulation. I would also like to thank all the staff of the Oxford physics department, especially Pierre Van Zijl, David Sharp, Robert Storey, Kieran McCall, Mike Tacon, Paul Bircher, Joe Tacon, and Johan Pretorius. Their support was essential to the successful construction and operation of the experimental apparatus.

I traveled to the Davis lab in Cork several times, staying there for almost three months in total. It was a great pleasure to collaborate with Jack Murphy and Jonathan Ward. Their contributions to the installation of the dilution refrigerator (Proteox) and the development of the spin noise spectrometer on the custom low-temperature vibration isolator were indispensable to the project's success. I thank

Catherine Dawson for cheerful support, especially in arranging frequent travel. I would also like to thank my spin noise colleagues, Jahnatta C. Dasini, Chaia Carroll, and Vincent Oliviero, for stimulating discussions and cheerful conversations. I would like to acknowledge labmates in Cork, Joseph P. Carroll, Jiahao Yan, Ge He, Huiyu Zhao, Jenny Davern, Patrick O'Callaghan, and Thomas Mohally, for their support.

I am deeply thankful to Pascal Puphal, Jürgen Nuss, Masahiko Isobe, Yosuke Matsumoto, and Prof. Hidenori Takagi at the Max Planck Institute for their support with the crystal synthesis and characterization. Without their expertise, I would not have been able to measure the compounds of interest. I thank Dharmalingam Prabhakaran for his help in crystal polishing. I am also grateful to Mitikorn (Ion) Wood-Thanan, Miguel Angel Sanchez Martinez, Michael R. Norman, and Felix Flicker for their contributions to the theoretical modeling and simulation of $\text{ZnCu}_3(\text{OH})_6\text{Cl}_2$. I would like to thank all the external collaborators who gave me valuable feedback on the projects, with special thanks to Jonathan N. Hallén.

Finally, I would like to express my sincere appreciation to my supervisor, Prof. J. C. Séamus Davis. His close and educative supervision, even day-to-day in the early years, provided a strong drive to advance the projects. I learned many valuable lessons by going through the entire experimental research process with him, from building the lab and equipment to performing measurements and analyzing data. I have been and will continue to be inspired by his enormous commitment to science.

Abstract

Spin liquids, not showing a spontaneous-symmetry-breaking order down to low temperature, serve as the platform for unconventional spin-correlated phenomena beyond the Landau paradigm. Numerous varieties of classical and quantum spin liquids (QSL) motivate the experimental identification of different spin liquid states. However, the lack of an unambiguous signature makes the identification attempts often unsuccessful. A new experimental approach is clearly needed, and an emerging concept is to use spin noise as the fingerprints of spin liquid states.

In this thesis, I perform spin noise spectroscopy on spin liquid compounds whose specific state has not been established. Chapter 1 presents an introduction to different classes of spin liquid states and the difficulty in their identification, motivating a new experimental approach. Chapter 2 explains the principle of spin noise spectroscopy, together with more conventional AC susceptometry. I also introduce a spin noise spectrometer that employs a Superconducting QUantum Interference Device (SQUID). In Chapter 3, I present the SQUID spin noise spectrometers that I designed and assembled during my DPhil. They have an extreme sensitivity approaching 10^{-14} T/ $\sqrt{\text{Hz}}$, broad bandwidth of DC to 100 kHz, and a temperature range of 10 mK to 6000 mK. I utilize them to study QSL candidate compounds with controversial spin liquid states. Chapter 4 presents the spin noise study of $\text{Ca}_{10}\text{Cr}_7\text{O}_{28}$, which has been hypothesized to be either a QSL or a spiral spin liquid (SSL). A powerful spin noise spanning a frequency range from 0.1 Hz to 50 kHz is discovered in $\text{Ca}_{10}\text{Cr}_7\text{O}_{28}$, and its overall correspondence with the prediction of SSL noise simulation evidences $\text{Ca}_{10}\text{Cr}_7\text{O}_{28}$ as a SSL. Lastly, Chapter 5 presents the spin noise study of $\text{ZnCu}_3(\text{OH})_6\text{Cl}_2$, an iconic QSL candidate with a spin-1/2 kagome lattice. Spins substituted in the interlayer are discovered to generate powerful spin noise spanning from 0.1 Hz to 100 Hz and to undergo a sharp transition at 260 mK. The experimental observations are consistent with spinon-mediated interactions between the interlayer spins, via the spectrum of spinons in a quantum spin liquid state within the kagome layer.

Contents

List of Figures	ix
List of Abbreviations	xiii
1 Fingerprinting Spin Liquids	1
1.1 Classical spin liquid	2
1.2 Quantum spin liquid	6
1.3 Non-spin-liquid where ordering is absent	13
1.4 Fingerprinting spin liquids with spin noise spectroscopy	15
2 Spin Noise Spectroscopy	21
2.1 Spin dynamics and AC susceptibility	21
2.2 Spin Noise	28
2.3 SQUID Spin Noise Spectrometer	38
2.4 Spin noise approach to fingerprinting different magnetic phases	48
3 SQUID Spin Noise Spectrometer	53
3.1 Spin noise spectrometer	53
3.2 Electronics	61
3.3 Vibration isolation	66
3.4 Refrigeration and sample thermalization	69
4 Spiral Spin Liquid Noise in $\text{Ca}_{10}\text{Cr}_7\text{O}_{28}$	75
4.1 Spin liquid candidate $\text{Ca}_{10}\text{Cr}_7\text{O}_{28}$	75
4.2 Quantum spin liquid or spiral spin liquid?	80
4.3 Prediction of quantum spin liquid noise and spiral spin liquid noise	81
4.4 Experiment	89
4.5 Experimental Analysis	94
4.6 Discussion	102

5	Spinon-Mediated Witness-Spin Interactions in $\text{ZnCu}_3(\text{OH})_6\text{Cl}_2$	107
5.1	Spin liquid candidate $\text{ZnCu}_3(\text{OH})_6\text{Cl}_2$	107
5.2	Prediction of witness-spin properties with spinon-mediated interactions	111
5.3	Experiment	117
5.4	Experimental Analysis	122
5.5	Discussion	128
 Appendices		
A	Derivations of equations	133
A.1	Relaxation time distribution for power-law AC susceptibility	133
A.2	AC susceptibility from Bloch equation	134
A.3	Spin noise spectrum from Bloch equation	135
A.4	Derivation of fluctuation-dissipation theorem	136
B	Technical details of spiral spin liquid simulation	139
B.1	Correspondence between Monte Carlo step and actual time	139
B.2	Estimate of magnetization noise from spin noise	140
B.3	Analysis of noise signal	141
C	Spiral spin liquid noise simulation for three-dimensional spins	143
References		145

List of Figures

1.1	Schematics of geometrically-frustrated classical spin liquids	3
1.2	Schematics of spiral spin liquid	5
1.3	Schematics of mean-field ansatz in parton construction	12
1.4	Schematics of non-ordered states that are not called spin liquids . .	14
2.1	Concept of AC susceptibility	25
2.2	Typical AC susceptibility of system with single relaxation time . . .	26
2.3	Concept of spin noise	29
2.4	Noise of system with single relaxation time	36
2.5	Examples of noise power spectral density	37
2.6	Basics of SQUID	39
2.7	Flux-locked loop and flux-modulation technique	42
2.8	Schematics of SQUID spin noise spectrometer and susceptometer .	46
3.1	Overview photo of SQUID spin noise spectrometers	54
3.2	Photos of pickup coils	55
3.3	Calibration of field coil	59
3.4	Electronics circuit of spin noise spectrometer and susceptometer . .	62
3.5	Transfer function and noise floor of SQ1200 SQUID	63
3.6	Voltage noise of electronics	65
3.7	Vibration isolator performance in ^3He and dilution refrigerators . .	69
3.8	Schematics of refrigerators	70
4.1	Bilayer kagome lattice of $\text{Ca}_{10}\text{Cr}_7\text{O}_{28}$	76
4.2	Spin liquid phenomena in $\text{Ca}_{10}\text{Cr}_7\text{O}_{28}$	77
4.3	Effective monolayer honeycomb network of $\text{Ca}_{10}\text{Cr}_7\text{O}_{28}$	79
4.4	Visualization of spins in equilibration process of spiral spin liquid Monte Carlo simulation	83
4.5	Simulated spiral spin liquid noise $\bar{\theta}_{x,y}(t_k, T)$	85
4.6	Power spectral density $S_{\bar{\theta}_x}(\omega_j, T)$ and normalized correlation func- tion $C_{\bar{\theta}_x}(t_k, T)/C_{\bar{\theta}_x}(0, T)$ of simulated spiral spin liquid noise $\bar{\theta}_x(t_k, T)$	87
4.7	Frequency power law $S_{\bar{\theta}_{x,y}}(\omega, T) \propto \omega^{-\alpha(T)}$ and variance $\sigma_{\bar{\theta}_{x,y}}^2(T)$ of simulated spiral spin liquid noise $\bar{\theta}_{x,y}(t_k, T)$	88

4.8	Synthesis of $\text{Ca}_{10}\text{Cr}_7\text{O}_{28}$ single crystals	90
4.9	Measured flux noise $\Phi(t_k, T)$ of $\text{Ca}_{10}\text{Cr}_7\text{O}_{28}$	92
4.10	Measured AC susceptibility of $\text{Ca}_{10}\text{Cr}_7\text{O}_{28}$	94
4.11	Contour plot of power spectral density $S_\Phi(\omega_j, T)$ of measured $\text{Ca}_{10}\text{Cr}_7\text{O}_{28}$ flux noise $\Phi(t_k, T)$	95
4.12	Power spectral density $S_\Phi(\omega_j, T)$ and normalized correlation function $C_\Phi(t_k, T)/C_\Phi(0, T)$ of measured $\text{Ca}_{10}\text{Cr}_7\text{O}_{28}$ flux noise $\Phi(t_k, T)$	96
4.13	Power spectral density $S_\Phi(\omega_j, T)$ of measured $\text{Ca}_{10}\text{Cr}_7\text{O}_{28}$ flux noise $\Phi(t_k, T)$ in extended frequency range	97
4.14	Frequency power law $S_\Phi(\omega, T) \propto \omega^{-\alpha(T)}$ and variance $\sigma_\Phi^2(T)$ of measured $\text{Ca}_{10}\text{Cr}_7\text{O}_{28}$ flux noise $\Phi(t_k, T)$	98
4.15	Fluctuation-dissipation theorem in $\text{Ca}_{10}\text{Cr}_7\text{O}_{28}$	99
4.16	Comparison of spin noise measured in three $\text{Ca}_{10}\text{Cr}_7\text{O}_{28}$ samples and a nylon sample	101
4.17	Power spectral density $S_{\bar{\theta}_x}(\omega_j, T)$ of simulated spiral spin liquid noise and $S_\Phi(\omega_j, T)$ of measured $\text{Ca}_{10}\text{Cr}_7\text{O}_{28}$ noise below T^*	102
5.1	Crystal lattice of $\text{ZnCu}_3(\text{OH})_6\text{Cl}_2$	108
5.2	Spin liquid phenomena in $\text{ZnCu}_3(\text{OH})_6\text{Cl}_2$	109
5.3	Spinon-mediated interactions among witness-spins	112
5.4	Power spectral density $S_{\bar{\theta}}(\omega)$ of witness-spin noise $\bar{\theta}(t)$ in spinon-mediated interaction simulation	114
5.5	Frequency power law $S_{\bar{\theta}}(\omega) \propto \omega^{-\alpha(T)}$ of witness-spin noise $\bar{\theta}(t)$ in spinon-mediated interaction simulation	115
5.6	DC susceptibility of witness-spins in spinon-mediated interaction simulation	116
5.7	Synthesis of $\text{ZnCu}_3(\text{OH})_6\text{Cl}_2$ single crystals	118
5.8	Measured flux noise $\Phi(t, T)$ of $\text{ZnCu}_3(\text{OH})_6\text{Cl}_2$ at 260 mK	120
5.9	Measured DC susceptibility of $\text{ZnCu}_3(\text{OH})_6\text{Cl}_2$	121
5.10	Measured squared flux noise $\Phi^2(t_k, T)$ of $\text{ZnCu}_3(\text{OH})_6\text{Cl}_2$ at different temperatures and distribution of $\Phi(t_k, T)$	122
5.11	Power spectral density $S_\Phi(\omega_j, T)$ of measured $\text{ZnCu}_3(\text{OH})_6\text{Cl}_2$ flux noise $\Phi(t_k, T)$	123
5.12	Frequency power law $S_\Phi(\omega, T) \propto \omega^{-\alpha(T)}$ and variance $\sigma_\Phi^2(T)$ of measured $\text{ZnCu}_3(\text{OH})_6\text{Cl}_2$ flux noise $\Phi(t_k, T)$	124
5.13	Long-term evolution of $\text{ZnCu}_3(\text{OH})_6\text{Cl}_2$ flux noise variance σ_Φ^2 and average DC flux Φ after sudden temperature drop from 400 mK	126
5.14	Comparison of spin noise measured in three $\text{ZnCu}_3(\text{OH})_6\text{Cl}_2$ samples and background noise	127

5.15	Comparison between $\text{ZnCu}_3(\text{OH})_6\text{Cl}_2$ measurement and witness-spin simulation with spinon-mediated interactions for DC susceptibility $\chi(T)$ and frequency-power-law exponent $\alpha(T)$	129
B.1	Spin flip rate in spiral spin liquid Monte Carlo simulation	140
C.1	Spiral spin liquid noise simulation for three-dimensional spins	144

List of Abbreviations

QSL	Quantum Spin Liquid
SSL	Spiral Spin Liquid
LSM	Lieb–Schultz–Mattis
IGG	Invariant Gauge Group
RKKY	Ruderman–Kittel–Kasuya–Yosida
FM	Ferromagnet or Ferromagnetic
AF	Antiferromagnet or Antiferromagnetic
1D	One-dimensional
2D	Two-dimensional
3D	Three-dimensional
SQUID	Superconducting Quantum Interference Device
DC	Direct Current
AC	Alternating Current
MC	Monte Carlo
PSD	Power Spectral Density

1

Fingerprinting Spin Liquids

Correlated spin systems exhibit a variety of phenomena. While spins are fully paramagnetic at high temperatures to maximize entropy, as the temperature is lowered, they tend to show correlated behaviors to minimize spin interaction energy. One of the most prominent examples of such low-temperature phases is a spontaneously-symmetry-broken phase, such as a ferromagnetic or antiferromagnetic state. These states have a finite local order parameter and have been given a general and straightforward explanation by the Ginzburg-Landau theory. A symmetry-breaking phase transition has defining signatures, such as a sharp transition peak in thermodynamic quantities (e.g. specific heat), which is usually identifiable in an experiment.

On the other hand, there are spin systems that do not show a symmetry-breaking order down to low temperature, even way below the spin interaction energy scale. A combination of geometric frustration, competing interactions, and low dimensionality prevent interacting spins from forming a local order parameter. Such a correlated spin phase without a symmetry-breaking order is altogether called a spin liquid [1–3].¹ In some systems, a symmetry-breaking phase transition is not detected at all down to the lowest temperatures so far accessed by an experiment. In other systems, a transition is observed at a finite temperature T_c , but T_c is

¹This is the conventional and most broad definition of spin liquid. In recent years, the term spin liquid is sometimes used in a more restricted manner, for example, to primarily refer to a quantum spin liquid with long-range quantum entanglement [3, 4].

much lower than the Curie-Weiss temperature T_{CW} that represents the scale of spin interaction energy. A parameter $f = |T_{\text{CW}}|/T_c$ [1] is useful to quantify the extent of frustration, and it can be as large as 1000 in certain compounds [5]. Spin liquid behavior in the temperature range $T_c \leq T \leq |T_{\text{CW}}|$ is expected to be distinct from that of a paramagnet or a symmetry-breaking ordered phase, and should have characteristics beyond the paradigm of Ginzburg-Landau theory.

Spin liquids indeed turn out to be a platform for diverse exotic phenomena. One example is a frustrated spin system with extensive ground state degeneracy. Fluctuations among the degenerate states can give rise to a peculiar behavior, for example, an algebraic (power-law) spin correlation function that is typically expected only in the proximity of critical points [6, 7]. Another example is the formation of topological order or, more generally, quantum order, which is a non-local order robust to a local perturbation [8]. A quantum order often shows unique properties originating from emergent gauge fields and fractional quasiparticles.

In the following sections, I will introduce two major classes of spin liquids: a classical spin liquid and a quantum spin liquid (QSL). I will also present several non-ordered phases that are typically not called spin liquids, although they deserve to be in the most broad definition. As will become clear, there are many different types of spin liquids, and they are by no means fully described by just an absence of an order. However, due to the lack of an explicit signature, such as a local order parameter in a spontaneously-symmetry-broken phase, identifying spin liquid types in a specific system/compound has been difficult. This thesis aims to present some new steps toward the long-term goal of achieving spin liquid identification.

1.1 Classical spin liquid

A classical spin liquid is a type of spin liquid that has extensively/sub-extensively degenerate classical ground states. The massive degeneracy leads to unique properties such as zero-point entropy and (sometimes) algebraic spin correlations. A comprehensive classification scheme of a classical spin liquid has not been established and is recently being worked out [7, 9, 10]. Here, I provide two examples that

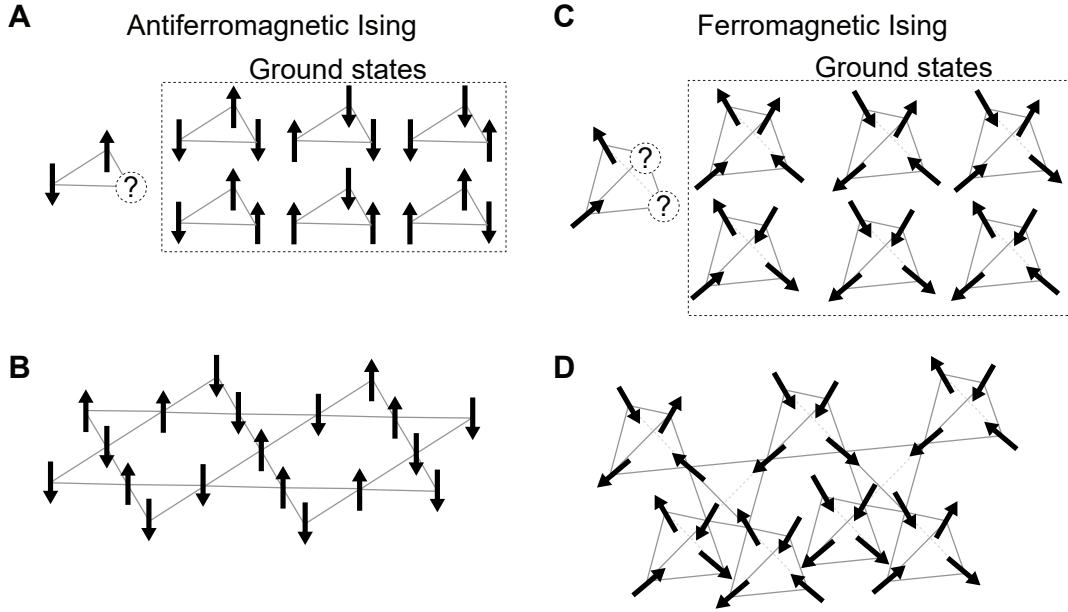


Figure 1.1: (A) Ising spins coupled antiferromagnetically on a triangle. The antiferromagnetic bonds cannot be simultaneously satisfied, so the spins are geometrically frustrated. The ground states are six-fold degenerate two-up-one-down or one-up-two-down configurations. (B) Frustrated Ising spins coupled antiferromagnetically on a kagome lattice comprising corner-shared triangles. (C) Ising spins coupled ferromagnetically on a tetrahedron. The easy axis of each Ising spin is toward the tetrahedron center. The ferromagnetic bonds cannot be simultaneously satisfied, so there is frustration. The ground states are six-fold degenerate two-in-two-out configurations. (D) Frustrated Ising spins coupled ferromagnetically on a pyrochlore lattice comprising corner-shared tetrahedra, realizing the so-called spin ice state.

illustrate the concept of classical spin liquids: geometrically frustrated spin liquids with extensive degeneracy and a spiral spin liquid with sub-extensive degeneracy.

1.1.1 Geometrically frustrated classical spin liquid

Geometrical frustration is a typical source of extensive degeneracy [1, 6]. Consider a case where three Ising spins at the vertices of a triangle interact antiferromagnetically. Two-up-one-down or one-up-two-down configurations minimize the energy. Thus, six out of possible $2^3 = 8$ states are degenerate ground states as shown in Fig. 1.1A. When the spins are on a kagome lattice comprised of corner-shared triangles as shown in Fig. 1.1B, the number of degenerate ground states increases exponentially to the number of triangles. This system thus has extensive degeneracy of ground states leading to zero-point entropy.

Four Ising spins at the vertices of a tetrahedron can also get geometrically frustrated. As shown in Fig. 1.1C, when the spin easy-axis is toward the center of the tetrahedron and interactions are ferromagnetic, two-in-two-out configurations minimize the energy. Thus, six out of possible $2^4 = 16$ states are degenerate. The ferromagnetic Ising model on a pyrochlore lattice comprises corner-shared tetrahedra of the two-in-two-out configurations as shown in Fig. 1.1D. This model is called spin ice in analogy to the two-covalent-bond-two-hydrogen-bond configuration of water ice. Spin ice shows various unique properties. It has extensive ground state degeneracy and exhibits characteristic power-law decaying spatial correlations [6]. The coarse-grained spin field $\mathbf{P}(\mathbf{r})$ satisfies the constraint $\nabla \cdot \mathbf{P}(\mathbf{r}) = 0$, which naturally introduces an emergent gauge field $\mathbf{A}(\mathbf{r})$ as $\mathbf{P}(\mathbf{r}) = \nabla \times \mathbf{A}(\mathbf{r})$. One spin-flip excitation fractionalizes into two magnetic monopole quasiparticles [6, 11, 12]. The signature of such magnetic monopoles has been observed in the paradigmatic spin ice compounds $\text{Dy}_2\text{Ti}_2\text{O}_7$ [13–15] and $\text{Ho}_2\text{Ti}_2\text{O}_7$ [16].

1.1.2 Spiral spin liquid

A spiral spin liquid [17, 18] is a class of classical spin liquid distinct from the geometrically frustrated case. Each degenerate ground state is a spiral spin configuration with a certain wavevector \mathbf{Q} . The degenerate-ground-state wavevectors form a continuous ‘spiral contour’ such as a ring in reciprocal space as shown in Fig. 1.2A. Such a spiral contour is experimentally observed in for example the 2D honeycomb lattice of FeCl_3 [19] and the 3D diamond lattices of MnSc_2S_4 [20] and LiYbO_2 [21]. Spin fluctuations persist down to low temperature via the \mathbf{Q} -direction fluctuations.

The degeneracy is sub-extensive, and the ground states are non-locally connected by a global rotation of the spiral direction. This is distinct from a geometrically frustrated case, where the degeneracy is extensive and the system hops among different ground states by flipping several local spins. A peculiar type of local vortex is predicted to appear in a spiral spin liquid [22]. A ‘momentum field’ (\sim spiral wavevector field) can be defined as the gradient of spins in a coarse-grained lattice, and there exists a topological defect of the momentum field dubbed

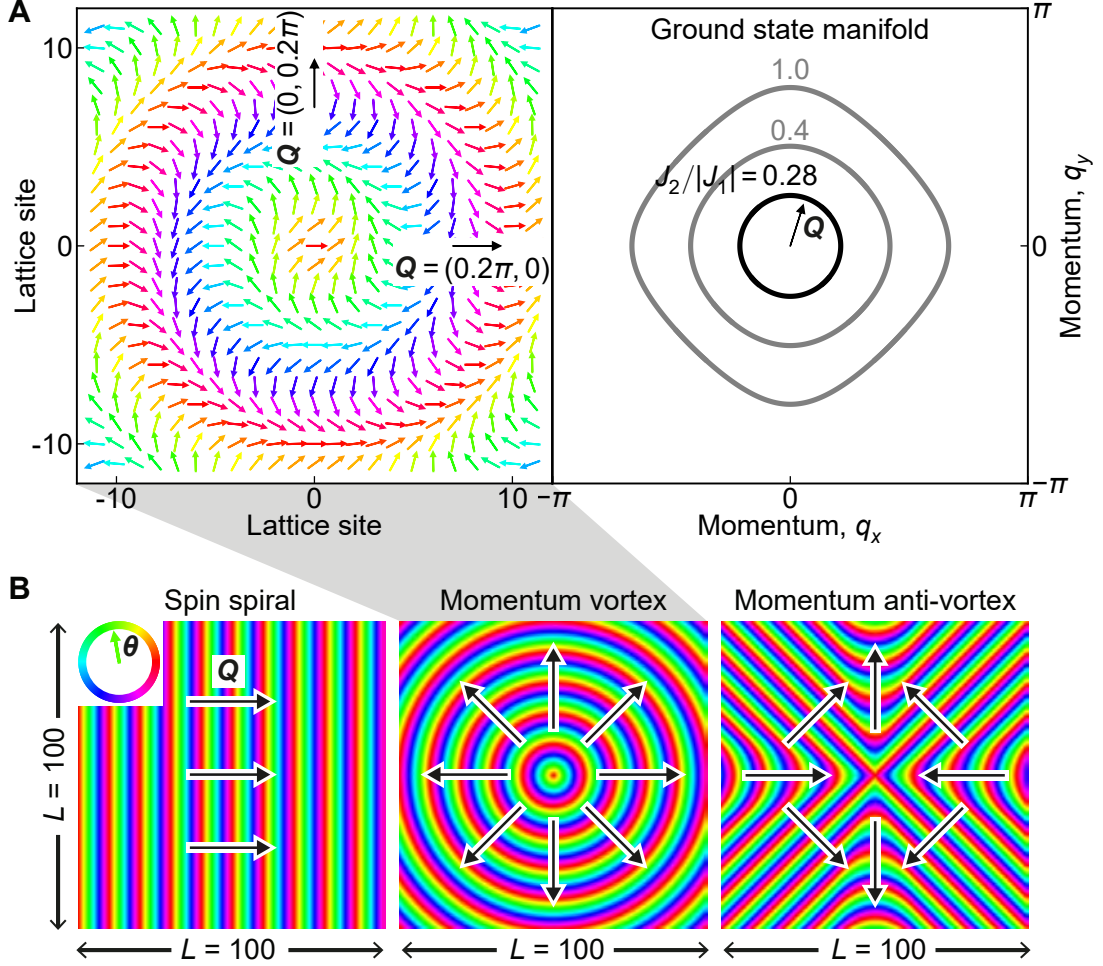


Figure 1.2: (A) Left: Schematic of a spin spiral in different directions. In a spiral spin liquid, the wavevector \mathbf{Q} of a ground-state spin spiral (black arrow) can point at any in-plane angle θ . The spin configuration shown here corresponds to a topological defect called a momentum vortex — the change of wavevector angle θ on any trajectory surrounding the center accumulates to $\int \nabla \theta \cdot d\mathbf{l} = 2\pi$. Right: Spiral contours formed by the degenerate-ground-state wavevector \mathbf{Q} of spiral spin liquid Hamiltonians (Eq. 4.3 for the different parameter values of J_2/J_1). (B) Schematic of spin configurations in the three simple cases of a spiral spin liquid. Left: a spin spiral without topological defects. Centre: a simple momentum vortex. Right: a simple momentum anti-vortex. Figures reproduced from Ref. [23] with a minor modification.

as a ‘momentum vortex,’ as illustrated in Fig. 1.2B. The momentum vortex is different from a spin vortex, and is predicted to govern the low-energy dynamics of a spiral spin liquid [22].

1.2 Quantum spin liquid

A quantum spin liquid (QSL) [3, 4, 8, 24, 25] is a state with long-range quantum entanglement, which cannot be disentangled into a product state by local transformations. Different patterns of long-range entanglement give rise to different types of QSL. A key signature shared by many QSL models is fractionalized quasiparticle excitations, which usually appear as a consequence of exotic long-range quantum entanglement. Detection of fractionalized quasiparticles is typically regarded as an experimental smoking gun of a QSL,² as a direct experimental probe of long-range entanglement has yet to be established.

A QSL is primarily categorized by whether or not the excitation spectrum is gapped. A gapped QSL is unambiguously characterized by a topological theory and is shown to have well-defined emergent quasiparticles. A gapless QSL is theoretically more complex but is also predicted to host rich physics, often admitting a quasiparticle description and exhibiting power-law correlations. As the theoretical framework to describe a general QSL, the low-energy effective theory involving emergent gauge fields has been found useful. When formulating particle fractionalization that is normally an unphysical process, a gauge field has to naturally emerge to keep the state physical. Deconfinement of emergent gauge fields leads to successful particle fractionalization, and the gauge structure combined with the symmetry operation can classify different types of QSL (projective symmetry group [8])

There are a few QSL states whose existence is established by an exactly solvable model, such as the Z_2 gapped QSL in the toric code model [24, 26] and the Z_2 gapless/gapped QSL in the Kitaev model [24, 27]. The existence of other types of QSL, such as a $U(1)/Z_2$ Dirac/Fermi surface spinon QSL, is proposed mostly from the mean-field solutions of a Heisenberg Hamiltonian in the parton construction, as discussed below. From a different perspective, a QSL state is presumed to

²There is a caveat that quantum entanglement is not the only route that gives rise to fractionalization. One example is the magnetic monopole quasiparticle excitations in a classical spin ice.

exist in a model satisfying the following conditions and not showing a symmetry-breaking order [24]: a local SU(2)-invariant spin Hamiltonian on a translationally invariant lattice, a total half-integer spin per unit cell, and periodic boundary conditions. In such a model, the Lieb-Schultz-Mattis (LSM) theorem [28] generally proves that there is either a ground state degeneracy or a bulk gapless excitation. Aside from symmetry-breaking order, topological order and non-trivial long-range entanglement are the prime known mechanisms that can protect the ground state degeneracy and the gapless excitation, respectively [24].

To illustrate the notions of a QSL explained so far, here I concisely introduce the parton construction of a Heisenberg Hamiltonian, which predicts QSLs of different gauge structures harboring spinon excitations.

1.2.1 Spinon quantum spin liquids from parton construction

Concept of parton construction

Using the parton construction [8, 24, 25], one can attempt to find a QSL state even when the model is not exactly solvable. The basic idea is to forcedly fractionalize spins by representing them as canonical bosons or fermions. For example, one can introduce Abrikosov fermions to represent spin-1/2 operators.

$$\hat{\mathbf{S}}_i = \frac{1}{2} \hat{f}_{i\alpha}^\dagger \boldsymbol{\sigma}_{\alpha\beta} \hat{f}_{i\beta}, \quad (1.1)$$

$$\text{where } \hat{f}_{i\alpha}^\dagger \hat{f}_{i\alpha} = 1, \quad (1.2)$$

$$\epsilon_{\alpha\beta} \hat{f}_{i\alpha} \hat{f}_{i\beta} = 0. \quad (1.3)$$

The Einstein summation convention is used. $\alpha, \beta = \uparrow, \downarrow$ are spin indices, $\boldsymbol{\sigma}_{\alpha\beta}$ represents the Pauli matrices, and $\epsilon_{\alpha\beta}$ is the antisymmetric tensor. From now on, I call the fractionalized particle created by $\hat{f}_{i\alpha}^\dagger$ a (fermionic) spinon. The spin operator expressed by the spinon operators has a local SU(2) gauge structure, which becomes clear by defining a matrix

$$\Psi_i = \begin{pmatrix} \hat{f}_{i\uparrow} & \hat{f}_{i\downarrow}^\dagger \\ \hat{f}_{i\downarrow} & -\hat{f}_{i\uparrow}^\dagger \end{pmatrix} \quad (1.4)$$

and rewriting the spin operator as

$$\hat{\mathbf{S}}_i = \frac{1}{4} \text{Tr}(\Psi_i^\dagger \boldsymbol{\sigma} \Psi_i), \quad (1.5)$$

$$\text{where } \text{Tr}(\Psi_i \boldsymbol{\sigma} \Psi_i^\dagger) = 0. \quad (1.6)$$

The equations are invariant under the following SU(2) transformation

$$\Psi_i \rightarrow \Psi'_i = \Psi_i W_i, \quad W_i \in \text{SU}(2). \quad (1.7)$$

The fermionic spinon representation of spins in Eq. 1.1 introduces redundant degrees of freedom and expands the Hilbert space. To remove the unphysical redundancy in the Hilbert space, namely the zero-spinon-occupancy and double-spinon-occupancy states, an infinite number of local constraints (Eqs. 1.2 and 1.3) exist. As the local constraints confine the fractionalized spinons back into the original spin state, the forced fractionalization usually does not lead to anything new. However, in a special case with long-range quantum entanglement (i.e. a QSL state), the fractionalized spinons may stay deconfined and get their own life despite the local constraints. This approach to obtaining a QSL state with fractionalized particles is called the parton construction. The parton construction has been demonstrated to be valid in the exactly solvable Kitaev honeycomb model, where the fractionalized Majorana particles get their own life in a \mathbb{Z}_2 QSL. Here, I discuss the parton construction of a Heisenberg model leading to QSLs of different gauge structures.

Mean-field solutions of Heisenberg model in parton construction

The Hamiltonian of an $S = 1/2$ antiferromagnetic Heisenberg model is rewritten by the fermionic spinon as follows.

$$\hat{H}_0 = J \sum_{\langle ij \rangle} \hat{\mathbf{S}}_i \cdot \hat{\mathbf{S}}_j = J \sum_{\langle ij \rangle} \frac{1}{4} \hat{f}_{i\alpha}^\dagger \boldsymbol{\sigma}_{\alpha\beta} \hat{f}_{i\beta} \cdot \hat{f}_{j\gamma}^\dagger \boldsymbol{\sigma}_{\gamma\delta} \hat{f}_{j\delta} \quad (1.8)$$

$$= J \sum_{\langle ij \rangle} \frac{1}{2} \hat{f}_{i\alpha}^\dagger \hat{f}_{i\beta} \hat{f}_{j\beta}^\dagger \hat{f}_{j\alpha} - J \sum_{\langle ij \rangle} \frac{1}{4} \hat{f}_{i\alpha}^\dagger \hat{f}_{i\alpha} \hat{f}_{j\beta}^\dagger \hat{f}_{j\beta}. \quad (1.9)$$

The infinite number of local constraints (Eqs. 1.2 and 1.3) make it difficult to solve the problem. One way is to solve the Hamiltonian forgetting the local constraints,

and then later perform the Gutzwiller projection $|\Psi\rangle \rightarrow P_G |\Psi\rangle$ that maps the solution to a physical state [24, 25]. Another way is to account for the local constraints by adding gauge field operators³ as

$$\hat{H} = \hat{H}_0 + \sum_i \left[\hat{a}_i^3 (\hat{f}_{i\alpha}^\dagger \hat{f}_{i\alpha} - 1) + \hat{a}_i^1 (\hat{f}_{i\alpha} \hat{f}_{i\beta} \epsilon_{\alpha\beta} + \text{h.c.}) + \hat{a}_i^2 i (\hat{f}_{i\alpha} \hat{f}_{i\beta} \epsilon_{\alpha\beta} - \text{h.c.}) \right] \quad (1.10)$$

$$= \hat{H}_0 + \sum_i \left[\hat{a}_i^3 (\hat{f}_{i\alpha}^\dagger \hat{f}_{i\alpha} - 1) + \left((\hat{a}_i^1 + i\hat{a}_i^2) \hat{f}_{i\alpha} \hat{f}_{i\beta} \epsilon_{\alpha\beta} + \text{h.c.} \right) \right]. \quad (1.11)$$

The gauge field operators can be regarded as Lagrange multipliers that will impose the local constraints Eqs. 1.2 and 1.3.⁴

A mean-field approximation can be used to solve the Hamiltonian \hat{H} . Assuming that the following equal-time expectation values acquire finite values,

$$\langle \hat{f}_{i\alpha} \hat{f}_{j\beta} \rangle = -\frac{1}{2} \eta_{ij} \epsilon_{\alpha\beta}, \quad (1.13)$$

$$\langle \hat{f}_{i\alpha}^\dagger \hat{f}_{j\beta} \rangle = \frac{1}{2} \chi_{ij} \delta_{\alpha\beta}, \quad (1.14)$$

$$\langle \hat{a}_i^l \rangle = a_i^l, \quad (1.15)$$

the general form of the mean-field Hamiltonian is obtained as

$$H_{\text{MF}} = - \sum_{ij} \frac{3}{8} J \left[(\chi_{ji} \hat{f}_{i\alpha}^\dagger \hat{f}_{j\alpha} + \eta_{ij} \hat{f}_{i\alpha}^\dagger \hat{f}_{j\beta} \epsilon_{\alpha\beta} + \text{h.c.}) - |\chi_{ij}|^2 - |\eta_{ij}|^2 \right] \quad (1.16)$$

$$+ \sum_i \left[a_i^3 (\hat{f}_{i\alpha}^\dagger \hat{f}_{i\alpha} - 1) + \left((a_i^1 + i a_i^2) \hat{f}_{i\alpha} \hat{f}_{i\beta} \epsilon_{\alpha\beta} + \text{h.c.} \right) \right]. \quad (1.17)$$

Note that changing the gauge field operators into the c-numbers (Eq. 1.15) has loosened the local constraints to the equilibrium version $\hat{f}_{i\alpha}^\dagger \hat{f}_{i\alpha} = 1 \rightarrow \langle \hat{f}_{i\alpha}^\dagger \hat{f}_{i\alpha} \rangle = 1$.

³The operators \hat{a}_i are called ‘gauge’ fields due to the following logic. The original Hamiltonian (Eq. 1.9) is invariant under the SU(2) transformation of the spinon operators (Eq. 1.7), and it is natural to impose the same gauge invariance to the Hamiltonian including the local constraints (Eq. 1.11). To ensure the gauge invariance, the ‘gauge’ fields \hat{a}_i transform together with the spinon operators (corresponding to the ‘matter’ fields), as later described in Eq. 1.20.

⁴The role of the gauge fields becomes clearer in the path integral formulation. Using coherent states satisfying $\hat{f}_{i\alpha} |f_{i\alpha}\rangle = f_{i\alpha} |f_{i\alpha}\rangle$ and $\hat{a}_i |a_i\rangle = a_i |a_i\rangle$, the partition function is expressed as

$$Z = \int \mathcal{D}[f, \bar{f}; a] \exp \left[- \int_0^\beta d\tau \left(\sum_{i\alpha} \bar{f}_{i\alpha} \partial_\tau f_{i\alpha} - H(f, \bar{f}; ia) \right) \right]. \quad (1.12)$$

Here, the operators are changed to the c-numbers as $f_{i\alpha}(\tau) = \langle f_{i\alpha, n} | \hat{f}_{i\alpha} | f_{i\alpha, n} \rangle$, $\bar{f}_{i\alpha}(\tau) = \langle f_{i\alpha, n} | \hat{f}_{i\alpha}^\dagger | f_{i\alpha, n} \rangle$, and $a_i(\tau) = \langle a_{i, n} | \hat{a}_i | a_{i, n} \rangle$, where $\tau = n\Delta t$ ($\Delta t \rightarrow 0$). When the gauge fields $a_i^1(t)$, $a_i^2(t)$, and $a_i^3(t)$ are integrated out, they give rise to delta functions that revive the local constraints Eqs. 1.2 and 1.3.

The obtained mean-field solution needs to undergo the Gutzwiller projection to be a physical state for certain. Also note that the mean-field solution is not necessarily reliable, even qualitatively, as the (gauge⁵) fluctuations of χ_{ij} , η_{ij} , and a_i^l around the mean-field value could drastically alter the solution. Accounting for the fluctuations of a_i^l is equivalent to reviving the original local constraints. Accounting for the fluctuations of χ_{ij} and η_{ij} is equivalent to reviving the original Hamiltonian. The mean-field solution is guaranteed to be reliable only when these fluctuations are weak, namely when the fluctuation modes are fully gapped.

The mean-field Hamiltonian should retain the SU(2) gauge structure originating from that of the fermionic representation (Eq. 1.7). By defining the matrices

$$\psi_i = \begin{pmatrix} \hat{f}_{i\uparrow} \\ \hat{f}_{i\downarrow} \end{pmatrix}, \quad U_{ij} = \begin{pmatrix} \chi_{ij}^* & \eta_{ij} \\ \eta_{ij}^* & -\chi_{ij} \end{pmatrix}, \quad (1.18)$$

the mean-field Hamiltonian can be rewritten as

$$H_{\text{MF}} = - \sum_{ij} \frac{3}{8} J \left[(\psi_i^\dagger U_{ij} \psi_j + \text{h.c.}) - \frac{1}{2} \text{Tr}(U_{ij}^\dagger U_{ij}) \right] + \sum_i \mathbf{a}_i \cdot (\psi_i^\dagger \boldsymbol{\sigma} \psi_i). \quad (1.19)$$

Note that the gauge fields have been redefined as $-2a_i^{1,2} \rightarrow a_i^{1,2}$ here. This Hamiltonian is invariant under the following SU(2) transformation with $W_i \in \text{SU}(2)$:

$$\begin{aligned} \psi_i &\rightarrow \psi'_i = W_i \psi_i, & U_{ij} &\rightarrow U'_{ij} = W_i U_{ij} W_j^\dagger, \\ \mathbf{a}_i \cdot \boldsymbol{\sigma} &\rightarrow \mathbf{a}'_i \cdot \boldsymbol{\sigma} = W_i (\mathbf{a}_i \cdot \boldsymbol{\sigma}) W_i^\dagger. \end{aligned} \quad (1.20)$$

The transformation of ψ_i in Eq. 1.20 is equivalent to that of Ψ_i in Eq. 1.7.

The mean-field ansatz (U_{ij}, \mathbf{a}_i) is classified by the so-called invariant gauge group (IGG). The IGG is the group of gauge transformations that do not alter the mean-field ansatz expression $\{W_i | U_{ij} = W_i U_{ij} W_j^\dagger, \mathbf{a}_i \cdot \boldsymbol{\sigma} = W_i (\mathbf{a}_i \cdot \boldsymbol{\sigma}) W_i^\dagger\}$. The possible IGG in the fermionic SU(2) formalism here is SU(2), U(1), and \mathbb{Z}_2 ; and the corresponding spin liquids are called the SU(2), U(1), and \mathbb{Z}_2 spin liquids, respectively. The IGG is important as it indicates the allowed gapless fluctuation around the mean-field ansatz [8]. When one writes $U_{ij} = \bar{U}_{ij} e^{i\mathbf{a}_{ij} \cdot \boldsymbol{\sigma}}$, the phase

⁵ χ_{ij} and η_{ij} are also called ‘gauge’ fields. To ensure the SU(2) gauge invariance of the mean-field Hamiltonian (Eq. 1.17), the ‘gauge’ fields χ_{ij} , η_{ij} , a_i transform together with the ‘matter’ fields $\hat{f}_{i\alpha}$ (Eq. 1.20).

fluctuation represented by \mathbf{a}_{ij} is gapless in any direction for an SU(2) spin liquid, gapless in one certain direction for a U(1) spin liquid, and fully gapped for a Z_2 spin liquid. The mean-field solution is guaranteed to be reliable only for a Z_2 spin liquid where the fluctuations are gapped.

Now, let us examine the properties of different mean-field ansatz in a square lattice example. The zero-flux state ansatz is given by

$$\chi_{ij} = \begin{cases} \chi & \text{nearest-neighbor bonds} \\ 0 & \text{others} \end{cases}, \quad \eta_{ij} = 0, \quad a_0^l = 0, \quad (1.21)$$

where χ is real. The χ_{ij} configuration is illustrated in Fig. 1.3A. This ansatz gives $U_{ij} = \chi\sigma^3$ and the IGG is SU(2). The mean-field spinon dispersion

$$E = \pm \frac{3}{4} J \chi (\cos k_x + \cos k_y) \quad (-\pi < k_x < \pi, -\pi < k_y < \pi) \quad (1.22)$$

is quadratic to form a large Fermi surface, as shown in Fig. 1.3A. Thus, the zero-flux state is an SU(2) spinon Fermi surface QSL.

Another example is the π -flux state

$$\chi_{i,i+\mu} = \begin{cases} i\chi, & \mu = x \\ i\chi(-1)^{i_x}, & \mu = y \end{cases}, \quad \eta_{ij} = 0, \quad a_0^l = 0. \quad (1.23)$$

This ansatz doubles the unit cell to the x -direction. $U_{i,i+x} = -i\chi I$ and $U_{i,i+y} = -i\chi I(-1)^{i_x}$ and the IGG is again SU(2). The mean-field spinon dispersion

$$E = \pm \frac{3}{4} J |\chi| \sqrt{\sin^2 k_x + \sin^2 k_y} \quad \left(-\frac{\pi}{2} < k_x < \frac{\pi}{2}, -\pi < k_y < \pi \right) \quad (1.24)$$

is linear with Dirac points at $\mathbf{k} = (0, 0), (0, \pi)$ as shown in Fig. 1.3B. Thus, the π -flux state is an SU(2) spinon Dirac QSL.

The staggered-flux state ansatz [8] is described by

$$\chi_{i,i+\mu} = \begin{cases} i\chi_0 + (-1)^{i_x+i_y}\chi_1 & \mu = x \\ i\chi_0 - (-1)^{i_x+i_y}\chi_1 & \mu = y \end{cases}, \quad \eta_{ij} = 0, \quad a_0^l = 0. \quad (1.25)$$

The IGG is U(1) and the spinon dispersion is linear with Dirac points. The staggered-flux state is a U(1) spinon Dirac QSL.

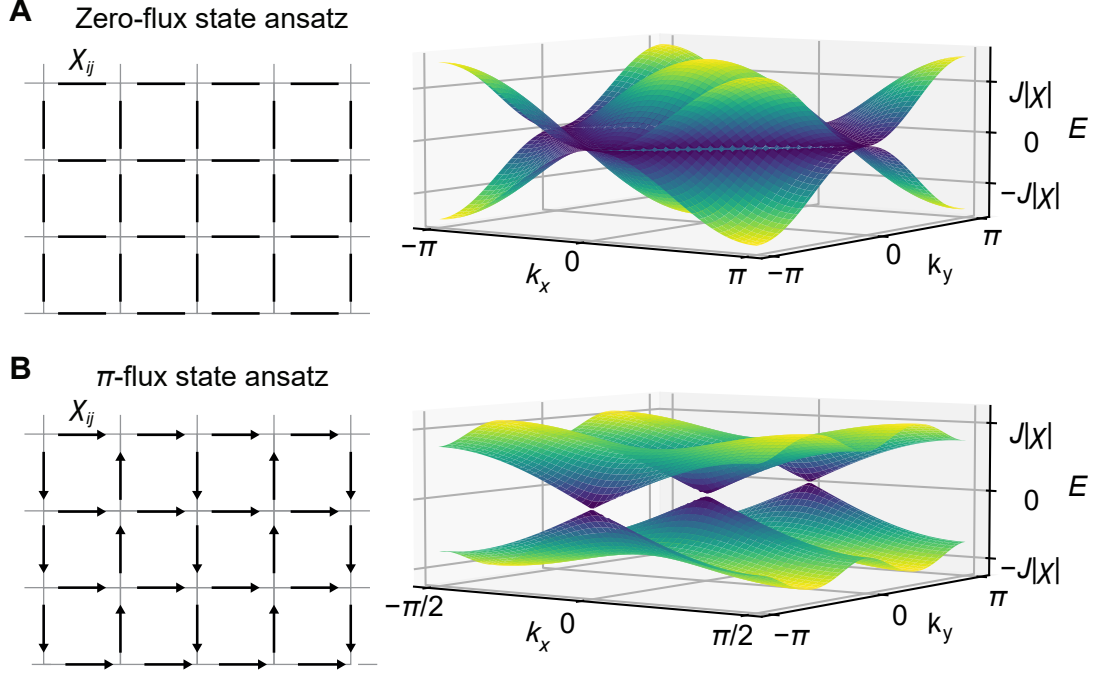


Figure 1.3: (A) Left: Mean-field ansatz χ_{ij} of the zero-flux state corresponding to Eq. 1.21. $\chi_{ij} = +\chi$ at each link. Right: Corresponding spinon dispersion which is quadratic with a large Fermi surface. (B) Left: The π -flux state ansatz corresponding to Eq. 1.23. The arrow direction corresponds to $\chi_{ij} = +i\chi$. Right: Corresponding spinon dispersion which is linear with Dirac points.

Finally, the following ansatz is one of the ansatz of a Z_2 spinon gapped QSL [8].

$$\chi_{i,i+x} = \chi_{i,i+y} = -\chi, \quad \eta_{i,i+x} = \eta_{i,i+y} = 0, \quad (1.26)$$

$$\chi_{i,i\pm x+y} = \chi_{i,i\mp x-y} = 0, \quad \eta_{i,i\pm x+y} = \eta_{i,i\mp x-y} = \eta_0 \mp i\eta_1, \quad (1.27)$$

$$a_0^1 \neq 0, \quad a_0^2 = a_0^3 = 0. \quad (1.28)$$

This way, spinon QSLs of different gauge structures are derived as a mean-field solution in the parton construction. Note that the gapless gauge field fluctuations, allowed in the SU(2) and U(1) case, mediate spinon-spinon interactions that could completely alter the properties of the solution. Among the examples above, only the Z_2 spinon QSL is guaranteed to have gapped gauge-field fluctuations so that the mean-field solution is qualitatively reliable.

1.3 Non-spin-liquid where ordering is absent

I list examples of phases that are not called spin liquids despite the absence of ordering.

1.3.1 Valence bond solid

When pairs of two quantum spin-1/2 form dimers, the ground state will be a valence bond solid, a tensor product of local singlet states. While a valence bond solid typically breaks lattice symmetry, there are some exceptions. One example is the lattice with an even number of spins in a unit cell, as shown in Fig. 1.4A. The dimer formation within the unit cell will not break the lattice symmetry. Another example is the certain higher-spin chains [29], where the valence bond solid state appears as an exact solution that retains the lattice symmetry. The valence bond state is usually not called a spin liquid, even in these cases where any symmetry breaking does not occur. Its ground state is gapped and non-degenerate, without massive degeneracy or long-range quantum entanglement.

1.3.2 Random singlet

A random singlet state (also called a valence bond glass state) comprises singlets with random coupling strengths. When quantum Heisenberg spins are coupled by antiferromagnetic interactions of randomly distributed coupling strength, a pair of spins coupled by the strongest antiferromagnetic interaction first forms a singlet and becomes magnetically inert. The singlet formation continues through the second, third, and subsequent strongest couplings until all the spins form singlets. The resulting state is an ensemble of singlets with distributed binding energy, as schematically shown in Fig. 1.4B. The renormalization group analysis [30,31] shows that the density of states (i.e. the distribution of the singlet binding energy) at low energy should have a power-law form $\rho(\varepsilon) \sim \varepsilon^{-\gamma}$. A random singlet state with spinful defects is predicted to occur in a weakly-disordered valence bond solid state [32, 33], and its relevance to QSL candidate compounds has been recently

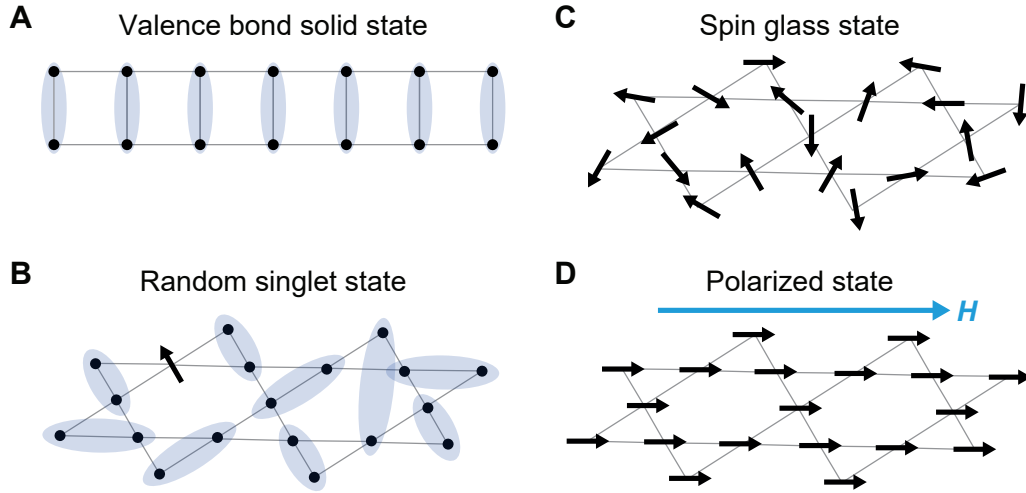


Figure 1.4: Schematic drawings of a valence bond solid state in a 1D chain with two spins per unit cell (**A**), a random singlet state on a 2D kagome lattice (**B**), a spin glass state (**C**), and a polarized state under an overwhelming external field (**D**). The blue ellipses represent singlets formed by two spin-1/2.

proposed [32, 34]. While a random singlet state is a quantum disordered state, it is typically distinguished from a QSL state.

1.3.3 Spin glass

A spin glass [35, 36] is a disordered magnetic state where spins are frozen in a random configuration, as shown in Fig. 1.4C. A canonical spin glass is a doped alloy such as AuFe or CuMn, where magnetic impurities of a small concentration are randomly distributed in metal. The Ruderman–Kittel–Kasuya–Yosida (RKKY) interaction mediated by the itinerant electrons induces random exchange interactions among the impurity spins. The relatively recent review [36] lists the four common signatures in such a canonical spin glass: (i) a cusp in magnetic susceptibility that shows a tiny shift with frequency ω , (ii) a hysteresis in DC-magnetization, (iii) an absence of a sharp specific heat divergence, (iv) aging of magnetization signifying the metastability.

While the understanding of the canonical spin glass has been significantly developed, a glassy behavior of spins has also been observed in various other systems. When the magnetic impurity concentration is increased, clusters of impurity spins are formed to slow down the spin dynamics (a cluster glass). Even presumably clean

systems, such as the spin ice compound $\text{Dy}_2\text{Ti}_2\text{O}_7$ [37–39] and a quasi-2D spin-3/2 triangular system with little doping $\text{SrCr}_{9p}\text{Ga}_{12-9p}\text{O}_{19}$ [40, 41], are found to exhibit glassy behavior. Due to the extant phenomena, the framework to explain the general glassy phenomena of spins has yet to be established. A spin glass is unique in the sense that it is a non-equilibrium state, and is usually distinguished from both the typical spontaneous-symmetry-broken phases and spin liquids. Note that an order parameter can be defined in a spin glass [42]; however, it is distinct from a typical local order parameter, and signatures of a symmetry-breaking transition such as a specific heat peak are absent in a spin glass.

1.3.4 Polarized state due to external field

When the Zeeman energy due to an external field exceeds the spin-spin interaction energy, the spins become polarized to the direction of the field as shown in Fig. 1.4D. This polarized state is non-degenerate and continuously connects to the high-temperature paramagnetic phase as the temperature exceeds the Zeeman energy. While the external field explicitly breaks time-reversal symmetry, no spontaneous symmetry breaking occurs down to zero temperature. Despite this absence of order, such a polarized state is usually considered trivial and is not called a spin liquid.

1.4 Fingerprinting spin liquids with spin noise spectroscopy

There are many types of spin liquid states and other non-ordered states. There is a clear motivation to identify and classify them. A spontaneously-symmetry-broken phase with a conventional magnetic order can be identified by various signatures, such as a clear phase-transition peak in specific heat or magnetic Bragg peaks in x-ray/neutron scattering experiments. On the other hand, spin liquids often lack an unambiguous signature, and one has to rely on a careful comparison between the experiment and the theory. Thermodynamic quantities are useful in distinguishing

Phase	Specific Heat		Magnetic susceptibility	
	$k_B T \ll J$	$J \ll k_B T$	$k_B T \ll J$	$J \ll k_B T$
2D Ising AF kagome	$e^{-J/k_B T}$	T^{-2}	T^{-1}	$(T + J)^{-1}$
2D spiral spin liquid	$c_0 + c_1 T$	T^{-2}	drop	$(T + J)^{-1}$
1D $S = 1/2$ Heisenberg AF	T	T^{-2}	$\chi_0 + 1/\ln(J/k_B T)$	$(T + J)^{-1}$
1D valence bond solid	$e^{-J/k_B T}$	T^{-2}	$e^{-J/k_B T}$	$(T + J)^{-1}$
Conventional spin glass	T	T^{-1}	drop (hysteresis)	$(T + J)^{-1}$

Table 1.1: Specific heat and magnetic susceptibility of several non-ordered magnetic phases. J is interaction energy scale and T is temperature. Specific heat ($k_B T \ll J$) of 2D spiral spin liquid is taken from the analytical prediction in Ref. [18]. Susceptibility ($k_B T \ll J$) of 2D spiral spin liquid is taken from experimental studies [19, 43], as I am not aware of a clear theoretical prediction. 1D $S = 1/2$ Heisenberg AF chain results are predictions from an exact solution [44]. Conventional spin glass results are empirical [36].

Phase	Spin excitation spectrum
2D Ising AF kagome	Continuum
2D spiral spin liquid	Ring-like continuum
1D $S = 1/2$ Heisenberg AF	Spinon continuum
1D valence bond solid	Triplet bands
Conventional spin glass	Continuum

Table 1.2: Spin excitation spectrum of several non-ordered magnetic phases.

non-ordered magnetic phases. A classical spin liquid can be evidenced by a zero-point entropy (derived from specific heat measurements), indicating massive degeneracy. A conventional spin glass is characterized by a magnetic susceptibility cusp, absence of a peak in specific heat, and hysteresis/aging in magnetization. Further, the temperature dependence of specific heat and magnetic susceptibility, shown in Table 1.1 for several non-ordered magnetic phases, can narrow down possible magnetic phases. However, the temperature dependence of thermodynamic quantities is usually not decisive. Different models show similar temperature dependence, and complexity in actual compounds (e.g. extra interactions and disorder) often makes the temperature dependence hard to extract.

Probing spin excitation spectra by scattering experiments, listed in Table 1.2, also serves as a strong identifier of magnetic phases. For example, observation of triplet bands can signify a 1D valence bond solid. A ring-like structure factor is the defining feature of a 2D spiral spin liquid, and fractional excitations such as spinon are the smoking gun of a quantum spin liquid state. However, when

a broad continuum is the defining feature of a magnetic phase, it is often challenging to experimentally identify a continuum type. Successful examples are 1D $S = 1/2$ Heisenberg antiferromagnetic spin chain compounds, such as KCuF_3 and $\text{CuSO}_4 \cdot 5(\text{D}_2\text{O})$. The characteristic excitation continuum observed by the scattering experiments [45, 46] is regarded as an experimental signature of spinons, although it is unclear from the experimental data alone whether the continuum excitation evidences spinon excitations. It is the precise comparison to the exact analytical prediction of the excitation continuum that substantiates the spinon identification.

In most of the frustrated spin systems, theoretical models are not exactly solvable. The prime example is the ground state phase of the spin-1/2 antiferromagnetic Heisenberg model on a 2D kagome lattice. As discussed in Section 1.2, the LSM theorem implies that the ground state of this highly frustrated model is likely to be a QSL, unless it shows a symmetry-breaking order. However, the exact ground state is still under debate. Various numerical methods, such as the exact diagonalization and the density matrix renormalization group, have been employed to predict the ground state and its energy spectrum. They pointed to various states with comparable energy, such as $U(1)/\mathbb{Z}_2$ Fermi surface/Dirac QSLs, gapped QSLs, and a valence bond solid [47, 48]. Even if the ideal theoretical model were solvable, the experimental identification of a state in a real compound would suffer a further complication. Subdominant interactions and quenched disorder that almost always exist in the real compound could significantly affect the ground states, especially in a frustrated system where the energy of qualitatively different states is close. $\text{ZnCu}_3(\text{OH})_6\text{Cl}_2$ [47, 48], which has been regarded as one of the best realizations of the kagome Heisenberg model, is no exception. The weak anisotropic interactions and the substitution between nonmagnetic Zn^{2+} and spin-1/2 Cu^{2+} could drive the realistic situation away from the presumed kagome Heisenberg model. Consequently, experimental studies have drawn many different conclusions about $\text{ZnCu}_3(\text{OH})_6\text{Cl}_2$.

Spin Noise Spectroscopy

There is a clear need for a new experimental technique to identify spin liquid states. The emerging new concept is to use spin noise as a fingerprint of a spin liquid compound. Ref. [49] theoretically proposes that spin correlations in space and time, revealed by spin noise measurements, are capable of probing different phases of cold fermionic gases: Bose-Einstein condensation, Cooper pairing, antiferromagnetic order, and the algebraic spin liquid. More recently, spin noise spectroscopy on a magnetic insulator is suggested to be capable of diagnosing different QSL states such as Z_2 Dirac, Z_2 Fermi surface, and $U(1)$ Fermi surface QSL; and random singlet states caused by disorder [50–53].

Theoretical proposals to detect spin noise have been made for different experimental techniques such as Superconducting QUantum Interference Device (SQUID) spin noise spectroscopy [54–56], laser spin noise spectroscopy [49], and Nitrogen-Vacancy (NV) center [50–53, 56–58]. To my knowledge, laser spin noise spectroscopy has been primarily applied in semiconductors and atomic gases where the Faraday effect is strong [59, 60]. The current NV center measurement sensitivity $\mu\text{T}/\sqrt{\text{Hz}}$ [61] is not sufficient to capture most spin noise signals in a reasonable experimental time. This thesis work employs the SQUID spin noise spectroscopy, which makes use of the most sensitive magnetic flux sensor approaching $\text{fT}/\sqrt{\text{Hz}}$ sensitivity and below.

The SQUID spin noise spectroscopy has recently proven its use in the study of magnetic monopole dynamics in the classical spin ice $\text{Dy}_2\text{Ti}_2\text{O}_7$ [15, 62, 63]. The observation of an anomalous exponent in magnetic noise led to the discovery of emergent fractal dynamics of monopoles. This thesis introduces such SQUID spin noise spectroscopy to general spin liquid studies. The goal is to fingerprint spin liquid compounds whose exact spin liquid state is unknown beforehand, with a particular focus on the QSL candidate compounds. When I embarked on this journey, to my knowledge, spin noise in QSL candidates had never been experimentally detected. Thus, the first goal was to demonstrate the viability of the spin noise measurement. It led me first to measure a 2D bilayer kagome QSL

candidate $\text{Ca}_{10}\text{Cr}_7\text{O}_{28}$, which I expected to generate a strong spin noise signal. After my successful experimental discovery of the spin noise signal in $\text{Ca}_{10}\text{Cr}_7\text{O}_{28}$, I moved on to measure spin noise in one of the most prominent QSL candidates: $\text{ZnCu}_3(\text{OH})_6\text{Cl}_2$.

2

Spin Noise Spectroscopy

Spin dynamics originate from various interactions in a spin system. Experimental studies of spin dynamics can provide a lot of insights into the ground state of a spin system and its spin excitations, making them a powerful tool for studying spin liquids. In this chapter, I introduce spin noise spectroscopy, a novel experimental approach to studying the dynamics of spin liquids. First, I will introduce the basic principles of spin dynamics from the AC susceptibility perspective. I will then explain the concept of spin noise and its relation to AC susceptibility. Afterward, I will present the Superconducting QUantum Interference Device (SQUID), the most sensitive detector of magnetic flux in existence, which plays a critical role in our spin noise spectrometer. Finally, I will compare different experimental techniques to study spin dynamics based on their scientific and technical merits.

2.1 Spin dynamics and AC susceptibility

2.1.1 Precessional and relaxational spin dynamics

Spin dynamics can be largely separated into three channels: the precessional dynamics driven by the spin Hamiltonian, the relaxational dynamics due to various couplings to the environment, and the random thermal and quantum fluctuations.

These concepts are illustrated by a simple local electron spin-1/2 under a constant magnetic field $\mathbf{H} = (0, 0, H_z)$.

Firstly, the spin \mathbf{s} precesses around the magnetic field with an angular frequency $\omega_E = 2\mu_0\mu_B H_z/\hbar$, as semiclassically described by

$$\frac{d\mathbf{s}}{dt} = -\mu_0 \frac{2\mu_B}{\hbar} \mathbf{s} \times \mathbf{H}. \quad (2.1)$$

This type of spin evolution due to the field is called the precessional dynamics. In a quantum mechanical picture, the precession can be understood as an x -direction spin state $(|+\rangle + |-\rangle)/\sqrt{2}$ precessing at an angular frequency $\omega_E = 2\mu_0\mu_B H_z/\hbar$, which corresponds to the spin excitation energy from the ground state $|-\rangle$ to the excited state $|+\rangle$. Thus, a precession process generally has a corresponding spin excitation process. As the field \mathbf{H} can be either from an external coil or an exchange field from neighboring spins, spin excitations in a general spin Hamiltonian give rise to the precessional dynamics. The precession is an energy-conservation process and also conserves the spin component parallel to the field, in this example the z -direction spin.

Secondly, due to an environmental coupling, the spin gradually approaches the minimum-energy state along the field \mathbf{H} . Such spin evolution involving an energy change is called relaxational dynamics. Many different mechanisms trigger relaxation, such as a scattering with thermal phonons, a coupling to environmental spins not considered in the Hamiltonian, and so on. Note that neither the precessional nor relaxational dynamics occur in the strict quantum mechanical ground state, where the spin is typically parallel to the field. Thermal fluctuation (or external field perturbation) is a necessary drive that excites the spin state and triggers the precessional or relaxational dynamics.

Finally, there are random thermal and quantum fluctuations. The thermal fluctuation arises from a stochastic interaction process with a thermal bath. Here, the thermal fluctuation specifically refers to the random spin evolution that averages out to zero, and is distinguished from the relaxational process that also has underlying stochastic nature but evolves spin on average. The quantum fluctuation

is due to the non-commutativity of spin operators in different directions. The quantum fluctuation is a purely quantum-mechanical effect and continues even down to the theoretical zero temperature.

A single spin has been assumed so far, but a similar discussion applies to a total spin $\mathbf{S} = \sum_i \mathbf{s}^i$ of a spin ensemble. One difference for the total spin is that the magnitude $|\mathbf{S}|$ is allowed to vary. Also note that the precessional dynamics purely due to intra-system spin-spin interactions conserve the total spin \mathbf{S} . Such precessional spin dynamics will not manifest in a strictly equal-weight sum of all the spins under consideration $\mathbf{S} = \sum_i \mathbf{s}^i$, but they are still detectable in realistic experimental measurements. It is because experiments typically measure a partial or weighted sum of spins $\mathbf{S} = \sum_i w_i \mathbf{s}^i$, where the weight w_i depends on specific conditions such as a distance to the experimental probe.

Spin dynamics in a system provide rich information about the underlying spin state. The precessional dynamics are controlled by either an external field or spin-spin interactions in the Hamiltonian, reflecting the spin excitations in the system. The frequency spans from the largest interaction in the spin Hamiltonian down to zero frequency in case the excitation spectrum is gapless. The relaxational dynamics occur via couplings to the environment and are theoretically more complex; however, their frequency and temperature dependence reflect the properties of the underlying spin state. For example, a characteristic \sim Hz slow relaxation, often with a broad frequency distribution, emerges when the spins turn into a superparamagnet state or a spin glass state upon cooling [64]. In a classical spin ice $\text{Dy}_2\text{Ti}_2\text{O}_7$, an almost temperature-independent \sim kHz relaxation is observed between 10 K and 3 K, due to thermal-energy-assisted quantum tunneling of Ising spins [65]. At even lower temperatures below \sim 2 K, the relaxational frequency drops to \sim Hz much more rapidly than the Arrhenius law, due to the underlying dynamical fractal structure that has been recently elucidated [63].

2.1.2 Definition of AC susceptibility

AC susceptibility [64] is a conventionally established measurement to characterize spin dynamics. Consider a magnetic system subject to an externally applied magnetic field oscillation, as schematically shown in Fig. 2.1A. When the applied field is a sinusoidal wave with a fixed frequency $\text{Re}[H(t; \omega_0)] = \text{Re}[H_0 e^{i\omega_0 t}] = H_0 \cos(\omega_0 t)$, the magnetization of the system oscillates with the same frequency but with a phase delay $\text{Re}[M(t; \omega_0)] = \text{Re}[M_0 e^{i(\omega_0 t - \phi)}] = M_0 \cos(\omega_0 t - \phi)$. When measured in an oscilloscope, the two signals look like Fig. 2.1B.

AC susceptibility is defined by the ratio of the induced magnetization to the applied field, with the phase delay considered.

$$\chi(\omega_0) = \frac{M(t; \omega_0)}{H(t; \omega_0)} = \frac{M_0}{H_0} e^{-i\phi} \quad (2.2)$$

$$= \frac{M_0}{H_0} \cos \phi - i \frac{M_0}{H_0} \sin \phi. \quad (2.3)$$

The real and imaginary components of the AC susceptibility, corresponding to the in-phase and out-of-phase response, respectively, are defined as $\chi = \chi' - i\chi''$.¹

$$\chi' = \frac{M_0}{H_0} \cos \phi, \quad (2.4)$$

$$\chi'' = \frac{M_0}{H_0} \sin \phi, \quad (2.5)$$

where the phase delay $\phi > 0$ satisfies causality. $\chi(\omega_0)$ is generally frequency-dependent, so the full-frequency AC susceptibility $\chi(\omega)$ is obtained by repeating the above measurements at a series of frequencies. The $H_0 \rightarrow 0$ limit is assumed analytically, although an appropriate field size that satisfies this assumption in a real experiment and simulation has to be scrutinized. In a zero-frequency limit, the AC susceptibility should result in the DC susceptibility.

$$\chi'(\omega \rightarrow 0) = \chi^{\text{DC}}, \quad (2.6)$$

$$\chi''(\omega \rightarrow 0) = 0. \quad (2.7)$$

¹The definition $\chi = \chi' - i\chi''$ gives $\chi'' = -\text{Im} \chi$. The negative sign disappears if the phase evolution over time is chosen to be negative: $H(t; \omega_0) = H_0 e^{-i\omega_0 t}$, $M(t; \omega_0) = M_0 e^{-i(\omega_0 t - \phi)}$, and then $\chi(\omega_0) = \frac{M_0}{H_0} e^{+i\phi} = \chi' + i\chi''$. These two conventions do not make physical differences. In this thesis, I chose the positive phase evolution that appears to be a natural choice.

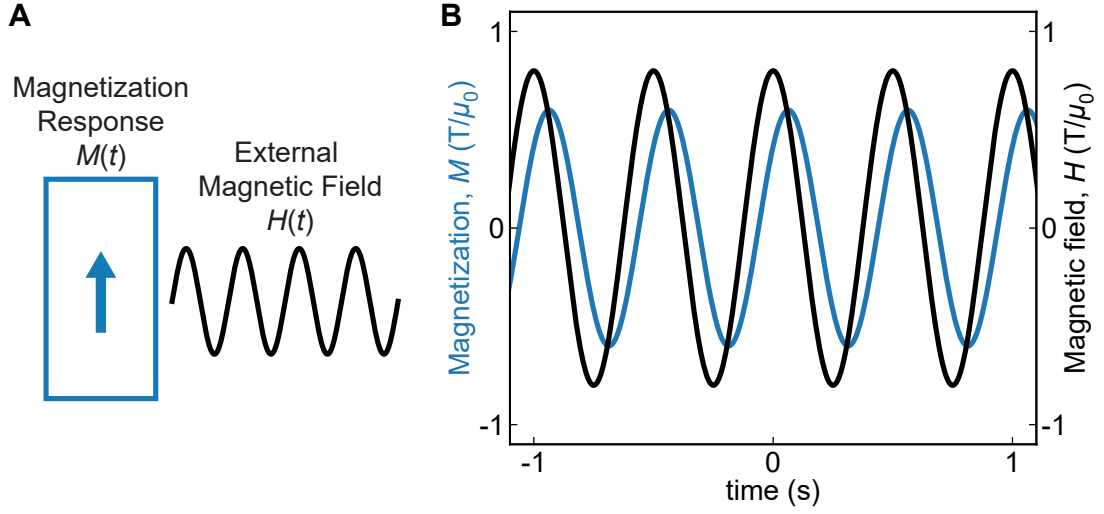


Figure 2.1: (A) Schematic illustration of a magnetization response to an external magnetic field oscillation. (B) Response of the magnetization $M_0 \cos(\omega_0 t - \phi)$, which is delayed from the external magnetic field $H_0 \cos(\omega_0 t)$.

2.1.3 AC susceptibility characterized by relaxation

AC susceptibility reflects the characteristic timescale/frequency in a magnetic system. In the following example, the relaxation process governs the AC susceptibility. Consider a simple paramagnet exposed to a small magnetic field H_z parallel to z -axis. When the z -axis magnetization M_z relaxes to an equilibrium value M^{eq} with a single relaxation time τ , the time evolution of M_z follows the simple Bloch equation

$$\frac{dM_z}{dt} = -\frac{M_z - M^{\text{eq}}}{\tau}. \quad (2.8)$$

When the applied field is constant, the equilibrium magnetization is expressed by the DC susceptibility as $M^{\text{eq}} = \chi^{\text{DC}} H_z$. Assuming that this relation holds for a general oscillating field $M^{\text{eq}}(t) = \chi^{\text{DC}} H_z(t)$, the differential equation can be rewritten as

$$\tau \frac{dM_z}{dt} + M_z = \chi^{\text{DC}} H_z(t). \quad (2.9)$$

This is equivalent to the equation of motion of a damped mechanical system with no inertia. The equation can be formally solved for each Fourier component as

$$\chi(\omega) = \frac{M_z(\omega)}{H_z(\omega)} = \chi^{\text{DC}} \frac{1}{1 + i\omega\tau}. \quad (2.10)$$

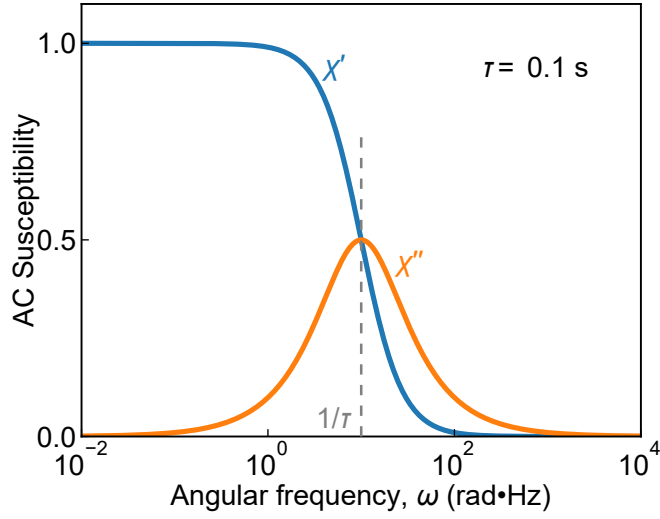


Figure 2.2: Frequency dependence of a typical AC susceptibility in a magnetic system with a single relaxation time. The blue (orange) line is the real (imaginary) part. The value of the parameters, DC susceptibility $\chi^{\text{DC}} = 1$ and relaxation time $\tau = 0.1$ s, are arbitrarily chosen.

Therefore, the typical form of the real and imaginary parts of the susceptibility will be

$$\chi' = \chi^{\text{DC}} \frac{1}{1 + \omega^2 \tau^2}, \quad (2.11)$$

$$\chi'' = \chi^{\text{DC}} \frac{\omega \tau}{1 + \omega^2 \tau^2}. \quad (2.12)$$

The frequency dependence of these functions is plotted in Fig. 2.2. The characteristic frequency $\omega_\tau = 1/\tau$ is inferred from the 50% drop of χ' and the peak position of χ'' .

The above phenomenological model of AC susceptibility can account for temperature dependence by making the parameters temperature dependent as $\chi^{\text{DC}}(T)$ and $\tau(T)$. This treatment is sufficient for a simple paramagnet. However, the assumption of a single relaxation time $\tau(T) = \tau_C(T)$ at each temperature can be overly simplistic for describing a complex spin system. The so-called Havriliak–Negami form is empirically known to be useful [64].

$$\chi_{\text{HN}}(\omega) = \chi^{\text{DC}} \frac{1}{\left(1 + (i\omega\tau_C)^{1-\alpha}\right)^\beta}. \quad (2.13)$$

A particular case of $\beta = 1$ is called the generalized Debye form, and $\alpha = 0$ is called the Cole–Davidson form. The Havriliak–Negami form arises in a spin ensemble

with a particular form of distributed relaxation times. If the susceptibility $\chi_\tau(\omega)$ of an individual relaxing component is given by Eq. 2.10, and the probability distribution of relaxation times $p(\tau)$ is assumed, then $\chi(\omega)$ is given by

$$\chi(\omega) = \int_0^\infty d\tau p(\tau)\chi_\tau(\omega) = \chi^{\text{DC}} \int_0^\infty d\tau p(\tau) \frac{1}{1 + i\omega\tau}. \quad (2.14)$$

The distribution function behind the Havriliak–Negami form is then inferred [64] to be

$$p(\tau) = \frac{1}{\pi\tau} \frac{\left(\frac{\tau}{\tau_c}\right)^{(1-\alpha)\beta} \sin\left(\beta \arctan\left|\frac{\sin\pi\alpha}{\left(\frac{\tau}{\tau_c}\right)^{1-\alpha} - \cos\pi\alpha}\right|\right)}{\left[\left(\frac{\tau}{\tau_c}\right)^{2(1-\alpha)} - 2\left(\frac{\tau}{\tau_c}\right)^{1-\alpha} \cos\pi\alpha + 1\right]^{\beta/2}}. \quad (2.15)$$

In certain cases, both the real and imaginary susceptibility are known to have a simple power-law dependence.

$$\chi'(\omega) \propto \omega^{-\alpha}, \quad (2.16)$$

$$\chi''(\omega) \propto \omega^{-\alpha}. \quad (2.17)$$

Such frequency dependence can be attributed to the following distribution of relaxation times (derivation in Appendix A).

$$p(\tau) = \begin{cases} a\tau^{\alpha-1} & (\tau_{\min} < \tau < \tau_{\max}) \\ 0 & (\text{otherwise}), \end{cases} \quad (2.18)$$

for $\tau_{\min} \ll 1/\omega \ll \tau_{\max}$ and $0 \leq \alpha \leq 1$. Specifically, when $\alpha = 0$, $\chi(\omega)$ is frequency-independent and the corresponding relaxation time distribution is $p(\tau) \propto 1/\tau$ [66].

2.1.4 AC susceptibility characterized by precession

AC susceptibility can also capture the precessional spin dynamics at an angular frequency ω_E , when there is a large enough density of states to be detected in the measured frequency range. Consider isotropic spin-1/2 electrons under an x -direction field H_x , which can be a magnetic field from a coil or an exchange field from surrounding spins. The precession frequency, corresponding to the spin excitation energy, is $\hbar\omega_E = 2\mu_0\mu_B H_x$. When a perturbative z -direction oscillating

field $H_z(t) \ll H_x$ is applied, the evolution of the spin ensemble is described by the following Bloch equation²

$$\frac{d\mathbf{M}}{dt} = \mu_0\gamma\mathbf{M} \times \mathbf{H} - \frac{\mathbf{M} - \chi^{\text{DC}}\mathbf{H}}{\tau}, \quad (2.19)$$

$$\mathbf{H} = (H_x, 0, H_z(t)) = \text{Re}[(H_x, 0, H_0 e^{i\omega_0 t})], \quad (2.20)$$

where the gyromagnetic ratio is $\gamma = -2\mu_B/\hbar$ for an electron spin. After some cumbersome calculations (see Appendix A), the real and imaginary susceptibility is obtained to be

$$\chi'(\omega) = \frac{\chi^{\text{DC}}}{2} \left(\frac{1 - \omega_E\tau(\omega - \omega_E)\tau}{1 + (\omega - \omega_E)^2\tau^2} + \frac{1 + \omega_E\tau(\omega + \omega_E)\tau}{1 + (\omega + \omega_E)^2\tau^2} \right), \quad (2.21)$$

$$\chi''(\omega) = \frac{\chi^{\text{DC}}}{2} \left(\frac{\omega\tau}{1 + (\omega - \omega_E)^2\tau^2} + \frac{\omega\tau}{1 + (\omega + \omega_E)^2\tau^2} \right). \quad (2.22)$$

Thus, the AC susceptibility shows a peak at a frequency close to ω_E . The precise fitting of $\chi'(\omega)$ and $\chi''(\omega)$ provides the DC susceptibility χ^{DC} , the precession frequency ω_E , and the relaxation time τ .

2.2 Spin Noise

2.2.1 Definition of spin noise

In our spin noise measurement [59], the fluctuation of magnetization is measured over time. Unlike the AC susceptibility measurement, an external perturbation field does not need to be applied. One might expect that the magnetization is constant without an external field perturbation, but that is only true for the mean value. The magnetization is driven by thermal and quantum fluctuations over time, showing a fluctuation as sketched in Fig. 2.3. This time series of magnetization

$$\text{Noise : } M(t) \quad (2.23)$$

has rich information on spin dynamics, which is detailed in this section.

²The relaxation time τ is assumed to be isotropic, although the relaxation along the external field (in this case x) and that perpendicular to the field (y, z) can generally be different. This simplification of the equation does not alter the conclusion qualitatively.

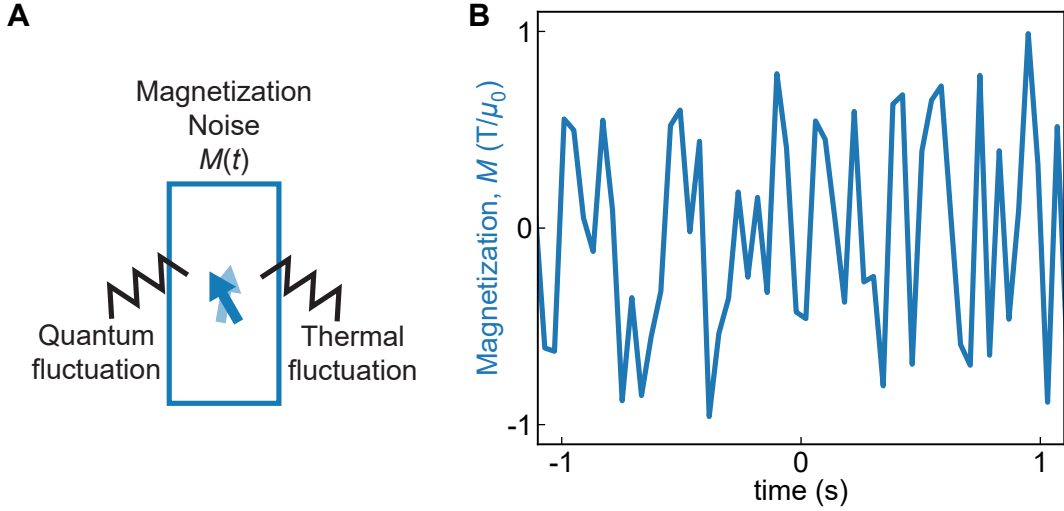


Figure 2.3: (A) Schematic of magnetization noise (\sim spin noise) originating from quantum and thermal fluctuations. (B) Typical time series of the magnetization noise.

The SQUID measurement scheme, employed in our spin noise spectrometer described in Chapter 3, directly probes magnetization noise rather than spin noise. In an insulator where free-electron current is negligible, electron spin fluctuations dominate magnetization fluctuations. As the total electron spins per volume \mathbf{S}/V and the magnetization \mathbf{M} are related by a simple constant

$$\mathbf{M} = \frac{1}{V} \sum_i \left(-\frac{2\mu_B}{\hbar} \right) \mathbf{s}^i = -\frac{2\mu_B}{\hbar} \frac{\mathbf{S}}{V}, \quad (2.24)$$

the terms ‘magnetization noise’ and ‘spin noise’ are used interchangeably in this thesis.

2.2.2 Noise formulated as random process

The magnetization noise time series $M(t)$, discrete in time as $M(t_i)$ in experimental data, can be regarded as the realization of a stochastic process [67]. A random process is probabilistically predicted based on a set of probability distributions p_n . The probability that the magnetization takes a value between M_i and $M_i + dM_i$ at each time instant t_i is expressed as

$$p_n(M_n, t_n; \dots; M_2, t_2; M_1, t_1) dM_n \dots dM_2 dM_1. \quad (2.25)$$

Note that p_n describes the probability distribution of magnetization not only at a single time but also at consecutive time instants. This formulation is necessary to treat a noise signal that is correlated in time.

The probability distributions p_n can also be expressed by conditional probabilities P_n . P_n is related to p_n by

$$p_n(M_n, t_n; \dots; M_1, t_1) = P_n(M_n, t_n \mid M_{n-1}, t_{n-1}; \dots; M_1, t_1) p_{n-1}(M_{n-1}, t_{n-1}; \dots; M_1, t_1) \quad (2.26)$$

$$= \left(\prod_{i=2}^n P_i \right) p_1(M_1, t_1). \quad (2.27)$$

Certain random processes satisfy special properties. In an ergodic random process, a time average defined using any realization $M(t)$ equals an ensemble average.

$$\bar{X} := \lim_{T \rightarrow \infty} \frac{1}{T} \int_{-T/2}^{T/2} dt X(M(t)), \quad (2.28)$$

$$\langle X \rangle := \int dM X(M) p_1(M), \quad (2.29)$$

$$\bar{X} = \langle X \rangle. \quad (2.30)$$

A random process is called Gaussian when its probability distributions are all Gaussian.

$$p_n(M_n, t_n; \dots; M_1, t_1) = A \exp \left(- \sum_{j=1}^n \sum_{k=1}^n \alpha_{jk} (M_j - \bar{M})(M_k - \bar{M}) \right). \quad (2.31)$$

A random process is called Markov when its most recently known value determines its future probabilities.

$$P_n(M_n, t_n \mid M_{n-1}, t_{n-1} \dots; M_1, t_1) = P_2(M_n, t_n \mid M_{n-1}, t_{n-1}). \quad (2.32)$$

A Markov process is completely characterized by $p_1(M_1, t_1)$ and $P_2(M_2, t_2 \mid M_1, t_1)$.

In a Gaussian-Markov process, the conditional probability distribution is characterized by only three parameters: the mean \bar{M} , the variance σ_M^2 , and the relaxation time τ [67].

$$P_2(M_2, t \mid M_1, 0) = \frac{1}{\sqrt{2\pi\sigma_{M_t}^2}} \exp \left[- \frac{(M_2 - \bar{M}_t)^2}{2\sigma_{M_t}^2} \right], \quad (2.33)$$

$$\text{where } \bar{M}_t = \bar{M} + e^{-t/\tau} (M_1 - \bar{M}), \quad (2.34)$$

$$\sigma_{M_t}^2 = (1 - e^{-2t/\tau}) \sigma_M^2. \quad (2.35)$$

This result is known as Doob's theorem. In a spin system with a single relaxation time, the spin noise is Markov and Doob's theorem applies. When the relaxation time is distributed in a spin system, the spin noise is not Markov.

2.2.3 Analysis of correlations in noise

One can extract various information from experimental spin noise data $M(t)$. First of all, the probability distribution $p(M)$ is examined. The distribution function is characterized by n -th order moments $\langle (M - a)^n \rangle$ where a is a constant, which equals to $\overline{(M - a)^n}$ in an ergodic process. When $\sim 10^{20}$ magnetic moments in a bulk system fluctuate randomly, the bulk magnetization noise tends to have a Gaussian distribution according to the central limit theorem. Therefore, it usually suffices to study mean \overline{M} and variance σ_M^2 , which are the first and second-order moments that fully characterize a Gaussian distribution.

$$\overline{M} = \overline{(M - 0)^1}, \quad (2.36)$$

$$\sigma_M^2 = \overline{(M - \overline{M})^2} = \overline{M^2} - \overline{M}^2. \quad (2.37)$$

The probability distribution may not be Gaussian when spins show a peculiar time correlation or when the number of degrees of freedom is small due to the formation of large ordered domains. In that case, higher-order moments could yield extra information about the complete functional form of the probability distribution.

Next, the correlations are studied in either the time or frequency domain. A correlation function extracts the simplest form of correlations in the time domain.

$$C_M(t) = \overline{M(s)M(s+t)}^s = \lim_{T \rightarrow \infty} \frac{1}{T} \int_{-T/2}^{T/2} ds M(s)M(s+t). \quad (2.38)$$

Specifically, the correlation at $t = 0$ equals the variance (+ the squared mean).

$$C_M(0) = \overline{M^2} = \sigma_M^2 + \overline{M}^2. \quad (2.39)$$

The correlation function is often normalized as $C_M(t)/C_M(0)$ to compare the time correlation in different conditions and systems.

The Fourier transform is used to study noise in the frequency domain. As the Fourier transform is divergent for a noise signal that goes on forever, the noise signal must be truncated first to ensure that the Fourier transform exists.

$$M_T(t) := \begin{cases} M(t) & \text{if } -T/2 < t < +T/2, \\ 0 & \text{otherwise.} \end{cases} \quad (2.40)$$

The Fourier transform is calculated from the truncated time series as

$$M_T(\omega) = \int_{-T/2}^{T/2} dt e^{-i\omega t} M_T(t). \quad (2.41)$$

The Fourier transform result has the full information about the original time series but is complex-valued. One instead uses a power spectral density (PSD)

$$S_M^{\text{two-sided}}(\omega) = \lim_{T \rightarrow \infty} \frac{1}{2\pi T} |M_T(\omega)|^2 \quad (2.42)$$

that has less information but is convenient to analyze. The PSD of real-valued $M(t)$ is an even function. One often folds the negative frequency contribution into the positive part, making it a one-sided PSD.

$$S_M^{\text{one-sided}}(\omega > 0) = 2S_M^{\text{two-sided}}(\omega > 0) = \lim_{T \rightarrow \infty} \frac{1}{\pi T} \left| \int_{-T/2}^{T/2} dt e^{-i\omega t} M_T(t) \right|^2. \quad (2.43)$$

In this thesis, a PSD denoted as $S_M(\omega)$ is one-sided unless explicitly specified otherwise.

$$S_M(\omega) := S_M^{\text{one-sided}}(\omega). \quad (2.44)$$

Theoretically, the correlation function and the PSD contain the precisely same information, as indicated by the Wiener-Khinchin theorem [67].

$$S_M(\omega) = \frac{2}{\pi} \int_0^\infty dt \cos(\omega t) C_M(t), \quad (2.45)$$

$$C_M(t) = \int_0^\infty d\omega \cos(\omega t) S_M(\omega). \quad (2.46)$$

Specifically, the $t = 0$ relation gives

$$\int_0^\infty d\omega S_M(\omega) = C_M(0) = \sigma_M^2 + \overline{M}^2. \quad (2.47)$$

Thus, the PSD describes the noise power distribution over different frequencies.

Finally, general higher-order correlators [59] are defined as

$$S^n(\omega_1, \dots, \omega_{n-1}) = \lim_{T \rightarrow \infty} \frac{1}{(2\pi T)^{n/2}} \left(\prod_{i=1}^{n-1} M_T(\omega_i) \right) M_T^* \left(\sum_{i=1}^{n-1} \omega_i \right). \quad (2.48)$$

The PSD is the second-order correlator, and the higher-order correlators reveal how the noise components at different frequencies are correlated.

2.2.4 Fluctuation-dissipation theorem of magnetization

The noise PSD is related to the AC susceptibility when the system is in equilibrium. Consider a magnetization operator $\hat{M}(t)$ of the system. When the magnetization noise is ergodic, the time-correlation function is expressed by an ensemble average

$$C(t) = \left\langle \frac{1}{2} \{ \hat{M}(t), \hat{M}(0) \} \right\rangle. \quad (2.49)$$

The anti-commutator is used to ensure that the defined correlation function is a real number [59]. The PSD is obtained by the Wiener–Khinchin theorem (Eq. 2.45)

$$S_M(\omega) = \frac{2}{\pi} \int_0^\infty dt \cos(\omega t) \left\langle \frac{1}{2} \{ \hat{M}(t), \hat{M}(0) \} \right\rangle. \quad (2.50)$$

On the other hand, the Kubo formula expresses the AC susceptibility as an expectation value in equilibrium. The response to an external field perturbation $-\mu_0 V \hat{M} H(t)$ is described by the following susceptibility [59]

$$\chi(\omega) = V \mu_0 \frac{i}{\hbar} \int_0^\infty dt e^{-i\omega t} \langle [\hat{M}(t), \hat{M}(0)] \rangle, \quad (2.51)$$

$$\therefore \chi''(\omega) = V \mu_0 \frac{i}{\hbar} \int_0^\infty dt \sin(\omega t) \langle [\hat{M}(t), \hat{M}(0)] \rangle. \quad (2.52)$$

A comparison of the two expressions Eqs. 2.50 and 2.52 leads to the fluctuation-dissipation theorem (detailed calculation in Appendix A)

$$\chi''(\omega) = V \mu_0 \frac{\pi}{\hbar} \tanh \left(\frac{\hbar\omega}{2k_B T} \right) S_M(\omega). \quad (2.53)$$

The relation can be rewritten as

$$S_M(\omega) = \frac{2\hbar}{V \mu_0 \pi} \left(\frac{1}{2} + \frac{1}{e^{\frac{\hbar\omega}{k_B T}} - 1} \right) \chi''(\omega). \quad (2.54)$$

The first term surviving at $T \rightarrow 0$ can be understood as a zero-point fluctuation of the degrees of freedom that comprise the thermal bath [67]. At a high-temperature limit $k_B T \gg \hbar\omega$, the second term driven by the thermal excitations in the bath becomes dominant. The fluctuation-dissipation theorem in this high-temperature limit is

$$S_M(\omega) = \frac{1}{V\mu_0\pi} \frac{2k_B T}{\omega} \chi''(\omega) \quad (k_B T \gg \hbar\omega). \quad (2.55)$$

The fluctuation-dissipation theorem is a powerful tool. Firstly, the validity of the theorem can be used as a test of equilibrium. When the independent measurements of the noise PSD and the AC susceptibility find the theorem to be invalid, the system is not in equilibrium. Secondly, the theorem enables a prediction of the noise PSD from the AC susceptibility and vice versa, which helps plan and implement experiments.

The magnetization noise PSD $S_M(\omega)$ can also be directly related to the magnetic structure factor $S^{zz}(\mathbf{q}, \omega)$ in scattering experiments. From a space-time spin-spin correlation function $\langle s_z(\mathbf{0}, 0) s_z(\mathbf{r}, t) \rangle$,

$$S_M(\omega) = \frac{1}{\pi V} \left(2\mu_B \frac{N}{V} \right)^2 \int_{-\infty}^{\infty} d\mathbf{r} w(\mathbf{r}) \int_{-\infty}^{\infty} dt e^{-i\omega t} \langle s_z(\mathbf{0}, 0) s_z(\mathbf{r}, t) \rangle, \quad (2.56)$$

where the function $w(\mathbf{r})$ is determined by the sample geometry and local sensitivity of a pickup coil, and

$$S^{zz}(\mathbf{q}, \omega) = \frac{1}{2\pi\hbar} \frac{N}{V} \int_{-\infty}^{\infty} d\mathbf{r} e^{-i\mathbf{q}\cdot\mathbf{r}} \int_{-\infty}^{\infty} dt e^{-i\omega t} \langle s_z(\mathbf{0}, 0) s_z(\mathbf{r}, t) \rangle. \quad (2.57)$$

The two quantities are related as

$$S_M(\omega) = \frac{2\hbar}{V} (2\mu_B)^2 \frac{N}{V} \int d\mathbf{q} \tilde{w}(\mathbf{q}) S^{zz}(\mathbf{q}, \omega), \quad (2.58)$$

where $\tilde{w}(\mathbf{q})$ is the Fourier transform of $w(\mathbf{r})$.

Measurement of magnetization noise PSD in SQUID spin noise spectroscopy is complementary to scattering experiments as it probes different parameter ranges. SQUID spin noise can probe down to sub-Hz (\sim feV) frequency with sub-Hz resolution, as discussed later in this chapter. If sensitivity of a pickup coil is

spatially independent, measuring spins in a size- d sample $w(|\mathbf{r}| < d) = 1$ roughly corresponds to q -space integration by $\tilde{w}(|\mathbf{q}| < 1/d) \sim 1$. The bulk spin noise measurement of a large sample probes $\mathbf{q} \sim \mathbf{0}$, while local measurements will allow detection of larger \mathbf{q} .

2.2.5 Noise PSD characterized by relaxation

A noise PSD reflects relaxation time in the same manner as AC susceptibility, as expected from the correspondence seen in the fluctuation-dissipation theorem. It can be directly shown by the Bloch equation model of $M(t)$. Instead of a perturbative AC magnetic field, $M(t)$ is driven by a quantum/thermal fluctuation $A_\xi \xi(t)$.

$$\frac{dM_z}{dt} = -\frac{M_z}{\tau} + A_\xi \xi(t), \quad (2.59)$$

where A_ξ is a fluctuation amplitude and $\xi(t)$ is a normalized white noise satisfying

$$\overline{\xi(t)\xi(t')} = \delta(t - t'), \quad (2.60)$$

$$S_\xi(\omega) = \frac{2}{\pi} \int_0^\infty dt \cos(\omega t) \delta(t) = \frac{1}{\pi}. \quad (2.61)$$

By solving the Bloch equation for each Fourier component,

$$i\omega M_z(\omega) = -\frac{M_z(\omega)}{\tau} + A_\xi \xi(\omega), \quad (2.62)$$

$$\therefore S_{M_z}(\omega) = \frac{\tau^2}{1 + \omega^2 \tau^2} |A_\xi|^2 S_\xi(\omega), \quad (2.63)$$

$$= \frac{1}{\pi} \frac{\tau^2}{1 + \omega^2 \tau^2} |A_\xi|^2. \quad (2.64)$$

The correct normalization of the noise is imposed as

$$A_\xi = \sqrt{\frac{2\sigma_{M_z}^2}{\tau}}, \quad (2.65)$$

$$S_{M_z}(\omega) = \frac{2\sigma_{M_z}^2}{\pi} \frac{\tau}{1 + \omega^2 \tau^2}. \quad (2.66)$$

Using the Wiener–Khinchin theorem, the exponentially-decaying correlation function is obtained from the PSD.

$$C_{M_z}(t) = \sigma_{M_z}^2 e^{-|t|/\tau}. \quad (2.67)$$

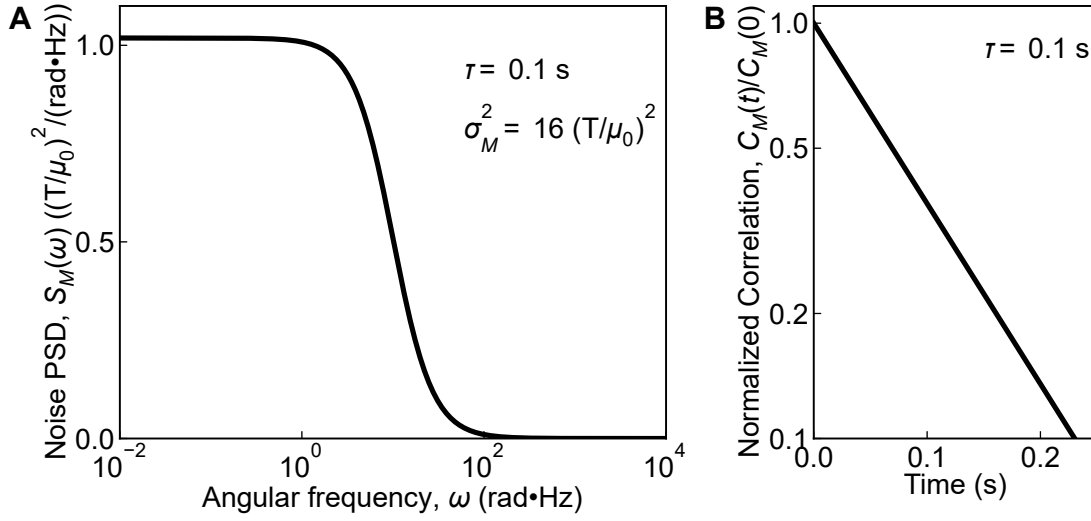


Figure 2.4: Typical form of the power spectral density (A) and the correlation function (B) in a system with a single relaxation time.

Eqs. 2.66 and 2.67 are plotted in Fig. 2.4. They are the standard form of the PSD and the correlation function in a system with a single relaxation time. One can confirm that Eqs. 2.12 and 2.66 satisfy the fluctuation-dissipation theorem in Eq. 2.55. The high-temperature limit of the theorem is appropriate here, as the Bloch equation formulation is (semi)classical.

The noise PSD is temperature dependent when the parameters $\tau(T)$ and $\sigma_{M_z}^2(T)$ are. In a simple paramagnet, where the relaxation time $\tau(T)$ generally prolongs upon cooling, the PSD should behave as shown in Fig. 2.5A. In a correlated spin state, the relaxation time can get distributed and the functional form of the PSD is modified accordingly. The empirically useful formula to fit the experimental PSD in a correlated spin state is

$$S_{M_z}(\omega) = \frac{2\sigma_{M_z}^2}{\pi} \frac{\tau}{(1 + (\omega\tau)^{2(1-\alpha)})^\beta}. \quad (2.68)$$

The way the parameters α and β are introduced is apparently similar to the Havriliak–Negami form of the AC susceptibility (Eq. 2.13), but α and β are not equivalent in the two formulas. When spins develop a strongly inhomogeneous state, the relaxation time distribution can be extremely broad over orders of magnitude. The PSD of such an inhomogeneous system can take a scale-invariant

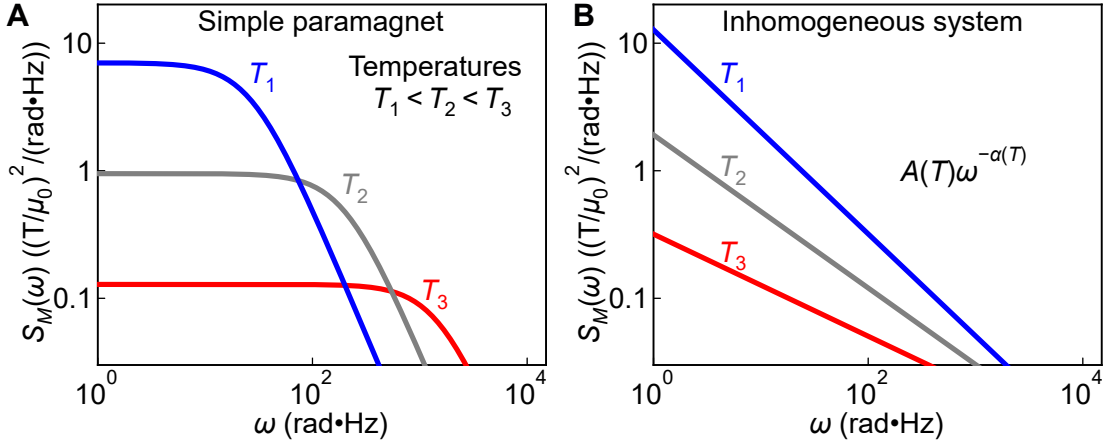


Figure 2.5: Examples of the magnetization noise power spectral density (M is in a unit of Tesla/ μ_0). (A) In a simple paramagnet, where a single relaxation time is prolonged upon cooling. (B) In an inhomogeneous spin state, where the distribution of relaxation times over orders of magnitude gives rise to a scale-invariant power-law form. The shown temperature dependence is just one example.

power-law form

$$S_{M_z}(\omega) = A\omega^{-\alpha}. \quad (2.69)$$

An example of the power-law PSD with an arbitrary temperature dependence is shown in Fig. 2.5B.

2.2.6 Noise PSD characterized by precession

A noise PSD also reflects the precessional dynamics, as AC susceptibility does.

The Bloch equation³ to be solved is

$$\frac{d\mathbf{M}}{dt} = \mu_0\gamma\mathbf{M} \times \mathbf{H} - \frac{\mathbf{M} - \chi^{\text{DC}}\mathbf{H}}{\tau} + \boldsymbol{\xi}, \quad (2.70)$$

$$\mathbf{H} = (H_x, 0, 0), \quad (2.71)$$

$$\boldsymbol{\xi} = \sqrt{\frac{2\sigma_M^2}{\tau}}(\xi_x, \xi_y, \xi_z). \quad (2.72)$$

After the cumbersome calculations in Appendix A, the z -direction magnetization noise PSD is obtained as

$$S_{M_z}(\omega) = \frac{\sigma_{M_z}^2}{\pi} \left(\frac{\tau}{1 + (\omega - \omega_E)^2\tau^2} + \frac{\tau}{1 + (\omega + \omega_E)^2\tau^2} \right). \quad (2.73)$$

³The relaxation time τ is assumed to be isotropic for simplicity.

The PSD peaks at a frequency close to the precession frequency (excitation energy) ω_E . One can confirm that Eqs. 2.22 and 2.73 satisfy the fluctuation-dissipation theorem Eq. 2.55. This precession contribution to PSD is generally complicated to derive (See for example Ref. [50, 52]).

2.2.7 Quantitative estimate of noise magnitude

The magnitude of spin noise depends on various factors: spin density, local spin magnitude, spin interactions, system size, and so on. In the case of non-interacting electron spins ($s = 1/2$) at a 1 nm spacing in a volume $V = 1 \text{ mm}^3$, independent 10^{18} spins will generate spin noise of magnitude

$$\sqrt{\sigma_M^2} \sim \frac{\mu_0 \mu_B \sqrt{N}}{V} = 1 \times 10^{-11} \text{ T} = 10 \text{ pT}. \quad (2.74)$$

Assuming that the spin noise PSD is almost flat up to a relaxation frequency of $\sim 10 \text{ kHz} \cdot \text{rad}$, the PSD will be of order

$$\sqrt{S_M(\omega)} \sim 1 \times 10^{-13} \text{ T} / \sqrt{\text{rad} \cdot \text{Hz}} = 100 \text{ fT} / \sqrt{\text{rad} \cdot \text{Hz}}. \quad (2.75)$$

The local spin density is usually higher than assumed here, so the PSD in a real system is larger than this estimate. Larger local spin magnitude such as $J \sim 5, 6$ from f-orbitals enhances the noise. Ferromagnetic interactions among the spins greatly enhance the magnetization noise, while antiferromagnetic interactions suppress it. In any case, to experimentally measure magnetization noise in a reasonable experimental time, one needs an extreme sensitivity of $\text{fT} / \sqrt{\text{rad} \cdot \text{Hz}}$ order, whereas laboratory magnetic field fluctuations have μT amplitudes.

2.3 SQUID Spin Noise Spectrometer

2.3.1 Principle of SQUID

The Superconducting QUantum Interference Device (SQUID) [68, 69] is the most sensitive sensor of magnetic flux in existence. A (DC) SQUID is a superconducting ring separated by two non-superconducting regions that play the role of Josephson junctions, as schematically shown in Fig. 2.6A. At a constant bias current I , the

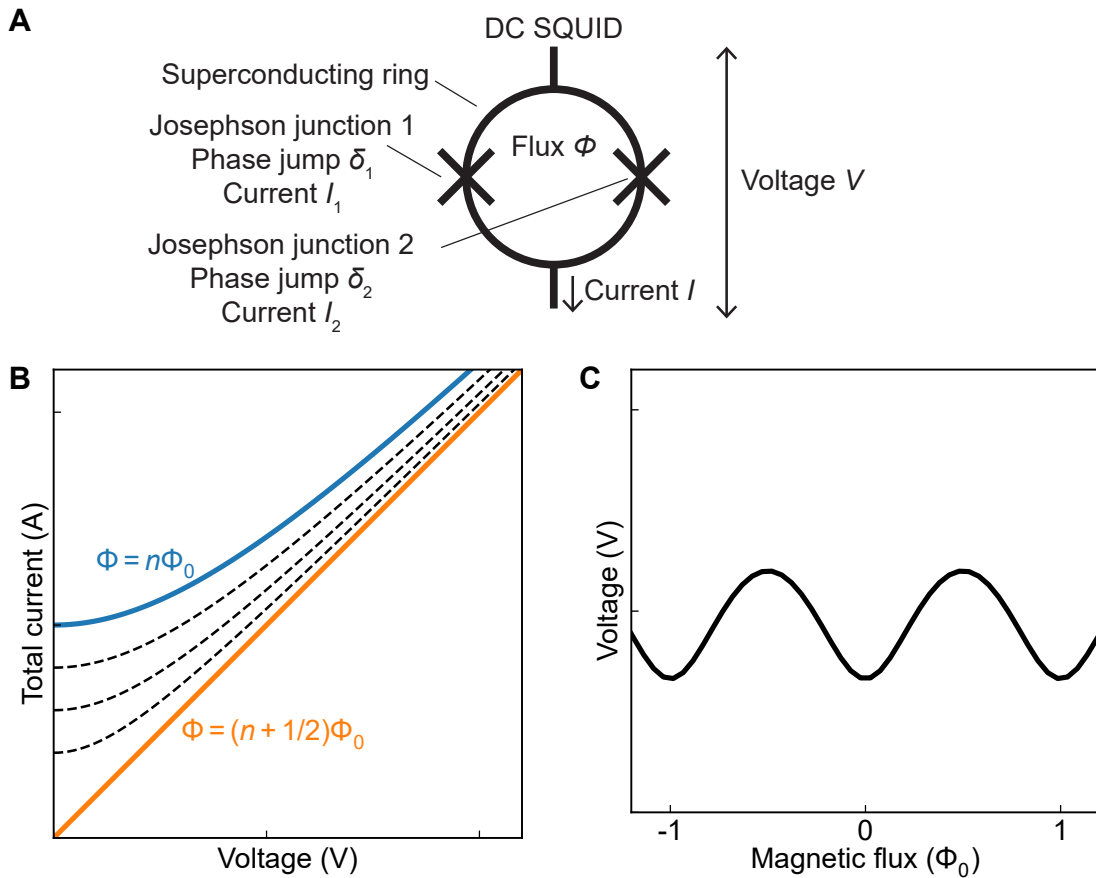


Figure 2.6: (A) Schematic diagram of a SQUID, a superconducting ring with two Josephson junctions. (B) $I - V$ relation of a SQUID for different values of flux Φ penetrating through the ring. (C) $V - \Phi$ relation of a SQUID at a constant bias current. The voltage is Φ_0 -periodic to Φ .

voltage V across the SQUID is Φ_0 -periodic in the magnetic flux Φ through the ring, as shown in Fig. 2.6C. The magnetic flux quantum $\Phi_0 = 2.07 \times 10^{-15} \text{ T}\cdot\text{m}^2$ is tiny, and the sharp slope of order $\frac{\partial V}{\partial \Phi} = 100 \mu\text{V}/\Phi_0$ [68] makes the SQUID an extremely sensitive magnetic flux sensor.

$V-\Phi$ relation of the SQUID

In a superconductor, a condensate of Cooper pairs forms a macroscopic wave function with a certain amplitude and phase. A Josephson junction is described by the phase difference δ between its two superconducting ends. Without inducing a voltage, superconducting current

$$I_J = I_0 \sin \delta \quad (2.76)$$

flows across the Josephson junction when $\delta \neq 0$. Here, I_0 is a parameter dependent on temperature, SQUID type, and geometry. When the voltage V across the Josephson junction is finite, the sum of normal current and supercurrent $I_J = V/R + I_0 \sin \delta$ flows across the junction, where R is the resistance between the terminals of the junction. Meanwhile, the phase difference evolves over time as

$$\dot{\delta} = (2\pi/\Phi_0)V. \quad (2.77)$$

A SQUID is characterized by the phase jump at each Josephson junction $\delta_{1,2}$ and the magnetic flux Φ threading the ring. They are bound by the condition

$$\delta_2 - \delta_1 = 2\pi \frac{\Phi}{\Phi_0}, \quad (2.78)$$

modulo 2π , imposed by the single-valuedness of the wave function around the SQUID ring. Consider when a bias current flowing from one side to another is externally set to a certain value $I_{\text{tot}} > 0$. For small I_{tot} , the value of phase jumps δ_1 and δ_2 evolve until they satisfy the relations in Eqs. 2.76 and 2.78, and supercurrent flows across the SQUID without inducing a voltage.

$$I_{\text{tot}} = I_0(\sin \delta_1 + \sin \delta_2) \quad (2.79)$$

$$= 2I_0 \sin \left(\frac{\delta_2 + \delta_1}{2} \right) \cos \left(\frac{\delta_2 - \delta_1}{2} \right) \quad (2.80)$$

$$= 2I_0 \sin \left(\frac{\delta_2 + \delta_1}{2} \right) \cos \left(\pi \frac{\Phi}{\Phi_0} \right) \quad (2.81)$$

$$= I_{\text{tot}}^c(\Phi) \sin \left(\frac{\delta_2 + \delta_1}{2} \right), \quad (2.82)$$

where

$$I_{\text{tot}}^c(\Phi) = 2I_0 \cos \left(\pi \frac{\Phi}{\Phi_0} \right). \quad (2.83)$$

$|I_{\text{tot}}^c|$, which is Φ_0 -periodic to Φ , is the maximum value that can be afforded by supercurrent alone.

When $I_{\text{tot}} > |I_{\text{tot}}^c|$, normal current starts flowing across the SQUID and induces finite voltage V . The current flowing across the Josephson junction is the sum of normal current and supercurrent $I_{\text{tot}} = V/R + I_0(\sin \delta_1 + \sin \delta_2)$, where R is

the resistance of the SQUID. This relation turns into a differential equation of δ_1 using Eqs. 2.77, 2.78, and 2.82.

$$I_{\text{tot}} = \frac{\Phi_0}{2\pi R} \dot{\delta}_1 + I_{\text{tot}}^c(\Phi) \sin\left(\delta_1 + \pi \frac{\Phi}{\Phi_0}\right). \quad (2.84)$$

This equation is analytically solvable and gives the time-averaged voltage

$$\bar{V}^t = \frac{\Phi_0}{2\pi} \dot{\delta}_1^{-t} = R \sqrt{(I_{\text{tot}})^2 - (I_{\text{tot}}^c(\Phi))^2}. \quad (2.85)$$

This V - I relation for the SQUID is plotted in Fig. 2.6B for different values of Φ . At a constant bias current $I_{\text{tot}} = \text{Const.}$, V is Φ_0 -periodic to Φ as shown in Fig. 2.6C.

The introduced SQUID model is a simplified version. The full model, which includes the capacitance across the Josephson junction and the inductance of the ring, quantitatively explains the realistic characteristics of a SQUID [68].

Flux-locked measurement

Despite the extreme sensitivity, a bare SQUID can measure only a tiny range of magnetic flux $-\Phi_0/4 < \Phi < +\Phi_0/4$. A SQUID typically has a negative feedback circuit that cancels out the external flux and extends the measurement range. When the flux at the SQUID is changed by $\Delta\Phi$, the feedback circuit will apply a cancellation flux $\Phi_{\text{fb}} := -G_{\text{open}}\Delta\Phi$, where G_{open} is an open-loop gain of the feedback circuit (i.e. a virtual gain when the SQUID does not sense the cancellation flux). As a result, the change of the total flux at the SQUID $\Delta\Phi_{\text{total}}$ caused by an external flux Φ_{ex} is suppressed.

$$\Delta\Phi_{\text{total}} = \Phi_{\text{ex}} + \Phi_{\text{fb}} = \Phi_{\text{ex}} - G_{\text{open}}\Delta\Phi_{\text{total}}. \quad (2.86)$$

$$\therefore \Delta\Phi_{\text{total}} = \frac{\Phi_{\text{ex}}}{1 + G_{\text{open}}} \sim \frac{\Phi_{\text{ex}}}{G_{\text{open}}}. \quad (2.87)$$

The working range of SQUID is extended to $-G_{\text{open}}\Phi_0/4 < \Phi_{\text{ex}} < +G_{\text{open}}\Phi_0/4$, and the exact value of the original external flux $\Phi_{\text{ex}} = -(1 + 1/G_{\text{open}})\Phi_{\text{fb}}$ can be precisely calculated from the voltage ($\propto \Phi_{\text{fb}}$) induced in the feedback circuit. This measurement scheme is called a flux-locked loop, as the total flux at the SQUID is almost locked at the initial value.

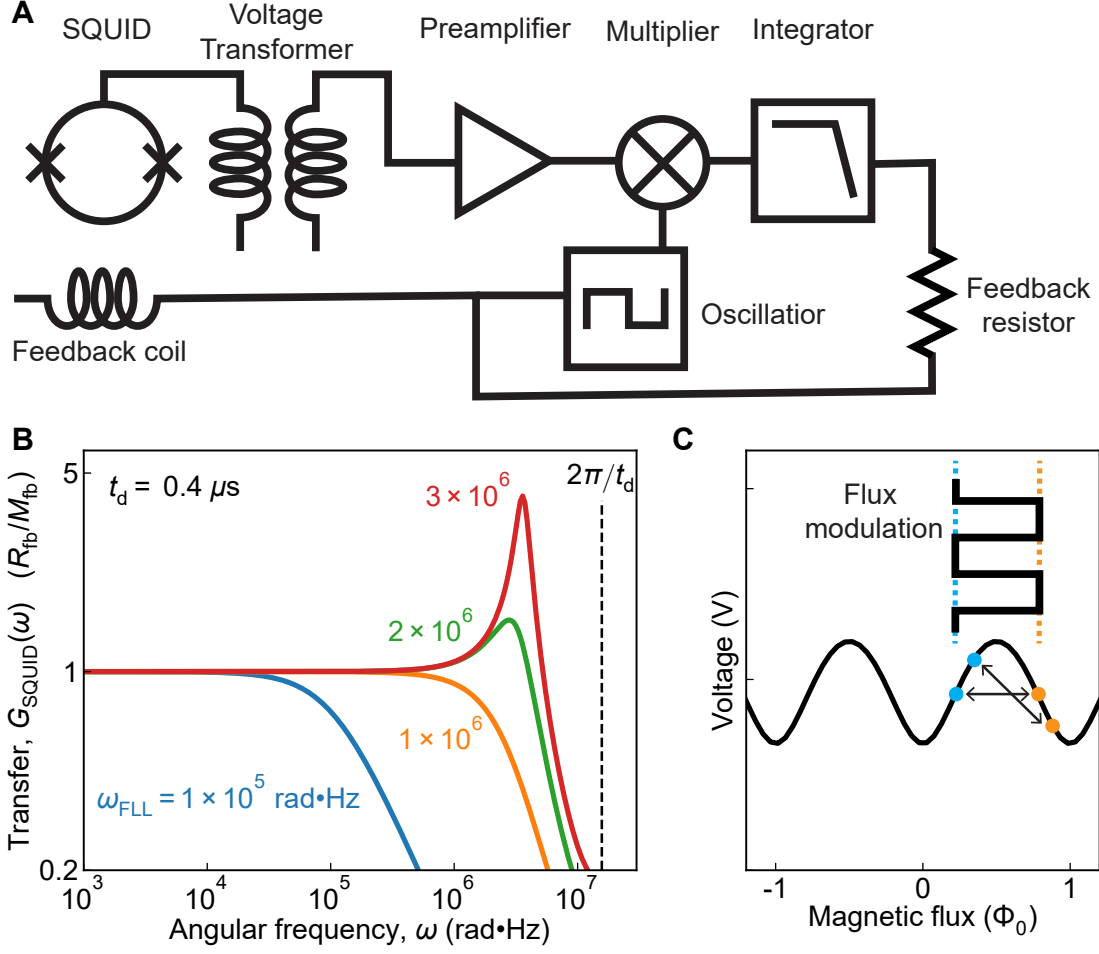


Figure 2.7: (A) Schematic circuit diagram of a flux-locked loop circuit that employs a flux-modulation technique. (B) Frequency dependence of a SQUID transfer function. (C) Schematic drawing of a flux-modulation technique.

Φ_{ex} is assumed to be a constant in the simple model above. However, $\Phi_{\text{ex}}(t)$ generally fluctuates over time, and the feedback flux is delayed by a short time t_d from the original flux fluctuation at the SQUID.

$$\Delta\Phi_{\text{total}}(t) = \Phi_{\text{ex}}(t) - G_{\text{open}}\Delta\Phi_{\text{total}}(t - t_d). \quad (2.88)$$

In order that the flux in this realistic feedback loop locks in a stable way $\Delta\Phi_{\text{total}}(t) \rightarrow \text{Const.}$, a signal integrator has to cut off high-frequency fluctuations at $\omega \gtrsim 2\pi/t_d$.

As schematically shown in Fig. 2.7A, a realistic feedback circuit consists of a SQUID with the bare transfer coefficient $\frac{\partial V}{\partial \Phi}$; the series of a voltage transformer, a preamplifier, and a multiplier giving the total gain G_{elec} ; an integrator comprising a resistor R_{int} and a capacitor C_{int} (cutoff at $\omega_{\text{int}} = 1/(R_{\text{int}}C_{\text{int}})$); a feedback resistor

R_{fb} ; and a feedback coil that couples to the SQUID with the mutual inductance M_{fb} . The voltage across the feedback resistor is read out as the output V_{out} . The feedback loop equation of the flux is

$$\Delta\Phi_{\text{total}}(t) = \Phi_{\text{ex}}(t) - M_{\text{fb}} \frac{1}{R_{\text{fb}}} \frac{1}{R_{\text{int}} C_{\text{int}}} \int_0^{t-t_d} dt' \left(G_{\text{elec}} \frac{\partial V}{\partial \Phi} \Delta\Phi_{\text{total}}(t') \right). \quad (2.89)$$

In the frequency domain, the open-loop gain of the feedback circuit is⁴

$$G_{\text{open}}(\omega) = M_{\text{fb}} \frac{1}{R_{\text{fb}}} \frac{1}{R_{\text{int}} C_{\text{int}}} \frac{1}{i\omega} e^{-i\omega t_d} G_{\text{elec}} \frac{\partial V}{\partial \Phi} = \frac{\omega_{\text{FLL}}}{i\omega} e^{-i\omega t_d}, \quad (2.90)$$

$$\text{where } \omega_{\text{FLL}} = M_{\text{fb}} \frac{1}{R_{\text{fb}}} \frac{1}{R_{\text{int}} C_{\text{int}}} G_{\text{elec}} \frac{\partial V}{\partial \Phi}. \quad (2.91)$$

The locked flux will be

$$|\Delta\Phi_{\text{total}}(\omega)| = \left| \frac{1}{1 + G_{\text{open}}(\omega)} \Phi_{\text{ex}}(\omega) \right| \quad (2.92)$$

$$= \left(1 / \sqrt{1 + \frac{\omega_{\text{FLL}}^2}{\omega^2} - 2 \frac{\omega_{\text{FLL}}}{\omega} \sin(\omega t_d)} \right) |\Phi_{\text{ex}}(\omega)|, \quad (2.93)$$

with the corresponding voltage output

$$|V_{\text{out}}(\omega)| = \frac{R_{\text{fb}}}{M_{\text{fb}}} |G_{\text{open}}(\omega)| |\Delta\Phi_{\text{total}}(\omega)| \quad (2.94)$$

$$= \frac{R_{\text{fb}}}{M_{\text{fb}}} \left(1 / \sqrt{1 + \frac{\omega^2}{\omega_{\text{FLL}}^2} - 2 \frac{\omega}{\omega_{\text{FLL}}} \sin(\omega t_d)} \right) |\Phi_{\text{ex}}(\omega)|. \quad (2.95)$$

The SQUID transfer function is defined by the ratio of voltage output to the externally applied flux as

$$G_{\text{SQUID}}(\omega) = \frac{|V_{\text{out}}(\omega)|}{|\Phi_{\text{ex}}(\omega)|}. \quad (2.96)$$

The frequency-dependence of $G_{\text{SQUID}}(\omega)$ is plotted in Fig. 2.7B for various ω_{FLL} . As long as $\omega \ll \omega_{\text{FLL}}$ and $\omega \ll 2\pi/t_d$, the SQUID transfer function takes the frequency-independent value

$$g_{\text{SQUID}} = G_{\text{SQUID}}(\omega \ll \omega_{\text{FLL}}, 2\pi/t_d) = \frac{R_{\text{fb}}}{M_{\text{fb}}}. \quad (2.97)$$

⁴The frequency response of the integrator $\omega_{\text{int}}/(i\omega)$ assumed here is ideal. More practical form is $1/(1 + i\omega/\omega_{\text{int}})$, which gives the unity gain at low frequency.

Above $\omega \sim \omega_{\text{FLL}}$ but still $\omega \ll 2\pi/t_d$, the frequency cutoff introduced by the integrator starts playing a role. The bandwidth of the flux-locked loop measurement defined by the 3dB cutoff frequency is

$$\omega_{3\text{dB}} = \omega_{\text{FLL}} = \frac{M_{\text{fb}}}{R_{\text{fb}}} \frac{1}{R_{\text{int}} C_{\text{int}}} G_{\text{elec}} \frac{\partial V}{\partial \Phi}. \quad (2.98)$$

While the bandwidth can be extended by changing the feedback resistor R_{fb} or the integrator resistor/capacitor $\omega_{\text{int}} = 1/(R_{\text{int}} C_{\text{int}})$, the behavior of the feedback circuit becomes more unstable as ω_{FLL} approaches $2\pi/t_d$. Ultimately, the frequency requirement $\omega \ll 2\pi/t_d$ imposed by the delay time limits the bandwidth of a stable flux-locked loop, which is about 100 MHz·rad due to the typical distance of 1 m between SQUID and the room-temperature electronics [68]. In a typical SQUID, the flux-modulation technique described in the next section further reduces the bandwidth from this flux-locked loop limit.

Flux-modulation technique

The output voltage of a bare SQUID is very small, with the intrinsic voltage noise level of the order $0.1 \text{ nV}/\sqrt{\text{Hz}}$ [68]. While this small voltage has to be amplified in the feedback circuit, the SQUID sensitivity is degraded if one directly uses an electronic amplifier whose typical input voltage noise level is 10 times larger at $1 \text{ nV}/\sqrt{\text{Hz}}$. This issue can be avoided by first using a voltage transformer to amplify the SQUID signal by ~ 10 , and then feeding the signal into an electronic preamplifier.

A flux modulation technique is typically employed to use the voltage transformer even for a low-frequency signal. An oscillator and a multiplier are incorporated into the feedback circuit as shown in Fig. 2.7A. A modulation signal from the oscillator, a square wave at an angular frequency $\omega_{\text{FM}} \gg \omega_{\text{FLL}}$, is applied to the SQUID via the feedback coil. Its amplitude is adjusted so that the SQUID state jumps between the two flux-locked points with an opposite sign of $\frac{\partial V}{\partial \Phi}$, as schematically shown in Fig. 2.7C. This modulates the SQUID output voltage as $V(t) \rightarrow V(t)f(t)$, where $f(t)$ is a square wave that flips sign at the modulation

frequency ω_{FM} . After the modulated SQUID output is successfully amplified via the voltage transformer and the electronic preamplifier, the modulation part $f(t)$ is removed by the multiplier (or the lock-in amplifier). While the concept is simple, a successful flux modulation technique requires a voltage transformer that has a flat frequency response in the wide frequency range from ω_{FM} to its harmonics $\sim 10\omega_{\text{FM}}$ [69]. With a commonly-used ω_{FM} of order 1 MHz·rad, the SQUID bandwidth typically gets limited in the range from 10 kHz·rad to several 100 kHz·rad. However, a SQUID system of 100 MHz·rad order bandwidth, close to the flux-locked loop limit, is also available. Such broad bandwidth is achieved by a flux modulation at $\omega_{\text{FM}} \sim 100$ MHz·rad, or a direct readout with additional positive feedback where a flux modulation is not involved [68].

2.3.2 SQUID spin noise spectrometer

To measure magnetization fluctuation noise $M_z(t)$ using a SQUID, a pickup coil is wound around a magnetic sample and coupled to the SQUID [68] as shown in Fig. 2.8A. The total magnetic flux penetrating through the pickup coil is

$$\Phi_p(t) = N_p A_p \mu_0 M_z(t), \quad (2.99)$$

where N_p and A_p are the number of turns and area of the pickup coil, respectively. The z direction is perpendicular to the cross-section of the coil. The pickup and SQUID input coils, whose inductance are L_p and L_i , respectively, form a superconducting loop to quantize the threading flux. When the sample generates magnetic flux fluctuation $\Phi_p(t)$ at the pickup coil, supercurrent $\Phi_p(t)/(L_p+L_i)$ flows in the loop to cancel it out. The supercurrent flowing through the SQUID input coil, coupled to the SQUID via the mutual inductance M_i , generates magnetic flux $\Phi_S(t)$ at the SQUID. Thus, the flux is transferred from the pickup coil to the SQUID as

$$\Phi_S(t) = \frac{M_i}{L_p + L_i} \Phi_p(t). \quad (2.100)$$

The SQUID output voltage is proportional to $\Phi_S(t)$.

$$V_{\text{out}}(t) = g_{\text{SQUID}} \Phi_S(t), \quad (2.101)$$

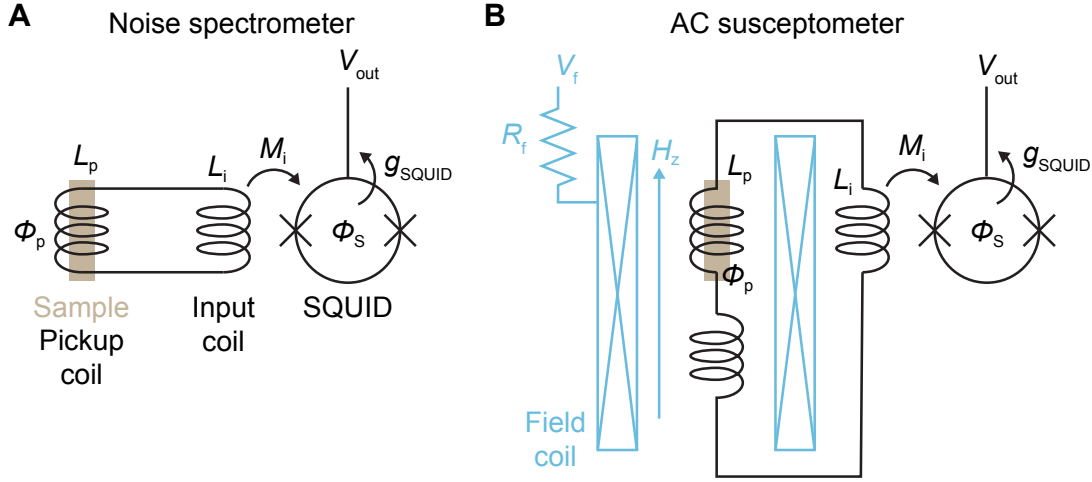


Figure 2.8: Schematic drawing of a SQUID spin noise spectrometer (A) and a SQUID susceptometer (B).

where g_{SQUID} is the transfer function in Eq. 2.97. Therefore, the SQUID output voltage can be converted to the flux and magnetization at the pickup coil by the following simple constants.

$$\Phi_p(t) = \alpha V_{\text{out}}(t), \quad \alpha = \frac{L_p + L_i}{M_i} \frac{1}{g_{\text{SQUID}}}, \quad (2.102)$$

$$M_z(t) = \alpha' V_{\text{out}}(t), \quad \alpha' = \frac{1}{N_p A_p \mu_0} \frac{L_p + L_i}{M_i} \frac{1}{g_{\text{SQUID}}}. \quad (2.103)$$

All the coefficients comprising α and α' are known or can be calibrated with high precision. Note that g_{SQUID} in Eqs. 2.101, 2.102, and 2.103 should be changed to $g_{\text{SQUID}} g_{\text{preamp}}$ when an electronic amplifier is used to contribute extra gain g_{preamp} (Section 3.2.3).

2.3.3 SQUID susceptometer

A conventional AC susceptometer measures magnetic flux via electromotive-force voltage $V^{\text{EMF}} = -\frac{d\Phi_p}{dt}$, but it has good sensitivity only at high frequency. The SQUID's extreme sensitivity, which extends to the DC signal, makes a good susceptometer with a broad frequency range. As shown in Fig. 2.8B, one needs to add a field coil around the pickup coil. The pickup coil is changed from a single coil to an in-series counter-wound coil, which cancels out the externally applied

uniform field and prevents the sample signal from being smeared out. The design of the in-series pickup coil is detailed in Chapter 3.

To measure AC susceptibility $\chi(\omega)$, an AC voltage $V_f = V_0 \cos(\omega t)$ is applied across the field coil. An AC magnetic field $H_z = H_0 \cos(\omega t)$ is induced in the z -direction. H_0 is related to V_0 by

$$H_0 = \frac{n_f}{R_f} V_0, \quad (2.104)$$

where n_f is the number density of the field coil turns and R_f is the resistance in series with the field coil. Consequently, the magnetization oscillation $M_z = M_0 \cos(\omega_0 t - \phi)$ in the z -direction is induced in the sample. The pickup coil captures the magnetization as the magnetic flux penetrating through it, which is given by

$$\Phi_p(t) = N_p A_p \mu_0 M_0 \cos(\omega t - \phi). \quad (2.105)$$

The output voltage of the SQUID will be

$$V_{\text{out}} = g_{\text{SQUID}} \frac{M_i}{L_p + L_i} N_p A_p \mu_0 M_0 \cos(\omega t - \phi). \quad (2.106)$$

Using a lock-in amplifier, V_{out} can be compared to the applied voltage V_f . The in-phase and out-of-phase components will be

$$V_X = g_{\text{SQUID}} \frac{M_i}{L_p + L_i} N_p A_p \mu_0 M_0 \cos \phi, \quad (2.107)$$

$$V_Y = g_{\text{SQUID}} \frac{M_i}{L_p + L_i} N_p A_p \mu_0 M_0 \sin \phi. \quad (2.108)$$

Therefore, the real and imaginary susceptibility can be converted from $V_{X,Y}$ using

$$\chi'(\omega) = \frac{M_0}{H_0} \cos \phi = \frac{R_f}{n_f} \frac{1}{g_{\text{SQUID}}} \frac{L_p + L_i}{M_i} \frac{1}{N_p A_p \mu_0} \frac{V_X}{V_0}, \quad (2.109)$$

$$\chi''(\omega) = \frac{M_0}{H_0} \sin \phi = \frac{R_f}{n_f} \frac{1}{g_{\text{SQUID}}} \frac{L_p + L_i}{M_i} \frac{1}{N_p A_p \mu_0} \frac{V_Y}{V_0}. \quad (2.110)$$

All the coefficients on the right-hand side are known or can be calibrated with high precision.

In the same manner, by applying a DC voltage V_0 and recording the output voltage V_{out} , the DC susceptibility χ^{DC} can be obtained using

$$\chi^{\text{DC}} = \frac{M_0}{H_0} = \frac{R_f}{n_f} \frac{1}{g_{\text{SQUID}}} \frac{L_p + L_i}{M_i} \frac{1}{N_p A_p \mu_0} \frac{V_{\text{out}}}{V_0}. \quad (2.111)$$

2.4 Spin noise approach to fingerprinting different magnetic phases

2.4.1 Capability of spin noise approach

Experimental detection of spin noise in spin liquids is challenging, largely because a spin noise signal is usually tiny. Since the pioneering work by Dusad *et al.*, a series of spin noise study has been performed in a classical spin ice $\text{Dy}_2\text{Ti}_2\text{O}_7$ [15, 62, 70]. I have further developed the technique to apply it for quantum spin liquid candidates $\text{Ca}_{10}\text{Cr}_7\text{O}_{28}$ [23] and $\text{ZnCu}_3(\text{OH})_6\text{Cl}_2$, the main work discussed in this thesis. The spin noise spectroscopy of quantum magnets is still in the early stage of development. Here I separately discuss what is possible with the current spectrometer and what is potentially possible with the future spectrometers.

With the current SQUID spin noise spectrometer, the accessible frequency range is from sub-Hz to 100 kHz (meV to neV), making it suitable for studying the slow dynamics of a magnetic system. The slow dynamics are often dominated by relaxational spin dynamics, unless precessional spin dynamics exist due to gapless excitations of massive density. With an extreme sub-Hz frequency resolution of a SQUID spin noise spectrometer, one can precisely fit a low-frequency power spectral density. The fitting is very sensitive to the distribution of relaxation time and can clearly distinguish a system with a single relaxation time (Eq. 2.66), narrowly distributed relaxation times (Eq. 2.68), and relaxation times broadly distributed over orders of magnitude (Eq. 2.69). This fitting enables a clear distinction between a homogeneous magnetic state (e.g. geometrically frustrated classical spin liquid, quantum spin liquid) and an inhomogeneous one (e.g. spiral spin liquid with momentum vortices, spin glass, random singlet state). Further, when the relaxation time distribution is relatively sharp, one can extract the value and distribution extent of relaxation time $\tau(T)$, whose temperature dependence hints at the spin excitation and its underlying ground state in the system. For example, the Arrhenius law $\tau(T) \propto e^{\Delta/k_B T}$ indicates the existence of an energy gap in local spin excitations. The precise study of the relaxation time led to

a discovery of fractal monopole dynamics in a classical spin ice $\text{Dy}_2\text{Ti}_2\text{O}_7$ [63]. Development of a general microscopic theory of relaxation time, which remains largely unexplored to my knowledge, could potentially enable further distinctions among different homogeneous magnetic states and distinctions among different inhomogeneous states through their relaxational dynamics. I also note that spin noise spectroscopy of “witness-spins” interacting with a magnetic system has the potential of evidencing quantum spin liquid, as later discussed in Chapter 5.

Commercial SQUID with a flux-locked loop is available with a bandwidth of 20 MHz (sub- μeV). Going beyond GHz (sub-meV) is also possible if one abandons the flux-locked loop. Further, using a microscale pickup coil will enable local spin noise spectroscopy $S_M(\mathbf{r}, \omega, T)$. When these developments are implemented, spin noise spectroscopy will also be suitable for studying the precessional spin dynamics of various spin excitations at different wave vectors and frequencies, as in scattering experiments. It is predicted that the parameter-dependence of the spin noise PSD $S_M(\mathbf{r}, \omega, T)$ can fingerprint different quantum spin liquids [50, 52]. Fingerprinting classical spin liquids is expected to be also possible, although comprehensive analytical/computational predictions of $S_M(\mathbf{r}, \omega, T)$ for classical spin liquids have not been made.

To summarize, the spin noise spectroscopy can clearly distinguish homogeneous magnetic states (e.g. geometrically frustrated classical spin liquid, quantum spin liquid, etc.) from inhomogeneous ones (e.g. spiral spin liquid with momentum vortices, spin glass, random singlet state, etc.) using relaxational dynamics, and can fingerprint different quantum spin liquids once precessional dynamics can be locally measured at high frequency. Predictions of relaxational dynamics in various magnetic states, which are still missing to my knowledge, could enable further clear distinction within homogeneous states and within inhomogeneous states. Also, predictions of spin dynamics $S_M(\mathbf{r}, \omega, T)$ in various classical spin liquids are strongly motivated to make the technique more useful.

I note that, to observe spontaneous spin noise, the relaxational or precessional dynamics must be excited thermally (or by external field perturbations). In a

magnetic system with an energy gap Δ , spin noise is expected to diminish rapidly as the temperature becomes smaller than the energy gap $k_B T \ll \Delta$. Thus, the spin noise technique is insensitive to a fully gapped system at low temperatures, which could in turn enable spin noise to distinguish between gapless and gapped systems with an extreme energy resolution of feV order.

2.4.2 Comparison of spin noise approach to other techniques

There are different types of established techniques to probe spin dynamics: inelastic neutron scattering, nuclear magnetic resonance, muon spin rotation, and so on. Different techniques have their own strengths. AC susceptometry and spin noise spectroscopy have the following advantages over other techniques.

1. They directly probe the magnetic response of electron spins, not particles interacting with it.
2. The probe is sensitive to only magnetic signals, so the signal is not contaminated by nonmagnetic contributions such as phonons.⁵ The magnetic response directly corresponds to spin dynamics in an insulator, where charge-current is negligible.
3. Zero (or minimal) magnetic field is applied, which enables the study of the unperturbed equilibrium state.
4. They can probe down to sub-Hz frequency regime with an extreme frequency resolution of $1 \text{ rad}\cdot\text{Hz} \sim 1 \text{ feV}$ energy scale, whereas the sensitivity of resonance techniques degrades with falling frequency.

Spin noise PSD is related to a magnetic structure factor in neutron/x-ray scattering (Eq. 2.58). SQUID spin noise spectroscopy is complementary to those techniques as it can probe much lower frequency and has an extreme frequency resolution, which enables the precise exploration of the spin relaxation dynamics. The functional

⁵The effect of nonmagnetic contribution is still observed as a second-order effect, such as scattering of magnetic spins due to phonon.

form of spin relaxation noise PSD provides a clear distinction between homogeneous and inhomogeneous magnetic states, and temperature dependence of relaxation time value and distribution can also reveal underlying magnetic states, as discussed in the previous subsection. Further, there is a potential for directly fingerprinting different spin liquid states when high-frequency and local spin noise measurement is achieved in the future.

Further, there are key advantages of pursuing spin noise spectroscopy over AC susceptometry.

1. Spin noise does not require the application of any field. This enables the measurement of an unambiguous zero-field equilibrium state, both experimentally and computationally. The zero-field condition is particularly important in studying spin liquids where small fields can easily alter the ground state.
2. Spin noise is a better probe of spin dynamics at low frequency. As the fluctuation-dissipation theorem at the high-temperature limit (Eq. 2.55) indicates, the spin noise PSD is enhanced by a factor $1/\omega$ compared to the imaginary susceptibility.
3. The spin noise study of an out-of-equilibrium system, such as a driven system or a glassy system, should yield information independent from the AC susceptibility. Also, higher-order correlators contain unique information on how the spin noise at different frequencies are correlated [59, 71].
4. Spin noise measures the full frequency spectrum in one go without a frequency sweep of the field, facilitating the study of frequency dependence. This not only critically saves the experimental time but also the computational time when one performs a numerical simulation to compare with the experiment.
5. The spin noise spectrometer design is much simpler than the AC susceptometer, as shown in Fig. 2.8. The absence of a field coil will simplify frequency range extension to MHz and GHz, and provide greater flexibility in the experimental configuration potentially enabling local spin noise measurement.

When spin noise PSD and imaginary susceptibility are independently measured, a comparison between them will be an experimental test of the fluctuation-dissipation theorem, the validity of which is not a priori guaranteed at low temperatures.

As a final remark, the Nitrogen Vacancy (NV) center measurement is rapidly being developed to perform high-precision magnetization measurements. However, its sensitivity $\text{pT}/\sqrt{\text{Hz}}$ is still three orders of magnitude lower than that of SQUID $\text{fT}/\sqrt{\text{Hz}}$ when this thesis is being written [61]. The three-order difference is critical because improving the signal-to-noise ratio by 10^3 requires averaging from 10^6 times longer measurements.

3

SQUID Spin Noise Spectrometer

In this chapter, I will introduce the development of Superconducting QUantum Interference Device (SQUID) spin noise spectrometers shown in Fig. 3.1. The spectrometers are designed to achieve an extreme field sensitivity approaching 10^{-14} T/ $\sqrt{\text{rad} \cdot \text{Hz}}$ under an ultra-low vibration condition, a maximum bandwidth of 1 MHz·rad, and a temperature range of $10 \text{ mK} \leq T \leq 6000 \text{ mK}$ ($270 \text{ mK} \leq T \leq 6000 \text{ mK}$) in the cryogen-free dilution (^3He) refrigerator.

3.1 Spin noise spectrometer

Fig. 3.2A shows the schematic of the SQUID spin noise spectrometer, which also serves as a susceptometer. It consists of a signal pickup coil, a SQUID chip, a field coil (optional), and magnetic-shielding cylinders. As explained in detail in Section 2.3.2, the pickup coil and the SQUID input coil form a superconducting loop that transfers the magnetic flux from the pickup coil to the SQUID.

3.1.1 Pickup coil

Pickup Coil fabrication

Pickup coils are manually made of a thin NbTi superconducting wire (Supercon). A wire whose bare (Formvar-insulated) diameter is 0.125 mm (0.152 mm) is used

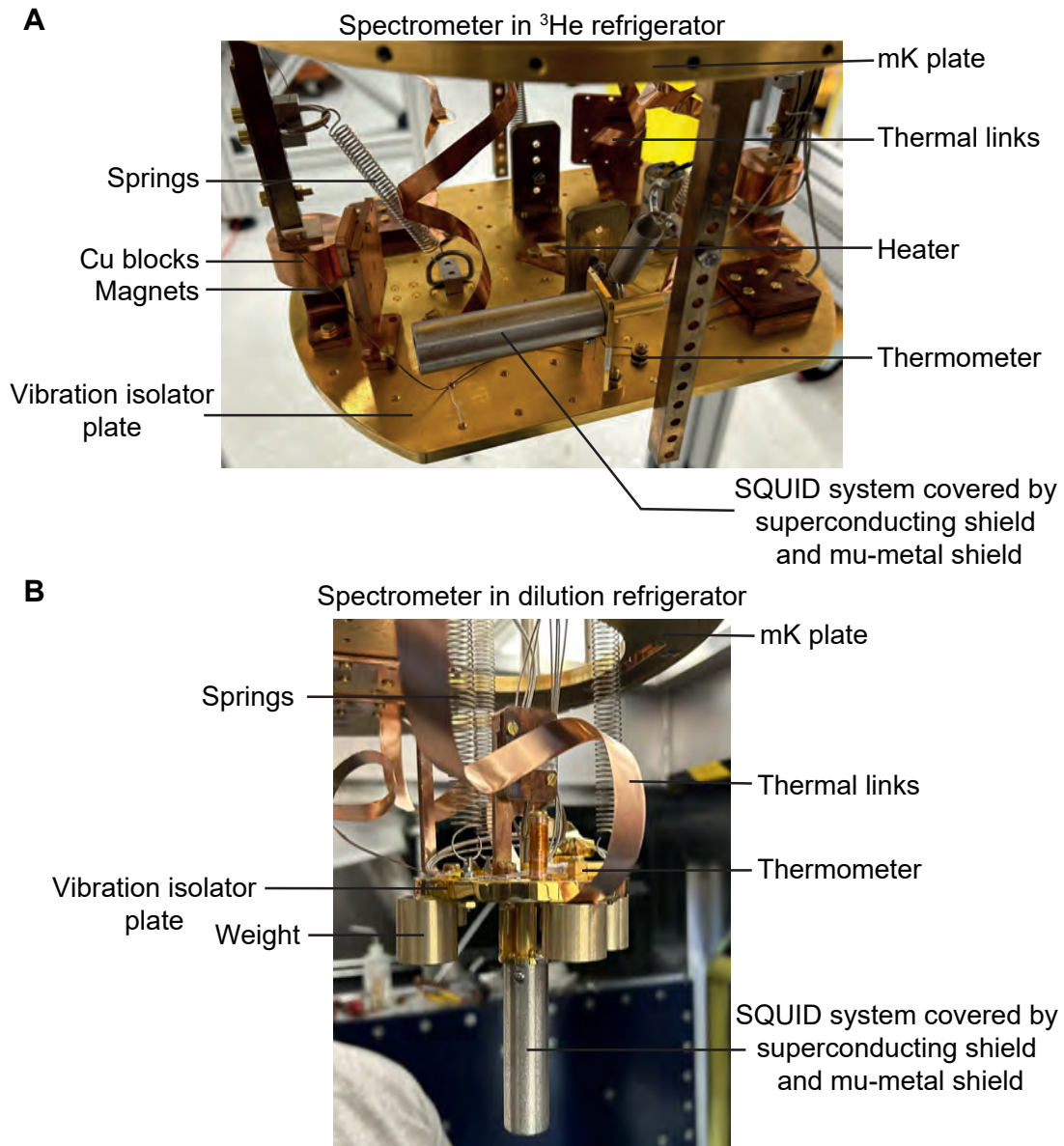


Figure 3.1: Overview photo of the SQUID spin noise spectrometer in the ^3He refrigerator (**A**) and dilution refrigerator (**B**).

in an initial developing stage, and it is later changed to 0.076 mm (0.091 mm) to achieve better sensitivity.

Two types of pickup coil were fabricated. The first type is a single coil, suitable for achieving the highest spectrometer sensitivity. An example of a single coil I fabricated is shown in Fig. 3.2B. This specific coil has 20 turns and a diameter of ~ 2 mm. The coil is designed to be freestanding without a solid sample holder, as the wall thickness of a holder will inevitably reduce the sample-filled fraction

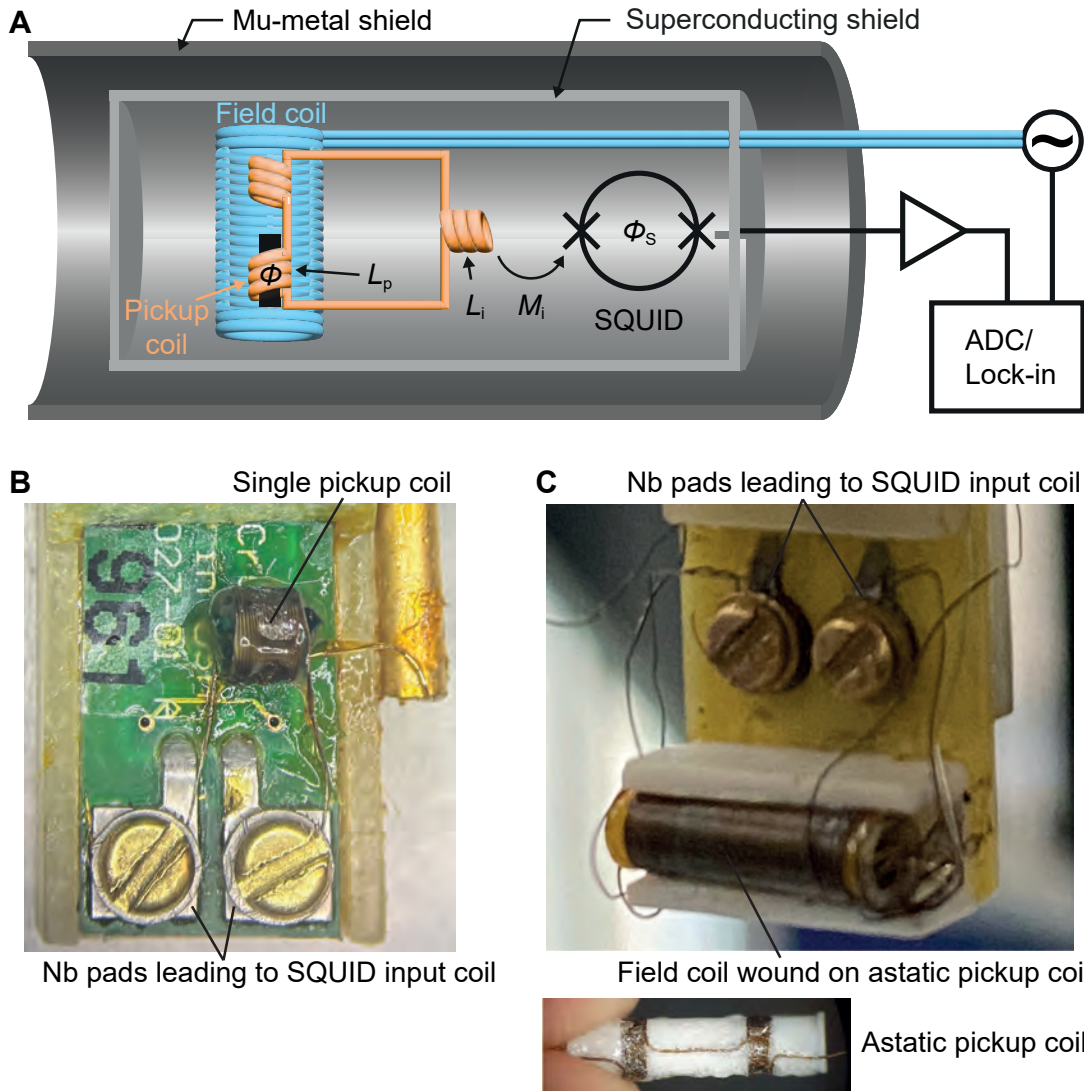


Figure 3.2: (A) Schematics of a SQUID spectrometer with an astatic pickup coil, which is equipped with a field coil to also serve as a susceptometer. (B) Photo of a single pickup coil mounted on an SQ1200 SQUID chip. The pickup coil makes a superconducting contact with the SQUID input circuit via the niobium pads. In this specific photo, a $\text{ZnCu}_3(\text{OH})_6\text{Cl}_2$ sample is in the pickup coil, and a 0.1 mm-diameter silver wire is glued to the sample using GE varnish. (C) Photo of an astatic pickup coil, on which a field coil is wound, mounted on an SP550 SQUID chip. In this specific photo, a $\text{Ca}_{10}\text{Cr}_7\text{O}_{28}$ sample is in the pickup coil, and a 0.1 mm-diameter silver wire is glued to the sample using GE varnish. (A) is reproduced from Ref. [23] with a minor modification.

of the coil and degrade the signal sensitivity. To fabricate a freestanding single coil, a wooden or metallic rod of an appropriate diameter of 1–2 mm is used as a temporary winding core. A 0.2 mm thick polytetrafluoroethylene (PTFE) film is wrapped around the core, and the NbTi wire is wound closely packed on the

PTFE film. A nonmagnetic epoxy (Stycast 1266) is carefully spread on top of the wire and is cured to fix the coil mechanically. After the epoxy fully hardens, the coil is pulled out from the core, which can be done without difficulty thanks to the flexibility of the PTFE film. Further, The PTFE film can also be mechanically removed from the fixed coil. A small amount of PTFE film remains glued inside the coil, but nonmagnetic PTFE does not generate any magnetic signal that will affect the measurements. The winding core diameter should be chosen to be close to the sample size, so that the sample-filled fraction of the finished coil is maximized.¹

The second type of coil is an astatic coil designed to measure susceptibility. As shown in Fig. 3.2C, it is made of two in-series counter-wound coils: a sample coil to capture the sample signal and a compensation coil to cancel out an externally applied uniform magnetic flux.² A freestanding coil is not appropriate here, as the two coils should be configured as equal as possible to cancel out the uniform flux. Thus, the astatic coil is wound on a macor sample holder with gaps guiding the coil position and direction. The diameter of the sample space is 1.6 mm, and the wall diameter of the sample holder is 0.2 mm — the thinnest limit with reasonable strength. The coil winding involves extra care so that the geometry of the two coils is as symmetric as possible. Loctite 495 superglue, which dries instantaneously and is removable by acetone, is used to fix the coil.

After the coils are fabricated, the Formvar insulation at the wire ends is removed by a razor blade. The pickup coil inductance of sub- μH is measured by an E4980 Precision LCR meter (Keysight) at 300 kHz using a series equivalent circuit model (Ls mode). A superconducting contact to the SQUID circuit is made by pressing the wire end between the SQUID niobium pad and a niobium washer, using a brass screw that contracts at low temperatures.

¹Winding a coil directly on a sample can further improve the sample-filled fraction than this freestanding-coil method. However, direct winding is difficult for a fragile single crystal that will easily break off. To measure $\text{Ca}_{10}\text{Cr}_7\text{O}_{28}$ and $\text{ZnCu}_3(\text{OH})_6\text{Cl}_2$, whose single crystals are relatively fragile, fabricating an empty freestanding coil first and inserting the sample later had a much lower risk of breaking the sample.

²The astatic coils for the experiments discussed in this thesis are wound by Xiaolong Liu and Jack Murphy. For a different experiment, I designed and fabricated an astatic coil with the same principle.

Optimization of coupling between pickup coil and SQUID

When one purchases a commercial SQUID, the following parameters are fixed: the inductance L_i of the SQUID input coil, the mutual inductance M_i between the input coil and the SQUID, and the intrinsic flux noise power spectral density (PSD) $S_{\phi_s}^{\text{int}}(\omega)$ at the SQUID. To maximize the measurement sensitivity of the flux noise PSD $S_{\phi_p}(\omega)$ at the pickup coil, one has to choose appropriate pickup coil parameters that can maximize the flux PSD $S_{\phi_s}(\omega)$ transferred at the SQUID. Here, the optimal pickup coil design is derived based on the following two assumptions.

1. The magnetization noise PSD $S_M(\omega)$ from the sample is inverse-proportional to the sample volume V covered by the pickup coil $S_M(\omega) \propto 1/V$.
2. The pickup coil is a solenoid whose wire turns are closely packed so that its length is $l_p = d_{\text{wire}}N_p$, and a sample completely fills in the pickup coil so that $V = d_{\text{wire}}N_pA_p$. Here, l_p , A_p , and N_p are the length, area, and number of turns of the pickup coil. d_{wire} is the diameter of the wire.

The inductance of the pickup coil is estimated to be $L_p = \mu_0N_pA_p(N_p/l_p) = \mu_0N_pA_p/d_{\text{wire}}$. As explained in Section 2.3.2, the flux PSD transferred at the SQUID is given by

$$S_{\phi_s}(\omega) = \left(\frac{M_i}{L_p + L_i} \right)^2 S_{\phi_p}(\omega) \quad (3.1)$$

$$= \left(\frac{M_i}{L_p + L_i} N_p A_p \mu_0 \right)^2 S_M(\omega) \quad (3.2)$$

$$\propto \left(\frac{M_i}{L_p + L_i} N_p A_p \mu_0 \right)^2 \frac{1}{d_{\text{wire}} N_p A_p} \quad (3.3)$$

$$= \mu_0 \left(\frac{M_i}{L_p + L_i} \right)^2 L_p =: X(L_p). \quad (3.4)$$

Matching the inductance between the pickup coil and the SQUID input coil $L_p = L_i$ will achieve the best sensitivity with $X(L_p) = \mu_0 M_i^2 / (4L_i)$.

Note that the sensitivity degradation due to a mismatch between L_p and L_i is not rapid. For example, $X(L_p)$ is 90% of the maximum for $L_p = L_i/2$, and 30% for even $L_p = L_i/10$. Practically, one tends to be more constrained by the size of

the single crystal available. If the available crystal is small, maximizing the filling fraction of the coil should be prioritized over matching the inductance.

3.1.2 SQUID chip

Two types of SQUID chips, an SQ1200 SQUID (Star Cryoelectronics) and an SP550 SQUID (Quantum Design), are used for different spectrometers. The two SQUID chips work in a similar principle, although they have different geometries and parameters. Fig. 3.2B shows the part of an SQ1200 SQUID chip around the niobium pads. The two niobium pads are the end of the SQUID input coil, and the pickup makes superconducting contact with them. Star Cryoelectronics reports the SQUID input coil inductance $L_i = 1.3 \mu\text{H}$, which couples to the SQUID with the mutual inductance $M_i = 16 \text{ nH}$ corresponding to $1/M_i = 0.13 \mu\text{A}/\Phi_0$. Fig. 3.2C shows the part of an SP550 SQUID chip around the niobium pads. Quantum Design reports $L_i = 1.7 \mu\text{H}$, and $M_i = 11 \text{ nH}$ corresponding to $1/M_i = 0.19 \mu\text{A}/\Phi_0$.

3.1.3 Field coil

A field coil enables susceptibility measurements, as well as spin noise measurements under a field. A field coil is incorporated into the spin noise spectrometer by winding it directly on the astatic pickup coil as shown in Fig. 3.2C.³ The NbTi superconducting wire with the insulated diameter of 0.091 mm, the same wire as the pickup coil, is used to wind the field coil with the approximate total length of $\sim 10 \text{ mm}$ and 101 turns.

Calibration of field strength and astatic coil imbalance

The magnetic field strength and the imbalance of the two coils in the astatic coil (the sample and compensation coil) can be calibrated. Let N be the number of turns of each coil, A_1 and A_2 be the area of the sample and compensation coil, respectively, and B/I be the magnetic flux density B generated by the field coil

³The field coils are wound by Xiaolong Liu and Jack Murphy.

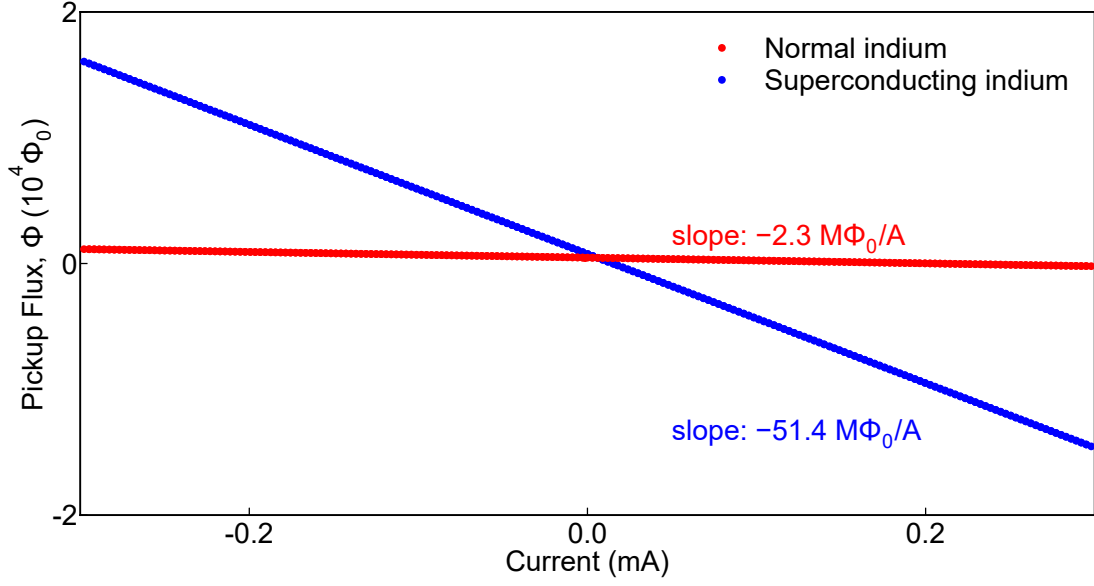


Figure 3.3: Total flux Φ picked up by an astatic coil when a 1 mm-diameter indium sample ($T_c \sim 3.4$ K) is in the sample coil. Above T_c (red), the magnetic susceptibility of the indium in the normal state is negligible compared to the superconducting state, and the slope $\Phi/I = -2.3 \times 10^6 \Phi_0/A$ is dominated by the coil imbalance. Below T_c (blue), the indium becomes superconducting and dominates the slope $-51.4 \times 10^6 \Phi_0/A$.

per applied current I . The total flux picked up by the empty astatic coil is

$$\Phi_{\text{empty}} = N(A_1 - A_2) \frac{B}{I} I. \quad (3.5)$$

When a thin rod of superconducting indium ($\chi = -1$) with a known cross-section A_{In} is placed in the sample coil, the total flux is given by

$$\Phi_{\text{In}} = N(A_1 - A_2 + (-1)A_{\text{In}}) \frac{B}{I} I. \quad (3.6)$$

By measuring these two Φ - I relations, $N(A_1 - A_2)(B/I)$ and $N(A_1 - A_2 - A_{\text{In}})(B/I)$ are determined accurately from the slope as shown in Fig. 3.3. The field strength per current (B/I) and the astatic coil imbalance $A_1 - A_2$ are thus obtained.

Fig. 3.3 shows the field sweep response of an $N = 10$ astatic coil when a 1 mm diameter indium sample ($T_c \sim 3.4$ K) is in the sample coil. Below T_c , the indium becomes superconducting and exhibits perfect diamagnetism ($\chi = -1$). Above T_c , the normal indium gives negligible susceptibility. From the measured slopes $N(A_1 - A_2) \frac{B}{I} = -2.3 \times 10^6 \Phi_0/A$ and $N(A_1 - A_2 - A_{\text{In}}) \frac{B}{I} = -51.4 \times 10^6 \Phi_0/A$,

one can calculate the parameters

$$\frac{B}{I} = 12.9 \text{ mT/A}, \quad (3.7)$$

$$A_1 - A_2 = -0.037 \text{ mm}^2. \quad (3.8)$$

The obtained B/I is close to the value estimated from the geometry

$$\left(\frac{B}{I}\right)_{\text{estimate}} = \mu_0 n \sim 12.7 \text{ mT/A}, \quad (3.9)$$

where n [/m] is the winding number density of the field coil. The pickup coil imbalance is as small as 1% of the pickup coil cross-sectional area $A_1 \sim 3 \text{ mm}^2$.

3.1.4 Magnetic Shielding

The whole SQUID spectrometer is shielded from environmental magnetic flux by a niobium cylinder and a mu-metal cylinder, as schematically shown in Fig. 3.2A. For an open-ended cylinder, both axial and transverse fields at the cylinder axis are attenuated with a factor $\exp(-z/a)$, where a is the radius of the cylinder, and z is the distance from the open end [72]. When either side of the cylinder is closed-ended, the shielding effect far away from the open end gets highly enhanced. The attenuation factor is of the order 1000 for an axial field and 100 for a transverse field for a one-side-closed-ended superconducting shield, when simulated for a cylinder whose height to radius ratio is 2.6 [73].

For the magnetic shielding of the SQ1200 SQUID spectrometer, a closed-ended niobium cylinder and an open-ended mu-metal cylinder from the SQUID supplier (Star Cryoelectronics) are used. The niobium cylinder has the length of 61 mm, the outer diameter of 17 mm, and the thickness of ~ 0.6 mm; and the mu-metal cylinder has corresponding dimensions of 76 mm, 21 mm, and ~ 1.3 mm, respectively. A samarium cobalt magnet for vibration isolation (described in Section 3.3) is located about 100 mm away from the SQUID spectrometer. The extra magnetic field contribution of the magnet is estimated to be $\sim 100 \mu\text{T}$, comparable to the earth's magnetic field. Therefore, this magnet does not significantly degrade the

SQUID spectrometer performance after shielding, as confirmed by the flat noise floor without vibration peaks in Fig. 3.5B.

For the SP550 SQUID spectrometer, in addition to a closed-ended niobium cylinder provided by the SQUID supplier (Quantum Design), another open-ended niobium cylinder and an open-ended mu-metal cylinder are used. The length, outer diameter, and thickness are 47 mm, 13 mm, and ~ 0.3 mm for the provided niobium cylinder; 153 mm, 52 mm, and 2 mm for the second niobium cylinder; and 300 mm, 60 mm, and 1 mm for the mu-metal cylinder, respectively. The residual magnetic field inside the shields was estimated to be smaller than 100 nT, as the application of 100 nT field flipped the sign of magnetization aging in $\text{ZnCu}_3(\text{OH})_6\text{Cl}_2$ (Chapter 5).

3.2 Electronics

The circuit diagrams for noise and susceptibility measurements are shown in Fig. 3.4. For simplicity, the feedback circuit of the SQUID (detailed in Section 2.3.1) is represented by the SQUID transfer function g_{SQUID} . The magnetization response of the sample is picked up as the magnetic flux and transferred to the SQUID. The output voltage of the SQUID is amplified and filtered at the voltage preamplifier, and the final signal is recorded by either an analog-to-digital converter or a lock-in amplifier. Each step is detailed below.

3.2.1 SQUID control

The four parameters control the SQUID and its feedback circuit: a bias current (BIAS), a modulation current amplitude (MOD) and phase shift (PHASE), and a bias flux (OFFSET). The bias current is set high enough so that the SQUID shows a proper $V - \Phi$ curve, as shown in Fig. 2.6C. The modulation current amplitude and phase shift are relevant to the flux-modulation technique (Section 2.3.1). They should be adjusted to maximize the multiplier output — the flux modulation amplitude should correspond to half a flux quantum, and the phase shift should compensate for the phase delay of the SQUID response reaching the multiplier. The bias flux is arbitrarily adjusted for convenience.

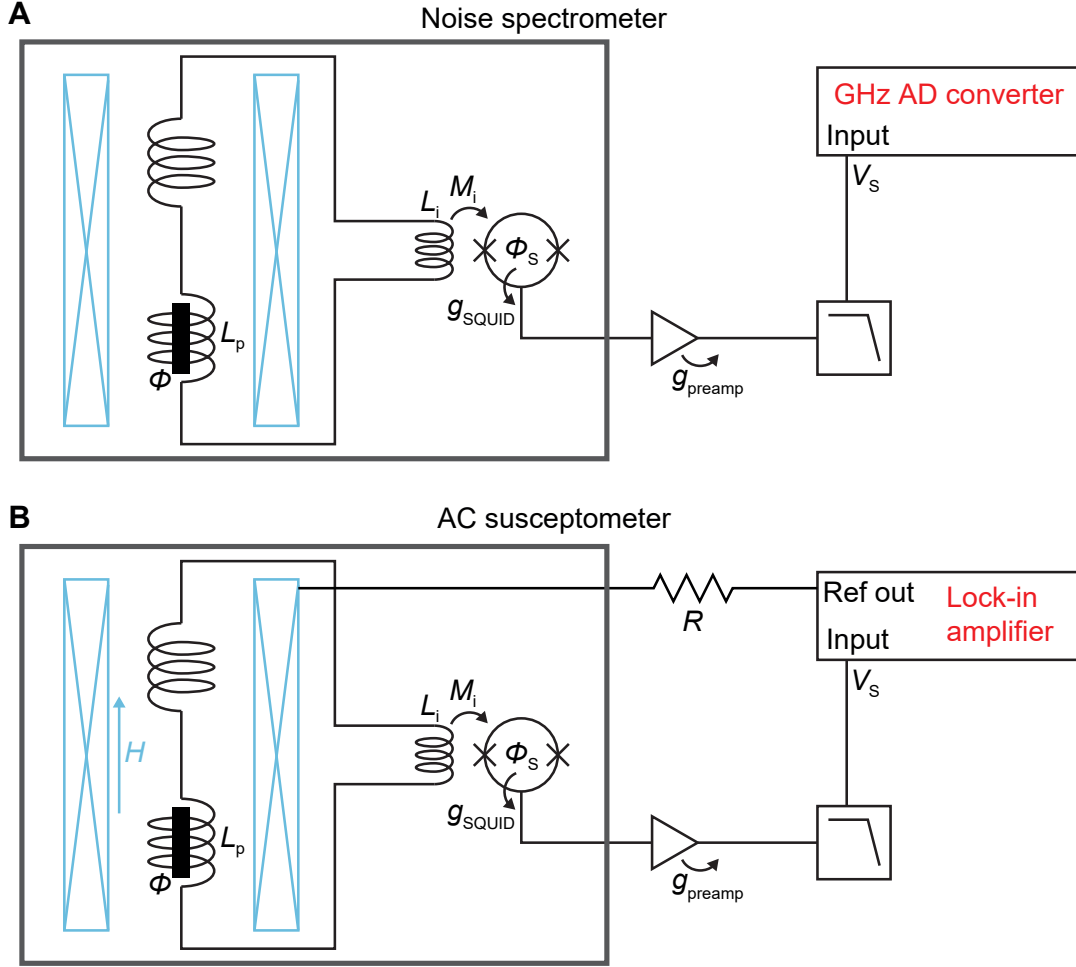


Figure 3.4: Circuit diagrams for spin noise measurement (A) and susceptibility measurement (B). The SQUID feedback circuit of the flux-locked loop is represented by the SQUID transfer function g_{SQUID} . Figures reproduced from Ref. [23] with a minor modification.

3.2.2 SQUID flux-locked loop

The SQ1200 SQUID chip is connected to a PFL-100 feedback loop system (Star Cryoelectronics), operated by a PCS-100 SQUID controller (Star Cryoelectronics). The nominal value of the mutual inductance between the feedback coil and the SQUID is $M_{\text{fb}} = 0.245$ nH corresponding to $1/M_{\text{fb}} = 8.43$ $\mu\text{A}/\Phi_0$. The feedback resistance in the High-sensitivity mode is $R_{\text{fb}} = 1$ M Ω . The integrator capacitance and resistance are $C_{\text{int}} = 1$ nF and $R_{\text{int}} = 10$ k Ω , respectively. The total gain of the feedback circuit is $G_{\text{amp}} = 1.6 \times 10^5$. The modulation frequency is 256 kHz. In some estimates in this section, I use a typical value of $\frac{\partial V}{\partial \Phi} = 100$ $\mu\text{V}/\Phi_0$ for

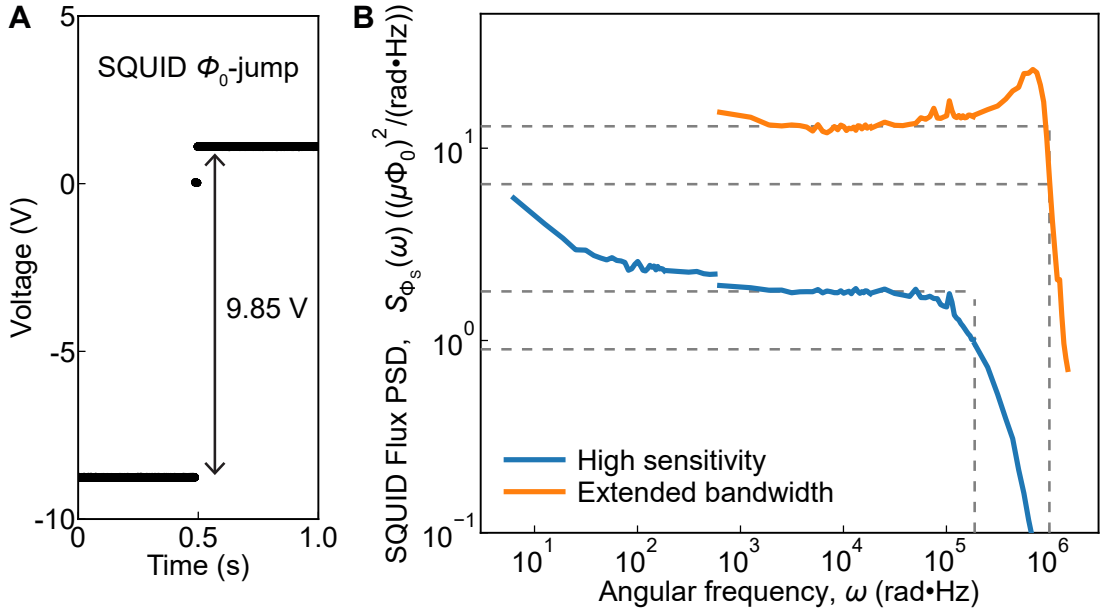


Figure 3.5: (A) SQUID output voltage jump triggered by a temporary opening of the SQUID feedback circuit (RESET operation), corresponding to a Φ_0 -change in the SQUID flux. The data is measured at 500 mK. (B) Power spectral density of the intrinsic SQUID flux noise in the High-sensitivity mode (blue) and the extended-bandwidth setting (orange). The spectrum below 600 rad·Hz is calculated from the 20 kSa/s data, while that above 600 rad·Hz is from the 1 MSa/s data. Gray dashed lines guide the eye to the noise floor and the 3 dB cutoff frequency.

the gain of a bare SQUID.

The High-sensitivity mode of the SQUID is typically used in the spin noise measurement. Fig. 3.5A shows a jump of the SQUID output voltage triggered by a temporary opening of the feedback circuit (RESET operation) at 500 mK. The jump corresponds to a Φ_0 -change in the SQUID flux. Thus, the SQUID transfer function is obtained as $g_{\text{SQUID}} \sim 9.85 \text{ V}/\Phi_0$. The transfer function has a slight temperature dependence of less than 1% in the temperature range $100 \text{ mK} \leq T \leq 1000 \text{ mK}$, which is ignored in the following experiments.

The SQUID flux noise PSD measured below 1 K is shown in Fig. 3.5B. The noise floor $S_{\Phi_s}(\omega) \sim 1.8 (\mu\Phi_0)^2/(\text{rad} \cdot \text{Hz})$ is comparable to the spec value $S_{\Phi_s}(\omega) = 2.5 (\mu\Phi_0)^2/(\text{rad} \cdot \text{Hz})$ at 4 K.⁴ The bandwidth defined by the 3 dB power cutoff is $\omega_{3\text{dB}} \sim 190 \text{ kHz}\cdot\text{rad}$ (i.e. $f_{3\text{dB}} \sim 30 \text{ kHz}$). The measured values of g_{SQUID} and $\omega_{3\text{dB}}$

⁴Note that a PSD $S(\omega)$ in the angular frequency domain (Eq. 2.43), is scaled from a typical PSD $S(f)$ defined in the frequency domain by $S(\omega) = S(f)/2\pi$. The SQUID flux noise in a spec sheet is typically denoted $\sqrt{S_{\Phi_s}(f)} = 4 \mu\Phi_0/\sqrt{\text{Hz}}$.

are consistent with the estimates from Eqs. 2.97 and 2.98.

$$g_{\text{SQUID}}^{\text{estimate}} = \frac{R_{\text{fb}}}{M_{\text{fb}}} = 8.4 \text{ V}/\Phi_0, \quad (3.10)$$

$$\omega_{3\text{dB}}^{\text{estimate}} = M_{\text{fb}}\omega_{\text{int}}G_{\text{amp}}\frac{1}{R_{\text{fb}}}\frac{\partial V}{\partial \Phi} = 190 \text{ kHz} \cdot \text{rad}. \quad (3.11)$$

The Quantum Design SP550 SQUID works using a similar principle. The following parameters are provided in the spec sheet: $M_{\text{fb}} = 1.4 \text{ nH}$ corresponding to $1/M_{\text{fb}} = 1.5 \text{ } \mu\text{A}/\Phi_0$, the feedback resistance $R_{\text{fb}} = 500 \text{ k}\Omega$ in the range 5 mode (highest sensitivity), and the modulation frequency 500 kHz . The SQUID transfer function $g_{\text{SQUID}} = 0.73 \text{ V}$, measured from a Φ_0 -jump, is consistent with the estimate $g_{\text{SQUID}}^{\text{estimate}} = \frac{R_{\text{fb}}}{M_{\text{fb}}} = 0.75 \text{ V}/\Phi_0$. The noise floor increases gradually above $5 \text{ kHz}\cdot\text{rad}$ to form a broad peak around $100 \text{ kHz}\cdot\text{rad}$, followed by a steep drop at a higher frequency, reminiscent of the example transfer function curve ($\omega_{\text{FLL}} = 2 \times 10^6 \text{ rad}\cdot\text{Hz}$ one) in Fig. 2.7B. Such frequency dependence is likely due to the time delay in the SQUID feedback circuit.

Extension of SQUID bandwidth in SQ1200

The SQ1200 SQUID system allows changes of the feedback resistor R_{fb} and the integrator capacitor C_{int} , with which one can extend the SQUID bandwidth $\omega_{3\text{dB}} \propto 1/(R_{\text{fb}}C_{\text{int}})$ (see Eq. 2.98). From the built-in choices of R_{fb} and C_{int} in the PFL-100 feedback loop, $R_{\text{fb}} = 100 \text{ k}\Omega$ and $C_{\text{int}} = 1 \text{ nF}$ are chosen so that the estimated extended bandwidth is $\omega_{3\text{dB}}^{\text{estimate}} \sim 2 \text{ MHz}\cdot\text{rad}$. This change simultaneously reduces the SQUID transfer function to $g_{\text{SQUID}} \sim 0.985 \text{ V}/\Phi_0$. The intrinsic SQUID noise in this extended-bandwidth setting is shown as the orange line in Fig. 3.5B. The actual extended bandwidth $\omega_{3\text{dB}} \sim 1 \text{ MHz}\cdot\text{rad}$ (i.e. $f_{3\text{dB}} \sim 160 \text{ kHz}$) is smaller than the estimate, likely due to the time delay in the feedback circuit. The noise floor has risen with a broad peak appearing around $600 \text{ kHz}\cdot\text{rad}$. Note that the SQUID is intentionally detuned in Fig. 3.5B; otherwise, the peak around $600 \text{ kHz}\cdot\text{rad}$ is much sharper.

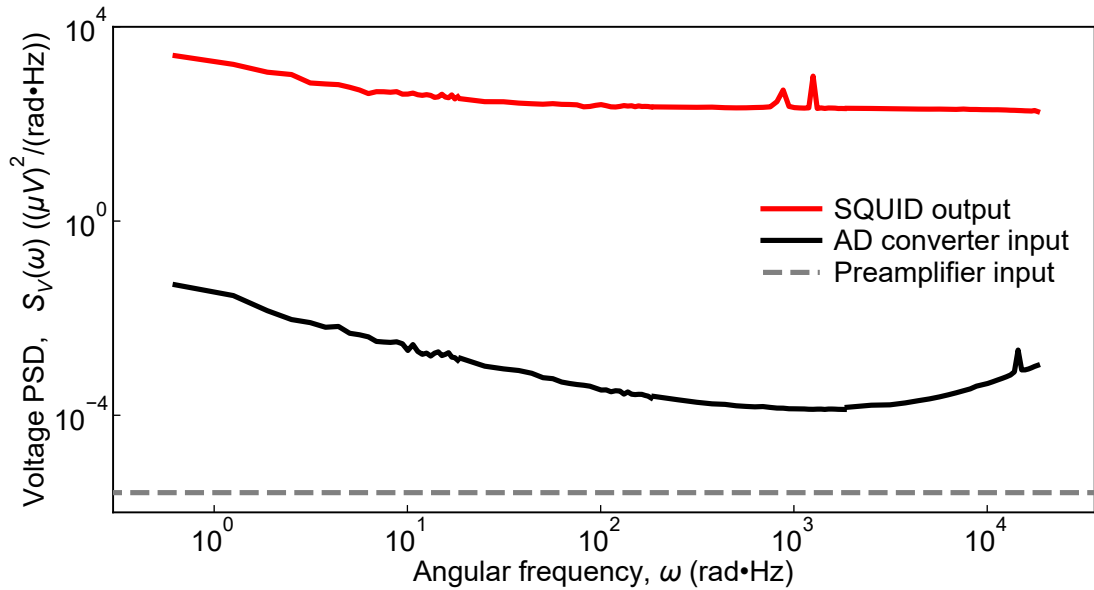


Figure 3.6: Voltage noise power spectral density of electronics. The input noise of an SR560 voltage preamplifier and that of a Moku:Pro analog-to-digital converter are orders of magnitude lower than the measured intrinsic output noise of an SQ1200 SQUID.

3.2.3 Voltage preamplifier

The output voltage of the SQUID controller is fed into an SR560 voltage preamplifier (Stanford Research Systems). It has an input noise level below $4 \text{ nV}/\sqrt{\text{Hz}}$ at 1 kHz, which is orders of magnitude below the intrinsic noise level of the SQUID output voltage as shown in Fig. 3.6. The preamplifier gain is chosen so that the preamplifier output spans the full input range of the analog-to-digital converter.

In typical spin noise measurements, 6 dB/oct 0.03 Hz high-pass and 6 dB/oct 30 kHz low-pass filters are applied at the voltage preamplifier to remove the DC component and the high-frequency components above the Nyquist frequency. For the SQ1200 SQUID, a 5 kHz 4-pole low-pass filter at the SQUID controller output is also typically applied. These filter choices are changed as appropriate depending on the frequency range of interests.

3.2.4 Analog-to-digital converter

A Moku:Pro (Liquid Instruments) is used as an analog-to-digital converter. While its maximum sampling rate is 5 GSa/s, the ‘Datalogger’ mode allowing a continuous measurement at a maximum sampling rate of 10 MSa/s with an 18-bit 400 mVpp

range is typically used. The input voltage noise level is below $500 \text{ nV}/\sqrt{\text{Hz}}$, which is orders of magnitude below the intrinsic noise level of the SQUID output voltage as shown in Fig. 3.6. The $1 \text{ M}\Omega$ input impedance, DC coupling, and 400 mVpp range setting is typically used. The Datalogger mode automatically applies a low-pass filter around the Nyquist frequency to prevent aliasing, but it did not play a critical role in my measurements. The frequency filters applied at the SQUID controller output and the voltage preamplifier attenuate high-frequency components beforehand.

3.2.5 Lock-in amplifier

An SR830 (Stanford Research Systems) is used as a lock-in amplifier. The time constant τ_{LI} and the low-pass filter slope determine the equivalent noise bandwidth f_{LI} of the signal detection. The slope of the low-pass filter is typically set to 18 dB/oct that renders $f_{\text{LI}} = 3/(32\tau_{\text{LI}})$. Large τ_{LI} is generally preferred to detect a signal in a narrow frequency range. On the other hand, there is a trade-off that one needs to wait for a long time $9\tau_{\text{LI}}$ until the lock-in amplifier output reaches 99% of the final value. For a lock-in measurement at frequency $f = \omega/(2\pi)$, τ_{LI} is set to $\tau_{\text{LI}} \geq 3/f$ so that the signal detection bandwidth is as small as $f_{\text{LI}} \leq f/32$ while the wait time $\sim 27/f$ before each measurement is not too long. In a typical lock-in amplifier measurement, 10 measurements are performed at each frequency and are averaged to increase the signal-to-noise ratio. The first measurement is performed $\sim 10\tau_{\text{LI}}$ after the signal is fed in, and the subsequent 9 measurements are performed with a minimum time interval of $\tau_{\text{LI}}/2$. The internal gain of SR830 ('Sensitivity') is chosen to be as high as possible without overloading the detector, and the 'Low Noise' dynamic reserve mode is used.

3.3 Vibration isolation

3.3.1 Vibration isolation principle

To achieve the low background noise floor without spikes, as shown in Fig. 3.5B, isolation of the spectrometer from environmental mechanical vibrations is critical.

A little magnetic flux will be left trapped inside the spectrometer even after the magnetic shielding, and a mechanically vibrating spectrometer could capture it as a strong peak signal.

The following differential equation describes the vibration of an object with a mass m under a damping constant b and a spring constant k .

$$m\ddot{z} + b\dot{z} + kz = f(t), \quad (3.12)$$

where $f(t)$ represents an external force. The solution of this equation gives the vibration spectrum

$$|z(\omega)|^2 = \frac{1}{(\omega^2 - \omega_0^2)^2 + (\gamma\omega)^2} \frac{1}{m^2} |f(\omega)|^2, \quad (3.13)$$

where $\omega_0 = \sqrt{k/m}$, $\gamma = b/m$. A Q -factor $Q = \omega_0/\gamma$ is typically used to quantify the vibration transmission.

One way to achieve good isolation is to make the mass very large. That will drive $\omega_0 \rightarrow 0$ and the vibration $|z(\omega)|^2 \sim 1/(m\omega)^2 |f(\omega)|^2$ is attenuated as $1/m^2$. Our dilution refrigerator is mounted on a 6-ton table and thus is isolated well from environmental vibration. However, this alone is insufficient for a cryogen-free refrigerator, in which an incorporated pulse tube generates a strong vibration that transmits to the bottom mK plate. An additional low-temperature vibration isolator has to be built under the mK plate, thereby isolating the spectrometer from the pulse tube vibration noise as well.

3.3.2 Vibration isolator design and performance

Different vibration isolators are designed for the ^3He and dilution refrigerators due to the different available refrigerator space. The vibration isolator in the ^3He refrigerator is shown in Fig. 3.1A, with the corresponding schematic in Fig. 3.8A.⁵ The vibration isolator plate weighs ~ 4 kg and is hung under the refrigerator mK plate with the two extension springs and the two compression springs of the spring constant $k \sim 1$ N/mm (room temperature spec). The two samarium cobalt

⁵The vibration isolator in the ^3He refrigerator was designed and assembled by Jack D. Enright and Jan Knapp.

magnets mounted on the isolator plate are at a symmetric position, above which the copper blocks are mounted on the rods descending from the mK plate. The magnets cause strong electromagnetic damping to the isolator plate motion by inducing eddy currents in the copper blocks.

The vibration isolator in the dilution refrigerator is shown in Fig. 3.1B, with the schematic in Fig. 3.8B.⁶ It is a two-stage vibration isolator. The first stage weighs ~ 1 kg and is hung under the refrigerator still plate with the three stainless-steel springs of $k \sim 0.03$ N/mm. The second stage, which I call the vibration isolator plate, weighs ~ 1 kg and is hung under the first stage with the three stainless-steel springs of $k \sim 0.02$ N/mm. These parameters will give a resonance frequency of order $\omega_0 \sim 10$ rad·Hz. For strong vibration damping, each stage is equipped with the neodymium magnet. It interacts with the suspended copper post fixed to the stage above.

The performance of the vibration isolators is evaluated by measuring the acceleration noise PSD of the mK plate and the vibration isolator plate. A vibration sensor GS-20DX (Geospace Technologies) is used. Fig. 3.7A and 3.7B show the measurement results in the ^3He and dilution refrigerator, respectively. In both refrigerators, the acceleration noise of the isolator is significantly attenuated at high frequency compared to that of the mK plate. The attenuation factor, defined as the acceleration noise ratio of the isolator to the mK plate, indeed rapidly drops above 100 rad·Hz as shown in Fig. 3.7C and 3.7D. There are a few resonant peaks at low frequency. In the ^3He refrigerator, the most dominant peak is at ~ 54 rad·Hz, and a Lorentzian fitting yields $\gamma = 1$ rad·Hz resulting in a Q -factor of ~ 50 . In the dilution refrigerator, the most dominant peak is again around 54 rad·Hz, and a Lorentzian fitting yields $\gamma = 4$ rad·Hz resulting in $Q \sim 14$.

⁶The vibration isolator in the dilution refrigerator was designed and assembled by Jack Murphy and Jonathan Ward.

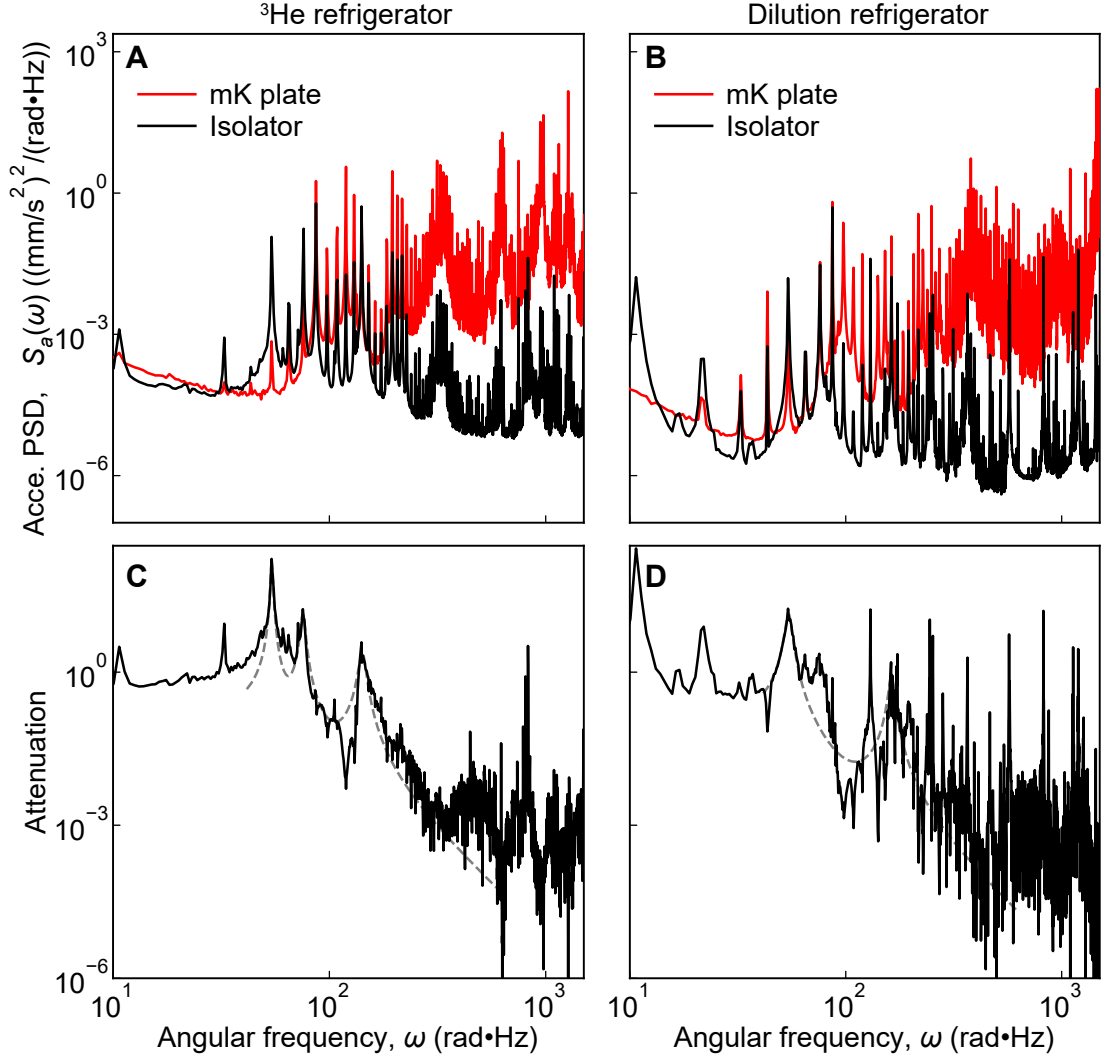


Figure 3.7: (A,B) Acceleration noise power spectral density of the mK plate (red) and the vibration isolator (black) in the ^3He refrigerator (A) and the dilution refrigerator (B). (C,D) Attenuation factor, calculated as the acceleration noise ratio of the isolator to the mK plate, in the ^3He refrigerator (C) and the dilution refrigerator (D). Gray dashed lines are fitting by three Lorentzians in (C) and two Lorentzians in (D).

3.4 Refrigeration and sample thermalization

3.4.1 Refrigeration

Cryogen-free ^3He refrigerator

The first spin noise spectrometer, which I used for my experiment, is built in a commercial cryogen-free ^3He refrigerator, Tertia (ICE Oxford). The schematic diagram of the refrigerator structure is shown in Fig. 3.8A. The refrigerator comprises four plates: a 50 K plate, a 4 K plate, a 1 K plate, and a mK plate. A pulse tube

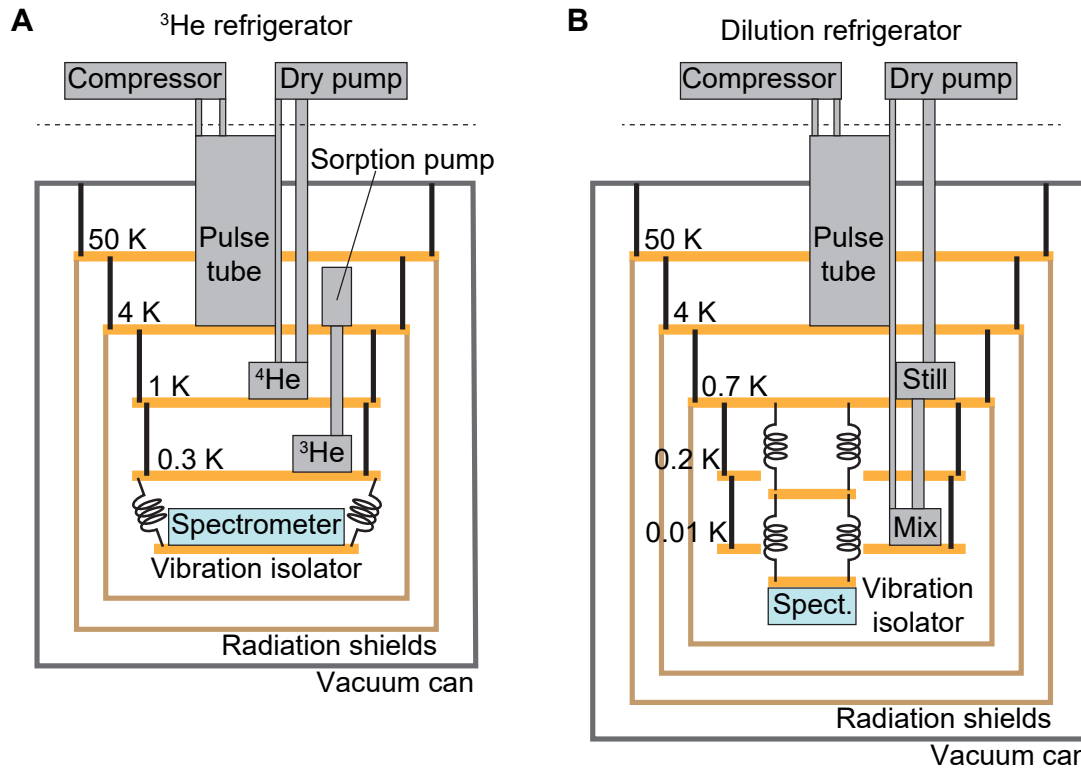


Figure 3.8: Schematics of a cryogen-free ^3He refrigerator (A) and a dilution refrigerator (B).

is incorporated to cool down the 50 K and 4 K plates. A ^4He circulation system is incorporated to cool down below 1 K. ^4He gas at room temperature is liquefied at the 4 K plate and drips down to a chamber on the 1 K plate. Active pumping of the ^4He chamber by a mechanical pump promotes the evaporation of the ^4He liquid, which cools down the 1 K plate. A closed ^3He system is incorporated to reach mK. A ^3He chamber on the mK plate is connected to a sorption pump on the 4 K plate, where ^3He gas is initially trapped. When the sorption pump is heated up to ~ 50 K, the ^3He gas is released and is liquefied at the 1 K plate to drip down to the chamber. When the sorption pump is cooled back to 4 K, the liquid ^3He is pumped out of the ^3He chamber to cool the mK plate to 270 mK. The maximum hold time at the base temperature is about 80 hours.

The refrigerator space is pumped below $p = 10^{-3}$ mbar at room temperature using a turbopump. This reduces the thermal conduction through the air and prevents gas condensation at low temperatures that will contribute extra specific

heat. Two radiation shields at 50 K and 4 K reduce the intense black body radiation from room-temperature objects, whose power is proportional to T^4 (Stefan-Boltzmann law).

The spin noise spectrometer is mounted on the vibration isolator that is hung under the mK plate, as shown in Fig. 3.1A. The four copper foils thermally connect the mK plate and the isolator. It takes one day to cool down the mK plate to the base temperature and two more days to cool down the vibration isolator fully.

Cryogen-free dilution refrigerator

The second spin noise spectrometer was built on a commercial cryogen-free dilution refrigerator, Proteox MX (Oxford Instruments). The refrigerator structure is schematically shown in Fig. 3.8B. The refrigerator comprises five plates: a 50 K plate, a 4 K plate, a still plate, a cold plate, and a mK plate. A pulse tube cools down the 50 K plate and the 4 K plate. A dilution unit consisting of a still chamber on the still plate and a mixing chamber on the mK plate cools down the bottom three plates. Both ^3He and ^4He condense into the mixing chamber, where a pure ^3He liquid phase and a $^3\text{He}/^4\text{He}$ mixture phase coexist. Active pumping of the still chamber creates an imbalance in the $^3\text{He}/^4\text{He}$ mixture concentration, and promotes the condensation of the pure ^3He into the mixture. This process cools the mK plate to 10 mK.

The spin noise spectrometer is mounted on the two-stage vibration isolator that is hung under the still plate as shown in Fig. 3.1B. The first and second stages are thermally connected to the cold and mK plates, respectively, with the three copper foils that are 0.3 mm thick and 12 mm wide. It takes two days to cool down the mK plate to the base temperature and three more days to cool down the vibration isolator below 50 mK.

3.4.2 Sample thermalization

Thermal conduction through a component is determined by its area A , length L , and the thermal conductivity of the raw material $\kappa(T)$. The cooling capacity

\dot{Q} is estimated by

$$\dot{Q} = \frac{A}{L} \int_{T_{\text{low}}}^{T_{\text{high}}} dT \kappa(T), \quad (3.14)$$

where T_{high} and T_{low} are the temperatures of the hot and cold ends, respectively. The time required to cool down an object with heat capacity $C(T)$ is calculated as $\int_{T_{\text{low}}}^{T_{\text{high}}} dT C(T)/\dot{Q}$.

In general, components to promote thermalization should be designed as thick and short as possible. Thermally conductive materials such as pure metal are generally preferred. On the other hand, pure metals with high electric conductivity are a source of Johnson noise and eddy currents that can affect the measurement of magnetization noise and AC susceptibility. One should carefully decide the amount and geometry of metallic components or use a thermally conductive insulator such as sapphire.

Sample thermalization in ^3He refrigerator

To thermalize a sample in the ^3He refrigerator, in the initial development, four 0.2 mm-diameter 20 mm-long brass wires were used. One end is attached to the pickup coil circuitry using GE varnish, to which the sample is also glued with GE varnish. The other end is in contact with a copper wire that exits the spectrometer and gets fixed to the mK plate at 270 mK. The cooling capacity of the brass wires, whose thermal conductivity is $\kappa \sim 6 \times 10^{-1}T$ W/(K·m) [74], is estimated to be

$$\dot{Q} = \frac{A}{L} \int_{0.27}^T dT \kappa(T) \sim 2 \times 10^{-6}(T^2 - 0.27^2) \text{ W}. \quad (3.15)$$

The cooling capacity of 30 nW is retained even when the sample is at 300 mK.

A 0.1 mm-diameter 50 mm-long silver wire was also used. The silver wire is glued directly to the sample using GE varnish. The thermal conductivity of 99.99% pure silver, whose RRR is estimated to be about 100, is $\kappa \sim 2 \times 10^2 T$ W/(K·m) [74]. The estimated cooling capacity $\dot{Q} \sim 2 \times 10^{-5}(T^2 - 0.27^2)$ W retains 300 nW even when the sample is at 300 mK.

As an idealized example of a cooling-time estimate, consider $\text{Ca}_{10}\text{Cr}_7\text{O}_{28}$ (described in Chapter 4). Below 500 mK, it has an approximately linear specific heat

$c(T) \sim 3.9 \times 10^{-5} T$ J/(mm³·K) [75]. Cooling a 4 mm³ Ca₁₀Cr₇O₂₈ sample from 500 mK to 300 mK through the silver wire will take

$$t_{0.5 \rightarrow 0.3} = \int_{0.3}^{0.5} dT \frac{4 \times 3.9 \times 10^{-5} T}{2 \times 10^{-5} (T^2 - 0.27^2)} \sim 9 \text{ s.} \quad (3.16)$$

Even in the brass wire setup, the cooling takes only 90 seconds. One should choose appropriate thermalization wires depending on a desired experimental configuration and a target temperature range.

Sample thermalization in dilution refrigerator

Three 0.2 mm-diameter 50 mm-long silver wires were directly glued to the sample for thermalization in the dilution refrigerator. When the other end is thermalized at the 10 mK plate, the cooling capacity

$$\dot{Q} = \frac{A}{L} \int_{0.01}^T dT \kappa(T) \sim 2 \times 10^{-4} (T^2 - 0.01^2) \text{ W} \quad (3.17)$$

retains 400 nW even when the sample is at 50 mK.

Estimate of flux noise from current Johnson noise

Current Johnson noise in metal generates magnetic flux noise. Ref. [76] provides the formulas to estimate the flux noise captured by a one-turn pickup coil tightly wrapped around a long metallic cylinder of radius r and electrical conductivity σ . The noise floor $S_{\Phi}(\omega = 0)$ and its cutoff frequency ω_c are

$$S_{\Phi}(\omega = 0) = \frac{1}{2\pi} 4k_B T \sigma \frac{G}{2\pi} \mu_0^2 r^3, \quad \omega_c \simeq 2\pi \frac{4.5}{\pi \mu_0 \sigma r^2}, \quad (3.18)$$

where $G \sim 1$ is a geometrical factor. Using the Wiedemann–Franz law $\sigma = \frac{\kappa}{L_0 T}$ with $L_0 = 2.44 \times 10^{-8}$ W Ω /K², one can estimate this flux noise from thermal conductivity.

Consider a one-turn pickup coil around a silver wire of a diameter 0.2 mm and a thermal conductivity $\kappa \sim 2 \times 10^2 T$ W/(K·m) (RRR = 100). At 100 mK, the flux noise at the pickup coil estimated from Eq. 3.18 is $S_{\Phi}(\omega = 0) = (20 \mu\Phi_0)^2/(\text{rad}\cdot\text{Hz})$. The flux transferred to the SQUID $S_{\Phi_s}(\omega = 0) \sim (0.2 \mu\Phi_0)^2/(\text{rad}\cdot\text{Hz})$ is smaller than the noise floor of the SQ1200 SQUID spectrometer $1.8 (\mu\Phi_0)^2/(\text{rad}\cdot\text{Hz})$, but

just by two orders of magnitude. In the realistic spin noise spectrometer, the pickup coil turns have a much larger diameter than the silver wire. These turns are less sensitive to the Johnson noise than assumed here. On the other hand, the multiple pickup coil turns will result in more Johnson noise detection, potentially making it comparable to the intrinsic SQUID noise at high temperatures.

Part of this chapter appears as:

arXiv:2405.02075 (2024)

— Hiroto Takahashi *et al.*

4

Spiral Spin Liquid Noise in $\text{Ca}_{10}\text{Cr}_7\text{O}_{28}$

To demonstrate the emerging concept of fingerprinting spin liquids from spin noise, I performed spin noise spectroscopy on $\text{Ca}_{10}\text{Cr}_7\text{O}_{28}$. It was initially introduced as a candidate for a quantum spin liquid (QSL), whereas an experimental observation of a ring-like spin correlation and semiclassical simulations propose a possible realization of a spiral spin liquid (SSL) state. However, it has not been established whether $\text{Ca}_{10}\text{Cr}_7\text{O}_{28}$ is a QSL or a SSL. As I will show in the following, the spin noise I discovered in $\text{Ca}_{10}\text{Cr}_7\text{O}_{28}$ is overall consistent with the predictions for a SSL but not those for a QSL, evidencing $\text{Ca}_{10}\text{Cr}_7\text{O}_{28}$ as a SSL.

4.1 Spin liquid candidate $\text{Ca}_{10}\text{Cr}_7\text{O}_{28}$

4.1.1 Structure

$\text{Ca}_{10}\text{Cr}_7\text{O}_{28}$ is a quasi-2D compound consisting of weakly coupled bilayers [77] as shown in Fig. 4.1. All Cr ions are configured with four O^{2-} ions to form highly distorted CrO_4 tetrahedra, which lift the degeneracy of Cr d-orbitals. Out of the seven Cr ions in the unit cell of $\text{Ca}_{10}\text{Cr}_7\text{O}_{28}$, six are in a Cr^{5+} state, and one is in Cr^{6+} . Magnetic Cr^{5+} with a singly occupied spin-1/2 forms a distorted bilayer kagome lattice, where each kagome layer consists of triangular plaquettes of alternating sizes.

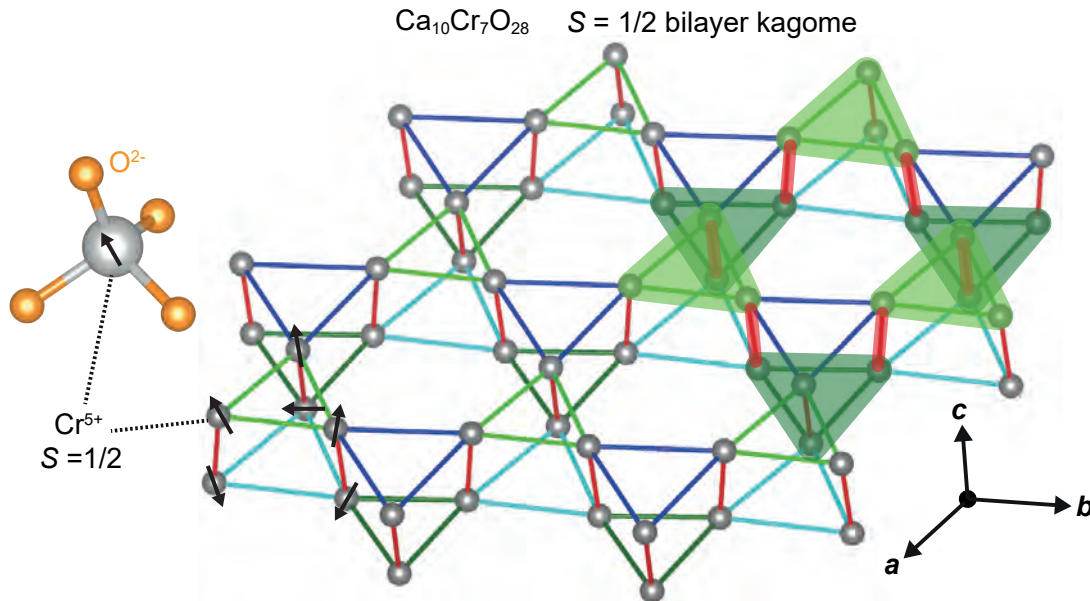


Figure 4.1: Schematic of the distorted bilayer kagome lattice of Cr^{5+} in $\text{Ca}_{10}\text{Cr}_7\text{O}_{28}$. Each Cr^{5+} ion has a singly-occupied spin-1/2 due to the distorted oxygen tetrahedron. There are six spin-1/2 sites per unit cell. The three spins at the vertices of green triangular plaquettes form an effective spin-3/2 at low temperatures due to relatively strong ferromagnetic interactions among them. Figure reproduced from Ref. [23] with a minor modification.

4.1.2 Physical properties

At high temperatures, $\text{Ca}_{10}\text{Cr}_7\text{O}_{28}$ shows paramagnetic behavior in the DC susceptibility [78, 79]. A Curie-Weiss fitting in the range $50 \text{ K} < T < 250 \text{ K}$ yields the effective magnetic moment $\mu_{\text{eff}} = 1.74\mu_{\text{B}}$ per Cr^{5+} ion, corresponding to that of a spin-1/2 $\mu_{\text{eff}} = 2\sqrt{S(S+1)}\mu_{\text{B}} = 1.73\mu_{\text{B}}$. The Curie-Weiss temperature $T_{\text{CW}} = +2.35 \text{ K}$ indicates ferromagnetic $\sim \text{meV}$ interaction, while the deviation below 5 K proposes a coexistence of antiferromagnetic interactions. The DC susceptibility is nearly isotropic down to 2 K ; however, the full isotropy of spins remains controversial. 2 K is higher than the proposed exchange interactions discussed below, and a possible existence of local anisotropic interactions (i.e. a sizable spin-orbit coupling effect) has been proposed as a Heisenberg Hamiltonian fails to reproduce the specific heat and the $\mathbf{q} = 0$ structure factor [80, 81].

$\text{Ca}_{10}\text{Cr}_7\text{O}_{28}$ is a potential spin liquid with neither a thermodynamic phase transition nor spin freezing reported down to 20 mK . The DC susceptibility does

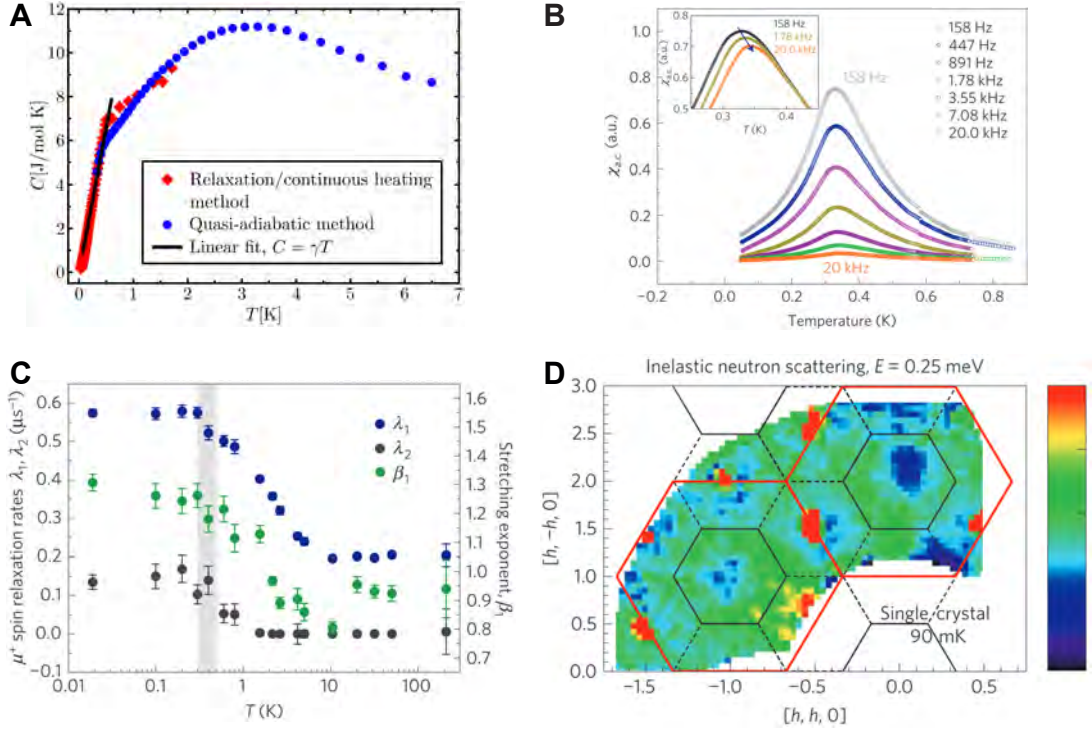


Figure 4.2: Spin liquid phenomena and crossover behavior at $T^* \sim 450 \text{ mK}$ observed in $\text{Ca}_{10}\text{Cr}_7\text{O}_{28}$. (A) Specific heat that does not show a phase-transition peak down to 40 mK . It shows an anomalous kink at $\sim 450 \text{ mK}$, below which $C(T)$ decreases approximately linearly. (B) AC susceptibility $|\chi(\omega)|$ that shows a broad peak at $300\text{--}350 \text{ mK}$ and is strongly frequency dependent from 100 Hz to 20 kHz . (C) Muon relaxation rates, which are extracted from the zero-field muon spin polarization data that does not show an oscillation due to a static field down to 20 mK . They indicate electron-spin fluctuations that slow down on cooling and become persistent below $300\text{--}500 \text{ mK}$. (D) Structure factor from inelastic neutron scattering at 90 mK showing a diffuse ring-like correlation instead of a well-defined spin-wave mode. (A) is reprinted with permission from Ref. [75] Copyright (2019) by the American Physical Society. (B, C, D) are reproduced from Ref. [78] with permission from Springer Nature.

not show a peak or a kink down to 2 K . The zero-field specific heat $C(T)$ [75, 78] in Fig. 4.2A does not exhibit a phase-transition peak down to 40 mK . The zero-field muon spin polarization measurements [78] detect no oscillation, excluding static magnetic field down to 20 mK . Different probes observe an anomaly around $T^* = 450 \text{ mK}$, which is discussed to be a crossover to correlated spin liquid behavior at low temperatures. The specific heat shows a weak kink around 450 mK and drops approximately linearly below that temperature. The high-frequency AC susceptibility $|\chi(\omega)|$ [78] shows a rapid growth down to $300\text{--}350 \text{ mK}$, followed by a precipitous drop as shown in Fig. 4.2B. The magnitude of AC susceptibility is

frequency dependent between 100 Hz and 20 kHz, indicating the presence of slow \sim kHz spin dynamics around T^* . The muon relaxation rates in Fig. 4.2C evidence electron-spin fluctuations that slow down on cooling and become persistent below 300–500 mK. The structure factor in Fig. 4.2D, observed by inelastic neutron scattering at 90 mK [75, 78, 79], is diffuse without a well-defined spin-wave mode. Such a diffuse structure factor excludes a magnetic ordering or a valence bond solid formation. The spectrum does not disperse along the out-of-plane direction, which indicates that the spin correlations develop within each bilayer [78]. Two bands are observed at 0.0–0.6 meV and 0.7–1.5 meV, showing a ring-like closed contour in q space.

All these observations point to the absence of magnetic order in $\text{Ca}_{10}\text{Cr}_7\text{O}_{28}$ and exclude non-ordered ‘trivial’ phases such as a spin glass or a valence bond solid. $\text{Ca}_{10}\text{Cr}_7\text{O}_{28}$ is a potential spin liquid state, with the likely onset of correlated behavior at $T^* \sim 450$ mK. The spins remain dynamic down to at least 20 mK without a symmetry-breaking order, which is orders of magnitude smaller than the exchange energy scale estimated from the Curie-Weiss temperature $T_{\text{CW}} \sim 2$ K.

4.1.3 Proposed Hamiltonian

The empirical Hamiltonian of $\text{Ca}_{10}\text{Cr}_7\text{O}_{28}$ is determined from inelastic neutron scattering of a polarized state at a high external field [79]. Spin interactions are assumed to be isotropic Heisenberg interactions, as described by

$$H = \sum_{\langle ij \rangle} J_{ij} \mathbf{S}_i \cdot \mathbf{S}_j, \quad (4.1)$$

although additional interactions, such as local anisotropic interactions, are proposed to exist in more recent work [80, 81]. The excitation spectrum is fitted by a model based on spin-wave theory to obtain the exchange parameters J_{ij} , for the five bonds that are not equivalent by lattice symmetry. Different colors represent these different bonds in Figs. 4.1 and 4.3. In agreement with the positive Curie-Weiss temperature in the DC susceptibility, the relatively dominant interactions are ferromagnetic: the light-green bonds on the top layer ($J = -0.27$ meV) and

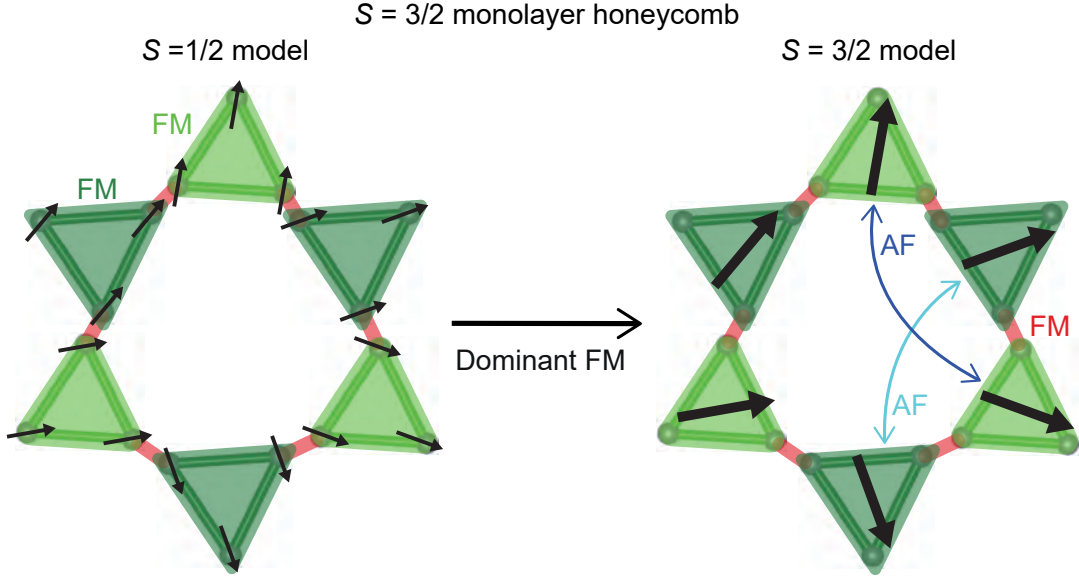


Figure 4.3: The effective model of $\text{Ca}_{10}\text{Cr}_7\text{O}_{28}$ mapped to a monolayer honeycomb network. Three spins at the vertices of triangular plaquettes on each layer are bound by a dominant ferromagnetic interaction to form a spin-3/2. The spin-3/2 network is frustrated due to the competition between nearest-neighbor ferromagnetic and next-nearest-neighbor antiferromagnetic interactions. Figure reproduced from Ref. [23] with a minor modification.

the dark-green ones on the bottom layer ($J = -0.76$ meV). The dark-blue bonds on the top layer ($J = 0.09$ meV) and the light-blue ones on the bottom layer ($J = 0.11$ meV) are antiferromagnetic. The interlayer interaction, represented by the red bonds, is ferromagnetic ($J = -0.08$ meV). The interlayer interaction being ferromagnetic instead of antiferromagnetic prevents the trivial singlet formation between the two layers that would lead to a valence bond solid state.

The so far discussed Heisenberg Hamiltonian of the bilayer kagome lattice can be simplified as shown in Fig. 4.3. When the three spins on alternative triangular plaquettes form a $S = 3/2$ state via the relatively dominant intralayer ferromagnetic interactions, the original model of interacting spin-1/2 on the distorted bilayer kagome lattice can be mapped to interacting spin-3/2 on a monolayer honeycomb lattice [75, 80, 82]. The original interlayer red-bond interaction turns into a nearest-neighbor ferromagnetic interaction, and the original intralayer blue-bond interactions become a next-nearest-neighbor antiferromagnetic interaction. These interactions frustrate the simplified $S = 3/2$ monolayer honeycomb model.

4.2 Quantum spin liquid or spiral spin liquid?

To describe the spin liquid behavior of $\text{Ca}_{10}\text{Cr}_7\text{O}_{28}$ below $T^* \sim 450$ mK, two spin liquid scenarios have been hypothesized. The first hypothesis is a QSL, whose concept I introduced in Section 1.2. The dispersion-less excitation spectrum is consistent with spinon excitations, which are fractional excitations, pointing to possible quantum entanglement [75, 78]. From the approximately linear temperature dependence of the specific heat and the low-energy spin structure factor, a QSL with a spinon Fermi surface has been deduced [75]. Additionally, numerical simulations using a pseudofermion functional renormalization group theory [78] and tensor network theory [83] predict a quantum magnetic ground state without a static magnetization.

Another hypothesis is a SSL.¹ As explained in Section 1.1.2, a SSL has degenerate wavevectors that form a continuous ‘spiral contour’ such as a ring in reciprocal space (Fig. 1.2A). The sub-extensive degeneracy in a SSL prevents long-range ordering [86]. The structure factor from inelastic neutron scattering exhibits a diffuse and ring-like contour [75, 78, 79]. The presumed formation of $S = 3/2$ via dominant ferromagnetic interactions (Fig. 4.3) renders spins more classical than $S = 1/2$. Furthermore, classical Monte Carlo simulation and semiclassical molecular dynamics simulation [80, 82] on the empirical Hamiltonian of $\text{Ca}_{10}\text{Cr}_7\text{O}_{28}$ (Eq. 4.1) predict a SSL with a ring-like spin correlation.

In $\text{Ca}_{10}\text{Cr}_7\text{O}_{28}$, a clear distinction between these two scenarios, a QSL and a SSL, has not been possible based on the existing observations. Here, I attempt to make this distinction using spin noise spectroscopy.

¹A SSL has been primarily studied in a classical situation, and accordingly, a typical classical SSL is considered here. The interplay between quantum mechanical effects and a degenerate spiral manifold leading to a ‘quantum SSL’ is a theoretical possibility [84, 85] but is still an open question.

4.3 Prediction of quantum spin liquid noise and spiral spin liquid noise

4.3.1 Prediction of quantum spin liquid noise properties

For a successful fingerprint of the spin liquid state in Ca₁₀Cr₇O₂₈, the spin noise spectrum expectation for a QSL and a SSL is necessary. A recent theoretical study in Ref. [50] predicts the spin noise spectra of different types of QSLs. The prediction depends on the two parameter ratios ω/T and $d\omega/v$, where ω is angular frequency, T is temperature, d is the measured length scale, and v is the spinon velocity. In the $\omega/T \ll 1$ and $d\omega/v \ll 1$ regime, which should be more relevant to our current SQUID-based spin noise experiment, a frequency-independent power spectral density

$$S(\omega) \propto \omega^0 \quad (4.2)$$

is predicted for all Z₂ Dirac, Z₂ Fermi surface, and U(1) Fermi surface QSLs, with distinct temperature dependences [50, 52].

4.3.2 Monte Carlo simulation of spiral spin liquid

Lattice and Hamiltonian

Next, to predict a SSL spin noise, I performed a classical Monte Carlo (MC) simulation tracking the evolution of spins. The low-energy properties of Ca₁₀Cr₇O₂₈ can be described fairly accurately by the effective $S = 3/2$ spins formed by the dominant ferromagnetic interactions [82], and the $S = 3/2$ spins can be approximated by classical terms. Past classical MC simulations and semiclassical molecular dynamics simulations on Ca₁₀Cr₇O₂₈ [80, 82] have successfully replicated the ring-like structure factor consistent with the experiments [75, 78, 79].

As a Hamiltonian to predict a SSL spin noise, I turned to the following generic model for a 2D SSL, whose low-temperature behavior is studied in detail and established by Ref. [22].

$$H = J_1 \sum_{\langle ij \rangle_1} \boldsymbol{\theta}_i \cdot \boldsymbol{\theta}_j + J_2 \sum_{\langle ij \rangle_2} \boldsymbol{\theta}_i \cdot \boldsymbol{\theta}_j + J_3 \sum_{\langle ij \rangle_3} \boldsymbol{\theta}_i \cdot \boldsymbol{\theta}_j. \quad (4.3)$$

Here, θ_i represents the spin at the site i of a square lattice with periodic boundary conditions. J_1 , J_2 , and J_3 are the first, second, and third nearest neighbor spin couplings on the square lattice. For $J_1 = -1$, $J_2 > 1/4$, $J_3 = J_2/2$, the Hamiltonian gives rise to a spiral contour of degenerate states in reciprocal space. The contour satisfies $2 \cos^2 Q_x + 2 \cos^2 Q_y + 4 \cos Q_x \cos Q_y = 1/(2J_2^2)$ and is shown in Fig. 1.2A for different values of J_2 . I use the same parameter values as Ref. [22]: $J_1 = -1.00$, $J_2 = 0.28$, $J_3 = 0.14$.

The square lattice assumed in the model is different from the honeycomb lattice in the effective $\text{Ca}_{10}\text{Cr}_7\text{O}_{28}$ model (Fig. 4.3). However, both exhibit a continuous spiral contour with an approximate circular shape, the key feature of the SSL physics. Therefore the model is expected to be a good approximation of $\text{Ca}_{10}\text{Cr}_7\text{O}_{28}$, as discussed in Ref. [22]. The appropriate choice of spin dimensionality is controversial, with the possible anisotropic effect proposed in $\text{Ca}_{10}\text{Cr}_7\text{O}_{28}$ [80,81]. This led me to perform the simulation both for two-dimensional XY (this section) and three-dimensional Heisenberg (Appendix C) spins. The SSL phase occurs regardless of whether the spins are XY [22] or Heisenberg [87], and the simulated spin noise predictions indeed share qualitatively comparable features. Here, I mainly discuss the XY-model simulation result, as it shows better agreement with the subsequently shown experimental spin noise in $\text{Ca}_{10}\text{Cr}_7\text{O}_{28}$.

Equilibration process

The simulation was performed for $N = L \times L$ spins, with $L = 40$ and $L = 100$. The initial direction of spins is randomly chosen with a uniform probability. The equilibrium spin configuration at each temperature is obtained by a gradual cooldown of the system from $T = 2|J_1|$ to $0.005|J_1|$ via a step-by-step equilibration at $T = 2 \times 0.95^r |J_1|$ where $0 \leq r \leq 117$ (exponential cooling protocol).

Two types of MC updates were employed in this step-by-step equilibration process, following Ref. [22]. The first update is the standard Metropolis update. A randomly picked spin attempts to flip to a new direction, which is randomly selected with a uniform probability. This flip is implemented only with a probability

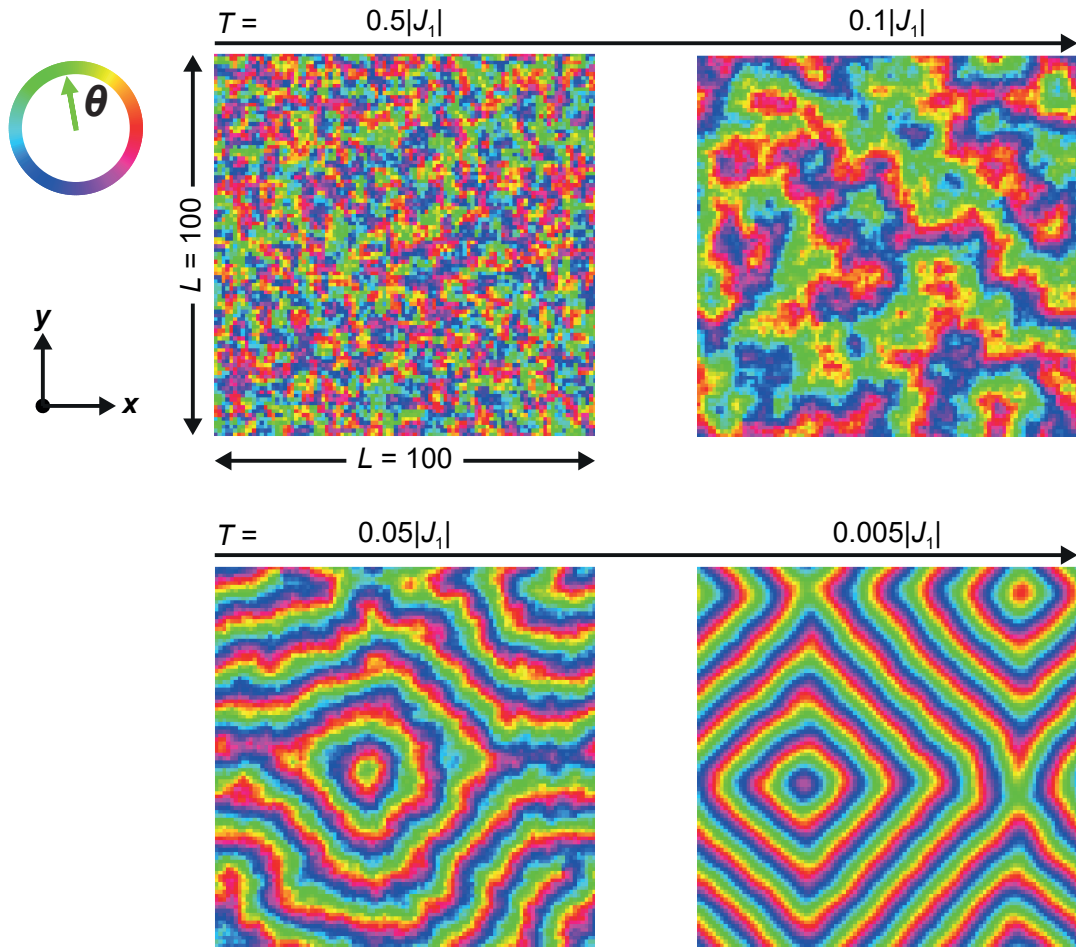


Figure 4.4: Visualization of the spins in the equilibration process of the $L = 100$ spiral spin liquid Monte Carlo simulation. The local spin direction is indicated by the corresponding color in the top-left color map. The spin direction is random at the high temperature $T = 0.5|J_1|$, while spatial correlations gradually grow as the system is cooled to $0.1|J_1|$, $0.05|J_1|$, and $0.005|J_1|$. $T = 0.05|J_1|$ corresponds to the spiral spin liquid state, showing momentum vortices. The equilibration process in the $L = 40$ system is comparable. Figure reproduced from Ref. [23] with a minor modification.

$\min(1, e^{-\Delta E/T})$, where ΔE is the projected energy change due to the spin flip. The second update is the over-relaxation update. A randomly picked spin θ_i is reflected about the local exchange field $\mathbf{H}_i = \sum_j J_{ij}\theta_j$. The over-relaxation update conserves energy and is empirically known to accelerate the equilibration [88]. In the equilibration process, each Metropolis update is followed by two over-relaxation updates so that one-third of the updates are Metropolis. N MC updates make up 1 MC step. 5×10^4 MC steps are carried out at each temperature of the step-by-step equilibration, amounting to the total of 6×10^6 MC steps from $T =$

$2|J_1|$ to $0.005|J_1|$.

The equilibration process of the $L = 100$ system is visualized in Fig. 4.4. Both the $L = 40$ and $L = 100$ results are in accordance with the $L = 400$ result reported in Ref. [22]. At high temperatures ($T = 0.5|J_1|$), the system is in a paramagnetic state with the spins pointing in random directions. When the system is cooled down, the spins develop a spatial correlation. The state at $T = 0.1|J_1|$ is called a pancake liquid state, as the corresponding structure factor in reciprocal space is a filled-circle [22, 87]. At $T = 0.05|J_1|$, the system is in a SSL state showing momentum vortices (Fig. 1.2). The spiral domains become clearer as the system is further cooled to $T = 0.005|J_1|$. The final spin configuration at each temperature is recorded as the equilibrated configuration, from which I initiate the subsequent simulation of the time evolution in equilibrium.

Time evolution in equilibrium

The time evolution of spins is simulated for the $L = 40$ system using the Metropolis Monte Carlo algorithm, which approximates the evolution of a spin system interacting with a thermal bath.² From the equilibrated configuration at each temperature, the spins are evolved with 10^7 MC steps consisting only of Metropolis updates. The MC time is converted to the actual time with the relation $1 \text{ MC step} = 1 \mu\text{s}$, as determined by comparing the spin-flip rate in the simulation and the experimental observation (Appendix B). This makes the total simulation time $\Gamma = 10 \text{ s}$.

The average spin x - and y -components

$$\bar{\theta}_x(t_k, T) = \frac{1}{N} \sum_i \theta_i^x(t_k, T), \quad (4.4)$$

$$\bar{\theta}_y(t_k, T) = \frac{1}{N} \sum_i \theta_i^y(t_k, T), \quad (4.5)$$

²The dynamics due to an equation of motion are not considered, as there is no z -direction exchange field that will give rise to an XY-spin precession. Even if a z -direction field were present, the interactions at the energy scale of 0.1 meV would only generate a rapid periodic precession at $\sim 20 \text{ GHz}$ ($\sim 10 \text{ ps}$). Such a fast precession will be averaged out on the timescale of the MC simulation and will also be out of the frequency range measured in the current experimental setup.

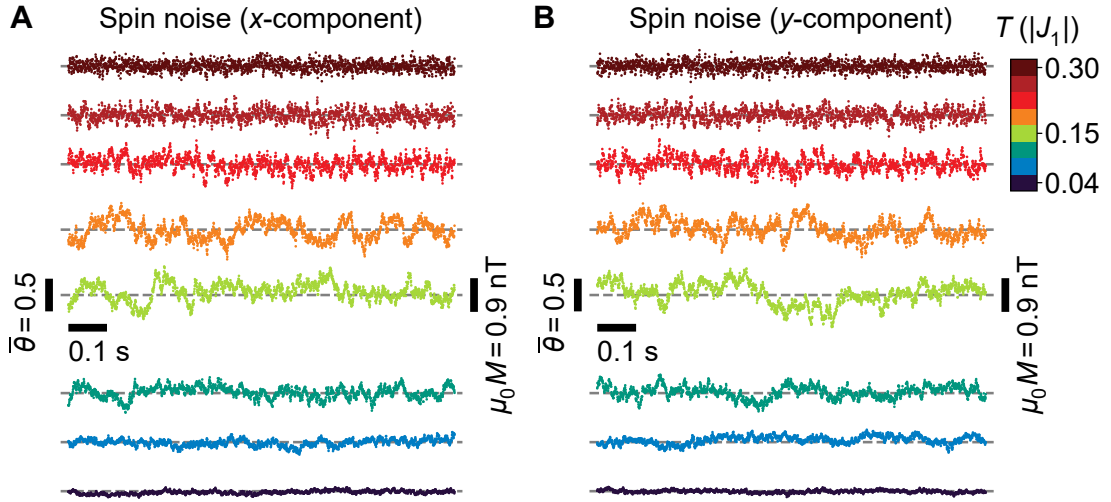


Figure 4.5: (A) Time sequences of the average x -component spin $\bar{\theta}_x(t_k, T)$ at eight selected temperatures in the $N = 40 \times 40$ spiral spin liquid simulation. They show fluctuations on a timescale longer than 0.1 s. The low-frequency noise amplitude increases as the system is cooled to $T = 0.15|J_1|$ and then rapidly drops below that temperature. 1 MC step is converted to $\tau = 1 \mu\text{s}$. For visual clarity, $\theta_x(t_k, T)$ is down sampled to every 500 MC steps. The frequency components above 1 kHz are filtered out. The magnitude of the corresponding magnetization noise estimated from Eq. B.5 is indicated by the bar on the right. (B) The average y -component spin $\bar{\theta}_y(t_k, T)$ that is statistically equivalent to the x -component. Figures reproduced from Ref. [23] with a minor modification.

are recorded over the evolution of the spins. They were only recorded every 10 MC steps due to the technical limitations of the data file size. Therefore, the resulting simulated SSL noise data $\bar{\theta}_{x,y}(t_k, T)$ has the total of $K = 10^6$ points ($0 \leq t_k \leq (K - 1)\Delta t$) with the time interval of $\Delta t = 10 \mu\text{s}$.

Figure 4.5 shows $\bar{\theta}_x(t_k, T)$ and $\bar{\theta}_y(t_k, T)$ at eight selected temperatures, after filtering out the high-frequency components above 1 kHz (Appendix B). The noise exhibits slow fluctuations on a timescale longer than 0.1 s. The noise magnitude grows down to $T \sim 0.15|J_1|$ and then rapidly drops below that temperature. The peak-to-peak value reaches almost $\bar{\theta} \sim 0.5$, corresponding to the estimated magnetization of $\mu_0 M \sim 0.9 \text{ nT}$ (Appendix B). As expected from the symmetry, $\bar{\theta}_x(t_k, T)$ and $\bar{\theta}_y(t_k, T)$ are statistically equivalent.

4.3.3 Prediction of spiral spin liquid noise properties

As already mentioned, the simulated SSL noise data at each temperature $\bar{\theta}_{x,y}(t_k, T)$ has the total duration of $\Gamma = 10$ s, with the time interval of $\Delta t = 10 \mu\text{s}$ between the $K = 10^6$ points ($0 \leq t_k \leq (K - 1)\Delta t$). To investigate the noise property in more detail, its power spectral density (PSD) $S_{\bar{\theta}_x}(\omega_j, T)$ is calculated using the formula

$$S_{\bar{\theta}_{x,y}}(\omega_j, T) = \frac{1}{\pi\Gamma} \left| \Delta t \sum_{k=0}^{K-1} e^{-i\omega_j t_k} \bar{\theta}_{x,y}(t_k, T) \right|^2, \quad (4.6)$$

where $\omega_j/(2\pi) = j/\Gamma$ ($0 \leq j \leq K/2$). An average is taken over 10 independent MC runs. To increase the signal-to-noise ratio, I averaged the calculation results from split segments as detailed in Appendix B. PSDs with the resolution of $\Delta\omega/(2\pi) = 1, 10, 100$ Hz are obtained by averaging PSDs from the $P = 10, 10^2, 10^3$ split segments, respectively. As shown in Fig. 4.6A, the obtained PSD grows in power to $T = 0.15|J_1|$, and rapidly drops below that temperature. The PSD becomes scale-invariant below $T = 0.15|J_1|$, showing the intense low-frequency noise down to at least $\omega/(2\pi) = 1$ Hz.

Next, the correlation function $C_{\bar{\theta}_{x,y}}(t_k, T)$ is calculated. To address the low-frequency fluctuations, as we later do in the experimental analysis, the fluctuations above 1 kHz are first filtered out from $\bar{\theta}_{x,y}(t_k, T)$ (See Appendix B). From this filtered data, the correlation function is calculated using the standard formula

$$C_{\bar{\theta}_{x,y}}(t_k, T) = \frac{1}{l_{\text{ave}}} \sum_{l=0}^{l_{\text{ave}}-1} \bar{\theta}_{x,y}(t_l, T) \bar{\theta}_{x,y}(t_{l+k}, T), \quad (4.7)$$

where $l_{\text{ave}} = 9 \times 10^5$. An average is taken over 10 independent MC runs. The obtained normalized correlation function $C_{\bar{\theta}_x}(t_k, T)/C_{\bar{\theta}_x}(0, T)$ is shown in Fig. 4.6B. The decay of the correlation is rapid at high temperatures, but it slows down upon cooling as the functional form approaches nearly $C_{\bar{\theta}_{x,y}}(t, T) \propto -\ln t$.

As the PSD is found to be scale-invariant below $T = 0.15|J_1|$, its frequency-power-law exponent is examined. Fig. 4.7A shows the fitting of the 1 Hz-resolution PSD $S_{\bar{\theta}_x}(\omega, T) \propto \omega^{-\alpha(T)}$ in the range $1 \text{ Hz} \leq \omega/(2\pi) \leq 500 \text{ Hz}$. The obtained exponent, plotted in Fig. 4.7B, approaches $\alpha(T) = 1.2 \pm 0.1$ at the lowest temperature. As discussed in Section 2.2.5, the standard PSD of a system with a

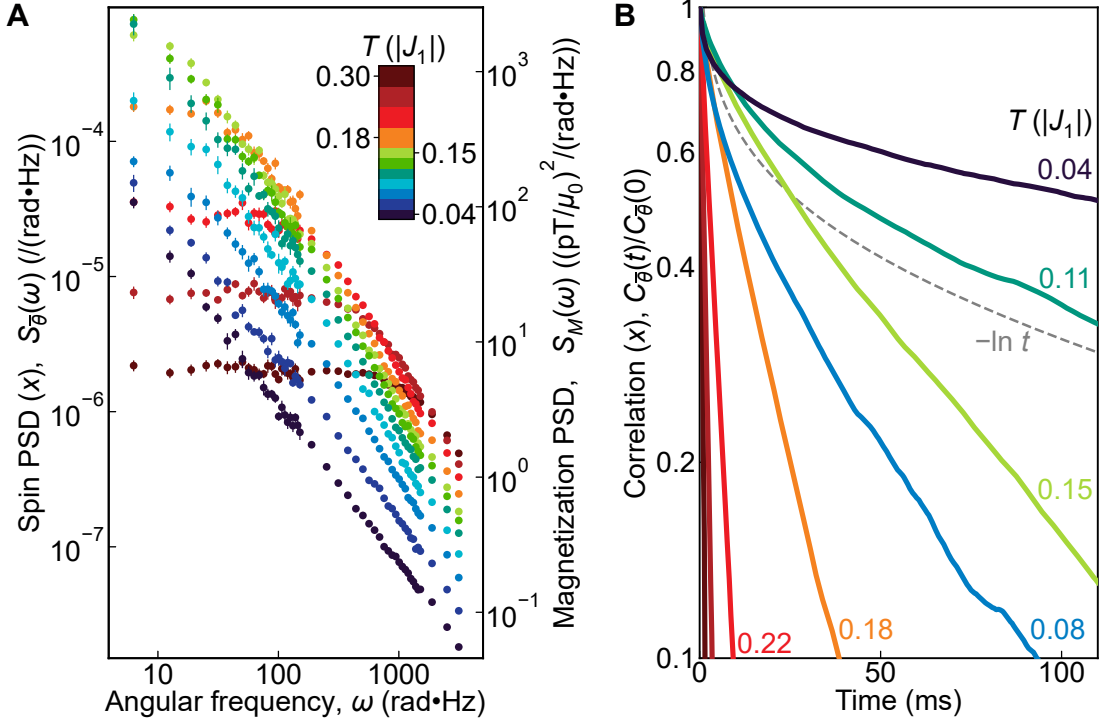


Figure 4.6: (A) Power spectral density $S_{\bar{\theta}_x}(\omega_j, T)$ of the simulated spiral spin liquid noise $\bar{\theta}_x(t_k, T)$ for eleven selected temperatures. It grows in power down to $T = 0.15|J_1|$ and then rapidly drops, having a scale-invariant form at low temperatures. The error bars are given by the standard error of averaging 10 independent Monte Carlo runs. The power spectral density of the corresponding magnetization noise $S_M(\omega_j, T)$ estimated from Eq. B.5 is shown on the right-hand axis. (B) Normalized correlation function $C_{\bar{\theta}_x}(t_k, T)/C_{\bar{\theta}_x}(0, T)$ of the simulated spiral spin liquid noise $\bar{\theta}_x(t_k, T)$, calculated after filtering out the fluctuations above 1 kHz, for eight selected temperatures. The decay of correlation is rapid at high temperatures. It slows down upon cooling and approaches nearly a logarithmic form, as can be compared to the exemplary logarithmic curve $1 - 0.15 \ln(t(\text{ms}))$ (dashed gray). Figures reproduced from Ref. [23] with a minor modification.

single-relaxation time shows a low-frequency plateau ω^0 and a high-frequency decay ω^{-2} (Eq. 2.66). The $\omega^{-1.2}$ slope is very different, and it cannot be attributed to a temporal crossover from ω^0 to ω^{-2} as the scale-invariant PSD spans the wide frequency range of nearly three orders. This could imply a broad distribution of relaxation times, which is in line with the spatially inhomogeneous spin texture in a spiral spin liquid phase (Fig. 4.4).

Finally, the variance corresponding to the total noise power is calculated from

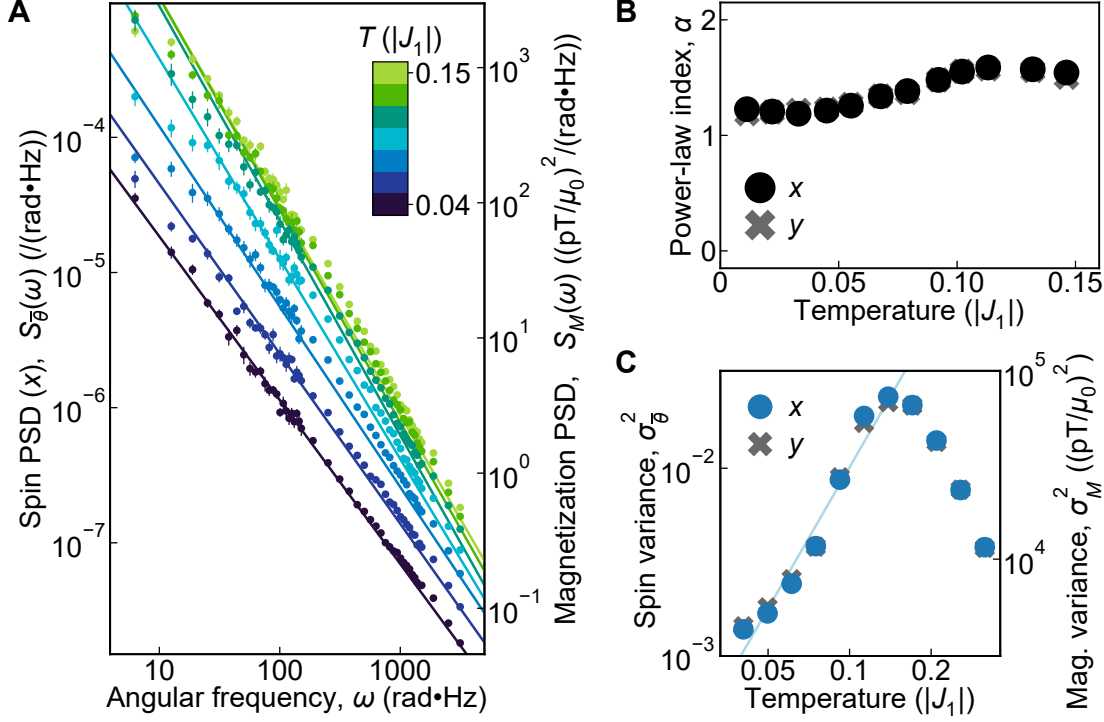


Figure 4.7: (A) Fitting of the 1 Hz-resolution power spectral density $S_{\bar{\theta}_x}(\omega, T) \propto \omega^{-\alpha(T)}$ of the simulated spiral spin liquid noise in the range $1 \text{ Hz} \leq \omega/(2\pi) \leq 500 \text{ Hz}$. (B) The obtained frequency-power-law exponent $\alpha(T)$ that reaches 1.2 ± 0.1 at the lowest temperatures. (C) Variance $\sigma_{\bar{\theta}_{x,y}}^2(T)$ of the simulated spiral spin liquid noise $\bar{\theta}_{x,y}(t_k, T)$, calculated after filtering out the fluctuations above 1 kHz. The variance grows down to $T = 0.15|J_1|$ and then decreases approximately as $T^{2.5}$ (blue line). The estimated value of the corresponding magnetization noise variance $\sigma_M^2(T)$ is shown on the right-hand axis. Figures reproduced from Ref. [23] with a minor modification.

the data with > 1 kHz fluctuations filtered.

$$\sigma_{\bar{\theta}_{x,y}}^2(T) = \frac{1}{K} \sum_{k=0}^{K-1} \bar{\theta}_{x,y}^2(t_k, T) - \left(\frac{1}{K} \sum_{k=0}^{K-1} \bar{\theta}_{x,y}(t_k, T) \right)^2. \quad (4.8)$$

An average is taken over 10 independent MC runs. The calculated variance in Fig. 4.7C increases down to $T = 0.15|J_1|$, then decreases below that temperature. Both the increase and decrease are very rapid, with the variance magnitude changing by at least one order in the shown temperature range. The decline below $T = 0.15|J_1|$ is approximately described by the $T^{2.5}$ temperature dependence.

In summary, the spin noise simulated with the SSL Hamiltonian (Eq. 4.3) has the following properties. Below $T = 0.15|J_1|$, the PSD becomes scale-invariant with the intense low-frequency noise spanning at least from 1 Hz to 500 Hz. The

frequency power law at the lowest temperature is approximately $\omega^{-1.2}$, close to ω^{-1} . The decay of the correlation function slows down upon cooling and approaches a nearly $-\ln t$ behavior. The variance rapidly increases down to $T = 0.15|J_1|$ and then decreases precipitously with the approximate power law $T^{2.5}$.

4.4 Experiment

4.4.1 Sample preparation

As described in Ref. [77], the $\text{Ca}_{10}\text{Cr}_7\text{O}_{28}$ crystals are synthesized in a two-step process: a solid-state reaction of $\text{Ca}_{10}\text{Cr}_7\text{O}_{28}$ powder and a traveling-solvent-floating-zone growth of single crystals.³ First, the powder of CaCO_3 and Cr_2O_3 was mixed with a molar ratio of 3:1, sintered at 1000 °C for 24 hours, and then rapidly quenched to room temperature. The sintering process was repeated after grinding and adding more Cr_2O_3 powder until the phase-pure powder of $\text{Ca}_{10}\text{Cr}_7\text{O}_{28}$ was obtained. This powder was formed into a rod and sintered at 1020 °C for 12 hours, followed by a rapid quench to room temperature. The obtained rod was used as the feed and base rod of the floating-zone growth. A solvent with lower melting temperature was separately prepared from the powder of CaCO_3 and Cr_2O_3 following the same procedure but with a different molar ratio of 5:2. The rods and the solvent are configured in an optical-floating-zone furnace as shown in Fig. 4.8A. The growth was performed at a 0.22 MPa oxygen pressure at a growth rate of 1 mm/hr. Figure 4.8B shows the photo of the growth process. The melted region is gradually shifted up so that a single crystal gradually grows on top of the base rod. The synthesized single crystal was washed with HCl and then with H_2O .

Figure 4.8C shows the photos of the synthesized $\text{Ca}_{10}\text{Cr}_7\text{O}_{28}$ single crystals. The c-axis of the sample is identified to be the long direction of the bar. Sample 1' and Sample 2 are separate parts from the same growth. Sample 3 is from a different growth. Sample 1 is obtained by polishing down Sample 1' so that it fits into the astatic pickup coil spectrometer (Fig. 3.2C).⁴ Powder x-ray diffraction on a small

³I synthesized $\text{Ca}_{10}\text{Cr}_7\text{O}_{28}$ crystals with the support of Masahiko Isobe.

⁴The crystal was polished by Dharmalingam Prabhakaran.

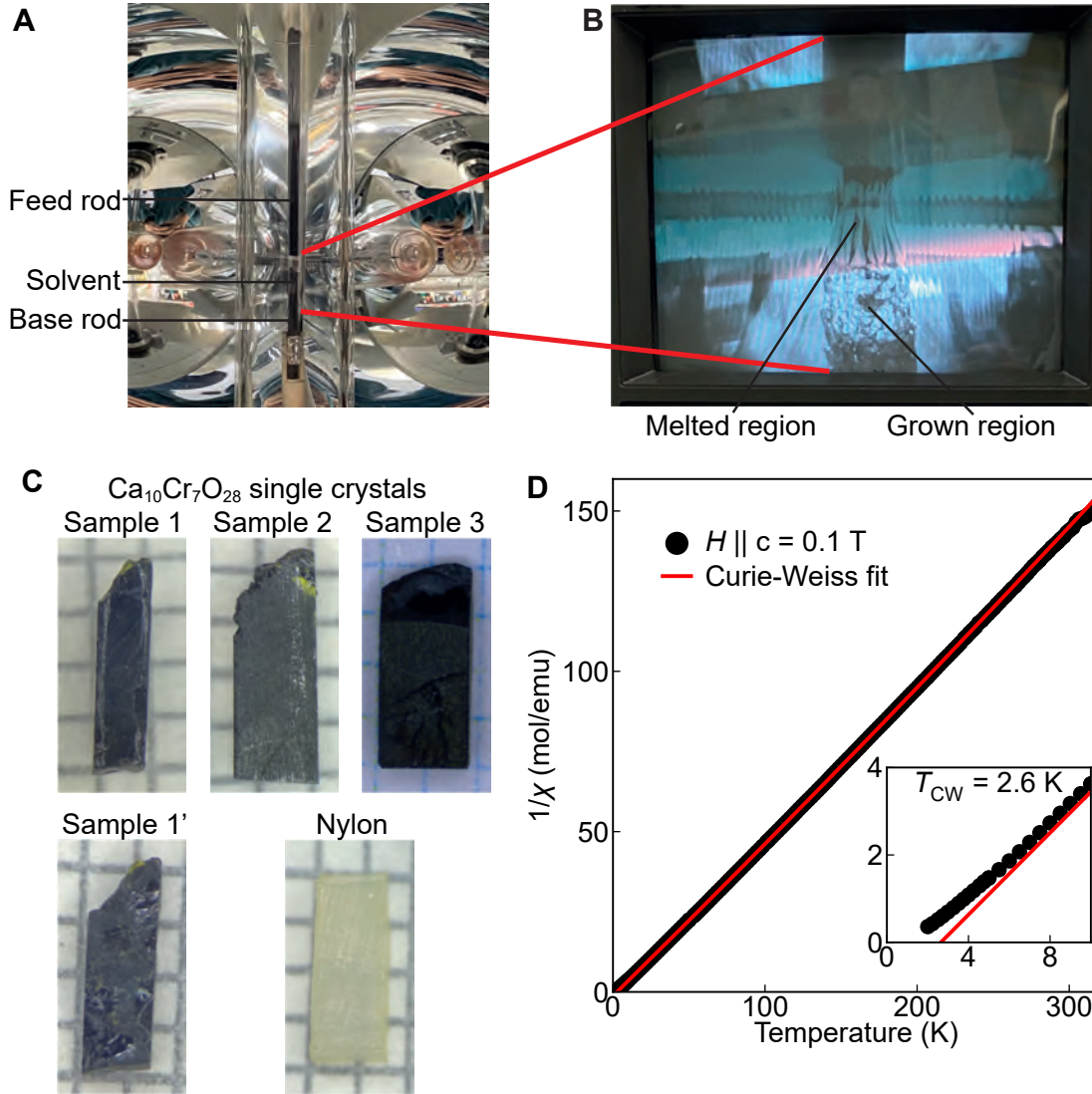


Figure 4.8: (A) Sintered $\text{Ca}_{10}\text{Cr}_7\text{O}_{28}$ rods and solvent configured in an optical zone furnace. (B) Floating-zone growth process of a $\text{Ca}_{10}\text{Cr}_7\text{O}_{28}$ single crystal. (C) Photos of the three synthesized $\text{Ca}_{10}\text{Cr}_7\text{O}_{28}$ single crystals. Sample 1 is obtained by polishing down Sample 1'. A nylon block of a similar size is used for the measurement of background noise. (D) DC susceptibility of Sample 3 measured by an MPMS. The result of a Curie-Weiss fitting $\chi = \chi_0 + \frac{C_{\text{Curie}}}{T - T_{\text{CW}}}$, which yields a Curie-Weiss temperature $T_{\text{CW}} = +2.6$ K and a Curie constant $C_{\text{Curie}} = 2.1$ K-emu/mol corresponding to an effective magnetic moment $\mu_{\text{eff}} = 1.69\mu_{\text{B}}$, is shown (red line). (C, D) are reproduced from Ref. [23] with a minor modification.

ground piece confirms the phase purity, and x-ray Laue diffraction confirms the lattice structure.⁵ Figure 4.8D shows the DC susceptibility of Sample 3 measured

⁵The x-ray Laue diffraction was performed by Pascal Puphal.

by an MPMS (Quantum Design). Fitting the data by the Curie-Weiss law

$$\chi = \chi_0 + \frac{C_{\text{Curie}}}{T - T_{\text{CW}}} \quad (4.9)$$

in the temperature range $50 \text{ K} \leq T \leq 250 \text{ K}$ yields a Curie-Weiss temperature $T_{\text{CW}} = +2.6 \text{ K}$ and a Curie constant $2.1 \text{ K}\cdot\text{emu/mol}$, corresponding to an effective magnetic moment $\mu_{\text{eff}} = 1.69\mu_{\text{B}}$. The value is consistent with the theoretical expectation for an $S = 1/2$ electron spin $\mu_{\text{eff}} = 1.73\mu_{\text{B}}$ and is comparable to the values previously reported for $\text{Ca}_{10}\text{Cr}_7\text{O}_{28}$ [79, 89].

4.4.2 Spin noise measurement

The spin noise measurements were performed in two spectrometers: an astatic coil connected to an SP550 SQUID (Quantum Design) in a dilution refrigerator and a single coil connected to an SQ1200 SQUID (Star Cryoelectronics) in a ^3He refrigerator. The design of the SQUID spin noise spectrometers is detailed in Chapter 3, with the circuit diagram shown in Fig. 3.4A. Here, I only summarize the important parameters. For the SP550 SQUID setup, the parameters were: pickup coil turns $N_{\text{p}} = 10$, the pickup coil inductance $L_{\text{p}} = 0.75 \mu\text{H}$, the input coil inductance $L_{\text{i}} = 1.74 \mu\text{H}$, the inverse input-coil-SQUID coupling $1/M_{\text{i}} = 0.19 \mu\text{A}/\Phi_0$, and the SQUID transfer function $g_{\text{SQUID}} = 0.73 \text{ V}/\Phi_0$. Four 0.2 mm-diameter brass wires were used to thermalize the sample. For the SQ1200 SQUID setup, the parameters were: $N_{\text{p}} = 10$, $L_{\text{p}} = 0.25 \mu\text{H}$, $L_{\text{i}} = 1.30 \mu\text{H}$, $1/M_{\text{i}} = 0.13 \mu\text{A}/\Phi_0$, and $g_{\text{SQUID}} = 9.85 \text{ V}/\Phi_0$. A 0.1 mm-diameter silver wire was glued to the sample for thermalization.

The primary spin noise data of $\text{Ca}_{10}\text{Cr}_7\text{O}_{28}$ consists of SQUID output voltage recordings of a 1000 s duration and a 20 kSa/s sampling rate (a time interval of 50 μs) at temperatures from 100 mK to 800 mK. Sample 1 was measured in the dilution refrigerator from 100 mK to 500 mK in steps of 50 mK, and Sample 2 was measured in ^3He refrigerator from 300 mK to 800 mK in steps of 100 mK. The measurement results from these two setups are combined as later described in Fig. 4.16C. In the both refrigerators, the temperature was controlled with a

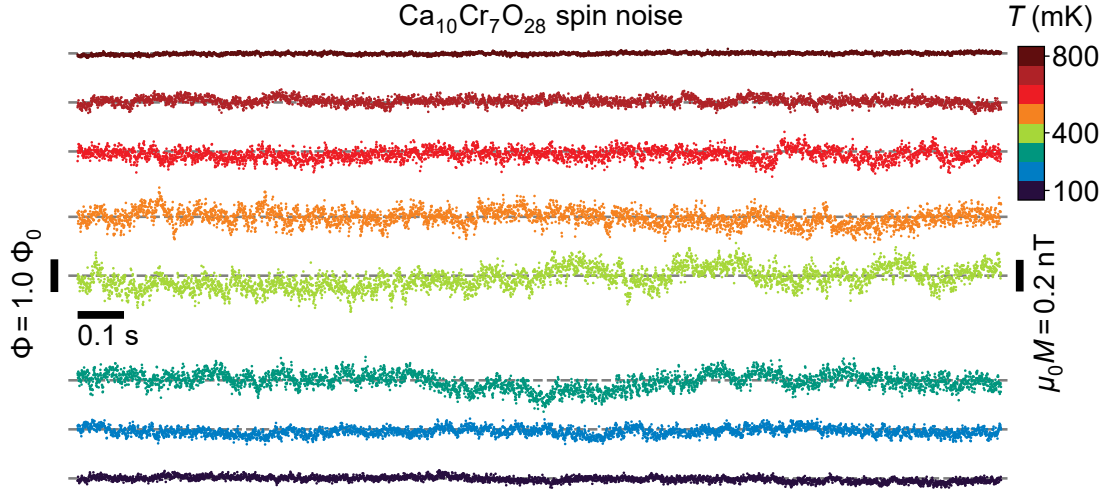


Figure 4.9: Time sequences of the flux noise $\Phi(t_k, T)$ measured in $\text{Ca}_{10}\text{Cr}_7\text{O}_{28}$ at eight selected temperatures. They show fluctuations on a timescale much longer than 0.1 s. The low-frequency noise amplitude grows as the system is cooled down to 400 mK and then rapidly drops below that temperature. For visual clarity, $\Phi(t_k, T)$ is down-sampled so that the time interval of plotted points is $500 \mu\text{s}$. The frequency components below 0.05 Hz and above 1 kHz are filtered out. The corresponding magnetization noise is indicated by the bar on the right. Figure reproduced from Ref. [23] with a minor modification.

stability of 1 mK by a heater, and the samples were thermalized for at least 15 minutes at the target temperature before the measurements. A preamplifier (SR560) with an appropriate gain was used to apply 0.03 Hz 6 dB/oct high-pass and 30 kHz 6 dB/oct low-pass filters, and the 5 kHz 4-pole low-pass filter of the SQ1200 SQUID system was also applied in the ^3He refrigerator. The SQUID background noise was measured for the nonmagnetic nylon sample at 800 mK in the ^3He refrigerator in the same condition.

The extended-bandwidth spin noise measurement (Section 3.2.2) of $\text{Ca}_{10}\text{Cr}_7\text{O}_{28}$ was performed for Sample 2 in the ^3He refrigerator. The SQUID bandwidth was extended to $f_{3\text{dB}} \sim 160$ kHz, which involved the SQUID transfer function change to $g_{\text{SQUID}} = 0.985 \text{ V}/\Phi_0$. The SQUID output voltage was recorded for 100 s at 1 MSa/s from 300 mK to 800 mK in steps of 100 mK. The SQUID background noise was measured for the nonmagnetic nylon sample for 10 s at 1 MSa/s at 275 mK.

The recorded SQUID output voltage $V(t, T)$ at each temperature is converted into the flux noise $\Phi(t, T)$ at the pickup coil and the magnetization noise $M(t, T)$

using Eqs. 2.102 and 2.103. Figure 4.9 shows the measured Ca₁₀Cr₇O₂₈ flux noise $\Phi(t, T)$ at eight selected temperatures, after filtering out the high-frequency components above 1 kHz (Appendix B). The noise exhibits slow fluctuations on a timescale much longer than 0.1 s. The noise magnitude grows down to $T \sim 400$ mK and then rapidly diminishes below that temperature. The peak-to-peak value of the corresponding magnetization noise is of the order $\mu_0 M \sim 0.2$ nT.

4.4.3 AC susceptibility measurement

The AC susceptibility measurements were performed in the same setup as the spin noise measurements, the astatic coil connected to the SP550 SQUID in the dilution refrigerator. The design of the SQUID susceptometer is detailed in Chapter 3, with the circuit diagram shown in Fig. 3.4B. The parameters are the same as those of the spin noise measurements, except that the SQUID is changed to the range 500 mode (lowest sensitivity) with $g_{\text{SQUID}} = 7.3$ mV/ Φ_0 . The reference output of the lock-in amplifier was connected to the field coil across a 20 k Ω resistor.

The measurements were performed for Sample 1 from 100 mK to 500 mK in steps of 50 mK. At each temperature, an AC magnetic field with a root-mean-square magnitude of $\mu_0 H_0 / \sqrt{2} = 60$ nT was applied in a frequency range $0.1 \text{ Hz} \leq \omega / (2\pi) \leq 101$ Hz, and the corresponding SQUID output voltage was fed into the lock-in amplifier to measure the in-phase and out-of-phase components. For the detection settings of the lock-in amplifier, the time constant was set to 30 s, 10 s, 3 s, and 300 ms for the frequencies 0.1–0.3 Hz, 0.5–0.9 Hz, 1–11 Hz, and 21–101 Hz, respectively. The 18 dB/oct low-pass filter slope was chosen for all the frequencies. The internal gain was appropriately chosen between 10 mV and 50 mV at different temperatures. At each frequency, 10 measurements were performed and the results were averaged. The temperature was controlled by a heater with a stability of 1 mK, and the sample was thermalized for at least 20 minutes at the target temperature before the measurements. The universal phase was set by referencing the phase outcome at 0.1 Hz in a calibration experiment, which measured a superconducting indium wire of a size comparable to the Ca₁₀Cr₇O₂₈ samples.

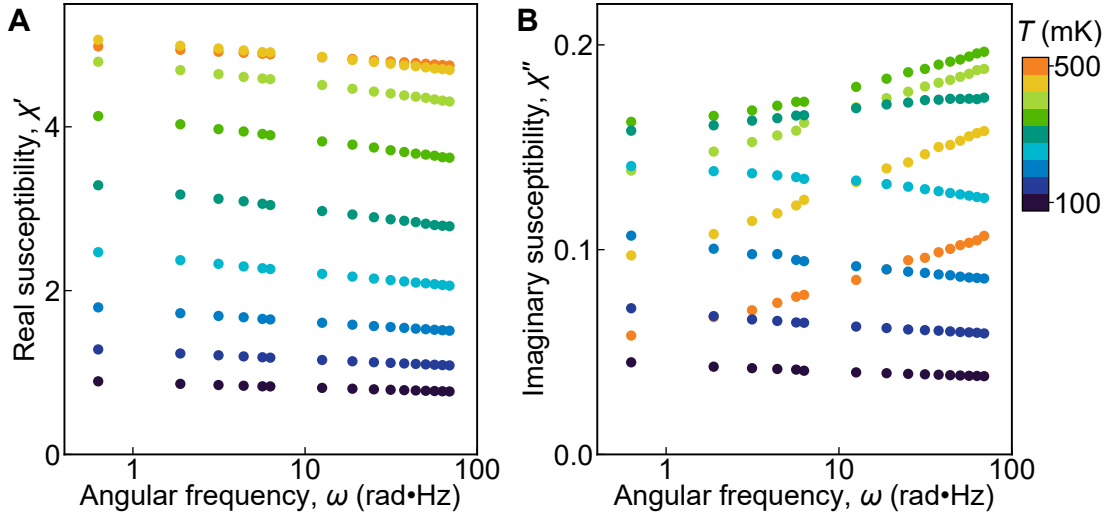


Figure 4.10: Measured real (A) and imaginary (B) part of the AC susceptibility of $\text{Ca}_{10}\text{Cr}_7\text{O}_{28}$ at nine selected temperatures. A 60 nT AC magnetic field was used for the measurement.

The real and imaginary susceptibility, obtained by converting the lock-in amplifier output voltage using Eq. 2.109 and 2.110, are shown in Fig. 4.10. The real part χ' is nearly frequency-independent in the measured frequency range. The imaginary part χ'' exhibits a positive slope at high temperatures but becomes nearly flat below 400 mK.

4.5 Experimental Analysis

4.5.1 Spin noise analysis

Each time sequence of the flux noise $\Phi(t_k, T)$ has the total duration of $\Gamma = 1000$ s, with the time interval of $\Delta t = 50$ μs between the $K = 2 \times 10^7$ data points ($0 \leq t_k \leq (K - 1)\Delta t$). Its PSD $S_\Phi(\omega_j, T)$ is calculated from the formula

$$S_\Phi(\omega_j, T) = \frac{1}{\pi\Gamma} \left| \Delta t \sum_{k=0}^{K-1} e^{-i\omega_j t_k} \Phi(t_k, T) \right|^2, \quad (4.10)$$

where $\omega_j/(2\pi) = j/\Gamma$ ($0 \leq j \leq K/2$). The obtained PSD is shown as a contour plot in Fig. 4.11 and as a typical xy plot in Fig. 4.12A. The PSDs with the resolution of $\Delta\omega/(2\pi) = 10^{-1}, 10^0, 10^1, 10^2$ Hz are calculated from the $P = 10^2, 10^3, 10^4, 10^5$ split segments (Appendix B). The PSD grows in power down to ~ 400 mK and then drops rapidly below that temperature, as shown in Fig. 4.11. The crossover

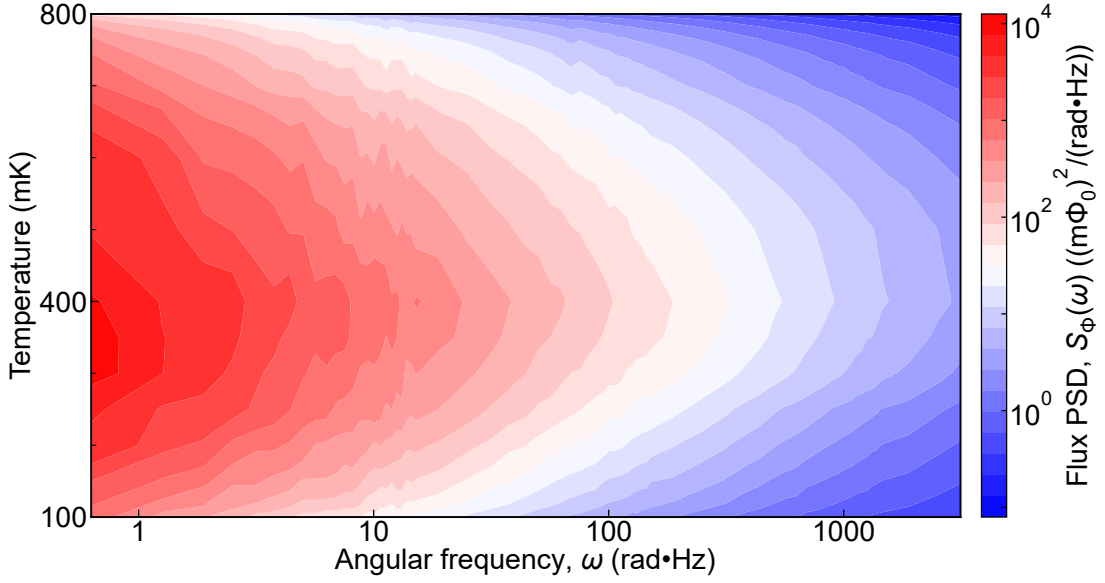


Figure 4.11: Contour plot of the power spectral density $S_{\Phi}(\omega_j, T)$ of the measured $\text{Ca}_{10}\text{Cr}_7\text{O}_{28}$ flux noise $\Phi(t_k, T)$ from 100 mK to 800 mK. The magnitude increases down to ~ 400 mK and then decreases rapidly below that temperature. Figure reproduced from Ref. [23] with a minor modification.

temperature ~ 400 mK is coincident with ~ 450 mK of the specific heat weak kink [75, 78], 300–350 mK of the AC susceptibility maximum [78], and 300–500 mK of the muon relaxation rate saturation [78]. This closeness in temperature proposes that the detected spin noise has the same origin as the spin liquid phenomena observed by the other experimental probes. The PSD is scale-invariant, showing the intense low-frequency noise down to at least $\omega/(2\pi) = 0.1$ Hz, as shown in Fig. 4.12A.

The PSD of the extended-frequency measurement is plotted in Fig. 4.13. The spectrum below 3 kHz is from the primary spin noise data. That above 3 kHz is from the extended-frequency measurement data, where the PSDs with the resolutions of $\Delta\omega/(2\pi) = 10^3$ and 10^4 Hz are calculated from the $P = 10^5$ and 10^6 split segments (Appendix B). The contribution of $\text{Ca}_{10}\text{Cr}_7\text{O}_{28}$ spin noise is clearly detected in the extended-frequency measurement, despite the elevated SQUID noise floor. The $\text{Ca}_{10}\text{Cr}_7\text{O}_{28}$ spin noise thus spans the wide frequency range at least from 0.1 Hz to 50 kHz.

Next, the correlation function $C_{\Phi}(t_k, T)$ is calculated. The analysis of the PSD

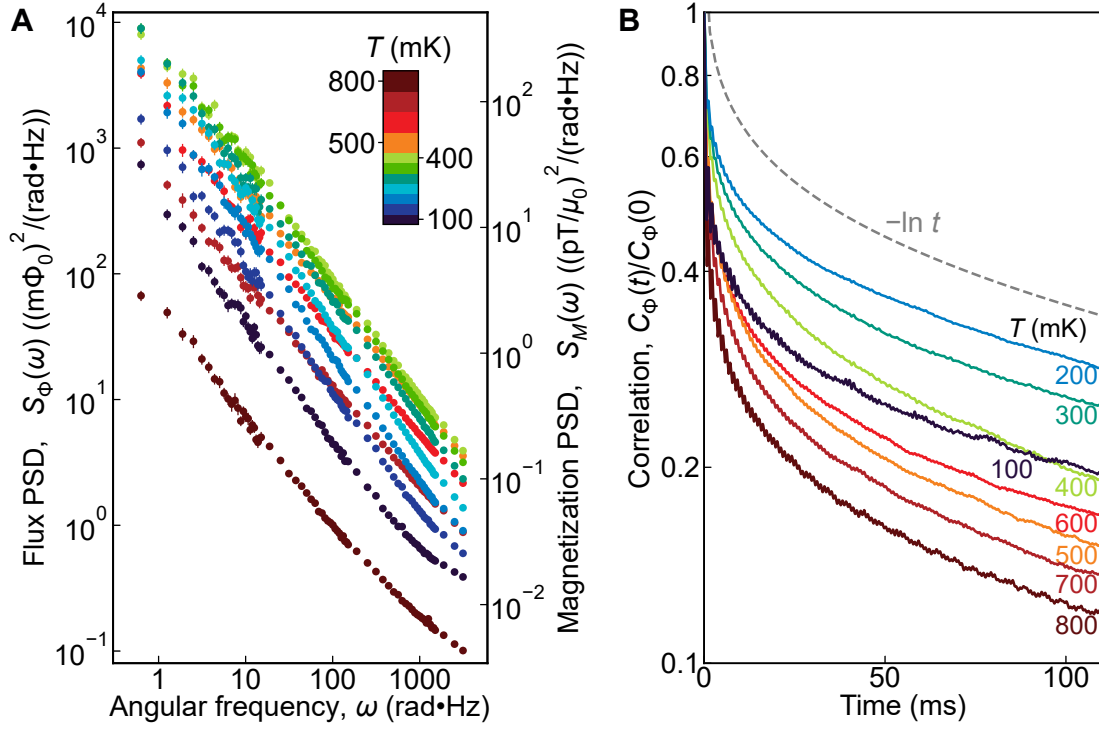


Figure 4.12: (A) Power spectral density $S_{\Phi}(\omega_j, T)$ of the measured $\text{Ca}_{10}\text{Cr}_7\text{O}_{28}$ flux noise $\Phi(t_k, T)$ for eleven selected temperatures. The spectrum is scale-invariant and shows the intense low-frequency noise down to $\omega/2\pi = 0.1$ Hz. The error bars are given by the standard error of averaging the PSDs from the split segments. The power spectral density of the corresponding magnetization noise $S_M(\omega_j, T)$ is shown on the right-hand axis. (B) Normalized correlation function $C_{\Phi}(t_k, T)/C_{\Phi}(0, T)$ of the measured $\text{Ca}_{10}\text{Cr}_7\text{O}_{28}$ flux noise $\Phi(t_k, T)$, calculated after filtering out the fluctuations below 0.05 Hz and above 1 kHz, for eight selected temperatures. The correlation decays logarithmically, as can be compared to the exemplary logarithmic curve $(1 - 0.14 \ln(t(\text{ms})))$ (dashed gray). Figures reproduced from Ref. [23] with a minor modification.

indicates that, above ~ 1 kHz, the SQUID noise in the SP550 setup is comparable to the $\text{Ca}_{10}\text{Cr}_7\text{O}_{28}$ spin noise contribution. Also, the fluctuations below 0.05 Hz could be affected by the slow temperature fluctuation. To address only the intact spin noise from the $\text{Ca}_{10}\text{Cr}_7\text{O}_{28}$ sample, I first filtered out the fluctuations below 0.05 Hz and above 1 kHz from $\Phi(t_k, T)$ (Appendix B). From this filtered data, the correlation function is calculated using the standard formula

$$C_{\Phi}(t_k, T) = \frac{1}{l_{\text{ave}}} \sum_{l=0}^{l_{\text{ave}}-1} \Phi(t_l, T) \Phi(t_{l+k}, T), \quad (4.11)$$

where $l_{\text{ave}} = 1.9 \times 10^7$. The normalized correlation function $C_{\Phi}(t_k, T)/C_{\Phi}(0, T)$, shown in Fig. 4.12B, exhibits the logarithmic decay $C_{\Phi}(t, T) \propto -\ln t$. It is distinct

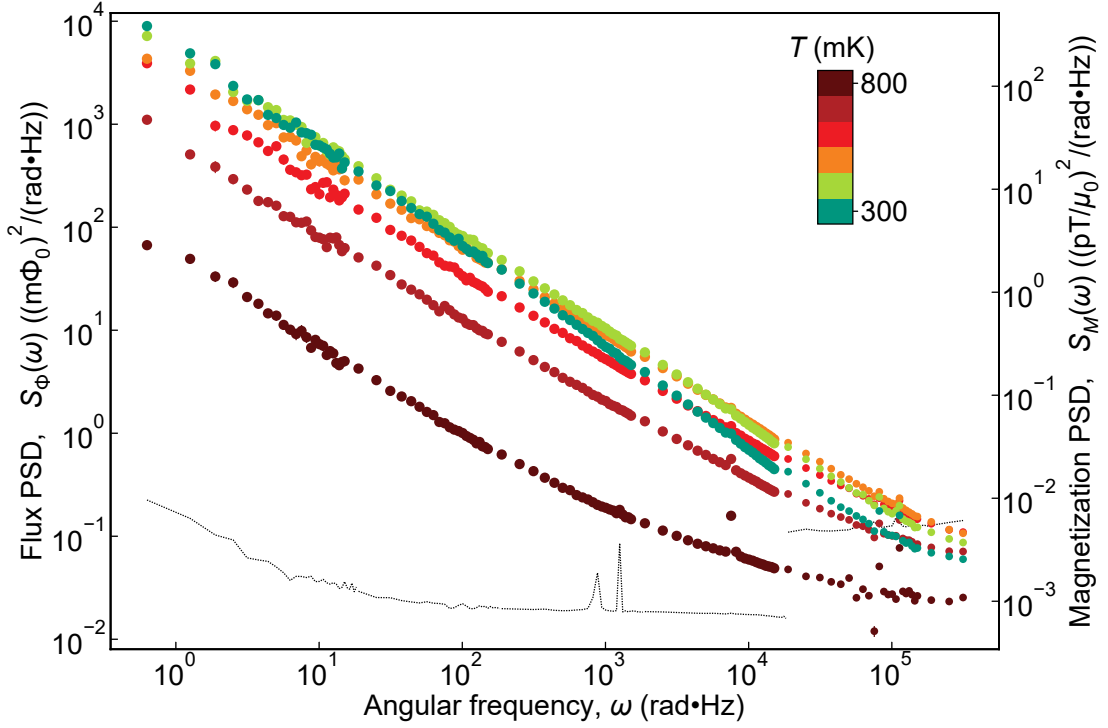


Figure 4.13: Power spectral density $S_{\Phi}(\omega_j, T)$ of the measured $\text{Ca}_{10}\text{Cr}_7\text{O}_{28}$ flux noise $\Phi(t_k, T)$ in the frequency range $0.1 \text{ Hz} \leq \omega/(2\pi) \leq 50 \text{ kHz}$ for six temperatures. The background noise from a nonmagnetic nylon block is also plotted (black-dotted line). The noise below 3 kHz is from the primary noise data, and that above 3 kHz is from the extended-frequency measurement with an elevated noise floor. The PSD of $\text{Ca}_{10}\text{Cr}_7\text{O}_{28}$ above 3 kHz is plotted after subtracting the background noise, resulting in the smooth PSD across 3 kHz. The power spectral density of the corresponding magnetization noise $S_M(\omega_j, T)$ is shown on the right-hand axis. Figure reproduced from Ref. [23] with a minor modification.

from a typical exponential decay with a single relaxation time, and could imply a broad distribution of relaxation times as $p(\tau) \propto 1/\tau$ [66].

The frequency-power-law exponent of the scale-invariant PSD is examined. Figure 4.14A shows the fitting of the 0.1 Hz-resolution PSD $S_{\Phi}(\omega_j, T) \propto \omega^{-\alpha(T)}$ in the range $0.1 \text{ Hz} \leq \omega/(2\pi) \leq 20 \text{ Hz}$, and the obtained exponent $\alpha(T)$ is plotted in Fig. 4.14B. The exponent is in the range $0.84 < \alpha(T) < 1.04$ at the measured temperatures, approaching 1 at the lowest temperature. This is very different from the low-frequency plateau ω^0 or the high-frequency decay ω^{-2} of a standard PSD with a single relaxation time (Eq. 2.66).

Finally, the variance corresponding to the total noise power is calculated from

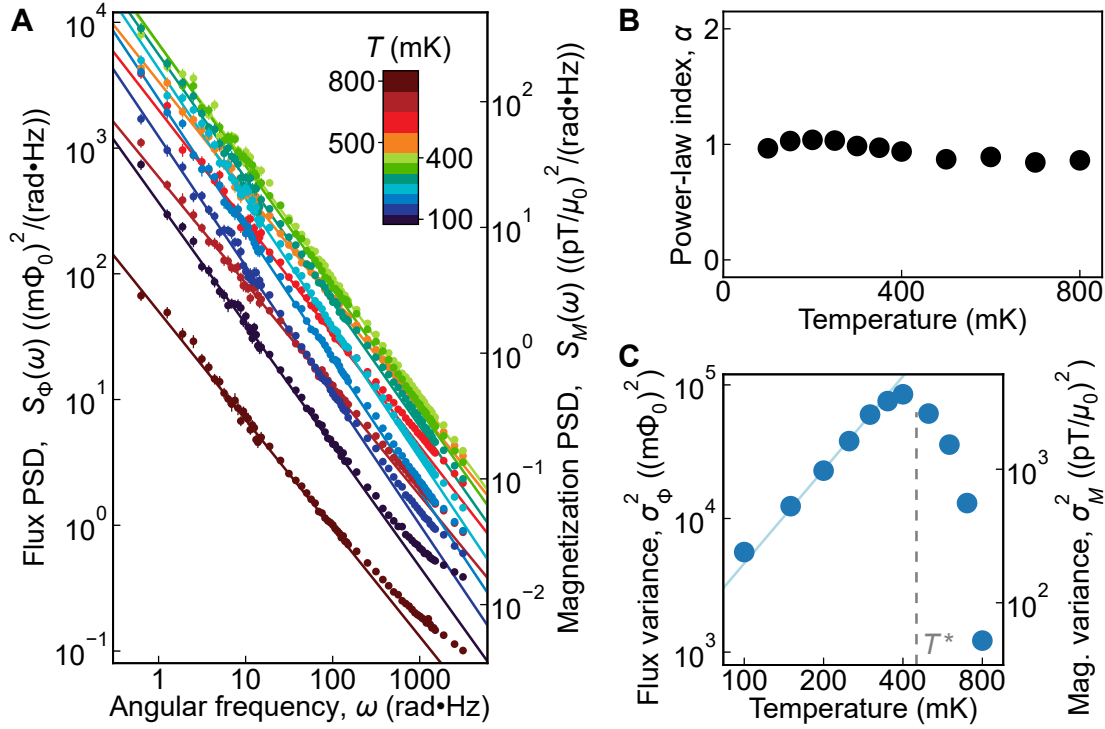


Figure 4.14: (A) Fitting of the 0.1 Hz-resolution power spectral density $S_\Phi(\omega, T) \propto \omega^{-\alpha(T)}$ of the experimental $\text{Ca}_{10}\text{Cr}_7\text{O}_{28}$ flux noise in the range $0.1 \text{ Hz} \leq \omega/(2\pi) \leq 20 \text{ Hz}$. (B) The obtained frequency-power-law exponent $\alpha(T)$ approaching 1 at the low temperatures. (C) Variance $\sigma_\Phi^2(T)$ of the measured $\text{Ca}_{10}\text{Cr}_7\text{O}_{28}$ flux noise $\Phi(t_k, T)$, calculated after filtering out fluctuations below 0.05 Hz and above 1 kHz. The variance grows down to $T \sim 400$ mK and then decreases as $T^{2.3}$ (blue line). The broad peak coincides with the crossover temperature $T^* = 450$ mK of the specific heat [78] (gray dashed line). The value of the corresponding magnetization noise variance $\sigma_M^2(T)$ is shown on the right-hand axis. Figures reproduced from Ref. [23] with a minor modification.

the data, whose < 0.05 Hz and > 1 kHz fluctuations are filtered out.

$$\sigma_\Phi^2(T) = \frac{1}{K} \sum_{k=0}^{K-1} \Phi^2(t_k, T) - \left(\frac{1}{K} \sum_{k=0}^{K-1} \Phi(t_k, T) \right)^2. \quad (4.12)$$

The calculated variance in Fig. 4.14C increases down to $T \sim 400$ mK and then decreases below that temperature. Both the increase and decrease are very rapid, with the variance magnitude changing by nearly two orders in the shown temperature range. The decline below the crossover peak is described by the power-law temperature dependence $\sigma_\Phi^2(T) \propto T^\beta$ with $\beta = 2.3 \pm 0.1$.

In summary, the experimentally measured spin noise in $\text{Ca}_{10}\text{Cr}_7\text{O}_{28}$ has the following properties. The PSD is scale-invariant with the intense low-frequency noise spanning at least from 0.1 Hz to 50 kHz. The frequency power law at

the low temperatures is $\sim \omega^{-1}$. The correlation function shows the logarithmic decay $-\ln t$. The variance rapidly grows down to $T \sim 400$ mK and then drops rapidly with the power law $T^{2.3}$.

4.5.2 Fluctuation-dissipation theorem

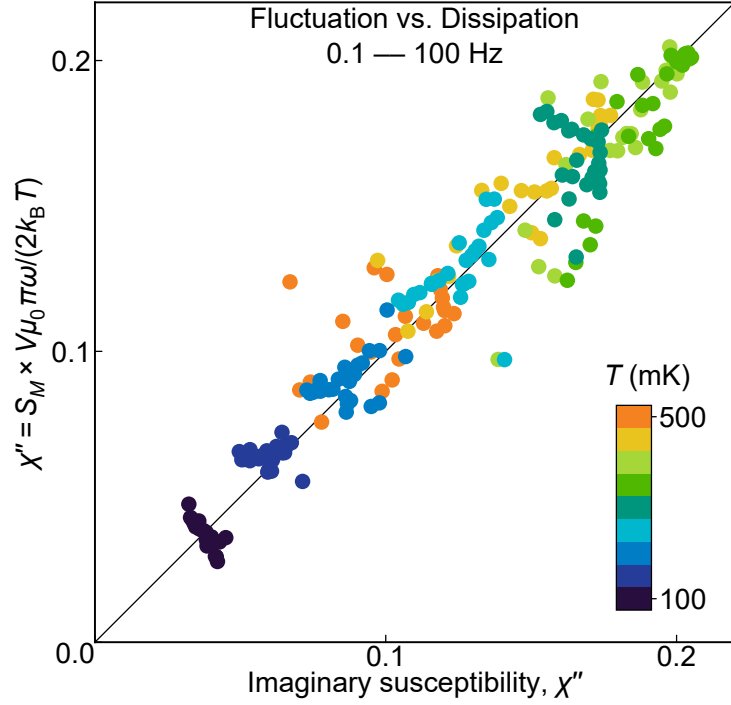


Figure 4.15: Comparison between the simultaneously measured magnetization noise power spectral density $S_M(\omega)$ and the imaginary susceptibility $\chi''(\omega)$ of $\text{Ca}_{10}\text{Cr}_7\text{O}_{28}$. $V\mu_0\frac{\pi\omega}{2k_B T}S_M(\omega)$ is plotted against $\chi''(\omega)$ over the frequency range $0.1 \text{ Hz} \leq \omega/(2\pi) \leq 100 \text{ Hz}$ and the temperature range $100 \text{ mK} \leq T \leq 500 \text{ mK}$. The plot is on a single line $y = x$, demonstrating that the fluctuation-dissipation theorem holds down to at least 0.1 Hz and 100 mK in $\text{Ca}_{10}\text{Cr}_7\text{O}_{28}$. Figure reproduced from Ref. [23] with a minor modification.

The magnetization noise PSD $S_M(\omega)$ and the AC susceptibility $\chi(\omega)$ of $\text{Ca}_{10}\text{Cr}_7\text{O}_{28}$ were measured in the same experimental setup, which allows a direct comparison. In Fig. 4.15, the magnetization PSD, converted as $V\mu_0\frac{\pi\omega}{2k_B T}S_M(\omega)$, is plotted against the imaginary susceptibility $\chi''(\omega)$. The data points are on a single line $y = x$, demonstrating that the fluctuation-dissipation theorem (Eq. 2.55) holds down to at least 0.1 Hz and 100 mK in $\text{Ca}_{10}\text{Cr}_7\text{O}_{28}$.

$$\chi''(\omega) = V\mu_0\frac{\pi\omega}{2k_B T}S_M(\omega). \quad (4.13)$$

This indicates that the dynamical equilibrium is maintained in the observed $\text{Ca}_{10}\text{Cr}_7\text{O}_{28}$ spin noise phenomena down to at least 0.1 Hz.

4.5.3 Reproducibility of $\text{Ca}_{10}\text{Cr}_7\text{O}_{28}$ spin noise

The reproducibility of the spin noise phenomena is examined by repeating the measurements. The three $\text{Ca}_{10}\text{Cr}_7\text{O}_{28}$ samples (Sample 1', Sample 2, and Sample 3) and the nonmagnetic nylon block, shown in Fig. 4.8C, were measured in the ^3He refrigerator. The SQUID output voltage was recorded for 100 s at 1 M Sa/s at the temperatures from 275 mK to 800 mK, in steps of 25 mK for the $\text{Ca}_{10}\text{Cr}_7\text{O}_{28}$ samples and 100 mK for the nylon sample. The only frequency filter used was the 1.6 Hz AC coupling filter at the analog-to-digital converter (Moku:Pro) input. The 0.1 Hz-resolution PSD calculated from the $P = 10^3$ split segments (Appendix B) is shown in Fig. 4.16A. The PSD at 300 mK, 500 mK, 700 mK, and 800 mK exhibits a scale-invariant form for all samples. On the other hand, the nylon noise floor barely changes over temperature and remains smaller than the $\text{Ca}_{10}\text{Cr}_7\text{O}_{28}$ noise. The variance, calculated after filtering out the fluctuations above 1 kHz, peaks at $T \sim 400$ mK for all the $\text{Ca}_{10}\text{Cr}_7\text{O}_{28}$ samples as shown in Fig. 4.16B. Thus, the reported spin noise phenomena in $\text{Ca}_{10}\text{Cr}_7\text{O}_{28}$ are confirmed to be robust.

The primary spin noise data, measured in the two $\text{Ca}_{10}\text{Cr}_7\text{O}_{28}$ samples (Sample 1 and Sample 2 in Fig. 4.8C) over the different temperature ranges, has been reconciled as follows. The amplitude of magnetization noise $M(t)$ depends on a sample volume, and the amplitude of flux noise $\Phi(t)$ further depends on the cross-sectional area of the sample. A scale factor is naturally required to combine noise measured in two samples with different geometry, and, in principle, one can only match the scale of either $\Phi(t)$ or $M(t)$. Throughout the $\text{Ca}_{10}\text{Cr}_7\text{O}_{28}$ noise discussion in this section, $\Phi(t)$ matching has been prioritized. $\Phi(t)$ of Sample 2 has been scaled from the original value by a factor of 0.95; namely, $\Phi(t, T) = \Phi_1(t, T)$ for Sample 1 data and $\Phi(t, T) = 0.95\Phi_2(t, T)$ for Sample 2 data. In this way, the flux noise power spectral densities of the two samples coincide, as exemplified by

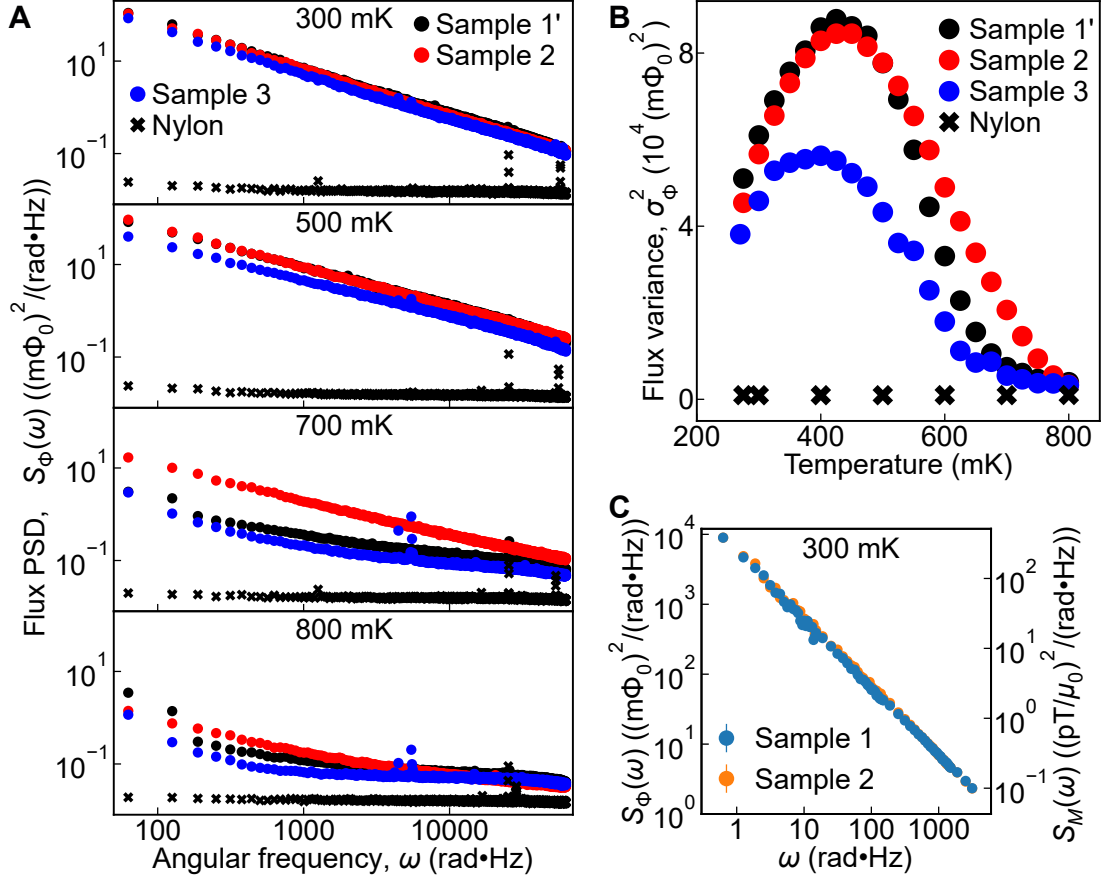


Figure 4.16: Comparison of the spin noise from three $\text{Ca}_{10}\text{Cr}_7\text{O}_{28}$ samples and a nonmagnetic nylon block. (A) Flux noise power spectral density $S_\phi(\omega, T)$. It is scale-invariant for all the $\text{Ca}_{10}\text{Cr}_7\text{O}_{28}$ samples, and the $\text{Ca}_{10}\text{Cr}_7\text{O}_{28}$ noise exceeds the nylon background noise. (B) Flux noise variance $\sigma_\phi^2(T)$ calculated after filtering out the fluctuations above 1 kHz. It shows a broad peak at $T \sim 400$ mK and a similar temperature dependence for all the $\text{Ca}_{10}\text{Cr}_7\text{O}_{28}$ samples. (C) Comparison of the flux noise power spectral density $S_\phi(\omega, T)$ of Sample 1 and Sample 2 at the same temperature 300 mK. $S_\phi(\omega)$ of Sample 2 is scaled by 0.95^2 , which makes the two flux noise power spectral densities nearly identical. The corresponding magnetization noise power spectral density $S_M(\omega, T)$ on the right axis is converted using the geometry of Sample 1. Figures reproduced from Ref. [23] with a minor modification.

the 300 mK data in Fig. 4.16C. $M(t, T)$ has been converted from $\Phi(t, T)$ using the geometry of Sample 1 for the both samples.

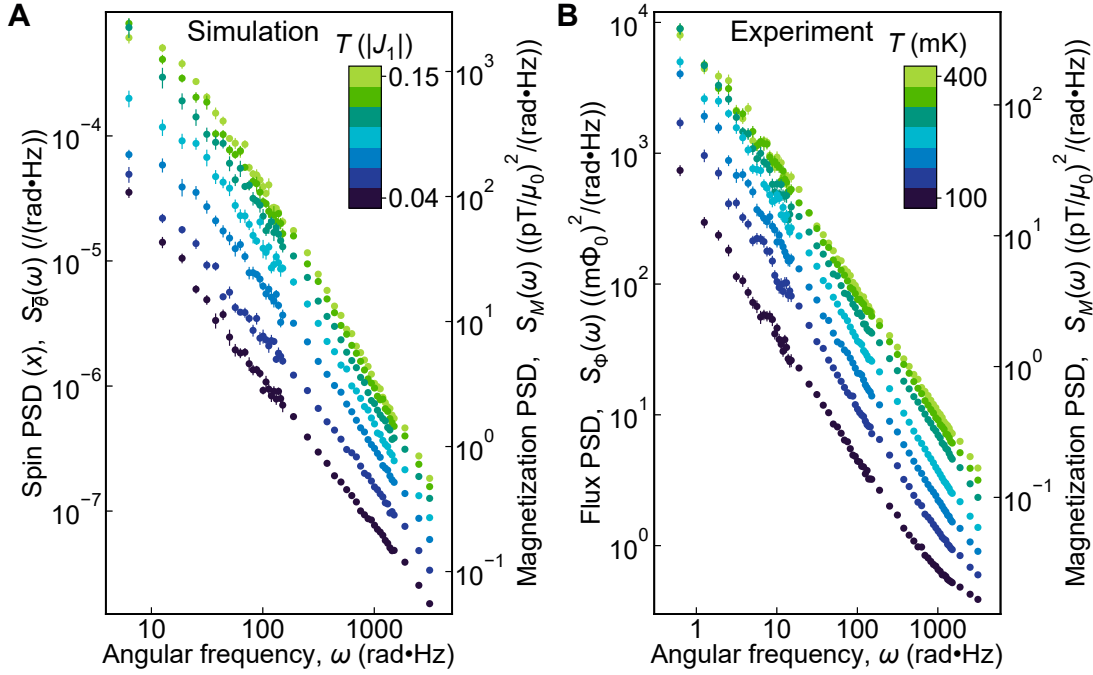


Figure 4.17: (A) Power spectral density $S_{\bar{\theta}_x}(\omega_j, T)$ of the simulated spiral spin liquid noise $\bar{\theta}_x(t_k, T)$ at the temperatures below $T = 0.15|J_1|$. (B) Power spectral density $S_{\Phi}(\omega_j, T)$ of the measured $\text{Ca}_{10}\text{Cr}_7\text{O}_{28}$ flux noise $\Phi(t_k, T)$ at the temperatures below $T = 400$ mK. Figures reproduced from Ref. [23] with a minor modification.

4.6 Discussion

4.6.1 Noise evidences $\text{Ca}_{10}\text{Cr}_7\text{O}_{28}$ as a spiral spin liquid

There is wide-ranging agreement between the predicted SSL spin noise and the measured $\text{Ca}_{10}\text{Cr}_7\text{O}_{28}$ spin noise, as directly compared in Fig. 4.17. Firstly, the magnetic field fluctuations of order 0.1 nT span the broad frequency range of at least $1 \text{ Hz} \leq \omega/2\pi \leq 500 \text{ Hz}$. The PSD is scale-invariant $S(\omega) \propto \omega^{-\alpha(T)}$, with the frequency power-law exponent $\alpha(T)$ approaching a value close to 1 at the low temperatures. Secondly, the correlation function decays with a nearly logarithmic form $C(t) \sim -\ln t$. Thirdly, the variance increases upon cooling and then rapidly decreases below the crossover temperature T^* , with the power-law temperature dependence of $\sim T^{2.5}$. On the other hand, the measured spin noise is distinct from the predictions for different QSLs, namely a frequency-independent PSD. Thus, the overall correspondences between the SSL simulation and the $\text{Ca}_{10}\text{Cr}_7\text{O}_{28}$ spin noise measurement evidence that $\text{Ca}_{10}\text{Cr}_7\text{O}_{28}$ is a SSL, not a QSL.

4.6.2 Possibility of conventional spin glass in Ca₁₀Cr₇O₂₈

The frequency dependence of the spin noise PSD, indicating the broad distribution of relaxation time, is reminiscent of a disorder-induced conventional spin glass. However, a conventional spin glass appears unlikely in Ca₁₀Cr₇O₂₈, if not fully ruled out. The experimental demonstration of the fluctuation-dissipation theorem in Fig. 4.15 indicates that spins in Ca₁₀Cr₇O₂₈ are not frozen to at least 0.1 Hz and 100 mK. This makes spin freezing in Ca₁₀Cr₇O₂₈ unlikely, although freezing at even lower frequency and temperature has not been fully excluded. I note aside that the temperature dependence of spin noise variance $\sigma_M^2(T) \sim T^{2.3}$, corresponding to DC susceptibility $\chi^{\text{DC}} \sim T^{1.3}$ (fluctuation-dissipation theorem), is exceptionally rapid. A spin glass explanation, if it exists, must explain such a rapid temperature dependence.

The saturating muon relaxation rate [78] evidences persistent spin fluctuations down to 20 mK, which is in accordance with non-freezing spins. Ref. [78] also reports AC susceptibility with a frequency-dependent peak, which is usually regarded as a signature of a conventional spin glass, but the relatively sharp distribution of relaxation time in the relevant ~ 10 kHz regime suggests that Ca₁₀Cr₇O₂₈ is different from a conventional spin glass.

A conventional mechanism of spin glass formation is inherent randomness due to disorder. Cr⁵⁺ bilayer kagome in Ca₁₀Cr₇O₂₈ is fully connected, and no disorder effect has been known. Two position choices of the nonmagnetic Cr⁶⁺ [77] could in principle introduce bond randomness in the rather distant magnetic Cr⁵⁺ network, but such effect has not been evidenced. The relatively sharp distribution of relaxation time at ~ 10 kHz [78] also appears against strong inherent randomness in Ca₁₀Cr₇O₂₈. The spiral spin liquid simulation, where an emergent non-local spiral pattern occurs, does not require inherent randomness to account for the slowing down of spin dynamics and inhomogeneity. Based on these discussions, spiral spin liquid appears more consistent for Ca₁₀Cr₇O₂₈ than a conventional spin glass.

4.6.3 Next developments in simulation and experiment

To make a clear identification of $\text{Ca}_{10}\text{Cr}_7\text{O}_{28}$ as a SSL, further refinement of the SSL simulation will be beneficial. Here I repeat that I turned to the well-studied generic Hamiltonian of a 2D SSL [22]. I compared it to the experiment under an assumption that the q -space spiral contour with an approximately circular shape, the key feature of the SSL physics shared by both the model and $\text{Ca}_{10}\text{Cr}_7\text{O}_{28}$, make them correspondent irrespective of the real-space lattice. However, there are simulation predictions that are not experimentally observed. Firstly, the simulation predicts a specific heat peak that is discussed as a non-symmetry-breaking transition [22], which is not experimentally observed in $\text{Ca}_{10}\text{Cr}_7\text{O}_{28}$ [75, 78]. Secondly, at $T > T^*$, the simulated PSD (Fig. 4.6A) starts showing a flat noise plateau, while the experimental PSD (Fig. 4.12A) retains the power-law behavior. These discrepancies indicate that some additional factors in actual $\text{Ca}_{10}\text{Cr}_7\text{O}_{28}$ are not fully considered in the generic model simulation. The simulation in the more realistic $\text{Ca}_{10}\text{Cr}_7\text{O}_{28}$ Hamiltonian is certainly sought after, although that first requires the refinement of the controversial $\text{Ca}_{10}\text{Cr}_7\text{O}_{28}$ Hamiltonian [80, 81]. In addition, in order to develop physical understanding, an analytical spin noise prediction of dynamical spin spirals is now posed as a key challenge for the field.

Spin noise spectroscopy of other 2D spiral spin liquid compounds, such as FeCl_3 [19], will be beneficial to firmly establish spiral spin liquid noise. That requires modification of the spin noise spectrometer design as FeCl_3 is air sensitive and reportedly shows a long-range magnetic order below 8.5 K. The sample has to be sealed in a vacuum container without sacrificing a pickup-coil filling factor too much, and the sample has to be warmed up separately from the superconducting spin noise spectrometer. Search for more 2D spiral spin liquid compounds is motivated.

Nevertheless, the overall agreement between the presented SSL simulation and the $\text{Ca}_{10}\text{Cr}_7\text{O}_{28}$ experiment evidences $\text{Ca}_{10}\text{Cr}_7\text{O}_{28}$ as a SSL. In a broader context, this work introduces the spin noise spectroscopy technique to spin liquid studies

and demonstrates its potential for fingerprinting a spin system, thereby opening a new avenue for spin liquid research.

5

Spinon-Mediated Witness-Spin Interactions in $\text{ZnCu}_3(\text{OH})_6\text{Cl}_2$

Herbertsmithite $\text{ZnCu}_3(\text{OH})_6\text{Cl}_2$ is an iconic quantum spin liquid candidate with a kagome layer of $S = 1/2$ spins and antiferromagnetic interactions of $J \sim 190$ K. Despite decades of study, the exact spin ground state of $\text{ZnCu}_3(\text{OH})_6\text{Cl}_2$ has remained controversial. While much research effort has focused on the kagome layer, I propose an alternative strategy to exploit interlayer Cu^{2+} spins due to $\text{Cu}^{2+}/\text{Zn}^{2+}$ intersubstitution. The interlayer spins interact with each other via the kagome layer, thus ‘witnessing’ the physical properties of the kagome spin dynamics. The spin noise I have discovered in $\text{ZnCu}_3(\text{OH})_6\text{Cl}_2$, attributed to the interlayer witness-spin dynamics, undergoes a sharp transition at 260 mK. The experimental observations are overall consistent with spinon-mediated interactions between interlayer Cu^{2+} spins, via the spectrum of spinons in a quantum spin liquid state within the kagome layer.

5.1 Spin liquid candidate $\text{ZnCu}_3(\text{OH})_6\text{Cl}_2$

5.1.1 Structure

$\text{ZnCu}_3(\text{OH})_6\text{Cl}_2$ [47,48] is a quasi-2D compound consisting of $S = 1/2$ Cu^{2+} kagome layers separated by nonmagnetic Zn^{2+} triangular layers as shown in Fig. 5.1. A

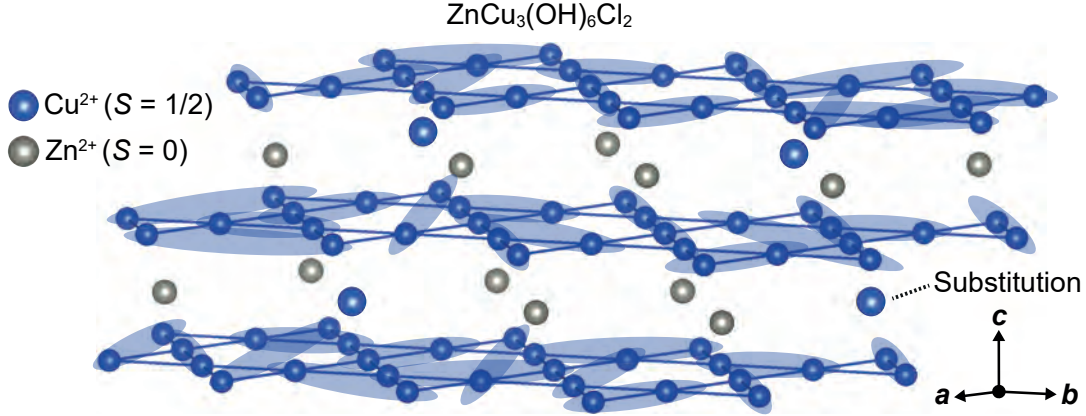


Figure 5.1: $\text{ZnCu}_3(\text{OH})_6\text{Cl}_2$ crystal lattice structure. $S = 1/2$ Cu^{2+} kagome layers are separated by nonmagnetic Zn^{2+} triangular layers. Substitution of the interlayer Zn^{2+} by Cu^{2+} exists. Substitution of the kagome Cu^{2+} by Zn^{2+} is also proposed although it is more controversial.

perfect kagome lattice with R3-m symmetry is indicated by single-crystal x-ray diffraction [90], making it one of the best realizations of the kagome $S = 1/2$ Heisenberg antiferromagnetic lattice. However, substitution between nonmagnetic Zn^{2+} and spin-1/2 Cu^{2+} exists due to their close ionic radii, as proposed by structural studies [91–94] and quasi-free spin contributions observed in DC susceptibility [95–97], specific heat [92,98–100], nuclear magnetic resonance [101–105], and so on. An exact percentage of the substitution remains to be determined. Neutron diffraction studies [91–93] propose that $\sim 30\%$ of the Zn^{2+} sites and $\sim 10\%$ of the Cu^{2+} sites are inter-substituted, meanwhile an x-ray anomalous dispersion study [93] indicates that 15% of the Zn^{2+} sites are replaced by Cu^{2+} and that the Cu^{2+} kagome plane remains intact so that the true stoichiometry is $\text{Zn}_{0.85}\text{Cu}_{3.15}(\text{OH})_6\text{Cl}_2$. Substitution percentages from different techniques and analyses range from 15% to 36% for the Zn^{2+} sites and from 0% to 10% for the Cu^{2+} sites. From now on, I will refer to the substitution-induced interlayer Cu^{2+} spins as ‘witness-spins’, for the reason explained later in Section 5.2.1.

5.1.2 Physical properties

$\text{ZnCu}_3(\text{OH})_6\text{Cl}_2$ is an insulator with the charge gap of ~ 3 eV [106], so the discussion of low-energy properties is primarily based on localized electrons. At high tempera-

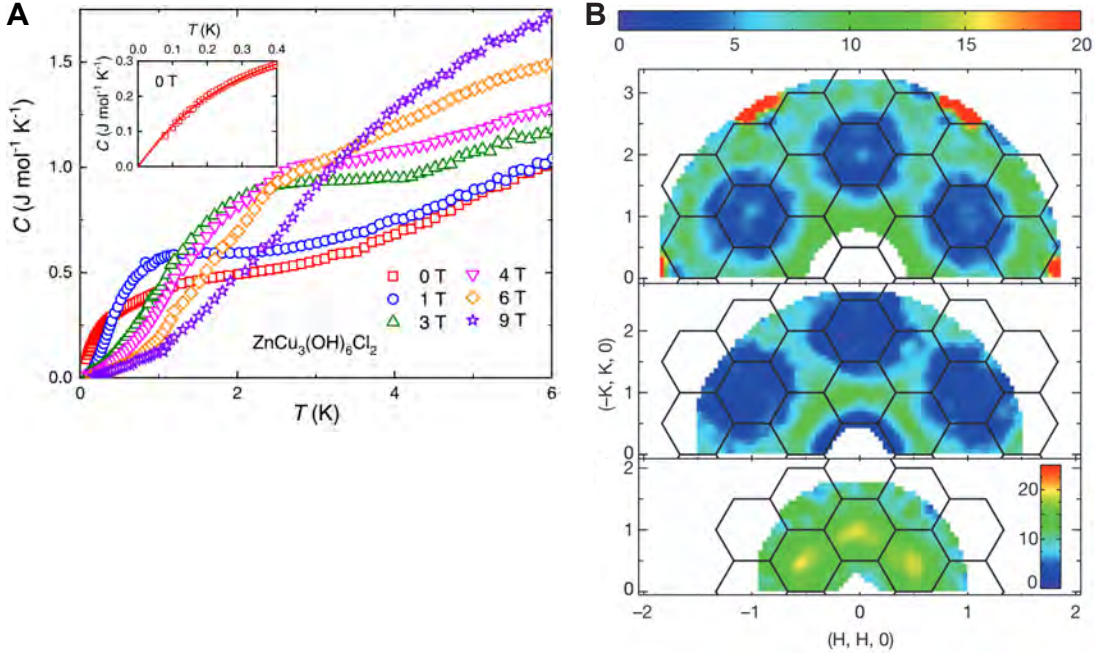


Figure 5.2: Spin liquid phenomena in $\text{ZnCu}_3(\text{OH})_6\text{Cl}_2$. (A) Specific heat that does not show a phase transition peak down to 80 mK. (B) Inelastic neutron scattering at 0.75 meV, 2.0 meV, and 6.0 meV showing diffuse excitations without a well-defined spin-wave mode. (A) is reprinted with permission from Ref. [108] Copyright (2021) by the American Physical Society. (B) is reproduced from Ref. [109] with permission from Springer Nature.

tures, the bulk DC susceptibility $\chi(T)$ [95,97] of $\text{ZnCu}_3(\text{OH})_6\text{Cl}_2$ exhibits the Curie-Weiss temperature $T_{\text{CW}} \sim -300$ K indicating the antiferromagnetic exchange of $J \sim 190$ K. At low temperatures in the range of $1 \text{ K} \leq T \leq 10 \text{ K}$, there is an additional Curie-Weiss contribution with $T_{\text{CW}} \sim -1$ K, whose magnitude corresponds to spin-1/2 witness-spins at $\sim 30\%$ of the Zn^{2+} sites [95–97]. Nuclear magnetic resonance (NMR) [101–105] observes a local susceptibility from the kagome layer, which contributes to the high-temperature bulk DC susceptibility and decreases below 100 K. The NMR [101–105] and electron spin resonance [107] studies attribute the low-temperature bulk DC susceptibility to quasi-free spins, which arise from the $\text{Cu}^{2+}/\text{Zn}^{2+}$ intersubstitution forming the reservoir of witness-spins.

$\text{ZnCu}_3(\text{OH})_6\text{Cl}_2$ is a potential spin liquid, with neither phase transition nor spin freezing definitely reported. The zero-field specific heat $C(T)$ [92, 99, 100, 108, 110] does not exhibit any phase-transition peak down to 80 mK, as shown in Fig. 5.2A. The DC susceptibility $\chi(T)$ at 0.1 T does not report a transition down to 10 mK [95].

Inelastic neutron scattering studies reveal the broad diffusive excitation spectrum in reciprocal space without a sharp spin-wave mode down to 50 mK [109,111].

Interpretation of the $\text{ZnCu}_3(\text{OH})_6\text{Cl}_2$ excitation spectrum is problematic. The low-energy diffuse scattering at 0.4 meV, located around $(HKL) = (100)$ and $(00\frac{3}{2})$, is attributed to the interlayer Cu^{2+} witness-spins. Those scatterings may be naturally explained by a nearest-neighbor antiferromagnetic spatial correlation between the interlayer spins [98,109]. The scatterings above ~ 1 meV are dominated by 2D excitations, indicating a contribution from the kagome layer [98], and resembles the simulation of randomly arranged nearest-neighbor singlets in the kagome layer [109]. While the excitation spectrum is gapless down to at least 0.13 meV [111], whether the kagome layer spin dynamics is ultimately gapped or gapless remains a mystery [104,105,112].

5.1.3 What is spin liquid state of $\text{ZnCu}_3(\text{OH})_6\text{Cl}_2$?

Different quantum magnetic ground states have been proposed for $\text{ZnCu}_3(\text{OH})_6\text{Cl}_2$. A prime candidate is the formation of a QSL state in the kagome layer. There are experimental investigations pointing to a gapless QSL [92,105,109,113], some specifying a U(1)-Dirac type [101,103,113], and also those pointing to a gapped QSL [98,104]. In addition, from the power-law behavior and the scaling law of the physical quantities, a spin liquid state close to a quantum critical point [99,110,114] or random-disordered states such as a random singlet state [32,34,100] and a Griffiths phase [110] are proposed. Thus, despite decades of study, the spin liquid state of $\text{ZnCu}_3(\text{OH})_6\text{Cl}_2$ has not been established. In an attempt to reveal the ground state of the kagome layer, here I introduce spin noise spectroscopy for the study of $\text{ZnCu}_3(\text{OH})_6\text{Cl}_2$.

5.2 Prediction of witness-spin properties with spinon-mediated interactions

5.2.1 Interlayer spins are ‘witnesses’ to kagome layer

As discussed in the previous section, 15%–36% of the interlayer $S = 0$ Zn^{2+} sites are replaced by $S = 1/2$ Cu^{2+} , and the resulting interlayer spins interact with each other. There is an antiferromagnetic correlation between nearest-neighbor interlayer spins [98], with an approximate energy scale of ~ 1 K [95]. The path of such a nearest-neighbor interaction has to cross the kagome layer, and therefore the interlayer $S = 1/2$ spins ‘witness’ the physics of the kagome layer. Hence, I will refer to the interlayer spins as ‘witness-spins’, and predict their properties.

5.2.2 Spinon-mediated interaction

Suppose the kagome layer is in a gapped QSL state, supporting gapped spinon excitations [98, 104]. Then the kagome layer should mediate spinon-mediated interaction among witness-spins [115].¹

Let us model two witness-spins $\mathbf{S}_i, \mathbf{S}_j$ at sites i, j interacting via a kagome layer, as shown in Fig. 5.3A. Each witness-spin couples to all three of their closest spins in the kagome layer, which then mediates the interaction between the witness-spins. The combined spin susceptibility between the two three-kagome-spin plaquettes can be defined as $\chi_{ij} = \sum_{a,b} \chi_{ij}^{ab}$, where the indices $1 \leq a, b \leq 3$ denote each kagome spin in the plaquette. The spinon-mediated interaction then can be described as $A\chi_{ij}\mathbf{S}_i \cdot \mathbf{S}_j$, where A is a parameter defining the overall interaction scale. Therefore, the Hamiltonian describing multiple witness-spins is

$$H = A \sum_{ij} \chi_{ij} \mathbf{S}_i \cdot \mathbf{S}_j. \quad (5.1)$$

The spin-spin susceptibility χ_{ij}^{ab} between spins in the kagome layer is calculated for a gapped $\text{Z}_2[0, \pi]\beta$ QSL, which is a leading contender for the $S = 1/2$ kagome

¹The modeling in this subsection and the Monte Carlo simulation data in the following subsection are contributed by Mitikorn (Ion) Wood-Thanan, Miguel Angel Sanchez Martinez, and Felix Flicker, with guidance from Michael R. Norman. I fitted the simulation results.

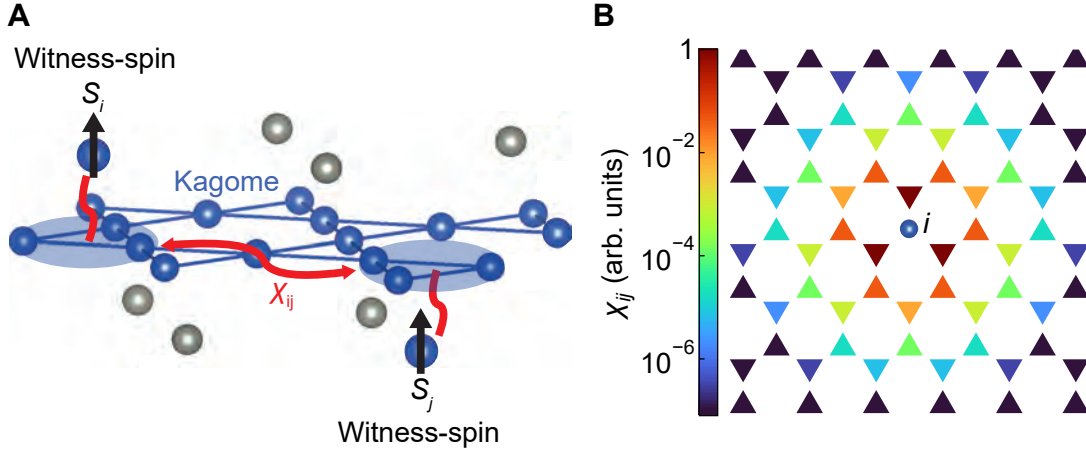


Figure 5.3: (A) Schematic of a spinon-mediated interaction between two witness-spins, mediated by a presumed quantum spin liquid state of a kagome layer. (B) Spin-spin susceptibility χ_{ij} of kagome spins for a gapped QSL, with a characteristic decay length $R_0 = 0.44d$ (d : Cu-Cu distance within the kagome layer).

Heisenberg model [116,117]. Due to the gap, χ_{ij}^{ab} is expected to decay approximately exponentially over distance $|\mathbf{R}_i^a - \mathbf{R}_j^b|$ as

$$\chi_{ij}^{ab} \propto \exp\left(-\frac{|\mathbf{R}_i^a - \mathbf{R}_j^b|}{R_0}\right). \quad (5.2)$$

The calculated χ_{ij} is visualized in Fig. 5.3B. The nearest-neighbor witness-spin interaction is antiferromagnetic, which is in line with the neutron scattering observation [98].

Two free parameters control the witness-spin Hamiltonian in Eq. 5.1: the interaction decay length R_0 and the overall interaction scale of $A\chi_{ij}$. We chose $R_0 = 0.44d$, which provides the best quantitative correspondence with the experimental ratio of the transition temperature to the Curie-Weiss temperature $T^*/T_{\text{CW}} = 0.24$ (discussed below). Then, the scale of $A\chi_{ij}$ is chosen to make the nearest-neighbor witness-spin interaction $A\chi_{\text{NN}} = 1.5$ K, so that the simulated T_{CW} of the witness-spin is consistent with the experimental value $T_{\text{CW}} = -1.1$ K (discussed below).

5.2.3 Monte Carlo simulation of witness-spins with spinon-mediated interactions

Simulation setup

A Monte Carlo (MC) simulation was performed to explore the properties of witness-spins governed by the spinon-mediated interactions in Eq. 5.1. The full lattice consists of $45 \times 15 \times 12$ Zn sites, where each site is occupied by spin-1/2 with a probability of 33%. The occupation percentage 33% is chosen based on the single crystal x-ray diffraction and low-temperature magnetic susceptibility of the $\text{ZnCu}_3(\text{OH})_6\text{Cl}_2$ single crystal used in my experiment (Section 5.3.1), and is consistent with the existing reports [91–93, 96, 97]. The resulting number of spin-occupied sites N is on average 2673, and N MC updates make up one MC step. The boundary condition is periodic in all directions. While the physical spins are quantum Heisenberg $S = 1/2$, a simplified model of classical Ising spins with easy c -axis is used in this simulation.² Accordingly, the Hamiltonian is simplified to the interactions among Ising spins

$$H = A \sum_{ij} \chi_{ij} S_i S_j. \quad (5.3)$$

As discussed in the previous section, the Hamiltonian parameters are chosen to be $R_0 = 0.44d$ and $A\chi_{\text{NN}} = 1.5$ K.

Spin Noise Prediction

The witness-spin spin noise is simulated for a temperature range from $T_{\text{ini}} = 500$ mK to $T_{\text{fin}} = 100$ mK in steps of $\Delta T = 20$ mK. A random site-occupation configuration is first prepared, as each site is occupied by a spin-1/2 with the probability of 33%. Starting from a random spin-direction configuration, the system is initially equilibrated at T_{ini} with 1000 MC steps. Then, consecutively from high to low

²The classicality is an assumption required to run a simple classical Monte Carlo simulation. While the classicality assumption does not have a clear physical justification, classical spins can also feel the spinon-mediated interactions, the key feature of the model, and are expected to provide useful information. The Ising assumption is again primarily an approximation. However, small anisotropies are known to cause Ising-like behavior in classical Heisenberg spin glasses [118] and could partially justify the Ising assumption.

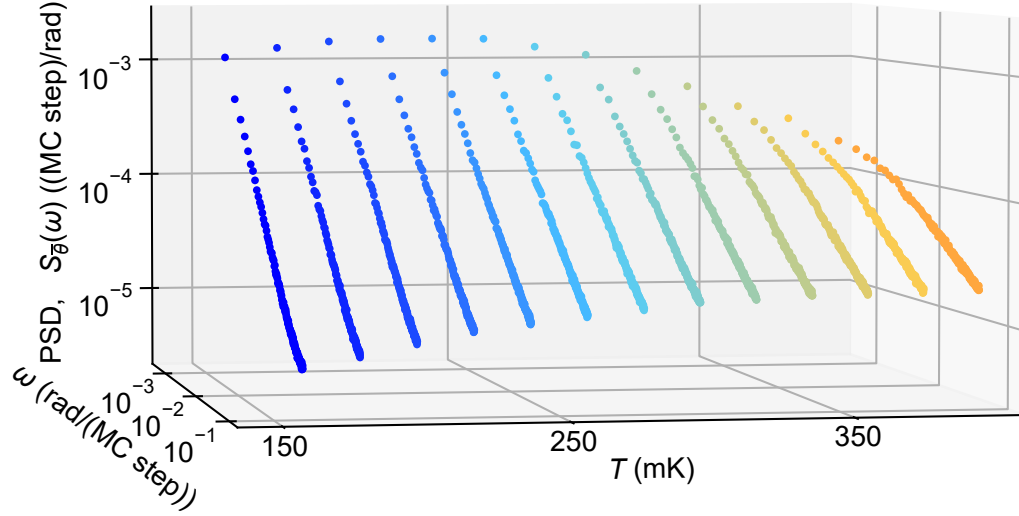


Figure 5.4: Power spectral density $S_{\bar{\theta}}(\omega)$ of simulated witness-spin noise $\bar{\theta}(t)$ with spinon-mediated interactions for fourteen selected temperatures. The power spectral density is nearly scale-invariant at all the temperatures with a temperature-dependent slope.

temperatures, the spin noise is simulated at each temperature T with the following procedure: 1000 MC steps are performed for equilibration at T , 10000 MC steps are performed to record the MC-time sequence $\theta_{\text{tot}}(t_k, T)$ of the total spin $\theta_{\text{tot}} = \sum_i S_i$, and then the simulation proceeds to the next temperature.³ The average spin noise $\bar{\theta}(t_k, T)$ is readily obtained as

$$\bar{\theta}(t_k, T) = \frac{1}{N} \theta_{\text{tot}}(t_k, T). \quad (5.4)$$

The data at each temperature has the length of $\Gamma = 10000$ MC step consisting of the $K = 10000$ points ($0 \leq t_k \leq (K-1)\Delta t$), with the MC-time interval of $\Delta t = 1$ MC step. To investigate the spin noise property, the power spectral density (PSD) $S_{\bar{\theta}}(\omega_j, T)$ is calculated using the formula

$$S_{\bar{\theta}}(\omega_j, T) = \frac{1}{\pi\Gamma} \left| \Delta t \sum_{k=0}^{K-1} e^{-i\omega_j t_k} \bar{\theta}(t_k, T) \right|^2, \quad (5.5)$$

where $\omega_j/(2\pi) = j/\Gamma$ ($0 \leq j \leq K/2$). The frequency resolution is $\Delta\omega/(2\pi) = 10^{-4}$ (MC step)⁻¹. The PSDs from 10 independent MC runs for each of the 128

³Here, I use the symbol θ_{tot} to represent the total spin, so that it will not be confused with the power spectral density symbol $S(\omega)$.

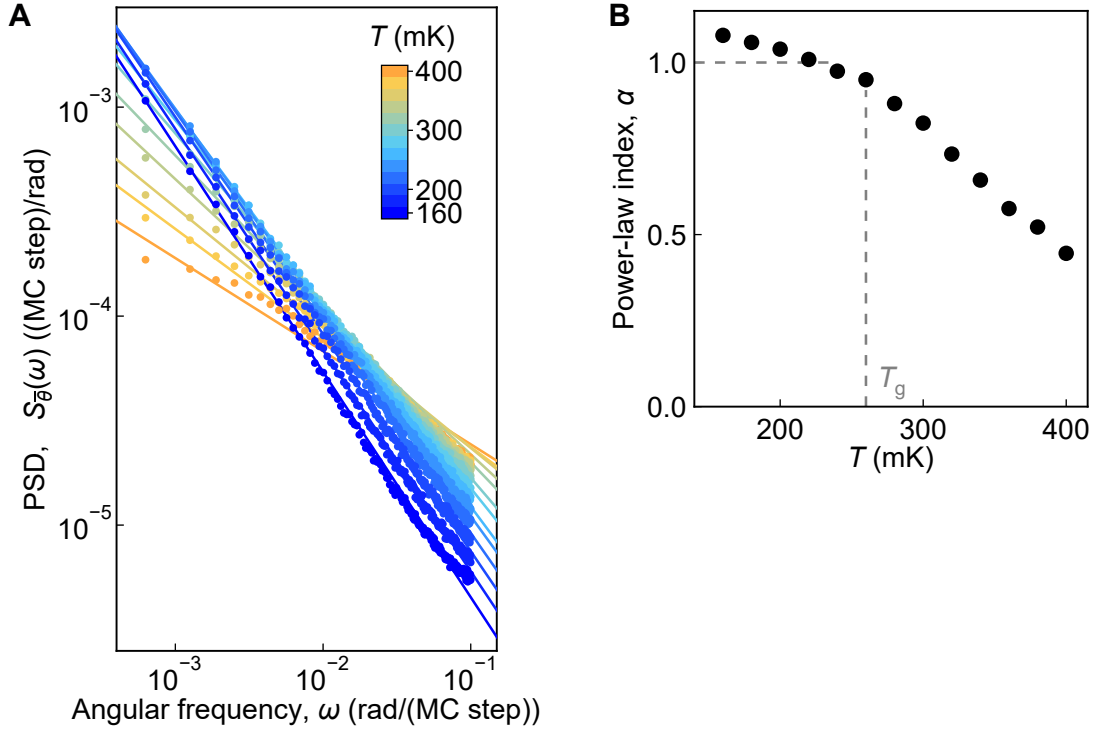


Figure 5.5: (A) Fitting of the power spectral density $S_{\bar{\theta}}(\omega, T) \propto \omega^{-\alpha(T)}$ of the witness-spin noise in the frequency range $10^{-3} (\text{MC step})^{-1} \leq \omega/(2\pi) \leq 1.6 \times 10^{-1} (\text{MC step})^{-1}$ (B) Obtained frequency-power-law exponent $\alpha(T)$, saturating at ~ 1 around $T_g = 260$ mK.

different site-occupation configuration are all averaged. The 3D plot of the obtained PSD is shown in Fig. 5.4. The PSD takes a nearly scale-invariant form at each temperature. The PSD slope becomes more steep as the temperature decreases.

The frequency-power-law exponent of the scale-invariant PSD is examined. As shown in Fig. 5.5A, the fitting of the PSD $S_{\bar{\theta}}(\omega, T) \propto \omega^{-\alpha(T)}$ is performed in the range $1\Delta\omega \leq \omega \leq 160\Delta\omega$. The obtained exponent $\alpha(T)$ is shown in Fig. 5.5B. $\alpha(T)$ grows upon cooling, saturating at ~ 1 around $T_g = 260$ mK.

DC susceptibility prediction

The witness-spin DC susceptibility $\chi(T)$ is simulated for three temperature ranges: from $T_{\text{ini}} = 10000$ mK to $T_{\text{fin}} = 2000$ mK in steps of $\Delta T = 200$ mK; $T_{\text{ini}} = 2000$ mK, $T_{\text{fin}} = 500$ mK, $\Delta T = 50$ mK; and $T_{\text{ini}} = 500$ mK, $T_{\text{fin}} = 50$ mK, $\Delta T = 10$ mK. In the same process as the spin noise simulation above, the evolutions of the total spin $\theta_{\text{tot}} = \sum_i S_i$ and its squared value θ_{tot}^2 are recorded at each temperature.

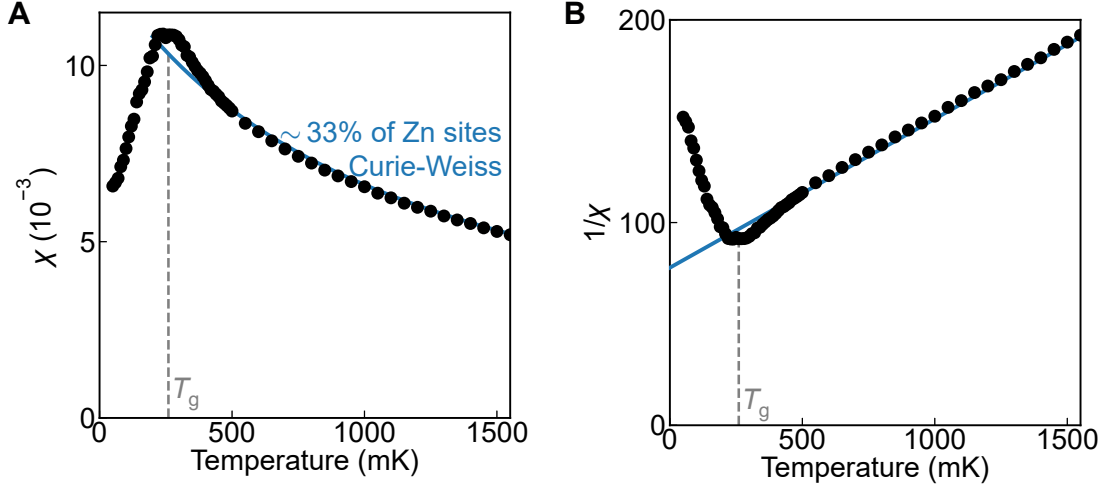


Figure 5.6: (A) Simulated witness-spin DC susceptibility $\chi(T)$ with spinon-mediated interactions, showing a transition cusp at $T_g = 260$ mK. (B) Inverse plot $1/\chi(T)$. The blue line is the Curie-Weiss fitting of the $2 \text{ K} \leq T \leq 10 \text{ K}$ data, which yields a Curie-Weiss temperature $T_{\text{CW}} = -1.15$ K.

The DC susceptibility per volume in $\text{ZnCu}_3(\text{OH})_6\text{Cl}_2$ is obtained using the formula

$$\chi(T) = \mu_0 (g\mu_B)^2 \rho_V \frac{1}{k_B T} \frac{\overline{\theta_{\text{tot}}^2} - \overline{\theta_{\text{tot}}}^2}{N}. \quad (5.6)$$

Here, $\overline{\theta_{\text{tot}}^2}$ and $\overline{\theta_{\text{tot}}}$ represent the average over the 10000 MC steps. μ_0 , g , μ_B , ρ_V , and k_B are the permeability of vacuum, the electron g -factor, the Bohr magneton, the number density of witness-spins in $\text{ZnCu}_3(\text{OH})_6\text{Cl}_2$, and the Boltzmann constant, respectively. During the 10000 MC steps, the total energy of the system E is also recorded to calculate the specific heat $C(T) \propto (\overline{E^2} - \overline{E}^2) / T^2$.

The simulation is repeated for 128 different site-occupation configurations, and $\chi(T)$ is averaged over them. The obtained witness-spin DC susceptibility $\chi(T)$ in the spinon-mediated interaction simulation is shown in Fig. 5.6A. It shows a sharp cusp at $T_g = 260$ mK. As the simulated specific heat does not show any sharp transition peak, the cusp in the DC susceptibility is not a transition to an antiferromagnetic order. The Curie-Weiss fitting of the high-temperature regime $2 \text{ K} \leq T \leq 10 \text{ K}$, shown in Fig. 5.6B, yields $T_{\text{CW}} = -1.15$ K.

The model reveals another key point: simple nearest-neighbor-only witness-spin interactions will not generate the DC susceptibility cusp. With the 33% occupation

probability, $\sim 10\%$ of the witness-spins are isolated without any nearest-neighbor witness-spins. They continue to behave paramagnetically down to low temperatures and generate diverging DC susceptibility.

In summary, witness-spins with the spinon-mediated interactions, simulated with the Hamiltonian in Eq. 5.3 ($A\chi_{\text{NN}} = 1.5$ K, $R_0 = 0.44d$, and 33% site-occupation), have the following properties. The spin noise PSD takes a scale-invariant form. The PSD slope grows upon cooling, saturating around T_g to the frequency power law ω^{-1} . DC susceptibility shows a cusp at $T_g = 260$ mK, with $T_{\text{CW}} \sim -1.15$ K. The transition at T_g is not an antiferromagnetic ordering transition, as a sharp peak is absent in the specific heat, and is attributable to a spin glass transition [35, 36].

5.3 Experiment

To test the spinon-mediated interaction predictions, which derive from the hypothesis that the kagome layer is in a quantum spin liquid, I experimentally measured DC susceptibility and spin noise of $\text{ZnCu}_3(\text{OH})_6\text{Cl}_2$.

5.3.1 Sample preparation

$\text{ZnCu}_3(\text{OH})_6\text{Cl}_2$ single crystals were synthesized by a recrystallization method as described in Ref. [119].⁴ Powder of ZnCl_2 , CuO , and H_2O was mixed with a ratio of 2.015 g : 0.235 g : 4.5 mL in a quartz tube, which was sealed under vacuum. The quartz tube was laid horizontally in a three-zone gradient furnace, with the hot and cold ends set at 180 °C and 160 °C, respectively. After 3 months, mm-scale single crystals were obtained.

Figure 5.7A shows photos of three $\text{ZnCu}_3(\text{OH})_6\text{Cl}_2$ single crystals from the same growth. I have measured two c -axis samples (Sample 1 and 2) and one a -axis sample (Sample 3). Sample 1 was obtained by polishing down Sample 1' so that it fits into the astatic-coil spectrometer (Fig. 3.2C) for susceptibility measurements.

⁴ $\text{ZnCu}_3(\text{OH})_6\text{Cl}_2$ single crystals synthesized by Pascal Puphal were used in the experiment. I performed the same synthesis with the support of Pascal Puphal, but the crystals I synthesized were smaller at 1 mm scale due to limited waiting time for recrystallization.

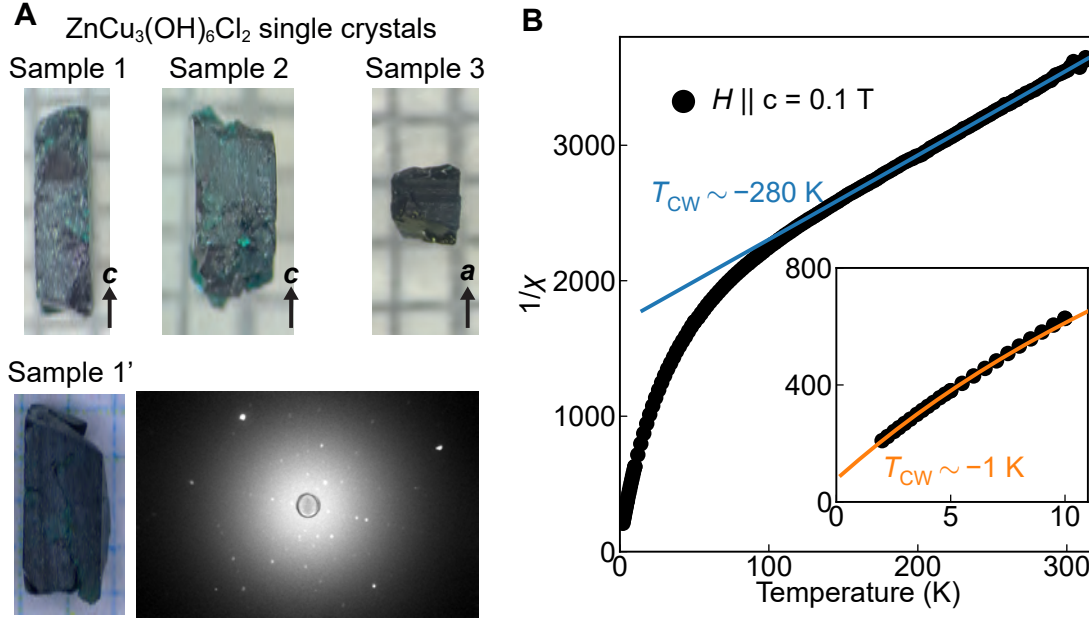


Figure 5.7: (A) Photos of three $\text{ZnCu}_3(\text{OH})_6\text{Cl}_2$ single crystals. Sample 1 is obtained by polishing down Sample 1'. The c -axis of Sample 1 and Sample 2 is identified to be the long direction of the bar shape. The Laue diffraction image of Sample 1' shows clear Bragg peaks. (B) DC susceptibility of Sample 1' measured by an MPMS. The solid lines are Curie-Weiss fitting results by $\chi = \chi_0 + \frac{C_{\text{Curie}}}{T - T_{\text{CW}}}$. Fitting of a high-temperature regime $150 \text{ K} \leq T \leq 320 \text{ K}$ (blue) yields $T_{\text{CW}} = -280 \text{ K}$, $C_{\text{Curie}} = 0.165 \text{ K}$, and $\chi_0 = -5 \times 10^{-6}$. Fitting of a low-temperature regime $2 \text{ K} \leq T \leq 6 \text{ K}$ (orange) range yields $T_{\text{CW}} = -1.1 \text{ K}$, $C_{\text{Curie}} = 0.013 \text{ K}$, and $\chi_0 = 4.2 \times 10^{-4}$.

The stoichiometry of Zn/Cu ratio was found to be 0.97:3.03 (± 0.02) in Sample 1' from inductively coupled plasma mass spectrometry.⁵ The lattice structure was confirmed by x-ray Laue diffraction in Sample 1' that shows clear Bragg peaks, as shown in Fig. 5.7A. A single crystal x-ray diffraction measurement indicates that 32.5% of the Zn^{2+} sites and 10.8% of the Cu^{2+} sites are inter-substituted, which is comparable to the value obtained by the past neutron diffraction studies [91–93].⁶ Figure 5.7B shows the DC susceptibility of Sample 1' measured in an MPMS (Quantum Design). Fitting by the Curie-Weiss law

$$\chi = \chi_0 + \frac{C_{\text{Curie}}}{T - T_{\text{CW}}} \quad (5.7)$$

in the temperature range $2 \text{ K} \leq T \leq 6 \text{ K}$ gives $T_{\text{CW}} = -1.1 \text{ K}$ and $C_{\text{Curie}} = 0.013 \text{ K}$, corresponding to $S = 1/2$ at $\sim 33\%$ of the Zn sites. This number is

⁵The inductively coupled plasma mass spectrometry was performed by Pascal Puphal.

⁶The single crystal x-ray diffraction was performed by Jürgen Nuss.

comparable to the past DC susceptibility studies [96, 97], and is also consistent with the aforementioned x-ray/neutron diffraction studies.

5.3.2 Spin noise measurement and long-term evolution study

The spin noise measurements were performed using a single coil connected to the SQ1200 SQUID (Star Cryoelectronics) in the dilution refrigerator. The design of the SQUID spin noise spectrometer is detailed in Chapter 3, with the circuit diagram shown in Fig. 3.4A. Here, I only summarize the important parameters: the pickup coil turns $N_p = 19$, the pickup coil inductance $L_p = 0.56 \mu\text{H}$, the input coil inductance $L_i = 1.30 \mu\text{H}$, the inverse input-coil-SQUID mutual inductance $1/M_i = 0.13 \mu\text{A}/\Phi_0$, and the SQUID transfer function $g_{\text{SQUID}} = 10.1 \text{ V}/\Phi_0$. Three 0.2 mm-diameter silver wires were glued to the $\text{ZnCu}_3(\text{OH})_6\text{Cl}_2$ single crystal for thermalization.

The spin noise data of $\text{ZnCu}_3(\text{OH})_6\text{Cl}_2$ (Sample 1) consists of SQUID output voltage recordings of a duration 1000 s and a sampling rate 20 kSa/s (a time interval of 50 μs), at temperatures from 150 mK to 400 mK in steps of 10 mK. The SQUID output voltage first went through a 5 kHz, 4-pole low-pass filter, and then an SR560 preamplifier with an appropriate gain and 0.03 Hz 6 dB/oct high-pass and 30 kHz 6 dB/oct low-pass filters, before was recorded by a Moku:Pro analog-to-digital converter. The temperature was controlled by a heater with a stability of 0.5 mK, and the sample was thermalized for at least 20 mins at the target temperature before the measurements. The SQUID background noise was measured for a free-standing coil without a sample.

The recorded SQUID output voltage $V(t, T)$ at different temperatures is converted into the flux noise $\Phi(t, T)$ at the pickup coil and the magnetization noise $M(t, T)$ using Eqs. 2.102 and 2.103. Figure 5.8 shows the measured $\text{ZnCu}_3(\text{OH})_6\text{Cl}_2$ flux noise $\Phi(t, T)$ at 260 mK for a 10-second duration, after filtering out the high-frequency components below 0.05 Hz and above 100 Hz (Appendix B). The

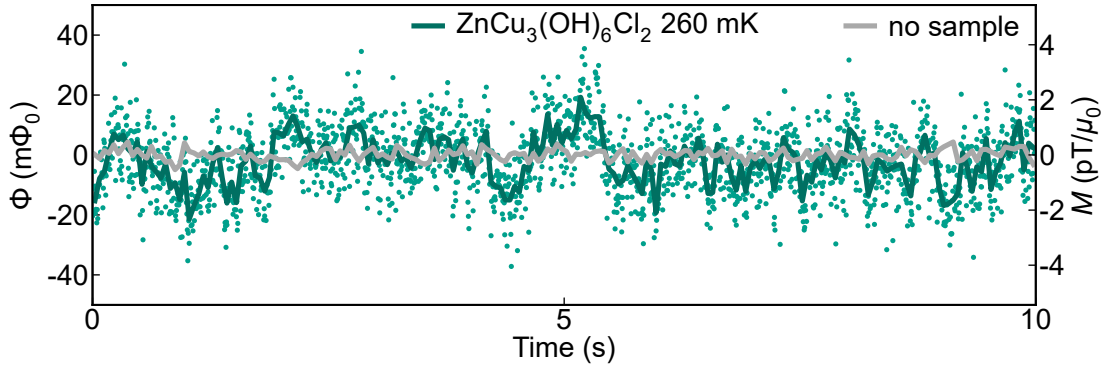


Figure 5.8: Measured $\text{ZnCu}_3(\text{OH})_6\text{Cl}_2$ flux noise $\Phi(t, T)$ at 260 mK shown for a 10-second duration (light green dots). The frequency components below 0.05 Hz and above 100 Hz are filtered out. For visual clarity, the plotted points are down-sampled to every 5 ms. The box-car average for every 50 ms is overlaid (dark green), which is highly distinct from the identically averaged signal of the empty coil (gray). The corresponding magnetization noise $M(t, T)$ is shown on the right-hand axis.

$\text{ZnCu}_3(\text{OH})_6\text{Cl}_2$ noise is clearly distinct from the empty-coil background, and exhibits slow fluctuations on a timescale of seconds. The $\sim 20 \text{ m}\Phi_0$ flux noise fluctuation here corresponds to the $\sim 2 \text{ pT}/\mu_0$ magnetization fluctuation.

In the same experimental setup, a long-term evolution of the spin state in $\text{ZnCu}_3(\text{OH})_6\text{Cl}_2$ was explored. Sample 1 was first thermalized for 1 hour at 400 mK, then the temperature was rapidly dropped to a lower temperature T_{low} , taking only a short time of ~ 3 minutes. After 20 mins of thermalization at T_{low} , the SQUID output voltage was recorded for 10^5 s (~ 28 hours) with 1 kSa/s. Separate measurements were performed for five T_{low} from 150 mK to 350 mK in steps of 50 mK. The SR560 preamplifier filter was set to 3 kHz 12 dB/oct low-pass and no high-pass so that the DC component evolution of the SQUID output voltage could be tracked. The result of this long-term spin noise measurement is later analyzed in Fig. 5.13.

5.3.3 High-precision sub-microTesla DC susceptibility measurements

The DC susceptibility measurements were performed using an astatic coil connected to the SP550 SQUID (Quantum Design) in the dilution refrigerator. The design of the SQUID susceptometer is detailed in Chapter 3, with the circuit diagram shown

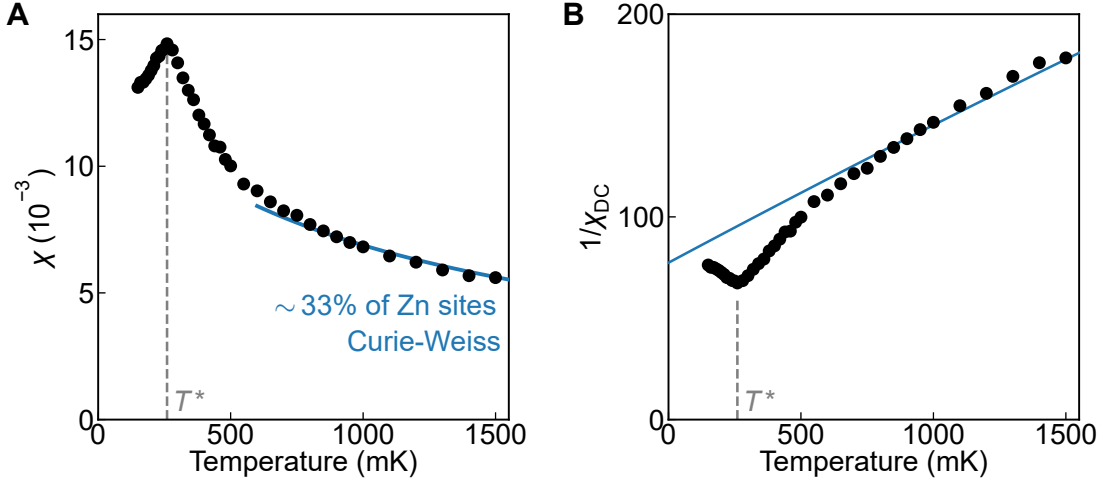


Figure 5.9: (A) Measured DC susceptibility $\chi(T)$ of $\text{ZnCu}_3(\text{OH})_6\text{Cl}_2$ in zero-field cooling condition, showing a cusp at 260 mK. Tiny field of 50 nT order was used. (B) Inverse DC susceptibility $1/\chi(T)$. The blue curve represents the extension of the Curie-Weiss curve obtained by a fitting in a higher-temperature range $2 \text{ K} \leq T \leq 6 \text{ K}$. Below 1 K, the measured susceptibility starts showing a more complex temperature dependence.

in Fig. 3.4B. Here, I only summarize the important parameters: the pickup coil turns $N_p = 8$, the pickup coil inductance $L_p = 0.71 \mu\text{H}$, the input coil inductance $L_i = 1.74 \mu\text{H}$, the inverse input-coil-SQUID mutual inductance $1/M_i = 0.19 \mu\text{A}/\Phi_0$, the SQUID transfer function $g_{\text{SQUID}} = 0.73 \text{ V}/\Phi_0$, and the field coil circuit resistance 222 k Ω . The calibrated astatic coil imbalance was about 10% for the specific astatic coil used in this experiment. A 0.1 mm-diameter silver wire was glued to the $\text{ZnCu}_3(\text{OH})_6\text{Cl}_2$ single crystal for thermalization.

The measurements were performed for Sample 1 from 100 mK to 400 mK in steps of 10 mK, from 400 mK to 1000 mK in steps of 50 mK, and 1000 mK to 3000 mK in steps of 100 mK. The sample was thermalized for at least 20 minutes at the target temperature before the measurements. At each temperature, the SQUID output voltage was recorded while a DC field $\mu_0 H$ was swept over $0 \text{ nT} \rightarrow -55 \text{ nT} \rightarrow 55 \text{ nT} \rightarrow -55 \text{ nT} \rightarrow 0 \text{ nT}$ in steps of 1.1 nT (zero-field cooling). The voltage at each field $V(H; T)$ was converted to the magnetization $M(H; T)$ using Eq. 2.103, and a fitting $M(H; T) = \chi(T)H$ yields the DC susceptibility $\chi(T)$. The coil imbalance contribution is subtracted so that the measured $\chi(T)$ becomes consistent with the MPMS result (Fig. 5.7B) at the overlapping temperatures.

The measured DC susceptibility is shown in Fig. 5.9A. The DC susceptibility shows a clear cusp at $T^* = 260$ mK. A Curie-Weiss fitting result in the higher temperature regime $2 \text{ K} \leq T \leq 6 \text{ K}$ naturally captures the DC susceptibility behavior down to 1 K. However, the temperature dependence becomes more complex below 1 K, as shown more clearly in the inverse susceptibility in Fig. 5.9B.

5.4 Experimental Analysis

5.4.1 Spin noise analysis

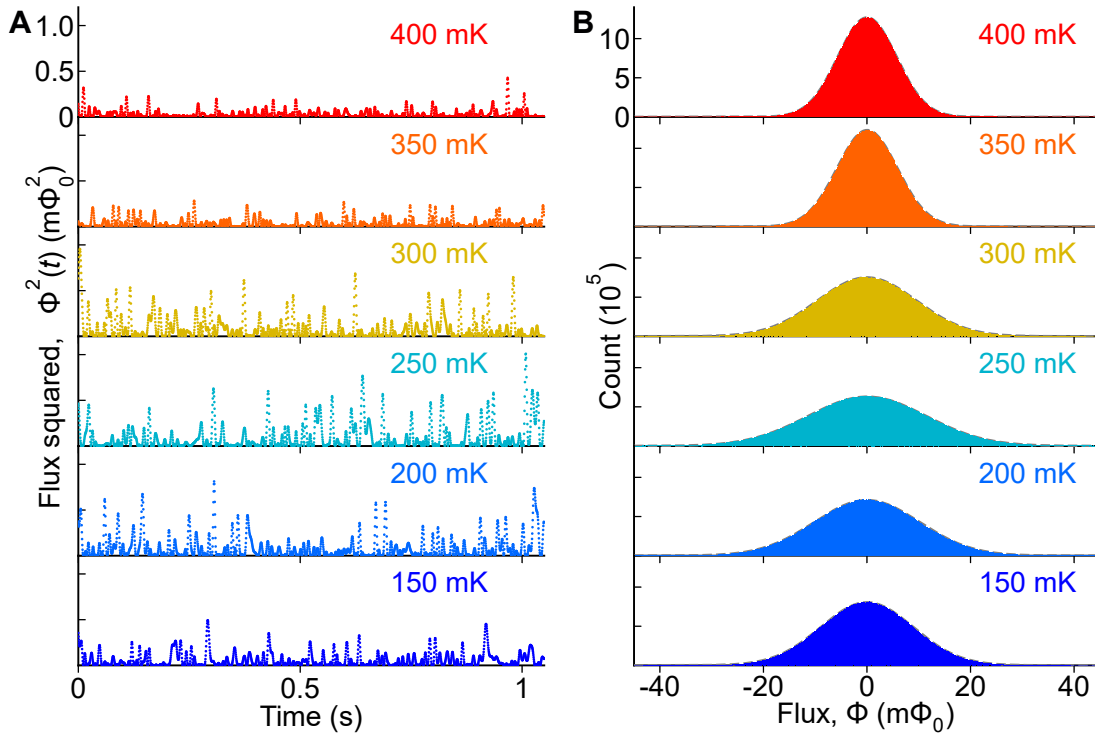


Figure 5.10: (A) Measured squared flux noise $\Phi^2(t, T)$ of $\text{ZnCu}_3(\text{OH})_6\text{Cl}_2$ shown for a one-second duration at six selected temperatures. For visual clarity, $\Phi(t, T)$ is down sampled so that the plotted time interval is $500 \mu\text{s}$. The frequency components below 0.05 Hz and above 100 Hz are filtered out. (B) Distribution of flux noise $\Phi(t, T)$ at the corresponding temperatures, each of which follows a Gaussian distribution with a temperature-varying width.

The measured $\text{ZnCu}_3(\text{OH})_6\text{Cl}_2$ spin noise exhibits a clear temperature dependence. Fig. 5.10A shows the squared flux noise $\Phi^2(t, T)$ at six selected temperatures. The noise at 400 mK is small and is dominated by the background SQUID noise. The intense noise from $\text{ZnCu}_3(\text{OH})_6\text{Cl}_2$ rapidly grows upon cooling, maximizing at

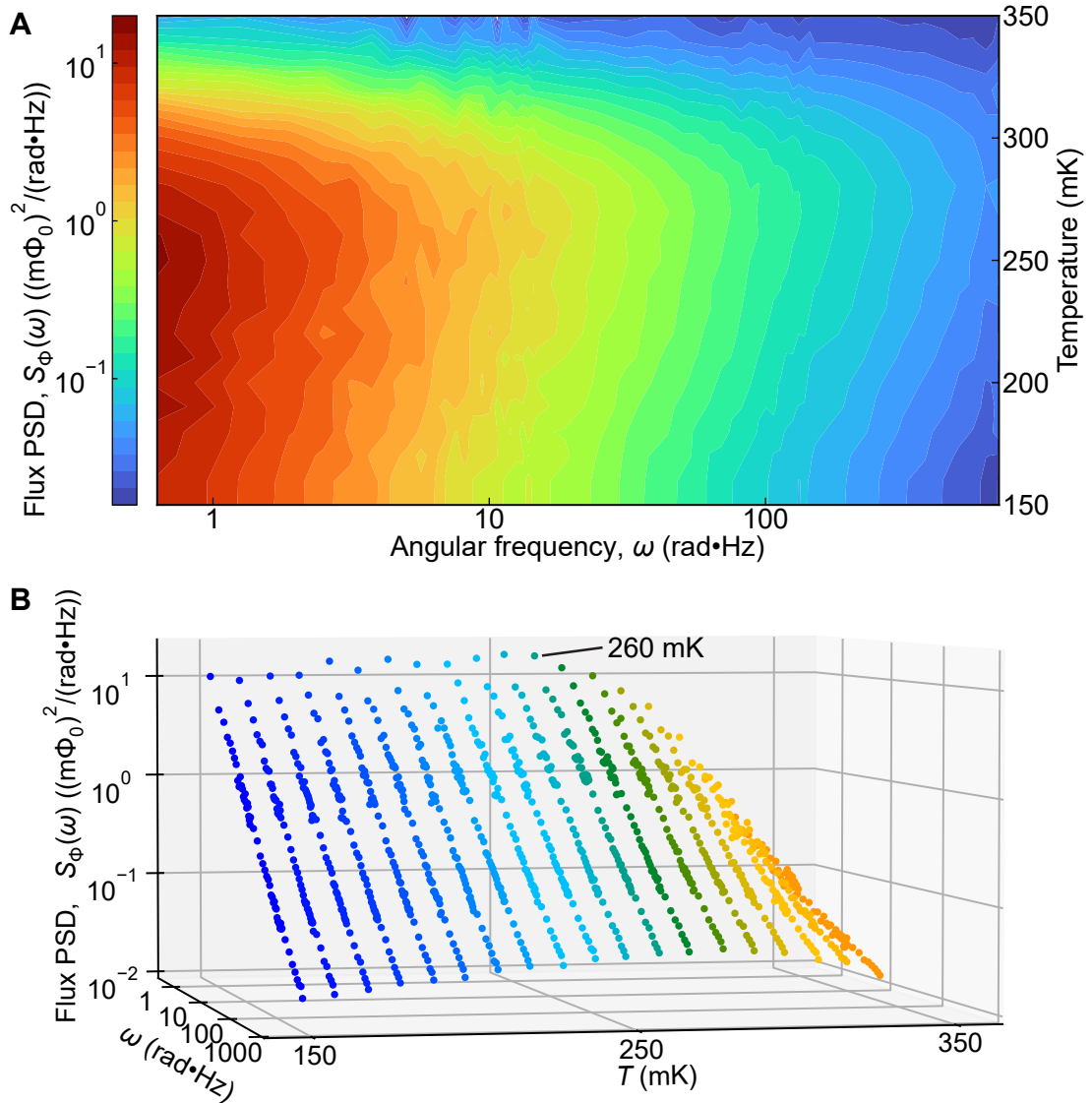


Figure 5.11: Power spectral density $S_\Phi(\omega_j, T)$ of the measured $\text{ZnCu}_3(\text{OH})_6\text{Cl}_2$ flux noise $\Phi(t_k, T)$ from 150 mK to 350 mK. The empty-coil background contribution is subtracted. (A) The contour plot. The power spectral density shows intense low-frequency fluctuations at least down to $\omega/(2\pi) = 0.1$ Hz. (B) The 3D plot. The power spectral density is scale-invariant with a temperature-dependent slope.

250 mK, then gently decreases. Such temperature dependence is also noticeable in the flux noise distribution histograms shown in Fig. 5.10B. The distribution rapidly broadens down to 250 mK, and then slowly narrows below that temperature. The distribution is well fit by a Gaussian curve at all the temperatures.

Next, the power spectral density (PSD) $S_\Phi(\omega_j, T)$ is calculated to investigate the noise property in more detail. As in the $\text{Ca}_{10}\text{Cr}_7\text{O}_{28}$ noise data in Chapter 4,

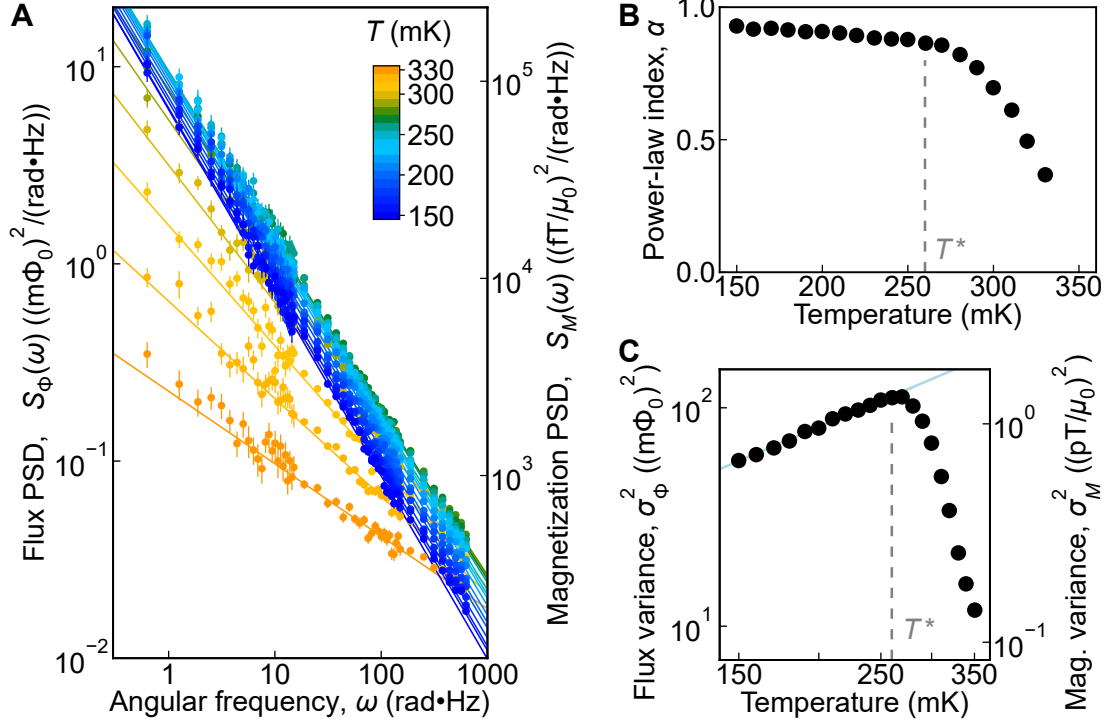


Figure 5.12: (A) Fitting of the $\text{ZnCu}_3(\text{OH})_6\text{Cl}_2$ flux noise power spectral density $S_{\Phi}(\omega, T) \propto \omega^{-\alpha(T)}$ in the range $0.1 \text{ Hz} \leq \omega/(2\pi) \leq 100 \text{ Hz}$. The empty-coil background is subtracted. The error bars are given by the standard error of segments-averaging. The corresponding value of magnetization noise power spectral density $S_M(\omega_j, T)$ is shown on the right-hand axis. (B) The obtained frequency-power-law exponent $\alpha(T)$, which shows a clear temperature dependence change around $T^* = 260 \text{ mK}$. (C) Variance $\sigma_{\Phi}^2(T)$ of the measured $\text{ZnCu}_3(\text{OH})_6\text{Cl}_2$ flux noise $\Phi(t_k, T)$, calculated after filtering out the fluctuations below 0.05 Hz and above 100 Hz . The background contribution is subtracted. The variance peaks at $T^* \sim 260 \text{ mK}$ and diminishes approximately as $T^{1.2}$ (blue line). The corresponding value of magnetization noise $\sigma_M^2(T)$ is shown on the right-hand axis.

each time sequence of the flux noise $\Phi(t_k, T)$ has the total duration of $\Gamma = 1000 \text{ s}$ with the time interval of $\Delta t = 50 \mu\text{s}$. Hence, there are $K = 2 \times 10^7$ data points ($0 \leq t_k \leq (K - 1)\Delta t$). The PSD is calculated from the formula

$$S_{\Phi}(\omega_j, T) = \frac{1}{\pi\Gamma} \left| \Delta t \sum_{k=0}^{K-1} e^{-i\omega_j t_k} \Phi(t_k, T) \right|^2, \quad (5.8)$$

where $\omega_j/(2\pi) = j/\Gamma$ ($0 \leq j \leq K/2$). PSDs with the resolution of $\Delta\omega/(2\pi) = 10^{-1}, 10^0, 10^1 \text{ Hz}$ are calculated from the $P = 10^2, 10^3, 10^4$ split segments, respectively, as detailed in Appendix B. The PSD shows intense low-frequency fluctuations down to at least $\omega/(2\pi) \sim 0.1 \text{ Hz}$, as shown in the contour plot in Fig. 5.11A. The PSD is scale-invariant with a temperature-dependent slope, as is visible in

the 3D plot in Fig. 5.11B.

There is a clear transition at $T^* = 260$ mK in the PSD slope. Fitting of the scale-invariant PSD $S_\Phi(\omega, T) \propto \omega^{-\alpha(T)}$ in the range $0.1 \text{ Hz} \leq \omega/(2\pi) \leq 100 \text{ Hz}$ is shown in Fig. 5.12A. The obtained frequency power-law exponent $\alpha(T)$ in Fig. 5.12B shows a transition around $T^* = 260$ mK. From a value as small as ~ 0.4 at high temperature, $\alpha(T)$ rapidly grows to a value close to 1.0 upon cooling. Below $\sim T^*$, $\alpha(T)$ stabilizes and gently approaches 1.0. The transition at $T^* = 260$ mK is also clearly visible in the noise power. The variance $\sigma_M^2(T)$ is calculated from the noise data after filtering out the fluctuations below 0.05 Hz and above 100 Hz (Appendix B).

$$\sigma_\Phi^2(T) = \frac{1}{K} \sum_{k=0}^{K-1} \Phi^2(t_k, T) - \left(\frac{1}{K} \sum_{k=0}^{K-1} \Phi(t_k, T) \right)^2. \quad (5.9)$$

The variance is plotted in Fig. 5.12C after subtracting the background contribution. The variance rapidly grows down to $\sim T^*$, below which it diminishes approximately as $T^{1.2}$.

5.4.2 Discovery of witness-spin aging at $T < T^*$

To explore a long-term evolution of the spin state in $\text{ZnCu}_3(\text{OH})_6\text{Cl}_2$, I analyze the 10^5 s spin noise data. As explained in Section 5.3.2, after the sample was thermalized for 1 hour at a high temperature 400 mK, the temperature was suddenly dropped to T_{low} in ~ 3 mins, and then the spin noise was measured. Firstly, the variance is calculated for every 1000 s segments, after the frequency components above 0.1 Hz are filtered out. As shown in Fig. 5.13A, the variance has an extra contribution in the first 10^4 s that disappears over time. This long-term evolution of the variance is observed from 150 mK to 250 mK, the temperatures below $T^* = 260$ mK. At high temperatures $T > T^*$, such an evolution of variance is not visible. Next, the time evolution of the DC component of the flux, averaged for every 100 s, is plotted in Fig. 5.13B. The DC component can be attributed to the response of $\text{ZnCu}_3(\text{OH})_6\text{Cl}_2$ to a small fixed DC magnetic field, which is trapped in the shielded environment of the spin noise spectrometer. Below T^* ,

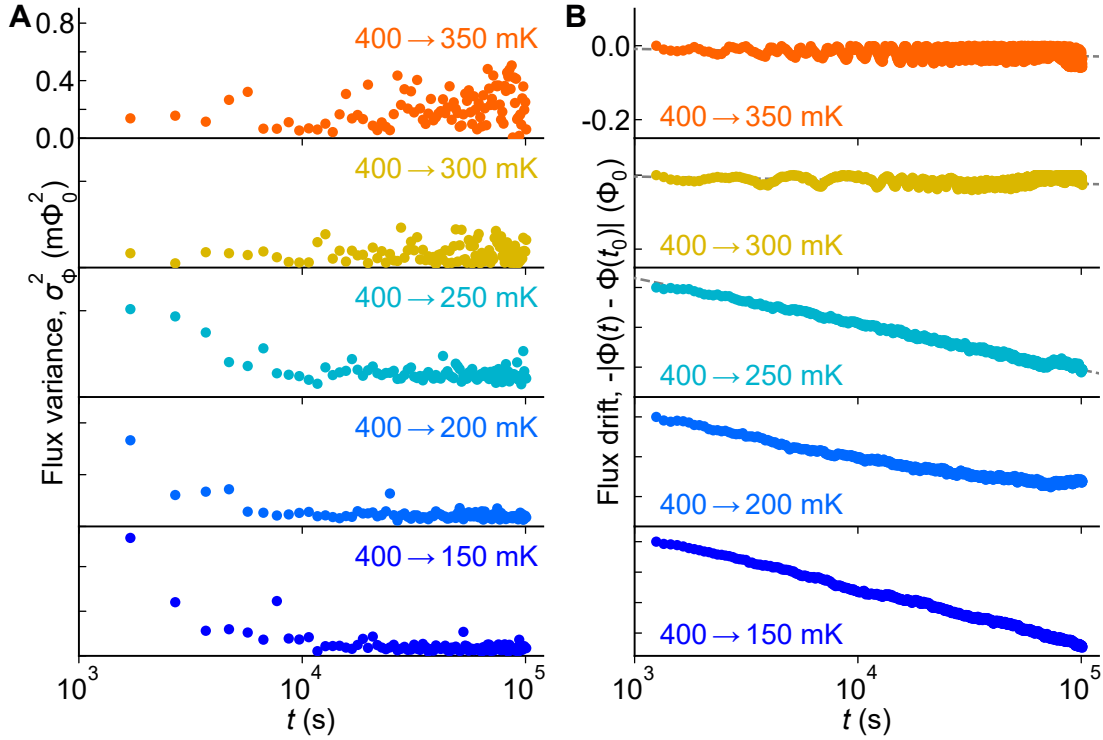


Figure 5.13: (A) Time evolution of the flux noise variance $\sigma_{\Phi}^2(T)$ after the temperature is suddenly dropped from a thermalized condition at 400 mK. Each data point is calculated from every 1000 s time-sequence segments after the frequency components above 0.1 Hz are filtered out. Below $T^* = 260$ mK, there is an extra variance contribution in the first 10000 s that disappears over time. At high temperatures $T > T^*$, such a contribution is absent. (B) Time evolution of the average flux after the temperature is suddenly dropped from a thermalized condition at 400 mK. The average flux, attributed to the response of $\text{ZnCu}_3(\text{OH})_6\text{Cl}_2$ to a small trapped DC field, shows a logarithmic evolution (gray dashed line) below T^* . No such evolution exists at high temperatures $T > T^*$. Weak oscillations of the signal observed at all temperatures are likely due to small temperature fluctuations.

there is a clear long-term evolution of the DC component lasting for 10^5 s. The evolution is logarithmic and is different from an exponential evolution expected for a typical thermalization process. At high temperatures $T > T^*$, such a logarithmic long-term evolution is absent.

Thus, the spin state of $\text{ZnCu}_3(\text{OH})_6\text{Cl}_2$ ‘ages’ as one waits for a long time at a fixed temperature. The aging evolution continues on the timescale of at least 10^5 s, occurring only below the transition temperature T^* . Such aging evolution of a spin-state is a crucial feature of a spin glass [120, 121], where a non-equilibrium spin state shows a long-lasting slow relaxation process. The observation of aging

in $\text{ZnCu}_3(\text{OH})_6\text{Cl}_2$ indicates that the witness-spins are in a glassy state at $T < T^*$.

5.4.3 Reproducibility of $\text{ZnCu}_3(\text{OH})_6\text{Cl}_2$ spin noise

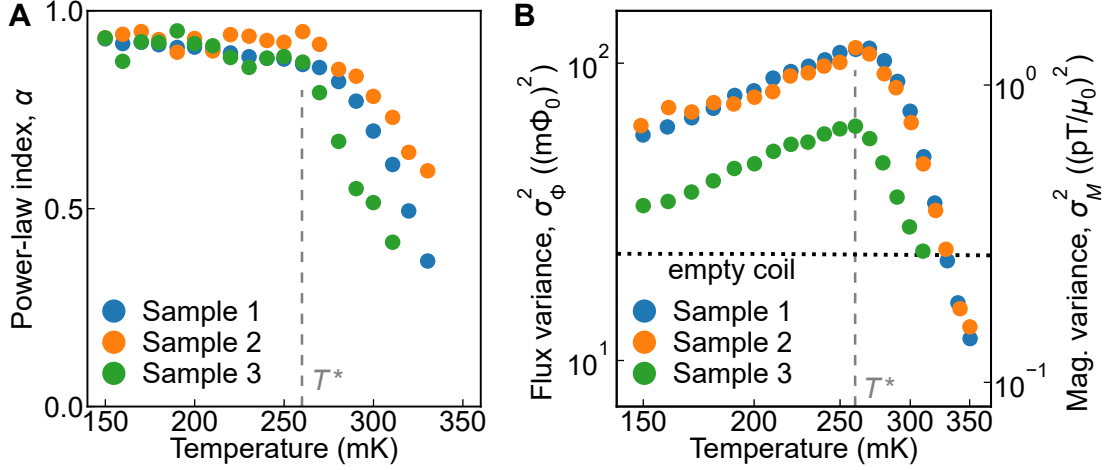


Figure 5.14: Comparison of spin noise from three $\text{ZnCu}_3(\text{OH})_6\text{Cl}_2$ samples and an empty coil. **(A)** Frequency-power-law exponent $\alpha(T)$ obtained by fitting the flux noise power spectral density $S_\Phi(\omega, T) \propto \omega^{-\alpha(T)}$. All three samples show a similar temperature dependence with a behavior change around $T^* = 260$ mK. The fitting range is $0.1 \text{ Hz} \leq \omega/(2\pi) \leq 100 \text{ Hz}$ for Sample 1 and 2. The narrower range $0.1 \text{ Hz} \leq \omega/(2\pi) \leq 10 \text{ Hz}$ is used for Sample 3 as an extra Johnson noise contribution from thermalization wires is observed at high frequency. **(B)** Flux noise variance $\sigma_\Phi^2(T)$. All three samples show a similar temperature dependence with a peak around $T^* = 260$ mK. The variance level of the empty coil, which is subtracted from the $\text{ZnCu}_3(\text{OH})_6\text{Cl}_2$ variances, is indicated by a block dotted line.

The reproducibility of the spin noise phenomena is examined by repeating the spin noise measurements in the three $\text{ZnCu}_3(\text{OH})_6\text{Cl}_2$ samples in Fig. 5.7A. Sample 1 and Sample 2 were measured for c -axis direction while Sample 3 for a -axis. The spin noise measurements of Sample 2 and Sample 3 were performed with the same procedure as the Sample 1 measurement described in Section 5.3.2. The frequency-power-law exponent $\alpha(T)$ obtained by fitting the scale-invariant PSD is shown in Fig. 5.14A. In all three samples, $\alpha(T)$ shows a rapid growth to ~ 1.0 upon cooling to $T^* = 260$ mK, below which the change is only gradual. The flux noise variance $\sigma_\Phi^2(T)$ in Fig. 5.14B shows a comparable temperature dependence for all three samples, with a variance peak around $T^* = 260$ mK. The smaller variance magnitude of Sample 3 can be attributed to the short sample length, which did

not fill up the full pickup-coil length. After scaling the variance of Sample 3 by a simple constant, the variance of all three samples overlap. Thus, the spin noise phenomena in $\text{ZnCu}_3(\text{OH})_6\text{Cl}_2$ are confirmed to be robust. I note that whether the spin noise is isotropic or not requires more careful experimental investigation.

5.5 Discussion

The experimental measurement in $\text{ZnCu}_3(\text{OH})_6\text{Cl}_2$ observes a clear transition at $T^* = 260$ mK in the DC susceptibility, the spin noise PSD, and the aging evolution.⁷

In $\text{ZnCu}_3(\text{OH})_6\text{Cl}_2$, the magnetic contribution of kagome layer is negligible compared to that of witness-spins at low temperature, as evidenced by the decrease of the local kagome susceptibility in nuclear magnetic resonance [101–105]. The low-temperature magnetic behavior in the experiment is naturally attributable to the witness-spins, and therefore can be directly compared to the witness-spin simulation with the spinon-mediated interactions. In both experiment and simulation, the DC susceptibility $\chi(T)$ exhibits the sharp transition cusp at $T^* = 260$ mK freezing the $\sim 33\%$ spin-1/2 contributions altogether (Fig. 5.15A). The Curie-Weiss fitting of the susceptibility above 2 K yields $T_{\text{CW}} = -1.1$ K. The frequency power-law exponent $\alpha(T)$ of the scale-invariant PSD $S(\omega, T) \propto \omega^{-\alpha(T)}$ rapidly approaches ~ 1 upon cooling to $\sim T^*$, below which the change becomes gradual (Fig. 5.15B). The antiferromagnetic correlation observed in neutron scattering [98] and the antiferromagnetic interaction between nearest-neighbor witness-spins derived in the spinon-mediated interaction are in agreement. Thus, all my experimental observations in $\text{ZnCu}_3(\text{OH})_6\text{Cl}_2$ are consistent with the spinon-mediated interactions among witness-spins.

⁷It is striking that the transition at 260 mK has not been detected for twenty years in $\text{ZnCu}_3(\text{OH})_6\text{Cl}_2$. Not many studies have probed low temperatures below 300 mK, likely due to the strong interaction $J \sim 190$ K in the kagome plane. DC susceptibility measurement in Ref. [95] did not observe a cusp down to 100 mK, which could be because a relatively large field of 0.1 T may have suppressed the cusp as in a spin glass $\text{Fe}_x\text{Mn}_{1-x}\text{TiO}_3$ [122]. Specific heat appears to show a slope change around 300 mK [108, 110], but the change is smooth and has not attracted much attention.

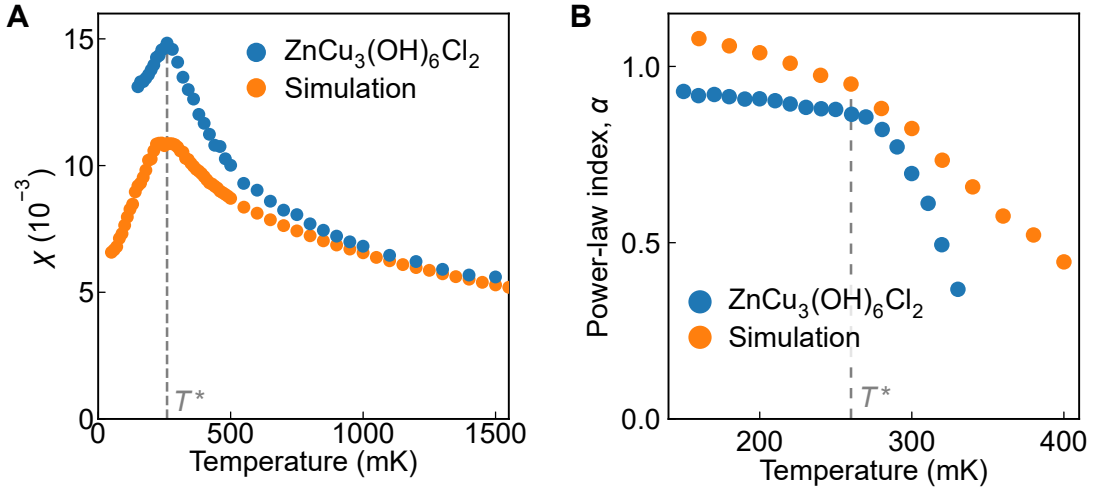


Figure 5.15: Comparison between the $\text{ZnCu}_3(\text{OH})_6\text{Cl}_2$ measurement and the witness-spin simulation with spinon-mediated interactions. (A) DC susceptibility $\chi(T)$ showing a cusp at $T^* = 260$ mK. (B) Frequency-power-law exponent $\alpha(T)$ of the scale-invariant power spectral density $S(\omega, T) \propto \omega^{-\alpha(T)}$. The exponent rapidly approaches ~ 1 upon cooling to $\sim T^*$, below which change of $\alpha(T)$ becomes gradual.

5.5.1 Next developments in simulation and experiment

In the simulation, the increase of $\alpha(T)$ upon cooling is slower. This difference could be resolved by increasing the total Monte Carlo steps that will extend the frequency range of the simulated PSD. The simulated PSD at high temperatures, shown in Fig. 5.4B, shows a gradual slope change at lower frequencies.

To further test the validity of the spinon-mediated interaction model, it would be beneficial to study compounds where the same model applies. For example, Cu-doped Herbertsmithite $\text{Zn}_x\text{Cu}_{4-x}(\text{OH})_6\text{Cl}_2$ ($x = 0.8, 0.9$) with more Cu on the Zn layer [119, 123] and Zn-Barlowite $\text{ZnCu}_3(\text{OH})_6\text{FBr}$ [124] that is discussed to have less Cu/Zn substitution than Herbertsmithite [94], are expected to exhibit the same physics. If the spinon-mediation scenario is correct, the witness-spin simulation with modified parameters will continue to be comparable to the experiment for these compounds.

Nevertheless, the experimental observations in $\text{ZnCu}_3(\text{OH})_6\text{Cl}_2$ are overall consistent with the spinon-mediated interactions among the witness-spins, proposing the underlying quantum spin liquid state within the kagome layer. The predicted

spinon-mediated interactions are based on a gapped $Z_2[0,\pi]\beta$ QSL, a leading contender for the $S = 1/2$ kagome Heisenberg model, with the interaction decay length $R_0 = 0.44d$. The value of R_0 , chosen by comparison with the experiment, could be used to determine the quantitative properties of the presumed $Z_2[0,\pi]\beta$ QSL in the kagome layer. This successful study of the $\text{ZnCu}_3(\text{OH})_6\text{Cl}_2$ witness-spin noise motivates general study on a quantum spin liquid state by exploiting witness-spins, which are naturally or artificially embedded nearby. It also encourages the future development of a spin noise spectrometer to perform local measurements, which will allow a detailed look into the different locations with varying witness-spin densities. Thus, my successful experimental discoveries of the spin noise in $\text{Ca}_{10}\text{Cr}_7\text{O}_{28}$ (Chapter 4) and $\text{ZnCu}_3(\text{OH})_6\text{Cl}_2$ demonstrate that the spin noise approach to fingerprinting spin liquid states, either by direct probing or by witness-spin probing, is a promising research avenue. The spin noise study of many more spin liquid compounds, the further development of the spin noise measurement technique, and last but not least, the analytical and computational spin noise predictions on various spin liquid states are now strongly encouraged.

Appendices

A

Derivations of equations

A.1 Relaxation time distribution for power-law AC susceptibility

Consider a spin ensemble where the relaxation time is distributed as Eq. 2.18. The AC susceptibility of the system will be

$$\chi'(\omega) = \chi^{\text{DC}} \int_{\tau_{\min}}^{\tau_{\max}} d\tau a\tau^{\alpha-1} \frac{1}{1 + \omega^2\tau^2} = \chi^{\text{DC}} \omega^{-\alpha} a \int_{\omega\tau_{\min}}^{\omega\tau_{\max}} dx \frac{x^{\alpha-1}}{1 + x^2}. \quad (\text{A.1})$$

$$\chi''(\omega) = \chi^{\text{DC}} \int_{\tau_{\min}}^{\tau_{\max}} d\tau a\tau^{\alpha-1} \frac{\omega\tau}{1 + \omega^2\tau^2} = \chi^{\text{DC}} \omega^{-\alpha} a \int_{\omega\tau_{\min}}^{\omega\tau_{\max}} dx \frac{x^\alpha}{1 + x^2}. \quad (\text{A.2})$$

The power-law dependences in Eqs. 2.16 and 2.17 are thus obtained, as the ω -dependence of the integral part is no stronger than logarithmic. In the frequency range $\tau_{\min} \ll 1/\omega \ll \tau_{\max}$, for different values of α ,

$$\int_{\omega\tau_{\min}}^{\omega\tau_{\max}} dx \frac{x^{\alpha-1}}{1 + x^2} = \begin{cases} -\log(\omega\tau_{\min}) & (\alpha = 0) \\ \frac{\pi}{2} \frac{1}{\sin(\alpha\pi/2)} & (0 < \alpha \leq 1). \end{cases} \quad (\text{A.3})$$

$$\int_{\omega\tau_{\min}}^{\omega\tau_{\max}} dx \frac{x^\alpha}{1 + x^2} = \begin{cases} \frac{\pi}{2} \frac{1}{\sin((\alpha+1)\pi/2)} & (0 \leq \alpha < 1) \\ \log(\omega\tau_{\max}) & (\alpha = 1). \end{cases} \quad (\text{A.4})$$

A.2 AC susceptibility from Bloch equation

I formally solve the following Bloch equations to derive the AC susceptibility when there are precessional dynamics due to a DC field and relaxational dynamics.

$$\frac{d\mathbf{M}}{dt} = \mu_0\gamma\mathbf{M} \times \mathbf{H} - \frac{\mathbf{M} - \chi^{\text{DC}}\mathbf{H}}{\tau}, \quad (\text{A.5})$$

$$\mathbf{H} = (H_x, 0, H_z(t)) = \text{Re}[(H_x, 0, H_0 e^{i\omega_0 t})], \quad (\text{A.6})$$

where $\gamma = -2\mu_B/\hbar$ for an electron spin, and the oscillating field is perturbative $H_0 \rightarrow 0$. For each Fourier component, the Bloch equation can be expanded as

$$i\omega M_x(\omega) = \mu_0\gamma H_0 M_y(\omega - \omega_0) - \frac{1}{\tau} M_x(\omega) + \frac{\chi^{\text{DC}}}{\tau} H_x \delta(\omega), \quad (\text{A.7})$$

$$i\omega M_y(\omega) = -\mu_0\gamma H_0 M_x(\omega - \omega_0) + \mu_0\gamma H_x M_z(\omega) - \frac{1}{\tau} M_y(\omega), \quad (\text{A.8})$$

$$i\omega M_z(\omega) = -\mu_0\gamma H_x M_y(\omega) - \frac{1}{\tau} M_z(\omega) + \frac{\chi^{\text{DC}}}{\tau} H_0 \delta(\omega - \omega_0). \quad (\text{A.9})$$

One can simplify the equation for $M_z(\omega)$ by substituting $M_x(\omega)$ and $M_y(\omega)$.

$$M_x(\omega) = \frac{1}{i\omega + 1/\tau} \frac{\chi^{\text{DC}}}{\tau} H_x \delta(\omega) + \mathcal{O}(H_0), \quad (\text{A.10})$$

$$M_y(\omega_0) = \frac{1}{i\omega_0 + 1/\tau} (-\mu_0\gamma H_0 M_x(0) + \mu_0\gamma H_x M_z(\omega_0)) \quad (\text{A.11})$$

$$= -\chi^{\text{DC}} \frac{\mu_0\gamma H_x H_0 \delta(0)}{i\omega_0 + 1/\tau} + \frac{\mu_0\gamma H_x}{i\omega_0 + 1/\tau} M_z(\omega_0) + \mathcal{O}(H_0^2), \quad (\text{A.12})$$

$$M_z(\omega_0) = \frac{1}{i\omega_0 + 1/\tau} \left(-\mu_0\gamma H_x M_y(\omega_0) + \frac{\chi^{\text{DC}}}{\tau} H_0 \delta(0) \right) \quad (\text{A.13})$$

$$= \chi^{\text{DC}} \frac{1}{i\omega_0 + 1/\tau} \left(\frac{(\mu_0\gamma H_x)^2}{i\omega_0 + 1/\tau} + \frac{1}{\tau} \right) H_0 \delta(0) - \frac{(\mu_0\gamma H_x)^2}{(i\omega_0 + 1/\tau)^2} M_z(\omega_0) + \mathcal{O}(H_0^2). \quad (\text{A.14})$$

Therefore,

$$M_z(\omega_0) = \frac{1}{1 + \frac{(\mu_0\gamma H_x)^2}{(i\omega_0 + 1/\tau)^2}} \chi^{\text{DC}} \frac{1}{i\omega_0 + 1/\tau} \left(\frac{(\mu_0\gamma H_x)^2}{i\omega_0 + 1/\tau} + \frac{1}{\tau} \right) H_0 \delta(0) + \mathcal{O}(H_0^2), \quad (\text{A.15})$$

$$\chi(\omega_0) = \frac{M_z(\omega_0)}{H_z(\omega_0)} = \frac{1}{1 + \frac{(\mu_0\gamma H_x)^2}{(i\omega_0 + 1/\tau)^2}} \chi^{\text{DC}} \frac{1}{i\omega_0 + 1/\tau} \left(\frac{(\mu_0\gamma H_x)^2}{i\omega_0 + 1/\tau} + \frac{1}{\tau} \right). \quad (\text{A.16})$$

Let us use $\omega_E = \mu_0|\gamma|H_x$ and change the symbol ω_0 to ω to express general frequency.

The expression can be simplified as follows:

$$\chi(\omega) = \chi^{\text{DC}} \frac{\omega_E^2 + (i\omega + 1/\tau)^{\frac{1}{\tau}}}{(i\omega + 1/\tau)^2 + \omega_E^2} \quad (\text{A.17})$$

$$= \chi^{\text{DC}} \frac{\omega_E^2 \tau^2 + (1 + i\omega\tau)}{(1 + i\omega\tau)^2 + \omega_E^2 \tau^2} \quad (\text{A.18})$$

$$= \frac{\chi^{\text{DC}}}{2} \left(\frac{1 - i\omega_E\tau}{1 + i(\omega - \omega_E)\tau} + \frac{1 + i\omega_E\tau}{1 + i(\omega + \omega_E)\tau} \right) \quad (\text{A.19})$$

$$= \frac{\chi^{\text{DC}}}{2} \left(\frac{1 - \omega_E\tau(\omega - \omega_E)\tau - i\omega\tau}{1 + (\omega - \omega_E)^2\tau^2} + \frac{1 + \omega_E\tau(\omega + \omega_E)\tau - i\omega\tau}{1 + (\omega + \omega_E)^2\tau^2} \right). \quad (\text{A.20})$$

The real and imaginary part of the AC susceptibility will then be

$$\text{Re } \chi(\omega) = \frac{\chi^{\text{DC}}}{2} \left(\frac{1 - \omega_E\tau(\omega - \omega_E)\tau}{1 + (\omega - \omega_E)^2\tau^2} + \frac{1 + \omega_E\tau(\omega + \omega_E)\tau}{1 + (\omega + \omega_E)^2\tau^2} \right), \quad (\text{A.21})$$

$$\text{Im } \chi(\omega) = \frac{\chi^{\text{DC}}}{2} \left(\frac{\omega\tau}{1 + (\omega - \omega_E)^2\tau^2} + \frac{\omega\tau}{1 + (\omega + \omega_E)^2\tau^2} \right). \quad (\text{A.22})$$

A.3 Spin noise spectrum from Bloch equation

I formally solve the following Bloch equation to derive the power spectral density of magnetization noise when there are precessional dynamics due to a DC field and relaxational dynamics.

$$\frac{d\mathbf{M}}{dt} = \mu_0\gamma\mathbf{M} \times \mathbf{H} - \frac{\mathbf{M} - \chi^{\text{DC}}\mathbf{H}}{\tau} + \boldsymbol{\xi}, \quad (\text{A.23})$$

$$\mathbf{H} = (H_x, 0, 0), \quad (\text{A.24})$$

$$\boldsymbol{\xi} = \sqrt{\frac{2\sigma_M^2}{\tau}}(\xi_x, \xi_y, \xi_z). \quad (\text{A.25})$$

For each Fourier component, the Bloch equation can be expanded as

$$i\omega M_x(\omega) = -\frac{1}{\tau}M_x(\omega) + \frac{\chi^{\text{DC}}}{\tau}H_x\delta(\omega) + \sqrt{\frac{2\sigma_M^2}{\tau}}\xi_x(\omega), \quad (\text{A.26})$$

$$i\omega M_y(\omega) = +\mu_0\gamma H_x M_z(\omega) - \frac{1}{\tau}M_y(\omega) + \sqrt{\frac{2\sigma_M^2}{\tau}}\xi_y(\omega), \quad (\text{A.27})$$

$$i\omega M_z(\omega) = -\mu_0\gamma H_x M_y(\omega) - \frac{1}{\tau}M_z(\omega) + \sqrt{\frac{2\sigma_M^2}{\tau}}\xi_z(\omega). \quad (\text{A.28})$$

One can simplify the equation for $M_z(\omega)$ by substituting $M_y(\omega)$.

$$M_y(\omega) = \frac{\tau}{1+i\omega\tau} \left(\mu_0\gamma H_x M_z(\omega) + \sqrt{\frac{2\sigma_M^2}{\tau}} \xi_y(\omega) \right), \quad (\text{A.29})$$

$$M_z(\omega) = \frac{\tau}{1+i\omega\tau} \left(\frac{\tau}{1+i\omega\tau} (-\mu_0\gamma H_x)^2 M_z(\omega) - \frac{\tau}{1+i\omega\tau} \mu_0\gamma H_x \sqrt{\frac{2\sigma_M^2}{\tau}} \xi_y(\omega) + \sqrt{\frac{2\sigma_M^2}{\tau}} \xi_z(\omega) \right) \quad (\text{A.30})$$

$$= \left(\frac{\tau}{1+i\omega\tau} \right)^2 \left(-(\mu_0\gamma H_x)^2 M_z(\omega) - \mu_0\gamma H_x \sqrt{\frac{2\sigma_M^2}{\tau}} \xi_y(\omega) + \frac{1+i\omega\tau}{\tau} \sqrt{\frac{2\sigma_M^2}{\tau}} \xi_z(\omega) \right). \quad (\text{A.31})$$

Therefore,

$$M_z(\omega) = \frac{-\mu_0\gamma H_x \sqrt{\frac{2\sigma_M^2}{\tau}} \xi_y + \frac{1+i\omega\tau}{\tau} \sqrt{\frac{2\sigma_M^2}{\tau}} \xi_z}{\frac{(1+i\omega\tau)^2}{\tau^2} + (\mu_0\gamma H_x)^2} \quad (\text{A.32})$$

$$= \frac{\omega_E \tau^2 \sqrt{\frac{2\sigma_M^2}{\tau}} \xi_y + (1+i\omega\tau) \tau \sqrt{\frac{2\sigma_M^2}{\tau}} \xi_z}{(1+i\omega\tau)^2 + \omega_E^2 \tau^2} \quad (\text{A.33})$$

$$= \frac{1}{2} \left(\frac{-i\sqrt{2\sigma_M^2} \tau \xi_y + \sqrt{2\sigma_M^2} \tau \xi_z}{1+i(\omega-\omega_E)\tau} + \frac{i\sqrt{2\sigma_M^2} \tau \xi_y + \sqrt{2\sigma_M^2} \tau \xi_z}{1+i(\omega+\omega_E)\tau} \right), \quad (\text{A.34})$$

$$S_{M_z}(\omega) = \frac{\sigma_{M_z}^2}{\pi} \left(\frac{\tau}{1+(\omega-\omega_E)^2 \tau^2} + \frac{\tau}{1+(\omega+\omega_E)^2 \tau^2} \right). \quad (\text{A.35})$$

A.4 Derivation of fluctuation-dissipation theorem

For a canonical ensemble, the population probability of a microstate $|m\rangle$ with energy $\hbar\omega_m$ is $p_m = \frac{1}{Z} e^{-\hbar\omega_m/(k_B T)}$, where Z is the partition function. Define $M_{mn} =$

$M_{nm}^* = \langle m | \hat{M} | n \rangle$ and $\omega_{mn} = -\omega_{nm} = \omega_m - \omega_n$. The expression of power spectral

density in Eq. 2.50 is expanded as

$$S_M(\omega) = \frac{2}{\pi} \int_0^\infty dt \cos(\omega t) \left\langle \frac{1}{2} \{ \hat{M}(t), \hat{M}(0) \} \right\rangle \quad (\text{A.36})$$

$$= \frac{2}{\pi} \int_0^\infty dt \cos(\omega t) \frac{1}{2} \sum_{mn} p_m \left(e^{i\omega_{mn}t} M_{mn} M_{nm} + e^{i\omega_{nm}t} M_{mn} M_{nm} \right) \quad (\text{A.37})$$

$$= \frac{2}{\pi} \int_0^\infty dt \cos(\omega t) \sum_{mn} p_m \cos(\omega_{mn}t) |M_{mn}|^2 \quad (\text{A.38})$$

$$= \frac{1}{\pi} \int_0^\infty dt \sum_{mn} p_m (\cos(\omega t - \omega_{mn}t) + \cos(\omega t + \omega_{mn}t)) |M_{mn}|^2 \quad (\text{A.39})$$

$$= \frac{1}{\pi} \int_0^\infty dt \sum_{mn} (p_m + p_n) \cos(\omega t - \omega_{mn}t) |M_{mn}|^2 \quad (\text{A.40})$$

$$= \frac{1}{\pi} \int_0^\infty dt \sum_{mn} p_n (1 + e^{-\hbar\omega_{mn}/(k_B T)}) \cos(\omega t - \omega_{mn}t) |M_{mn}|^2 \quad (\text{A.41})$$

$$= \sum_{mn} p_n (1 + e^{-\hbar\omega_{mn}/(k_B T)}) \delta(\omega - \omega_{mn}) |M_{mn}|^2 \quad (\text{A.42})$$

$$= (1 + e^{-\hbar\omega/(k_B T)}) \sum_{mn} p_n \delta(\omega - \omega_{mn}) |M_{mn}|^2. \quad (\text{A.43})$$

The relation $\int_0^\infty dt \cos(\omega t - \omega_{mn}t) = \pi \delta(\omega - \omega_{mn})$ is used. In the same manner, the expression of imaginary susceptibility in Eq. 2.52 is expanded as

$$\chi''(\omega) = V\mu_0 \frac{i}{\hbar} \int_0^\infty dt \sin(\omega t) \left\langle [\hat{M}(t), \hat{M}(0)] \right\rangle \quad (\text{A.44})$$

$$= V\mu_0 \frac{i}{\hbar} \int_0^\infty dt \sin(\omega t) \sum_{mn} p_m \left(e^{i\omega_{mn}t} M_{mn} M_{nm} - e^{i\omega_{nm}t} M_{mn} M_{nm} \right) \quad (\text{A.45})$$

$$= -2V\mu_0 \frac{1}{\hbar} \int_0^\infty dt \sin(\omega t) \sum_{mn} p_m \sin(\omega_{mn}t) |M_{mn}|^2 \quad (\text{A.46})$$

$$= -V\mu_0 \frac{1}{\hbar} \int_0^\infty dt \sum_{mn} p_m (\cos(\omega t - \omega_{mn}t) - \cos(\omega t + \omega_{mn}t)) |M_{mn}|^2 \quad (\text{A.47})$$

$$= -V\mu_0 \frac{1}{\hbar} \int_0^\infty dt \sum_{mn} (p_m - p_n) \cos(\omega t - \omega_{mn}t) |M_{mn}|^2 \quad (\text{A.48})$$

$$= V\mu_0 \frac{1}{\hbar} \int_0^\infty dt \sum_{mn} p_n (1 - e^{-\hbar\omega_{mn}/(k_B T)}) \cos(\omega t - \omega_{mn}t) |M_{mn}|^2 \quad (\text{A.49})$$

$$= V\mu_0 \frac{\pi}{\hbar} \sum_{mn} p_n (1 - e^{-\hbar\omega_{mn}/(k_B T)}) \delta(\omega - \omega_{mn}) |M_{mn}|^2 \quad (\text{A.50})$$

$$= V\mu_0 \frac{\pi}{\hbar} (1 - e^{-\hbar\omega/(k_B T)}) \sum_{mn} p_n \delta(\omega - \omega_{mn}) |M_{mn}|^2. \quad (\text{A.51})$$

The comparison of these two expressions leads to the fluctuation-dissipation theorem

$$\chi''(\omega) = V\mu_0 \frac{\pi}{\hbar} \tanh\left(\frac{\hbar\omega}{2k_B T}\right) S_M(\omega). \quad (\text{A.52})$$

Note that the derived expressions of power spectral density and AC susceptibility based on microstates explicitly reveal the contribution of precessional dynamics at frequencies corresponding to energy excitation.

B

Technical details of spiral spin liquid simulation

B.1 Correspondence between Monte Carlo step and actual time

The correspondence between the Monte Carlo (MC) time and the actual time is determined by comparing the spin-flip rate in the simulation and the experimental observation. Figure B.1 shows the rate of spin flips at each temperature in the spiral spin liquid simulation. As a flip by a tiny angle causes little change to a spin state, spin flips by an angle larger than 5 degrees are only considered. The rate is calculated by counting such spin flips in the first 5×10^4 MC steps of the $L = 40$ system evolution in equilibrium. The spin-flip rate of $0.1 \text{ (MC step)}^{-1}$ at $T \sim 0.15|J_1|$ indicates the elementary local relaxation process at the timescale of approximately $\tau_{\text{elem}} = 10 \text{ (MC step)}$ in the simulation. Ref. [78] reports the AC susceptibility measurement of $\text{Ca}_{10}\text{Cr}_7\text{O}_{28}$ in the form of a Cole-Cole plot in the frequency range from 100 Hz to 20 kHz. Although there is an appreciable deviation at the low frequency, the high-frequency data forms a semicircle with the Cole-Cole parameter 0.05–0.11. This indicates a relatively narrow distribution of relaxation times [64] at the high frequency, say $\omega/(2\pi) \sim 10 \text{ kHz}$. From this measurement, the elementary relaxation process in $\text{Ca}_{10}\text{Cr}_7\text{O}_{28}$ can be estimated

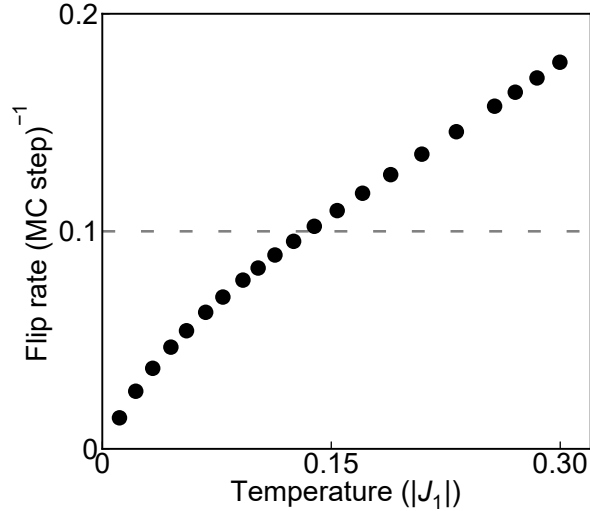


Figure B.1: The rate of spin flips by an angle larger than 5 degrees at each temperature in the spiral spin liquid simulation. This is calculated by counting spin flips in the first 5×10^4 MC steps of the $L = 40$ system evolution in equilibrium. The spin-flip rate of $0.1 \text{ (MC step)}^{-1}$ at $T \sim 0.15|J_1|$ indicates the elementary local relaxation process at the timescale of approximately $\tau_{\text{elem}} = 10 \text{ (MC step)}$.

to be $\tau_{\text{elem}} \sim 10 \mu\text{s}$. By comparing τ_{elem} in the simulation and the experiment, the relation $1 \text{ MC step} = 1 \mu\text{s}$ is obtained.

B.2 Estimate of magnetization noise from spin noise

The magnitude of the magnetization noise corresponding to the average-spin noise in the simulation is estimated as follows. Consider N spins of a magnitude s in a volume V . For large N , the fluctuation amplitude of the average spin $\Delta\bar{\theta}$ and the magnetization $\mu_0\Delta M$ in unit of tesla will approximately follow

$$\Delta\bar{\theta} \propto \frac{s\sqrt{N}}{N} = \frac{s}{\sqrt{N}}, \quad (\text{B.1})$$

$$\mu_0\Delta M \propto \mu_0(2\mu_B) \frac{s\sqrt{N}}{V} = 2\mu_0\mu_B \frac{N}{V} \Delta\bar{\theta}. \quad (\text{B.2})$$

The simulation setup with N^{sim} and s^{sim} can be related to the experimental sample with N^{exp} , s^{exp} , and V^{exp} as

$$\Delta\bar{\theta}^{\text{exp}} = \frac{s^{\text{exp}}}{s^{\text{sim}}} \frac{\sqrt{N^{\text{sim}}}}{\sqrt{N^{\text{exp}}}} \Delta\bar{\theta}^{\text{sim}}, \quad (\text{B.3})$$

$$\mu_0 \Delta M^{\text{exp}} = 2\mu_0 \mu_B \frac{N^{\text{exp}}}{V^{\text{exp}}} \Delta\bar{\theta}^{\text{exp}} = 2\mu_0 \mu_B \frac{s^{\text{exp}}}{s^{\text{sim}}} \frac{\sqrt{N^{\text{sim}} N^{\text{exp}}}}{V^{\text{exp}}} \Delta\bar{\theta}^{\text{sim}}. \quad (\text{B.4})$$

Let us estimate the noise in a $\text{Ca}_{10}\text{Cr}_7\text{O}_{28}$ sample of a volume $V^{\text{exp}} = 2 \text{ nm}^3$. The number density of spin-1/2 Cr^{5+} is 9.4 nm^{-3} i.e. the density of bundled spin-3/2 is 3.1 nm^{-3} , so that $N^{\text{exp}} = 6.2 \times 10^{18}$ and $s^{\text{exp}} = 3/2$. The conversion factor to estimate $\mu_0 \Delta M^{\text{exp}}$ from the simulation result $\Delta\bar{\theta}^{\text{sim}}$ ($N^{\text{sim}} = 1600$ and $s^{\text{sim}} = 1$) is

$$\frac{\mu_0 \Delta M^{\text{exp}}}{\Delta\bar{\theta}^{\text{sim}}} = 2\mu_0 \mu_B \frac{s^{\text{exp}}}{s^{\text{sim}}} \frac{\sqrt{N^{\text{sim}} N^{\text{exp}}}}{V^{\text{exp}}} = 1.7 \times 10^{-9} \text{ T}. \quad (\text{B.5})$$

Thus, the peak-to-peak value of $\bar{\theta} \sim 0.5$ in Fig. 4.5 corresponds to $\mu_0 M \sim 0.9 \text{ nT}$.

B.3 Analysis of noise signal

The simulated SSL noise data at each temperature $\bar{\theta}(t_k, T)$ has the total duration of Γ , with the time interval of Δt between the K points ($0 \leq t_k \leq (K-1)\Delta t$). Note that the analysis method in this section applies to general noise data, including the experimental noise data $\Phi(t_k, T)$.

Calculation of power spectral density from segments

To increase the signal-to-noise ratio of the power spectral density (PSD), I average the calculation results from split segments. The original time sequence $\bar{\theta}(t_k, T)$ is first split into P shorter segments $\bar{\theta}^p(t_k, T)$ ($0 \leq p \leq P-1$). Each segment has the duration $\gamma = \Gamma/P$ and the $K_p = K/P$ data points. The PSD of each segment is calculated using the standard formula as

$$S_{\bar{\theta}^p}(\omega_j, T) = \frac{1}{\pi\gamma} \left| \Delta t \sum_{k=0}^{K_p-1} e^{-i\omega_j t_k} \bar{\theta}^p(t_k, T) \right|^2, \quad (\text{B.6})$$

where $\omega_j/(2\pi) = j/\gamma$ ($0 \leq j \leq K_p/2$). The final PSD is obtained by averaging the PSDs from all the segments as

$$S_{\bar{\theta}}(\omega_j, T) = \frac{1}{P} \sum_{p=0}^{P-1} S_{\bar{\theta}^p}(\omega_j, T). \quad (\text{B.7})$$

The standard error of this segments-averaging can be used as the error bar of the PSD. In the simulation, an average is further taken over 10 independent MC runs to exclude the possible dependence on initial conditions, and the standard error of this independent-run-averaging is used as the error bar. Larger P improves the signal-to-noise ratio but degrades the frequency resolution $\Delta\omega/(2\pi) = 1/\gamma = P/T$.

Filtering of frequency components

Filtering of Fourier components is useful to explore noise properties in a certain frequency range. This is achieved by calculating the Fourier components as

$$\bar{\theta}(\omega_j, T) = \Delta t \sum_{k=0}^{K-1} e^{-i\omega_j t_k} \bar{\theta}(t_k, T), \quad (\text{B.8})$$

setting $\bar{\theta}(\omega_j, T) = 0$ at the frequencies out of interest, and then performing an inverse Fourier transform on the remaining non-zero Fourier components.

C

Spiral spin liquid noise simulation for three-dimensional spins

I performed the spiral spin liquid (SSL) simulation explained in Chapter 4 also for Heisenberg spins. The only difference is the extension of the spin configuration space from two-dimensional XY to three-dimensional Heisenberg, and everything else is kept unchanged: the system size $L = 40$, the SSL Hamiltonian Eq. 4.3, and the simulation methods. Just one independent MC run is performed, so the error bars of the power spectral density are the standard error of averaging the PSDs from the split segments (Appendix B).

The equilibrated spin configurations at four different temperatures in Fig. C.1A illustrate that the spatial spin correlations grow upon cooling also for Heisenberg spins. The power spectral density $S_{\bar{\theta}_x}(\omega_j, T)$ in Fig. C.1B is in a nearly scale-invariant form and exhibits the powerful low-frequency fluctuation. The noise variance $\sigma_{\bar{\theta}_{x,y,z}}^2(T)$ in Fig. C.1C grows down to the crossover peak at $T \sim 0.1|J_1|$, below which it gently drops with the slope of approximately T^1 . These observations demonstrate that the qualitative features of the XY-model SSL noise explained in Chapter 4 arise regardless of the spin dimension. Nevertheless, the XY-spin simulation results reproduce the experimental $\text{Ca}_{10}\text{Cr}_7\text{O}_{28}$ noise quantitatively better.

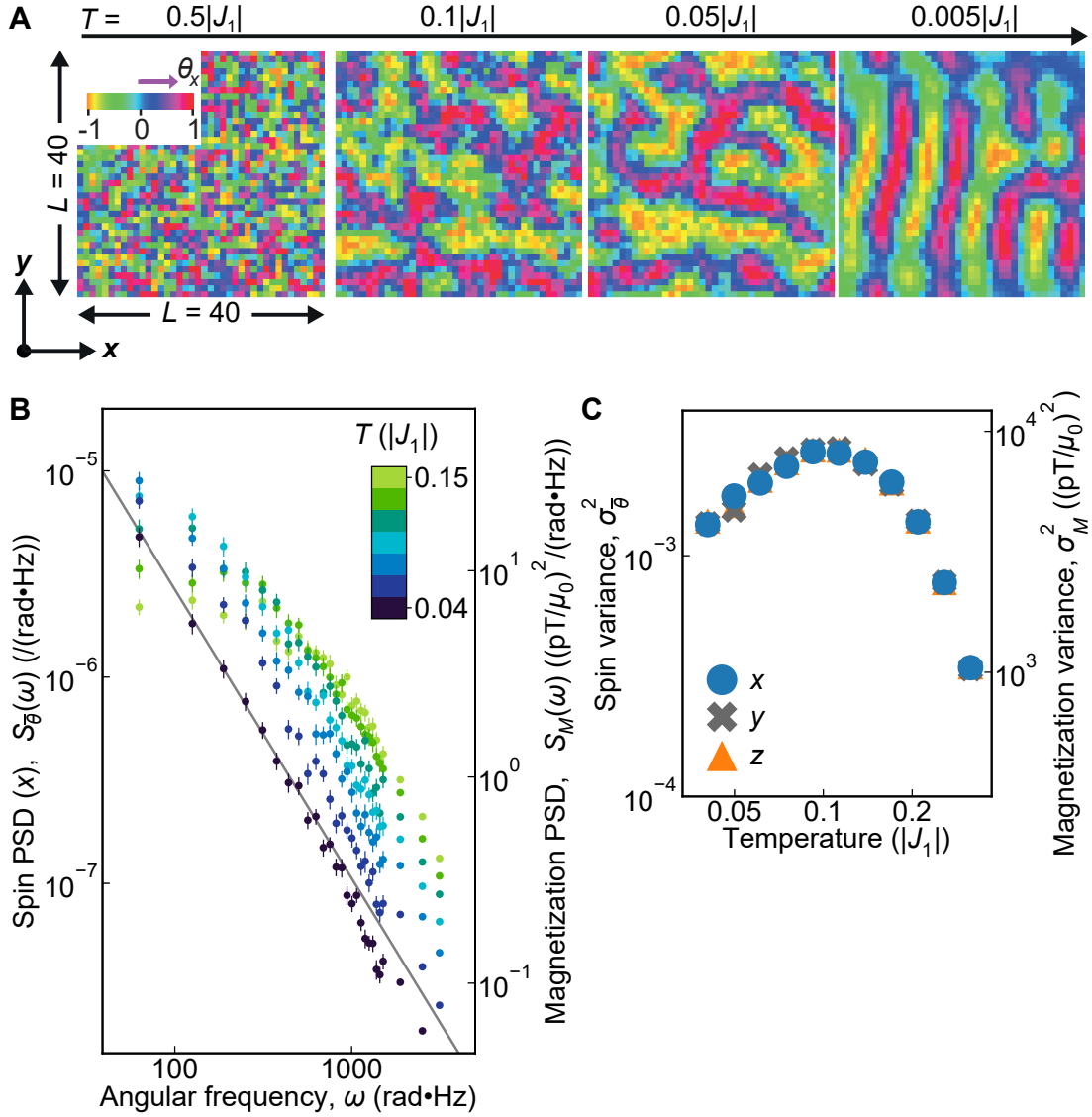


Figure C.1: The results of the $L = 40$ spiral spin liquid Monte Carlo simulation for three-dimensional spins. (A) Visualization of the spins in the equilibration process. The local x -direction spin θ_x is indicated by the corresponding color in the top-left color map. The spatial spin correlation is scarce at the high temperature $T = 0.5|J_1|$ but develops as the system is cooled down to $0.1|J_1|$, $0.05|J_1|$, and $0.005|J_1|$. (B) Power spectral density $S_{\bar{\theta}_x}(\omega_j, T)$ of the simulated spiral spin liquid noise $\bar{\theta}_x(t_k, T)$ for seven selected temperatures. It shows the intense low-frequency fluctuation down to at least 10 Hz with a nearly scale-invariant form. 1 MC time step is taken to be 1 μ s. The error bars are given by the standard error of averaging the power spectral densities from the split segments. The power spectral density $S_M(\omega_j, T)$ of the corresponding magnetization noise estimated from Eq. B.5 is shown on the right-hand axis. $\omega^{-1.4}$ line (gray) is drawn as a guide to the eye. (C) Variance $\sigma_{\bar{\theta}}^2(T)$ of the simulated spiral spin liquid noise $\bar{\theta}_{x,y,z}(t_k, T)$, calculated after filtering out the fluctuations above 1 kHz. The variance increases down to $T \sim 0.1|J_1|$ and then decreases approximately as T^1 . The estimated value of the corresponding magnetization noise variance $\sigma_M^2(T)$ is shown on the right-hand axis.

References

- [1] A. P. Ramirez, Strongly Geometrically Frustrated Magnets, *Annu. Rev. Mater. Sci.* **24**, 453 (1994).
- [2] L. Balents, Spin liquids in frustrated magnets, *Nature* **464**, 199 (2010).
- [3] J. Knolle, R. Moessner, A Field Guide to Spin Liquids, *Annu. Rev. Cond. Mat. Phys.* **10**, 451 (2019).
- [4] C. Broholm *et al.*, Quantum spin liquids, *Science* **367**, eaay0668 (2020).
- [5] S. J. Blundell, Molecular magnets, *Contemp. Phys.* **48**, 275 (2007).
- [6] C. L. Henley, The “Coulomb Phase” in Frustrated Systems, *Annu. Rev. Cond. Mat. Phys.* **1**, 179 (2010).
- [7] H. Yan, O. Benton, A. H. Nevidomskyy, R. Moessner, Classification of classical spin liquids: Detailed formalism and suite of examples, *Phys. Rev. B* **109**, 174421 (2024).
- [8] X.-G. Wen, *Quantum Field Theory of Many-Body Systems* (Oxford Univ. Press, Oxford, UK, 2004).
- [9] K. Roychowdhury, M. J. Lawler, Classification of magnetic frustration and metamaterials from topology, *Phys. Rev. B* **98**, 094432 (2018).
- [10] H. Yan, O. Benton, R. Moessner, A. H. Nevidomskyy, Classification of classical spin liquids: Typology and resulting landscape, *Phys. Rev. B* **110**, L020402 (2024).
- [11] C. Castelnovo, R. Moessner, S. L. Sondhi, Magnetic monopoles in spin ice, *Nature* **451**, 42 (2008).
- [12] C. Castelnovo, R. Moessner, S. Sondhi, Spin Ice, Fractionalization, and Topological Order, *Annu. Rev. Cond. Mat. Phys.* **3**, 35 (2012).
- [13] L. D. C. Jaubert, P. C. W. Holdsworth, Signature of magnetic monopole and Dirac string dynamics in spin ice, *Nat. Phys.* **5**, 258 (2009).
- [14] D. J. P. Morris *et al.*, Dirac Strings and Magnetic Monopoles in the Spin Ice $\text{Dy}_2\text{Ti}_2\text{O}_7$, *Science* **326**, 411 (2009).
- [15] R. Dusad *et al.*, Magnetic monopole noise, *Nature* **571**, 234 (2019).
- [16] T. Fennell *et al.*, Magnetic Coulomb Phase in the Spin Ice $\text{Ho}_2\text{Ti}_2\text{O}_7$, *Science* **326**, 415 (2009).

- [17] D. Bergman, J. Alicea, E. Gull, S. Trebst, L. Balents, Order-by-disorder and spiral spin-liquid in frustrated diamond-lattice antiferromagnets, *Nat. Phys.* **3**, 487 (2007).
- [18] X.-P. Yao, J. Q. Liu, C.-J. Huang, X. Wang, G. Chen, Generic spiral spin liquids, *Front. Phys.* **16**, 53303 (2021).
- [19] S. Gao *et al.*, Spiral Spin Liquid on a Honeycomb Lattice, *Phys. Rev. Lett.* **128**, 227201 (2022).
- [20] S. Gao *et al.*, Spiral spin-liquid and the emergence of a vortex-like state in MnSc_2S_4 , *Nat. Phys.* **13**, 157 (2017).
- [21] J. N. Graham *et al.*, Experimental Evidence for the Spiral Spin Liquid in LiYbO_2 , *Phys. Rev. Lett.* **130**, 166703 (2023).
- [22] H. Yan, J. Reuther, Low-energy structure of spiral spin liquids, *Phys. Rev. Res.* **4**, 023175 (2022).
- [23] H. Takahashi *et al.*, Spiral Spin Liquid Noise, arXiv:2405.02075 (2024).
- [24] L. Savary, L. Balents, Quantum spin liquids: A review, *Rep. Prog. Phys.* **80**, 016502 (2017).
- [25] Y. Zhou, K. Kanoda, T.-K. Ng, Quantum spin liquid states, *Rev. Mod. Phys.* **89**, 25003 (2017).
- [26] A.Yu. Kitaev, Fault-tolerant quantum computation by anyons, *Ann. Phys. (NY)* **303**, 2 (2003).
- [27] M. Hermanns, I. Kimchi, J. Knolle, Physics of the Kitaev Model: Fractionalization, Dynamic Correlations, and Material Connections, *Annu. Rev. Cond. Mat. Phys.* **9**, 17 (2018).
- [28] E. Lieb, T. Schultz, D. Mattis, Two Soluble Models of an Antiferromagnetic Chain, *Ann. Phys. (NY)* **16**, 407 (1961).
- [29] I. Affleck, T. Kennedy, E. H. Lieb, H. Tasaki, Rigorous results on valence-bond ground states in antiferromagnets, *Phys. Rev. Lett.* **59**, 799 (1987).
- [30] C. Dasgupta, S.-k. Ma, Low-temperature properties of the random Heisenberg antiferromagnetic chain, *Phys. Rev. B* **22**, 1305 (1980).
- [31] D. S. Fisher, Random antiferromagnetic quantum spin chains, *Phys. Rev. B* **50**, 3799 (1994).
- [32] I. Kimchi, A. Nahum, T. Senthil, Valence Bonds in Random Quantum Magnets: Theory and Application to YbMgGaO_4 , *Phys. Rev. X* **8**, 031028 (2018).
- [33] L. Liu, H. Shao, Y.-C. Lin, W. Guo, A. W. Sandvik, Random-Singlet Phase in Disordered Two-Dimensional Quantum Magnets, *Phys. Rev. X* **8**, 041040 (2018).

- [34] I. Kimchi, J. P. Sheckelton, T. M. McQueen, P. A. Lee, Scaling and data collapse from local moments in frustrated disordered quantum spin systems, *Nat. Commun.* **9**, 4367 (2018).
- [35] K. Binder, A. P. Young, Spin glasses: Experimental facts, theoretical concepts, and open questions, *Rev. Mod. Phys.* **58**, 801 (1986).
- [36] J. A. Mydosh, Spin glasses: Redux: An updated experimental/materials survey, *Rep. Prog. Phys.* **78**, 052501 (2015).
- [37] E. R. Kassner *et al.*, Supercooled spin liquid state in the frustrated pyrochlore $\text{Dy}_2\text{Ti}_2\text{O}_7$, *Proc. Nat. Acad. Sci. USA* **112**, 8549 (2015).
- [38] A. M. Samarakoon *et al.*, Structural magnetic glassiness in the spin ice $\text{Dy}_2\text{Ti}_2\text{O}_7$, *Phys. Rev. Res.* **4**, 033159 (2022).
- [39] V. Raban, L. Berthier, P. C. W. Holdsworth, Violation of the fluctuation-dissipation theorem and effective temperatures in spin ice, *Phys. Rev. B* **105**, 134431 (2022).
- [40] J. Yang *et al.*, Spin jam induced by quantum fluctuations in a frustrated magnet, *Proc. Nat. Acad. Sci. USA* **112**, 11519 (2015).
- [41] A. Samarakoon *et al.*, Aging, memory, and nonhierarchical energy landscape of spin jam, *Proc. Nat. Acad. Sci. USA* **113**, 11806 (2016).
- [42] G. Parisi, Order Parameter for Spin-Glasses, *Phys. Rev. Lett.* **50**, 1946 (1983).
- [43] N. D. Andriushin *et al.*, Observation of the spiral spin liquid in a triangular-lattice material, arXiv:2410.04954 (2024).
- [44] H.-J. Mikeska, A. K. Kolezhuk, *Quantum Magnetism* (Springer-Verlag Berlin, Heidelberg, 2004), pp. 1–83.
- [45] S. E. Nagler, D. A. Tennant, R. A. Cowley, T. G. Perring, S. K. Satija, Spin dynamics in the quantum antiferromagnetic chain compound KCuF_3 , *Phys. Rev. B* **44**, 12361 (1991).
- [46] M. Mourigal *et al.*, Fractional spinon excitations in the quantum Heisenberg antiferromagnetic chain, *Nat. Phys.* **9**, 435 (2013).
- [47] M. R. Norman, *Colloquium* : Herbertsmithite and the search for the quantum spin liquid, *Rev. Mod. Phys.* **88**, 041002 (2016).
- [48] P. Mendels, F. Bert, Quantum kagome frustrated antiferromagnets: One route to quantum spin liquids, *C. R. Physique* **17**, 455 (2016).
- [49] G. M. Bruun, B. M. Andersen, E. Demler, A. S. Sørensen, Probing Spatial Spin Correlations of Ultracold Gases by Quantum Noise Spectroscopy, *Phys. Rev. Lett.* **102**, 030401 (2009).
- [50] S. Chatterjee, J. F. Rodriguez-Nieva, E. Demler, Diagnosing phases of magnetic insulators via noise magnetometry with spin qubits, *Phys. Rev. B* **99**, 104425 (2019).

- [51] J. Y. Khoo, F. Pientka, I. Sodemann, The universal shear conductivity of Fermi liquids and spinon Fermi surface states and its detection via spin qubit noise magnetometry, *New J. Phys.* **23**, 113009 (2021).
- [52] J. Y. Khoo, F. Pientka, P. A. Lee, I. S. Villadiego, Probing the quantum noise of the spinon Fermi surface with NV centers, *Phys. Rev. B* **106**, 115108 (2022).
- [53] P. A. Lee, S. Morampudi, Proposal to detect emergent gauge field and its Meissner effect in spin liquids using NV centers, *Phys. Rev. B* **107**, 195102 (2023).
- [54] J. Atalaya, J. Clarke, G. Schön, A. Shnirman, Flux $1/f^\alpha$ noise in two-dimensional Heisenberg spin glasses: Effects of weak anisotropic interactions, *Phys. Rev. B* **90**, 014206 (2014).
- [55] K. Agarwal, E. Demler, I. Martin, $1/f^\alpha$ noise and generalized diffusion in random Heisenberg spin systems, *Phys. Rev. B* **92**, 184203 (2015).
- [56] F. K. K. Kirschner, F. Flicker, A. Yacoby, N. Y. Yao, S. J. Blundell, Proposal for the detection of magnetic monopoles in spin ice via nanoscale magnetometry, *Phys. Rev. B* **97**, 140402 (2018).
- [57] K. Agarwal *et al.*, Magnetic noise spectroscopy as a probe of local electronic correlations in two-dimensional systems, *Phys. Rev. B* **95**, 155107 (2017).
- [58] J. F. Rodriguez-Nieva *et al.*, Probing one-dimensional systems via noise magnetometry with single spin qubits, *Phys. Rev. B* **98**, 195433 (2018).
- [59] N. A. Sinitsyn, Y. V. Pershin, The theory of spin noise spectroscopy: A review, *Rep. Prog. Phys.* **79**, 106501 (2016).
- [60] G. G. Kozlov, I. I. Ryzhov, A. V. Kavokin, V. Zapasskii, Development of laser spectroscopy of spin noise, *Phys.-Uspekhi* **67**, 251 (2024).
- [61] J. F. Barry *et al.*, Sensitivity optimization for NV-diamond magnetometry, *Rev. Mod. Phys.* **92**, 015004 (2020).
- [62] A. M. Samarakoon *et al.*, Anomalous magnetic noise in an imperfectly flat landscape in the topological magnet $\text{Dy}_2\text{Ti}_2\text{O}_7$, *Proc. Nat. Acad. Sci. USA* **119**, e2117453119 (2022).
- [63] J. N. Hallén, S. A. Grigera, D. A. Tennant, C. Castellano, R. Moessner, Dynamical fractal and anomalous noise in a clean magnetic crystal, *Science* **378**, 1218 (2022).
- [64] C. V. Topping, S. J. Blundell, A.C. susceptibility as a probe of low-frequency magnetic dynamics, *J. Phys.: Condens. Matter* **31**, 013001 (2019).
- [65] J. Snyder *et al.*, Low-temperature spin freezing in the $\text{Dy}_2\text{Ti}_2\text{O}_7$ spin ice, *Phys. Rev. B* **69**, 064414 (2004).
- [66] S. Kogan, *Electronic Noise and Fluctuations in Solids* (Cambridge University Press, Cambridge, 1996), pp. 203–286.

- [67] K. S. Thorne, R. D. Blandford, *Modern Classical Physics: Optics, Fluids, Plasmas, Elasticity, Relativity, and Statistical Physics* (Princeton University Press, Princeton, 2017), pp. 283–346.
- [68] J. Clarke, A. I. Braginski, *The SQUID Handbook Fundamentals and Technology of SQUIDS and SQUID Systems*, vol. 1 (Wiley-VCH, Weinheim, 2006).
- [69] Y. Zhang, H. Dong, H.-J. Krause, G. Zhang, X. Xie, *SQUID Readout Electronics and Magnetometric Systems for Practical Applications* (Wiley-VCH, Weinheim, 2020), first edn.
- [70] J. Dasini *et al.*, Discovery of Dynamical Heterogeneity in a Supercooled Magnetic Monopole Fluid, arXiv:2408.00460 (2024).
- [71] F. Li, S. A. Crooker, N. A. Sinitsyn, Higher-order spin-noise spectroscopy of atomic spins in fluctuating external fields, *Phys. Rev. A* **93**, 033814 (2016).
- [72] J. R. Claycomb, J. H. Miller, Superconducting magnetic shields for SQUID applications, *Rev. Sci. Instrum.* **70**, 4562 (1999).
- [73] J. F. Fagnard, B. Vanderheyden, E. Pardo, P. Vanderbemden, Magnetic shielding of various geometries of bulk semi-closed superconducting cylinders subjected to axial and transverse fields, *Supercond. Sci. Technol.* **32**, 074007 (2019).
- [74] F. Pobell, *Matter and Methods at Low Temperatures* (Springer-Verlag Berlin, Heidelberg, 2007), third edn.
- [75] J. Sonnenschein *et al.*, Signatures for spinons in the quantum spin liquid candidate $\text{Ca}_{10}\text{Cr}_7\text{O}_{28}$, *Phys. Rev. B* **100**, 174428 (2019).
- [76] D. Rothfuß, A. Reiser, A. Fleischmann, C. Enss, Noise thermometry at ultra low temperatures, *Appl. Phys. Lett.* **103**, 052605 (2013).
- [77] C. Balz *et al.*, Crystal growth, structure and magnetic properties of $\text{Ca}_{10}\text{Cr}_7\text{O}_{28}$, *J. Phys.: Condens. Matter* **29**, 225802 (2017).
- [78] C. Balz *et al.*, Physical realization of a quantum spin liquid based on a complex frustration mechanism, *Nat. Phys.* **12**, 942 (2016).
- [79] C. Balz *et al.*, Magnetic Hamiltonian and phase diagram of the quantum spin liquid $\text{Ca}_{10}\text{Cr}_7\text{O}_{28}$, *Phys. Rev. B* **95**, 174414 (2017).
- [80] R. Pohle, H. Yan, N. Shannon, Theory of $\text{Ca}_{10}\text{Cr}_7\text{O}_{28}$ as a bilayer breathing-kagome magnet: Classical thermodynamics and semiclassical dynamics, *Phys. Rev. B* **104**, 024426 (2021).
- [81] J. Crossley, C. Hooley, Origin of the intermediate-temperature magnetic specific heat capacity in the spin-liquid candidate $\text{Ca}_{10}\text{Cr}_7\text{O}_{28}$, *Phys. Rev. B* **109**, 165138 (2024).
- [82] S. Biswas, K. Damle, Semiclassical theory for liquidlike behavior of the frustrated magnet $\text{Ca}_{10}\text{Cr}_7\text{O}_{28}$, *Phys. Rev. B* **97**, 115102 (2018).

- [83] A. Kshetrimayum, C. Balz, B. Lake, J. Eisert, Tensor network investigation of the double layer Kagome compound $\text{Ca}_{10}\text{Cr}_7\text{O}_{28}$, *Ann. Phys. (NY)* **421**, 168292 (2020).
- [84] F. L. Buessen, M. Hering, J. Reuther, S. Trebst, Quantum Spin Liquids in Frustrated Spin-1 Diamond Antiferromagnets, *Phys. Rev. Lett.* **120**, 057201 (2018).
- [85] N. Niggemann, M. Hering, J. Reuther, Classical spiral spin liquids as a possible route to quantum spin liquids, *J. Phys.: Condens. Matter* **32**, 024001 (2020).
- [86] Z. Nussinov, Avoided phase transitions and glassy dynamics in geometrically frustrated systems and non-Abelian theories, *Phys. Rev. B* **69**, 014208 (2004).
- [87] T. Shimokawa, H. Kawamura, Ripple State in the Frustrated Honeycomb-Lattice Antiferromagnet, *Phys. Rev. Lett.* **123**, 057202 (2019).
- [88] L. W. Lee, A. P. Young, Large-scale Monte Carlo simulations of the isotropic three-dimensional Heisenberg spin glass, *Phys. Rev. B* **76**, 024405 (2007).
- [89] A. Balodhi, Y. Singh, Synthesis and pressure and field-dependent magnetic properties of the kagome-bilayer spin liquid $\text{Ca}_{10}\text{Cr}_7\text{O}_{28}$, *Phys. Rev. Mater.* **1**, 024407 (2017).
- [90] M. P. Shores, E. A. Nytko, B. M. Bartlett, D. G. Nocera, A structurally perfect $S = 1/2$ kagomé antiferromagnet, *J. Am. Chem. Soc.* **127**, 13462 (2005).
- [91] S.-H. Lee *et al.*, Quantum-spin-liquid states in the two-dimensional kagome antiferromagnets $\text{Zn}_x\text{Cu}_{4-x}(\text{OH})_6\text{Cl}_2$, *Nat. Mater.* **6**, 853 (2007).
- [92] M. A. de Vries, K. V. Kamenev, W. A. Kockelmann, J. Sanchez-Benitez, A. Harrison, Magnetic ground state of an experimental $S = 1/2$ kagome antiferromagnet, *Phys. Rev. Lett.* **100**, 157205 (2008).
- [93] D. E. Freedman *et al.*, Site Specific X-ray Anomalous Dispersion of the Geometrically Frustrated Kagomé Magnet, Herbertsmithite, $\text{ZnCu}_3(\text{OH})_6\text{Cl}_2$, *J. Am. Chem. Soc.* **132**, 16185 (2010).
- [94] R. W. Smaha *et al.*, Site-specific structure at multiple length scales in kagome quantum spin liquid candidates, *Phys. Rev. Mater.* **4**, 124406 (2020).
- [95] F. Bert *et al.*, Low temperature magnetization of the $S = 1/2$ kagome antiferromagnet $\text{ZnCu}_3(\text{OH})_6\text{Cl}_2$, *Phys. Rev. B* **76**, 132411 (2007).
- [96] Z. Hiroi, H. Yoshida, Y. Okamoto, M. Takigawa, Spin-1/2 kagome compounds: Volborthite vs Herbertsmithite, *J. Phys. Conf. Ser.* **145**, 012002 (2009).
- [97] T. Han, S. Chu, Y. S. Lee, Refining the Spin Hamiltonian in the Spin-1/2 Kagome Lattice Antiferromagnet $\text{ZnCu}_3(\text{OH})_6\text{Cl}_2$ Using Single Crystals, *Phys. Rev. Lett.* **108**, 157202 (2012).

- [98] T.-H. Han *et al.*, Correlated impurities and intrinsic spin-liquid physics in the kagome material herbertsmithite, *Phys. Rev. B* **94**, 060409 (2016).
- [99] Q. Barthélemy *et al.*, Specific Heat of the Kagome Antiferromagnet Herbertsmithite in High Magnetic Fields, *Phys. Rev. X* **12**, 011014 (2022).
- [100] H. Murayama *et al.*, Universal scaling of specific heat in the $S = 1/2$ quantum kagome antiferromagnet herbertsmithite, *Phys. Rev. B* **106**, 174406 (2022).
- [101] T. Imai, E. A. Nytko, B. M. Bartlett, M. P. Shores, D. G. Nocera, ^{63}Cu , ^{35}Cl , and ^1H NMR in the $S = 1/2$ Kagome Lattice $\text{ZnCu}_3(\text{OH})_6\text{Cl}_2$, *Phys. Rev. Lett.* **100**, 077203 (2008).
- [102] A. Olariu *et al.*, ^{17}O NMR Study of the Intrinsic Magnetic Susceptibility and Spin Dynamics of the Quantum Kagome Antiferromagnet $\text{ZnCu}_3(\text{OH})_6\text{Cl}_2$, *Phys. Rev. Lett.* **100**, 87202 (2008).
- [103] T. Imai, M. Fu, T. H. Han, Y. S. Lee, Local spin susceptibility of the $S = 1/2$ kagome lattice in $\text{ZnCu}_3(\text{OD})_6\text{Cl}_2$, *Phys. Rev. B* **84**, 020411 (2011).
- [104] M. Fu, T. Imai, T.-H. Han, Y. S. Lee, Evidence for a gapped spin-liquid ground state in a kagome Heisenberg antiferromagnet, *Science* **350**, 655 (2015).
- [105] P. Khuntia *et al.*, Gapless ground state in the archetypal quantum kagome antiferromagnet $\text{ZnCu}_3(\text{OH})_6\text{Cl}_2$, *Nat. Phys.* **16**, 469 (2020).
- [106] A. Pustogow *et al.*, Nature of optical excitations in the frustrated kagome compound herbertsmithite, *Phys. Rev. B* **96**, 241114 (2017).
- [107] A. Zorko *et al.*, Symmetry Reduction in the Quantum Kagome Antiferromagnet Herbertsmithite, *Phys. Rev. Lett.* **118**, 017202 (2017).
- [108] Y. Y. Huang *et al.*, Heat Transport in Herbertsmithite: Can a Quantum Spin Liquid Survive Disorder?, *Phys. Rev. Lett.* **127**, 267202 (2021).
- [109] T.-H. Han *et al.*, Fractionalized excitations in the spin-liquid state of a kagome-lattice antiferromagnet, *Nature* **492**, 406 (2012).
- [110] J. S. Helton *et al.*, Spin dynamics of the spin-1/2 kagome lattice antiferromagnet $\text{ZnCu}_3(\text{OH})_6\text{Cl}_2$, *Phys. Rev. Lett.* **98**, 107204 (2007).
- [111] G. J. Nilsen, M. A. de Vries, J. R. Stewart, A. Harrison, H. M. Rønnow, Low-energy spin dynamics of the $s = 1/2$ kagome system herbertsmithite, *J. Phys.: Condens. Matter* **25**, 106001 (2013).
- [112] J. Wang *et al.*, Emergence of spin singlets with inhomogeneous gaps in the kagome lattice Heisenberg antiferromagnets Zn-barlowite and herbertsmithite, *Nat. Phys.* **17**, 1109 (2021).
- [113] D. V. Pilon *et al.*, Spin-Induced Optical Conductivity in the Spin-Liquid Candidate Herbertsmithite, *Phys. Rev. Lett.* **111**, 127401 (2013).
- [114] J. S. Helton *et al.*, Dynamic Scaling in the Susceptibility of the Spin-1/2 Kagome Lattice Antiferromagnet Herbertsmithite, *Phys. Rev. Lett.* **104**, 147201 (2010).

- [115] H. F. Legg, B. Braunecker, Spin liquid mediated RKKY interaction, *Sci. Rep.* **9**, 17697 (2019).
- [116] Y.-M. Lu, Y. Ran, P. A. Lee, Z_2 spin liquids in the $S = 1/2$ Heisenberg model on the kagome lattice: A projective symmetry-group study of Schwinger fermion mean-field states, *Phys. Rev. B* **83**, 224413 (2011).
- [117] S. Yan, D. A. Huse, S. R. White, Spin-Liquid Ground State of the $S = 1/2$ Kagome Heisenberg Antiferromagnet, *Science* **332**, 1173 (2011).
- [118] K. H. Fischer, J. A. Hertz, *Spin Glasses* (Cambridge University Press, Cambridge, 1991), first edn.
- [119] T. H. Han *et al.*, Synthesis and characterization of single crystals of the spin-1/2 kagome-lattice antiferromagnets $Zn_xCu_{4-x}(OH)_6Cl_2$, *Phys. Rev. B* **83**, 100402 (2011).
- [120] E. Vincent, *Ageing and the Glass Transition*, M. Henkel, M. Pleimling, R. Sanctuary, eds., no. 716 in Lecture Notes in Physics (Springer, Berlin, Heidelberg, 2007), pp. 7–60.
- [121] M. Ocio, H. Bouchiat, P. Monod, Observation of $1/f$ magnetic fluctuations in spin glasses, *J. Magn. Magn. Mater.* **54–57**, 11 (1986).
- [122] H. Aruga Katori, A. Ito, Experimental Study of the de Almeida-Thouless Line by Using Typical Ising Spin-Glass $Fe_xMn_{1-x}TiO_3$ with $x = 0.41, 0.50, 0.55$ and 0.57 , *J. Phys. Soc. Japan* **63**, 3122 (1994).
- [123] M. Velazquez *et al.*, Aqueous solution growth at 200 °C and characterizations of pure, ^{17}O - or D- based herbertsmithite $Zn_xCu_{4-x}(OH)_6Cl_2$ single crystals, *J. Cryst. Growth* **531**, 125372 (2020).
- [124] Z. Feng *et al.*, Gapped Spin-1/2 Spinon Excitations in a New Kagome Quantum Spin Liquid Compound $Cu_3Zn(OH)_6FBr$, *Chin. Phys. Lett.* **34**, 077502 (2017).